Optimization and Novel Applications of Luminescent Solar Concentrators

by

Martyn James Fisher

Submitted for the degree of

Doctor of Philosophy

From the Department of Physics

Imperial College London

November 2013

Abstract

The luminescent solar concentrator (LSC) was first proposed in the 1970s as a means to reduce the high cost of generating solar energy. The basic design was simple: a large transparent plate doped with an appropriate luminescent material which is able to absorb both direct and diffuse sunlight, and then guide photons produced by photoluminescence to its narrow edges where they are converted by photovoltaic cells. Unfortunately, the LSC has suffered from numerous efficiency losses and short lifetimes. Therefore, new luminescent species and novel approaches are needed for its practical application.

Novel luminescent species studied in this thesis include arrays of vertical, self-aligned CdSe/CdS nanorods. The nanorods emit preferentially in the waveguiding plane and were characterised to ascertain the extent of self-alignment, and to determine their viability and this alignment technique for LSCs. Furthermore, a number of generations of bio-derived Phycobillisomes, a light absorbing pigment found in species of red algae, have been also been investigated and are a possible source of cheap and abundant luminescent material. Lastly, several luminescent species consisting of metal complexes and oligomers with high Stokes-shift were investigated. High Stokes-shift materials are essential if LSC efficiencies are to be increased as they mitigate the re-absorption that generally constitutes the dominant loss mechanism.

This thesis features two novel LSC applications. The first is a large area, flexible LSC system for portable power generation. Computational raytrace simulations reveal the device is feasible but will require high Stokes-shift materials. The second novel approach utilises a tandem LSC system in conjunction with a photoelectrochemical cell (PEC). In the tandem design the upper concentrator provides blue light to excite a Fe_2O_3 photoanode for water oxidation while the lower concentrator provides red light that is converted by Si cells producing sufficient voltage to enable hydrogen production at a Pt electrode contained within the PEC.

Declaration of Originality

I, Martyn Fisher, Declare that the work in this thesis: “Optimization and Novel Applications of Luminescent Solar Concentrators”, is my own work, with the exception of the material which has been referenced. Any contribution(s) my collaborators have been acknowledge, where applicable, in this thesis.

Copyright Declaration

‘The copyright of this thesis rests with the author and is made available under a Creative Commons Attribution Non-Commercial No Derivatives licence. Researchers are free to copy, distribute or transmit the thesis on the condition that they attribute it, that they do not use it for commercial purposes and that they do not alter, transform or build upon it. For any reuse or redistribution, researchers must make clear to others the licence terms of this work’

Acknowledgements

There are many people who I would like to acknowledge for their help and support throughout the course of my PhD. Firstly, my primary and secondary supervisors, Amanda Chatten and Paul Stavrinou, whose support, guidance and wisdom has allowed me to carry out this PhD, and allowed me to do some very interesting research. Special thanks should also go to Daniel Farrell, for being an excellent mentor, friend and source of knowledge and ideas; without him PhD life would have been far less exciting. Of course I would also like to thank all the other members of the quantum photovoltaics group at Imperial College, as well as members of Paul Stavrinou's group and Sachetan Tuladhar, who were always a valuable source of knowledge and fun! Ned Ekins-Daukes in particular was a great source of support throughout my PhD, and always helped to keep me focused at times when PhD life became stressful.

I have also had the opportunity to collaborate with a number of great people during the course of this PhD, and particular thanks should go out to Robert Walters and his team at the Naval Research Laboratory for sharing knowledge, equipment, funding and for being great fun to be around. Andreas Buechtemann from the Fraunofer Institute, has been an excellent supplier of LSC samples, and advice related to thin-film manufacturing techniques. Lastly, I wish to thank Federico Pesci, for teaching me about photoelectrochemical cells, and for all our entertaining conversations!

I would also like to thank my family and friends for their encouragement and support, in particular; my parents, my girlfriend Jingjing Li, and my friends, Daniel Farrell, Alvin Chan, Ye Xiao and Sophie Li.

I also thank the Engineering and Physical Sciences research Council and the Office of Naval Research Global for their funding during my PhD.

Abbreviations

AM	Air Mass
AR	Anti-Reflection
α-SI	Amorphous Silicon
BIPV	Building Integrated Photovoltaics
CoII	Cobalt Phosphate
CPV	Concentrator Photovoltaics
CW	Continuous Wave
EM	Electromagnetic
EQE	External Quantum Efficiency
EU	European Union
FIT's	Feed-in-Tariff's
FRET	Förster Resonant Energy Transfer
IPCE	Incident Photon to Current Efficiency
IR	Infrared
LQY	Luminescent Quantum Yield
LSC	Luminescent Solar Concentrator
MO	Microscope Objective
OPV	Organic Photovoltaics
OOS	Ocean Optics Spetrometer
PL	Photoluminescence
PLE	Photoluminescent Efficiency
PMMA	Poly(methyl methacrylate)
PEEK	Polyether ether ketone
PIF	Polyindinoflurene
PIF-DBT	poly(6,6',12,12'-tetraoctylindeno[fluorine-co-4,7-bis(2-thienyl)-2,1,3-benzothiadiazole)

PIF-DTP	poly(6,6',12,12'-tetraoctylindeno[fluorine-co-4,7-bis(2-thienyl)-2,1,3-benzothiadiazole)
PV	Photovoltaics
PF	Polyfluorenes
QE	Quantum Efficiency
REE	Rare Earth Element
RPM	Revolutions per Minute
R-PE	R- Phycoerythrin
SGP	Second Generation Phycobillisomes
SP	Surface Plasmon
SPP	Surface Plasmon Polariton
SPV	Space Photovoltaics
ST	Solar Thermal
THF	Tetrahydrofuran
UV	Ultra Violet
Vis	Visible
WBC	Wire-Bar Coater

List of Symbols

η_{opt}	Optical Efficiency
P_E	Total number of photons emitted from edge
P_T	Total number of photons
C_G	Geometric Concentration
A_E	Area Edge(s)
A_S	Area Surface
l	Length
w	Width
d	Depth
C_p	Photon Concentration
ϕ_E	Photon Flux from LSC Edge(s)
ϕ_S	Photon Flux Entering LSC Surface
T	Transmission
S	Scatter
I	Intensity of Transmitted Light
I_0	Intensity of Incident Light
A	Absorbance
ε	Extinction Coefficient
c_{mol}	Molar Concentration
α	Absorption Coefficient
n	Refractive Index
θ_t	Angle of Refraction
θ_i	Angle of Incidence
R_s	*S*-polarised Reflection
R_p	*P*-polarised Reflection
R	Distance between Donor and Acceptor Molecule
R_0	Förster Radius

E_{FRET}	Förster Resonant Energy Transfer Efficiency
v	Velocity of Light in a Given Material
η_{trap}	Photon Trapping efficiency
Ω_{escape}	Solid Angle of Escape Cone
η_{escape}	Fraction of Escaping Photons
Ω_{total}	Solid Angle of a Sphere, 4π
E_g	Bandgap Energy
E_f	Energy Final State
E_i	Energy Initial State
E_p	Photon Energy
h	Planks Constant
ω	Angular Frequency
$W_{i\rightarrow f}$	Fermi's golden rule
n_{eff}	Effective Refractive Index
n_H	Refractive Index of Higher Index Material
n_L	Refractive Index of Lower Index Material
F_L	Volume Fraction of Lower Index Material
Ω_{escape}	Escape Cone Solid Angle
I_{ref}	Reflected Light Intensity
I_{inc}	Incident Light Intensity
U_{op}	Operating Potential
J_{op}	Operating Current

Contents

Abstract……2

Declaration of Originality……3

Copyright Declaration……4

Acknowledgements……..5

Abbreviations……...6

List of Symbols……8

List of Figures……15

List of Tables……...21

Chapter 1: Introduction……22

1.1 The Need for Renewable Energy……..22

1.2 Solar Energy……...28

1.3 The Luminescent Solar Concentrator……..31

Chapter 2: LSC Properties and Operation……39

2.1 Introduction……39

2.2 The Solar Energy Spectrum.....39

2.3 Spectral Units (Flux and Power)……..……44

2.4 Principal LSC Concepts…….……44

2.4.1 Optical Efficiency…….44

2.4.2 Geometric Concentration…….45

2.4.3 Photon Concentration ……..45

2.4.4 Photon Absorption & Waveguiding…….46

2.5 Luminescent Centres (Absorption and Emission)……...52

2.5.1 Absorption and Emission of Inorganic Nanocrystals ……..52

2.5.2 Absorption and Emission for Organic Luminescent Species ……..54

2.5.3 Phosphorescence……..57

2.6 Sources of Optical Efficiency Loss……59

2.6.1 Surface Reflections……..59

2.6.2 Non Unity Luminescent Quantum Yield (LQY)……..61

2.6.3 Light Cone/Escape Losses……...61

2.6.4 Reabsorption Losses…….....62

2.7 Alternate Geometries…….65

2.8 LSC Cost……..…68

2.9 Photovoltaics……..71

2.9.1 Silicon (Si) Solar Cells…….73

2.9.2 Gallium Arsenide Cells……75

2.9.3 Solar Cell and Photoelectrochemical Cell (PEC) Characterisation Parameters……..…….75

2.10 Water Splitting……...78

2.10.1 Photoelectrochemical Cell……79

2.10.2 Electrodes…….81

2.10.3 Electrolyte……83

2.10.4 Photoelectrochemical Cell Characterisation Parameters…….....83

2.11 Conclusion……...84

Chapter 3: LSC Efficiency Enhancements and Luminescent Species…....…….90

3.1 Introduction……..…..91

3.2 Methods to Increase LSC Efficiency……91

3.2.1 Metallic Mirrors and Scattering Layers……91

3.2.2 Reducing Escape Cone Losses…….95

3.2.3 Wavelength Selective Mirrors……..96

3.2.3.1 Cholesteric Mirrors……..96

3.2.3.2 Distributed Bragg Reflectors (DBR), and Dichroic Mirrors……98

3.2.4 Plasmonics……..102

3.2.5 Alignment……...103

3.2.6 Multiple LSC Stacks……..106

3.2.7 Multiple Dyes……108

3.3 Types of Luminescent Centres……111

3.3.1 Conjugated Polymers……112

3.3.2 Organic Dyes……..113

3.3.3 Phycobilisomes……..114
3.3.4 Nanocrystals……...116
3.3.4.1 Quantum Dots (Nanocrystals)……117
3.3.4.2 Nanorods……118
3.3.5 Rare Earth/Metal Complexes…….119
3.4 Conclusion…….120
Chapter 4: Experimental, Fabrication & Computational Methodologies ….……...128
4.1 Introduction……..129
4.2 The Solar Simulator Spectrum……...129
4.3 Experimental Methods…….131
4.4 Transmission/Absorption……131
4.4.1 Transmission Measurements Using UV-Vis…….131
4.4.2 Transmission Measurements Utilising an Ocean Optics Fibre Spectrometer……..134
4.5 Photoluminescence Measurements ……136
4.5.1 Top Surface Emission Measurements (Fluoromax)……...137
4.5.2 Edge Emission Measurements (Using Ocean Optics Fibre Spectrometer)……139
4.6 Photoluminescent Efficiency (PLE)……140
4.7 Luminescent Quantum Yield (LQY)……..142
4.8 External Quantum Efficiency (EQE)…….146
4.9 Short Circuit Current……..148
4.10 Light and Dark IV……153
4.11 Angular Dependent Measurements……155
4.11.1 Angular Dependent Transmission……..156
4.11.2 Angular Dependent Reflectance and Surface Scatter Measurement..157
4.12 Measuring Thin-Film Thicknesses…….160
4.13 Fabrication Methods……162
4.13.1 Thin-Film Solution Production Methods……...163

4.13.2 Spin-Coating Methodology……164

4.13.3 Wire Bar Coater Methodology……...167

4.14 Computational Methods……..169

4.14.1 Raytrace Methodology……...170

4.15 List of Samples……..175

Chapter 5: Utilising Vertical Aligned CdSe/CdS Nanorods Within an LSC…..……...181

5.1 Introduction……..181

5.2 SEM Images of Nanorod Samples……..182

5.3 Dipole Behaviour……..183

5.4 Basic Characterisation (Ensemble Absorptivity, Top Surface Emission and LQY)……..185

5.4.1 Absorption & Emission Spectra…….185

5.4.2 Luminescent Quantum Yield……..187

5.5 Spectroscopic Signatures of Nanorod Alignment: Surface Mapping…..189

5.5.1 Absorptivity Map……...189

5.5.2 Thin-Film Thickness Measurements……..191

5.6 Spectroscopic Signatures of Nanorod Alignment: Angular Absorption Profiling……195

5.6.1 Theoretical Absorptivity: Nanorod and Control Samples……..196

5.6.1.1 Reflectance…….197

5.6.1.2 Theoretical Transmission Values……...200

5.6.2 Scatter and Reflection Results……202

5.6.3 Absorptivity: Measured and Theoretical Comparison……...204

5.6.4 Refractive Index of Nanorod Samples (Effective Medium Theory)..212

5.7 Optical Efficiency Results for the Nanorod LSC……..216

5.8 Computational Simulations of Vertically, Horizontally and Isotropically Aligned Nanorod Samples…….217

5.8.1 Direct Irradiance…….218

5.8.2 Diffuse Irradiance……...219

5.9 Conclusions……...221

Chapter 6: Flexible LSCs Novel Luminescent Species…….……...225

6.1 Introduction and Premise……225

6.2 Luminescent Materials……226

6.2.1 PE-610 (Phycobilisome Derived Luminophore)……226

6.2.1.1 PE-610 LSC Optical Efficiency…….235

6.2.1.2 PE-610 Simulations……236

6.2.2 High Stokes-Shift Luminescent Materials…….238

6.2.2.1 ADS065BE……239

6.2.2.2 Optical Efficiency for High Stokes-Shift Materials ……246

6.2.2.3 ADS065BE Simulations…….248

6.3 Flexible LSC Prototype……251

6.3.1 LSC Holder……251

6.3.2 First generation Flexible LSC Prototype……253

6.3.3 Second Generation Flexible LSC Prototype……..256

6.3.4 Considerations of the Number of Solar Cells/Mirrors used with a Flexible LSC…….……...259

6.4 Conclusions……...266

Chapter 7: LSC Utilisation to Enhance Water Splitting……...……...270

7.1 Introduction……..270

7.2 Design Specifications for LSC/Electrode Device…….....272

7.2.1 LSCs and LSC Sample Holder……...272

7.2.2 The Photoelectrochemical Cell (PEC)……...274

7.3 LSC Absorption and Emission…..……..275

7.3.1 Absorptivity……273

7.3.2 Emission Spectra……279

7.4 IPCE……..283

7.5 LSC Short Circuit Current Measurements, Photon Concentration and Optical Efficiency……285

7.6 Dark IV, EQE, Chronoamperometry and Light IV for Solar Cells and PEC.....293

7.6.1 Dark IV……...294

7.6.2 EQE……295

7.6.3 Light and Dark IV for the Photoelectrochemical Cell……...297

7.6.4 Combined Light/Dark IV curves for the Silicon Solar Cells and the PEC Cell……295

7.6.5 Chronoampereomtry……..301

7.7 Red LSC Incremental light exposure…….304

7.8 Conclusions……...306

Chapter 8: Conclusion…….....311

8.1 Outlook……..317

Appendix A……...320

List of Figures

Figure 1-1 Graph showing that in the USA (excluding Hawaii), traditional sources oil reached "peak-oil" in the 1970's. However, non-traditional sources of oil are forecast to shift this peak further into the future. Reproduced with permission from The Economist magazine [7]……...24

Figure 1-2 Illustration of different types of solar power generating technologies. A) rooftop solar thermal technology, B) rooftop photovoltaic technology……..28

Figure 1-3 Solar cell efficiency chart for the year 2013. Chart produced by the National Renewable Energy Laboratory, NREL (reproduced with permission) [28]…….31

Figure 1-4 Shows the possible fates of photons incident with the surface of an LSC [33]……...32

Figure 1-5 Images of cuboidal and cylindrical LSCs, image reproduced with permission from OSA [35]....…….....33

Figure 2-1 Diagram depicting the parameters in equation 2.1, diagram adapted from [1]……41

Figure 2-2 Graphs of AM15.g solar spectrum in terms of normalised photon flux and irradiance power…….....42

Figure 2-3 Plot of the AM1.5global, direct and diffuse spectra in units of absolute irradiance, data from [6]……..43

Figure 2-4 Graph showing *p* and *s* polarised reflectance for at an air/PMMA interface, calculated using the Fresnel equations (see equations 2.5 and 2.6)……47

Figure 2-5 Plot of reflection of light propagating out of the LSC, demonstrating TIR at a PMMA/air boundary, refractive indices 1.49 and 1.0003 respectively and a critical angle of ~42°……...51

Figure 2-6 Schematic diagram of a LSC diagram illustrating the difference between an emitted photon impinging the LSC top surface at an angle greater than the critical angle (TIR photon), and a photon incident with the surface at an angle less than the critical angle (photon lost via an escape cone)……...…52

Figure 2-7 Electronic transitions in an organic molecule, adapted from [14]……...56

Figure 2-8 Electron energy transition diagram featuring inter-system crossing and phosphorescence, adapted from [14]……...59

Figure 2-9 Chart illustrating the variation of the fraction of un-polarised light reflected with angle of incidence, for an air/glass boundary where the glass has a refractive index of 1.52…….....60

Figure 2-10 Graph showing the region of spectral overlap between the absorption and emission spectra for PbSe nanorods. Spectral overlap is an unwanted property since it leads to reabsorption losses……..65

Figure 2-11 A) and B) show emission edges of homogeneously doped and thin-film coated cylindrical LSCs respectively. C) and D) show the long axis view of homogeneously doped and thin-film coated cylindrical LSCs respectively…….....66

Figure 2-12 Graph showing the dramatic reduction in the price of crystalline silicon solar cells between 1977 and 2013, reproduced with permission from "The Economist" magazine [35]…….69

Figure 2-13 Diagrams showing the differences in Fermi level energies for *n-type* doping, *p-type* doping and an intrinsic semiconductor respectively (figure adapted from [1])……..…72

Figure 2-14 Band diagram for an ideal metal oxide semiconductor, adapted from [44]……..….80

Figure 3-1side diagrams of LSCs utilising A) a bottom surface reflective mirror, and B) a bottom surface scatter layer……92

Figure 3-2 Schematic diagram of an LSC utilising a wavelength selective mirror on its top surface. It can be seen that the wavelength selective mirror prevents an emitted photon, impinging on the LSC surface with an angle lower than the critical angle from escaping……96

Figure 3-3 Diagram of constructive interference from an anti-reflection coating (diagram adapted from [27])……...……99

Figure 3-4 Side-view diagrams of horizontally and vertically aligned dipolar emitters respectively. Horizontal alignment has strong incident light absorption, but high top and bottom surface escape cone losses, whilst the opposite is true for the vertically aligned sample…….104

Figure 3-5 Diagram of A) a 3 stack LSC with solar cells affixed, B) the corresponding absorption and emission spectra for the 3 plates (figure adapted from [57]……107

Figure 3-6 Graph from Bailey *et al*. [12] (reproduced with permission from Elsevier Limited) showing the combined absorption spectrum of their three dyes (__), the absorption spectrums of the 3 individual dyes (----), and the emission spectrum the combined dyes (---)……110

Figure 3-7 Image reproduced with permission from John Wiley and Sons [78] showing the different proteins and the energy transfer mechanism within a Phycobilisome……..…115

Figure 4-1Steuernagel Lichttechnik solar simulator spectrum (no UV filter)…….....130

Figure 4-2 Top-down view of a transmission measurement performed using a UV-Vis spectrometer…….133

Figure 4-3 Diagram of experimental setup for a transmission measurement using an Ocean Optic spectrometer and a solar simulator light source……...…136

Figure 4-4 Top-down view of top surface emission measurement inside a Fluoromax 3 system……..138

Figure 4-5 Diagram of the edge emission PL setup, utilising an ocean optics fibre spectrometer and a solar simulator light source……..140

Figure 4-6 Diagram showing side-view cross sections of the integrating sphere used in the LQY experiments. A) corresponds to experiment a with no LSC sample B) illustrates experiment B with the incident light beam indirectly illuminating the sample. C) corresponds to experiment C where the incident light is targeted directly onto the sample……...142

Figure 4-7 Plot of the excitation peak, L_A, used to stimulate photoluminescence in an LSC sample. This graph corresponds to experiment A…….....144

Figure 4-8 Plot of the excitation, L_B, and emission peaks, P_B, of an LSC for experiment B (indirect sample illumination)……144

Figure 4-9 Plot of the excitation, L_C, and emission peaks, P_C, of an LSC for experiment C (direct sample illumination)……145

Figure 4-10 Diagram of the EQE experimental setup. The photodetetector and solar cell are interchangeable depending on whether a reference or a measurement are being taken respectively……..147

Figure 4-11 Side-view diagrams of the experimental setup used to measure incident photon flux. A) features the setup with the LSC in place, while B) shows the LSC removed……..149

Figure 4-12 Diagram of top-down view of incident photon flux measurements…….....150

Figure 4-13 Diagram illustrating the short circuit current measurement experimental setup (part of the measurements required to determine the edge emission photon flux)…….152

Figure 4-14 Side-view of the photon flux measurement locations on the edge of an LSC. ……..152

Figure 4-15 Diagram illustrating the light IV experimental setup……...155

Figure 4-16 Diagram of angular dependent transmission experimental setup…….…156

Figure 4-17 Diagram showing the conical laser scatter distribution and reflected laser beam from the surface of an LSC sample……158

Figure 4-18 Top-down diagram of the reflection/scatter experimental setup……..160

Figure 4-19 Diagram of alpha-step profilometer with sample. Stylus and sample sizes enlarged for clarity……...159

Figure 4-20 Diagram of scored thin-film and the stylus just prior to the start of a measurement…….....161

Figure 4-21 Diagram featuring the spin-coater sample fabrication setup……....165

Figure 4-22 Diagram of wire-bar coater sample fabrication setup……..…167

Figure 4-23 Flow chart showing the methodology employed by the PVtrace computer program……....174

Figure 5-1 A) SEM top-down image of largely vertically aligned nanorods and B) SEM side-view of vertically aligned nanorods, figures courtesy of [5]……....182

Figure 5-2 Absorptivity and top surface emission spectra of the nanorod sample……..…186

Figure 5-3 A position dependant absorptivity map of the nanorod sample using a 473nm laser as a light source……...191

Figure 5-4 Diagram showing the general locations of the thin-film thickness measurements……..…….192

Figure 5-5 Diagram showing a side-view of the different material boundaries (each of which with a different refractive index) present in the nanorod sample……...197

Figure 5-6 Logarithmic graph of the percentage reflectance loss between each of the boundaries present in the nanorod sample, as a function of incident laser angle……...198

Figure 5-7 Logarithmic graph of the percentage reflectance loss between each of the boundaries present in the control sample, as a function of incident laser angle…….198

Figure 5-8 Logarithmic graph of the percentage reflectance loss between each of the boundaries present in the nanorod sample, as a function of internal/external angle……..199

Figure 5-9 Logarithmic graph of the percentage reflectance loss between each of the boundaries present in the control sample, as a function of internal/external angle……200

Figure 5-10 Graph of the position dependent percentage scatter/reflectance losses, for the nanorod sample, relative to the angle of incidence of the 473nm laser…….203

Figure 5-11 Graph of the position dependent percentage scatter/reflectance losses, for the Lumogen red 305 control sample, relative to the angle of incidence of the 473nm laser……....203

Figure 5-12 Graph of the angular dependent absorptivity at positions 12.5mm, 18.5mm and 21.5mm on the nanorod sample…….205

Figure 5-13 Angular dependent absorptivity at position 12.5mm for the nanorod sample, as well as the theoretical dipolar and isotropic angular absorptivity distribution……..206

Figure 5-14 Angular dependent absorptivity at position 18.5mm for the nanorod sample, as well as the theoretical dipolar and isotropic angular absorptivity distribution……..208

Figure 5-15 Angular dependent absorptivity at position 21.5mm for the nanorod sample, as well as the theoretical dipolar and isotropic angular absorptivity distribution……..208

Figure 5-16 Graph of the angular dependent absorptivity at positions 12.5mm, 18.5mm and 21.5mm on the Lumogen red 305 control sample……..210

Figure 5-17 Diagram showing a unit cell of vertically aligned nanorods. Diagram highlights the different refractive indices present in the nanorod thin-film……...……213

Figure 5-18 Graph showing how the final (second step) effective medium calculation refractive index varies as the volume ratio of the organic and inorganic nanorod components varies. Note the nanorod volume ratio does not contain the air trapped in the thin-film.….....216

Figure 6-1 Absorption coefficient and top surface PL emission spectra for different concentrations of PE-610 dye solution (in pH neutral buffer solution)……...….227

Figure 6-2 Peak normalised absorption spectra for the different concentrations of PE-610 luminescent species……..…228

Figure 6-3 Rhodamine B and R-PE absorptivity spectra in relation to the PE-610 tandem dye's spectrum. The rhodamine B spectrum was produced by extracting data from [6], and the R-PE data was extracted from [7]…….……229

Figure 6-4 A) photoluminescence efficiency (PLE) against wavelength for different concentrations of PE-610 dye in buffer solution. Reproduced with permission from IEEE [12]. Plot B) peak normalised data……...231

Figure 6-5 Comparisons between absorption coefficient and PLE for different concentrations of PE-610 dye…….233

Figure 6-6 Absorptivity and top surface PL spectra for LSC samples utilising ADS065BE at a number of different concentrations……..…240

Figure 6-7 Chemical structure of ADS065BE. Reproduced with permission from American Dye Source [14]……...241

Figure 6-8 Compares the absorption spectrum of ADS065BE with the AM1.5g solar spectrum……...242

Figure 6-9 Variation of LQY with dye concentration wt% for ADS065BE……...243

Figure 6-10 Plot showing the respective peaks of the incident light beam, and resulting emission in experiments A, B and C of the LQY measurement on sample ADS065BE 4wt%.....245

Figure 6-11 Measured optical efficiency against weight percentage concentration for material ADS065BE, includes a second order polynomial trend line as a guide for the eye…….....247

Figure 6-12 Diagram of a flexible LSC attached to the holder. Image reproduced with permission from IEEE [12]…….252

Figure 6-13 Diagram of the open holder without the solar cell Supplied by Kelly Trautz (NRL)……..…….252

Figure 6-14 plot of dark *iv* of the silicon solar cell(s) (Solaronix), measured when mounted in the LSC holder (data extracted from [17])…….253

Figure 6-15 Plot of the EQE of the silicon solar cells used in the LSC holder. EQE measurements performed while cell was mounted in the LSC holder (data extracted from [17])……...…253

Figure 6-16 Power generated by first generation flexible LSC and LSC holder, containing Si solar cells (Solaronix), against time……..255

Figure 6-17A) Shows the normalised photon flux spectrum from the NRL's solar simulator. B) gives the normalised absorption and emission spectrum from the Lumogen red 300 used in the initial flexible LSC prototype…….256

Figure 6-18 Photograph of a second generation prototype flexible LSC utilising Lumogen 305 red dye(BASF); dimensions 90 by 59 by 0.5mm, and a thin-film 0.110mm thick……257

Figure 6-19 A graph of displaying the absorptivity of Lumogen red 305 prototype flexible LSC…….…….257

Figure 6-20 Transmission spectrum of the PLEXIGLAS film clear 99524 flexible substrate material……..…257

Figure 6-21 Plot of simulated optical efficiency (calculated for collection from all 4 edges) for the second generation flexible LSC prototype with a range of dye concentrations under AM1.5g at normal incidence……..261

Figure 7-1 Diagram of the LSC sample holder used to hold the LSCs and provide sufficient spacing between them to allow the solar cells and PEC cell to be attached…….……...….273

Figure 7-2 Schematic diagram of the PEC cell used in this work…….…..275

Figure 7-3 Absorptivity spectrum of the 2.5wt% Kremer violet LSC plate……....276

Figure 7-4 Absorptivity spectrum of the 3wt% Lumogen red 305 LSC plate…….278

Figure 7-5 A) Shows how edge emission was collected from the LSCs when placed on sample mount, and B) when the LSCs were mounted in the holder. The distance *l* is the same in both a) and B)……..280

Figure 7-6 Lumogen red 305 LSC plate edge emission in terms of peak normalised photon flux……..…….281

Figure 7-7 Fluorescent violet LSC plate edge emission in terms of normalised photon flux……..…….282

Figure 7-8 IPCE of the un-doped Fe_2O_3 working electrode of the PEC, figure supplied by Federico Pesci [6]…….……...284

Figure 7-9 Side-on view of the LSC showing the locations of three measurement positions as well as the upper and lower solar cell locations……..…….286

Figure 7-10 Schematic diagram of the side-on view of the LSC sample holder with the violet and red LSCs protruding slightly from the open edge…….…...291

Figure 7-11 Silicon solar cells connected in series mounted on a circuit board…….…….294

Figure 7-12 Dark IV curves for the 3 silicon solar cells measured individually and the average for the 3…….....295

Figure 7-13 EQE spectra for each of the 3 silicon solar cells as well as an average of the 3……296

Figure 7-14 Diagram of the PEC cell light IV setup. The LSC sample holder is not shown to make the diagram clearer…….298

Figure 7-15 Light and dark IV curves for the fe2o3 electrode, both doped and un-doped, in the PEC, where vs. RHE means with respect to the reversible hydrogen electrode……..…….299

Figure 7-16 Combined light and dark IV measurements on the un-doped Fe2O3 working electrode and the silicon solar cells in the completed PEC/LSC/solar cell device. Where RHE stands for reference hydrogen electrode……...…301

Figure 7-17 Diagram of the chronoamperometry/PEC light IV setup., the LSC sample holder is not shown to make the diagram clearer……...…302

Figure 7-18 Chronoamperometry results (current against time) for both the Co(ii) doped Fe_2O_3 working electrode, and the un-doped working electrode…….....303

Figure 7-19 Light IV data with the red LSC coupled to the silicon solar cells, with different fractions of the red LSC's surface obstructed to control the quantity of incident light……..304

Figure 7-20 Diagram of red LSC/silicon solar cell incident light intensity obstruction……....305

List of Tables

TABLE 5-1 MEASUREMENTS OF THE THIN-FILM THICKNESS OF THE CONTROL SAMPLE AT THE 3 POSITIONS COINCIDING WITH THE ANGULAR DEPENDENT ABSORPTION MEASUREMENTS (SEE SECTION 5.6). 193
TABLE 5-2 MEASUREMENTS OF THE THIN-FILM THICKNESS OF THE NANOROD SAMPLE AT THE 3 POSITIONS MEASURED DURING ANGULAR DEPENDENT ABSORPTION MEASUREMENTS. 195
TABLE 5-3 TABLE CONTAINING THE REFRACTIVE INDICES FOR THE DIFFERENT COMPONENTS OF THE NANOROD THIN-FILM LAYER. 215
TABLE 5-4 TABLE SHOWS THE OPTICAL EFFICIENCIES MEASURED FROM THE NANOROD SAMPLE. 217
TABLE 5-5 OPTICAL EFFICIENCIES CALCULATED FROM COMPUTATIONAL RAY-TRACE SIMULATIONS FOR IDEALLY ALIGNED NANOROD SAMPLES UNDER DIRECT NORMAL IRRADIANCE. 219
TABLE 5-6 OPTICAL EFFICIENCIES CALCULATED FROM COMPUTATIONAL RAYTRACE SIMULATIONS FOR IDEALLY ALIGNED NANOROD SAMPLES UNDER DIFFUSE IRRADIANCE.220

TABLE 6-1TABLE CONTAINING THE DYE CONCENTRATION DEPENDENT ABSORPTION COEFFICIENTS AND LIGHT ABSORPTION FRACTIONS AT 375NM AND 575NM. 234
TABLE 6-2 TABLE GIVING THE OPTICAL EFFICIENCY WHEN FRESH AND WHEN AGED, FOR A THIN-FILM LSC CONSISTING OF PE-610 MEASURED USING A STEUERNAGEL LICHTTECHNIK SOLAR SIMULATOR AS THE LIGHT SOURCE. 235
TABLE 6-3 SIMULATED OPTICAL EFFICIENCIES USING THE FULL AM1.5G SOLAR SPECTRUM AS THE INCIDENT LIGHT SOURCE AS WELL AS THE SPECTRAL AND PHYSICAL PROPERTIES OF THE PE-610 PLATE, FOR A NUMBER OF LSC GEOMETRIES. DATA EXTRACTED FROM [12]. 237
TABLE 6-4 OPTICAL EFFICIENCIES, AVERAGE THIN-FILM THICKNESSES AND MEASURED LQY FOR ALL THE HIGH STOKES-SHIFT SAMPLES STUDIED IN THIS CHAPTER. 247
TABLE 6-5 OPTICAL EFFICIENCIES FOR THE RAYTRACE SIMULATIONS FOR THIN-FILM LSCS CONTAINING THE HIGH STOKES-SHIFT LUMINESCENT SPECIES. THIN-FILM LAYER = 100μM, AND THE INCIDENT LIGHT SOURCE WAS THE FULL AM1.5G SOLAR SPECTRUM. 249
TABLE 6-6 VARIATION IN POWER OUTPUT OVER TIME OF THE FIRST GENERATION FLEXIBLE LSC PROTOTYPE DIRECTLY COUPLED TO THE LSC HOLDER WITH SI SOLAR CELLS INSIDE. 255
TABLE 6-7 TABLE FEATURING OPTIMISED FLEXIBLE LSC SIMULATION RESULTS, USING 5WT% LUMOGEN RED 305 DYE.. 264

TABLE 6-8 A TABLE CONTAINING COMPUTATIONALLY MODELLED OPTICAL EFFICIENCIES FOR LSC SAMPLES CONTAINING LUMOGEN RED 305. ALL THIN-FILM THICKNESSES ARE 100μM, SUBSTRATES ARE 0.5MM THICK AND THE ABSORPTION COEFFICIENT AT THE PEAK ABSORPTION WAVELENGTH IS MATCHED TO THAT OF THE ADS065BE SAMPLE. 264

TABLE 7-1 THE SHORT CIRCUIT CURRENTS, OPTICAL EFFICIENCY AND PHOTON CONCENTRATION DATA FOR THE VIOLET LSC, FROM EACH EDGE. 287
TABLE 7-2 TABLE SHOWS THE PHOTON FLUX, OPTICAL EFFICIENCY AND PHOTON CONCENTRATION DATA FOR THE RED LSC, FROM EACH EDGE. 289
TABLE 7-3 TABLE SHOWING THE AVERAGE PHOTON CONCENTRATION OF FROM ONE EDGE OF THE VIOLET LSC FACTORING IN IPCE OF THE PEC CELL. 290
TABLE 7-4 TABLE SHOWING THE AVERAGE PHOTON CONCENTRATION OF FROM ONE EDGE OF THE RED LSC FACTORING IN EQE OF THE SILICON SOLAR CELLS. 290
TABLE 7-5 THIN-FILM THICKNESS MEASUREMENTS TAKEN AT THE CENTRE POINT OF EACH LSC EDGE, FOR THE VIOLET AND RED LSCS. 292

Chapter 1
Introduction

1.1 The Need for Renewable Energy

In recent years it has become increasingly apparent that modern civilisation's reliance on fossil fuels is unsustainable, due to factors including climate change, reduced availability, political motivations and economics. As a result renewable sources of energy, principally wind, solar, hydroelectric, and also nuclear will be used more and more to replace fossil fuel based power capacity, by the year 2035 renewables are predicted to make up one third of the world electricity generation energy mix[1].

Global climate change has the potential to have an enormous effect on economy, political systems, agriculture and human health, and there have been several papers which have tried to identify costs in terms of loss of GDP per geographical region [2,3]. In 2011 it was estimated that global CO_2 emissions reached 31.2Gt, and that for the year 2035 the International Energy Agency, IEA, predicts global CO_2 emissions will be as high as 37Gt [1]. However, the 2035 estimate is based on the assumption that the IEA's "new policies scenario" is followed, in which governments follow through with what are currently only proposed commitments to reduce greenhouse gas emissions. This policy will lead to an average predicted long term global temperature rise of 3.6°C, which is above the 2°C temperature rise tipping point that many climate scientists consider critical to avoid [4]. A large percentage of the increase in CO_2 emissions over the intervening years will largely be driven by the rapid growth in the developing world [1]. Non-OECD (Organisation for

Economic Co-operation and Development) nations are expected to be responsible for 65% of increased energy demand world-wide by 2035, compared to 55% in 2010.

Over the coming years climate change mitigation will become more and more necessary to prevent draught, and other damage from extreme weather conditions, as well as the likely political instability such changes will cause. The wet regions of the globe are expected to get wetter and the dry regions to get dryer, with Africa, the Middle East, West Central Asia, Southern Europe and the south West of the United States experiencing the brunt of the dryer conditions [5]. The risk of civil unrest and conflict is expected to rise as the climate changes, and large scale migrations of people within nations may become more common. Africa is likely to suffer harshly due to the importance of agriculture to its economy, and parts of Asia also, where extreme weather is already common, will probably suffer more such weather conditions in the future.

In the long term it is inevitable that our reliance on fossil fuels will have to come to an end as extraction rates will eventually be surpassed by consumption rates, for oil this is a phenomenon known as “peak oil” [6]. The production of oil anywhere in the world follows a roughly bell shaped graph as per Hubberts Peak Theory [6], the point at which the extraction rate is highest is called peak oil (see Figure 1-1). After peak oil is reached, the rate of oil extraction from the ever reducing number of new oil deposits found and developed, to replace old depleted deposits, will at some point be surpassed by the amount being used. It is unclear when peak oil will be reached as the rate of oil use and or extraction can be affected by numerous factors. One example is sources of oil, which until recently were financially non-viable, such as oil sands in Canada now becoming financially viable as global demand for oil has grown. Such events will undoubtedly push back the date of peak oil.

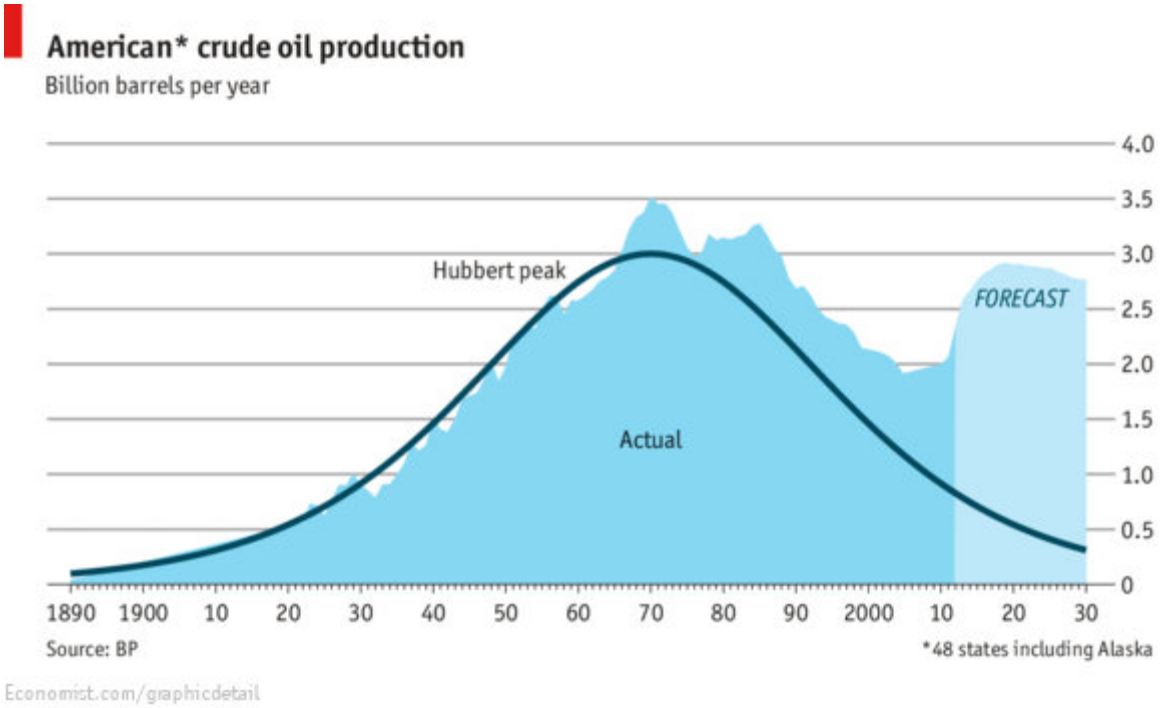


Figure 1-1 Graph Showing that in the USA (excluding Hawaii), traditional sources oil reached "peak-oil" in the 1970's. However, non-traditional sources of oil are forecast to shift this peak further into the future. Reproduced with permission from the Economist magazine [7].

Peak coal is similar to peak oil whereby coal extraction rates eventually start to decline, and can no longer meet growing demand. A report by the World Energy Group in 2007 [8] identifies 2025 as the year for peak coal, though they concede that the data for worldwide proven reserves is poor, as some countries do not change their stated values of reserves often and so do not take production of these reserves into account [8]. It is also important to note the energy intensity of the remaining coal reserves, for instance in the United States which in 2007 had 30% of the world's proven coal reserves. Although America has the largest coal deposits of any country, in 1990 the US reached peak coal in terms of high quality, energy rich coal. Despite this the overall date for peak coal in the US has been pushed back by augmenting the supply with lower energy density subbituminous coal [8].

There are a number obvious political motivations aiding the push towards renewable energy sources such as: energy security, concerns about public safety related to other energy sources (notably nuclear power and shale gas accessed by hydraulic fracturing), growing public concern related to environmental damage, a growing perception among the public that extreme weather is related to human induced climate change and lastly, international treaties obligating nations to reduce greenhouse gas emissions.

Energy security is determined by a nations' ability to have sufficient and stable access to low cost energy sources in order to benefit said nations' people, economy and security. Renewable energy sources have great potential to enhance energy security as they will lead to a reduction in costs and import dependency, and unlike other sources of energy (fossil fuels, uranium), renewable energy sources are not geographically limited to a few specific regions of the world [9]. However, it is not just renewable sources that are being developed to provide for energy security, in the last few years there has been much interest in hydraulic fracturing technology, and the development of vast deposits of Canadian oil sands, which has become financially viable for development, thus allowing access to previously inaccessible sources of shale gas and light tight oil respectively. In conjunction with enhanced energy efficiency, North America is expected to become a net oil exporter by 2030, whereas in the year 2012 the United States imported 20% of its energy requirement [9]. However, there are concerns about the possible environmental and human health damage that may be caused by chemicals and, or, methane gas, by-products of hydraulic fracturing, polluting sources of drinking water [10].

Growth in the nuclear power industry may also help to boost national energy supplies, with the International Atomic Energy Agency, IAEA, annual report for 2011 [11] predicting nuclear energy to account for 501GW of installed electricity capacity by 2030 at the lowest estimate, and 746GW at the highest, an increase from the 2011 level of 369GW of installed

capacity [11]. However, growth has been somewhat diminished by nuclear safety concerns in the wake of the 2011 disaster at the Fukushima Dai-Ichi nuclear power station. The IAEA believes the disaster will reduce the predicted 2030 installed capacity by between 7 and 8% compared to the aforementioned predictions.

There are now significant economic drivers for utilising a higher percentage of renewables in a nations' energy mix such as the previously mentioned damage to GDP brought about by climate change [1,2]. Indeed, over the past few years investment in renewable energy has rapidly increased, with worldwide renewables investments reaching $257 billion in 2011, 6 times the 2004 value, and a 17% increase on the 2010 total [12]. There is also the rising price of fossil fuels to contend with, as well as the large scale financial investment in renewable energies which is producing a vast new industry, the potential financial gains of which will result in countries competing for a share of the growing market. The cost of power generation using renewables is also declining, with operation and maintenance contract costs for wind farms declining by 38% between 2008 and 2012 [13] and the cost of photovoltaics (PV) dropping to a new low in the third quarter of 2012 [13]. The fact that some Chinese companies are selling multicrystalline silicon modules at prices between $0.60/W and $0.50/W, (see 2.12, chapter 2) shows how dramatic the reductions in price have been. The dramatic price decline is the result of mass production, improvements in technology and significantly, over production of modules [14], suggesting prices may increase again after the excess capacity is sold.

In an effort to support the nascent solar energy market and boost uptake of renewable energies, a number of countries including but not limited to Spain, Germany, Italy and the UK have introduced Feed-In-Tariffs (FITs) whereby a person or persons supplying energy generated by renewable energy sources to the energy grid will be paid a premium rate [8]. In 2011 FITs in Italy and Germany were largely responsible for growth in excess of 7GW

installed capacity. However, with the rapidly declining cost of solar modules and the increase in solar power generation, a number of governments, including Italy and Germany, have been scaling back subsidies, with additional factors such as the global economic situation and the much reduced gas prices in the United States leading to further reductions in subsidies for renewable energy.

In addition to FIT's, another political motivation for the growth in renewable energy uptake is the Kyoto Protocol, an international political effort which aims to curb the greenhouse gas emissions of industrialised nations, due to their relatively long history of industrialisation and relative wealth [15]. The target of the protocol was to reduce greenhouse gas emissions by an average of 5%, when compared to 1990 levels, for the period 2008-2012. Officially, the Kyoto Protocol came into force on the 16th of February 2005, with 191 contributing parties [16]. Between November 26th and December 7th 2012 the Doha Climate Change Conference was held, with the intention of reaching an agreement between the nations of the UN to replace the Kyoto Protocol after it elapses at the end of 2012 [17].

Another prominent anti-climate change initiative is the European Union (EU) 20-20-20 target. This initiative, which is in place across the entirety of the EU, aims to achieve a 20% reduction in greenhouse emissions (from 1990 levels), 20% of energy derived from renewable energy sources, and energy efficiency enhancements of 20% across the EU; all of which is intended to occur by the year 2020 [18]. Furthermore, there are plans for perhaps a 30% reduction in greenhouse gas emission by 2020, in place of the original 20% target. However, this increase in emission reductions is dependent on other prominent non-EU nations making greenhouse gas mitigation efforts which the EU commission deems sufficient. The 20-20-20 plan includes four components: an emission trading scheme which reduces the total emission cap each year, nation specific reductions in non-traded emissions (for wealthy nations this is an actual reduction in emissions and a limiting of emissions

growth for poorer nations), a nation specific increase in renewable energy sources, and lastly, a set of laws which allow for safe and effective carbon capture and storage techniques.

1.2 Solar Energy

As discussed in section 1.1, renewable energy sources are rapidly increasing their share of the world's energy mix, and solar energy is no exception. There are two main types of solar energy technology, PV and solar thermal (ST). PV converts solar photons absorbed by the PV cell into charge which can be collected and used to generate electrical power, whereas ST technology utilises heat energy from the sun to heat a fluid. PV can be found in a variety locations (see Figure 1-2) from the PV cells on a calculator to vast multi mega Watt generating power stations, there are numerous ways of implementing the technology such as building integrated photovoltaics (BIPV), concentrator photovoltaics (CPV), and space photovoltaics (SPV).



Figure 1-2 Illustration of different types of solar power generating technologies. A) rooftop solar thermal technology, B) rooftop photovoltaic technology.

In the EU alone, in the PV sector, the strategic energy and technology (SET) Plan [19] expects that, "in the long term, new and emerging technologies will come to the market" and that "The estimated maximum potential for PV systems in the EU-27 is up to 125 GW by 2020 and 665 GW by 2030.". The SET Plan further states that "Research is vital for

increasing the performance of PV systems and accelerating the deployment of the technology".

The record power conversion efficiency for a single junction solar module under one sun illumination stands at 23.5% (2012), fabricated using thin-film GaAs by Alta Devices [20], though individual, single junction cells can reach higher efficiencies. However, for large scale power stations CPV technology is typically used CPV uses mirrors and lenses to concentrate many hundreds of solar intensities upon the surface of small, highly efficient, multi-junction solar cells. Multi junction solar cells are expensive as they are fabricated from expensive III-V semiconducting materials. However, they do have much higher power conversion efficiencies than single junction solar cells since they are essentially multiple solar cells on top of one another, allowing for a larger percentage of the power of the solar spectrum to be utilized. As of 2012, the highest confirmed power conversion efficiency for a multi junction solar cell stands at 43.5% [21,22], attained by Solar Junction and Sharp. However, the ultimate calculated PV efficiency is 86.8% [23], although this is a highly theoretical value, only possible in an idealised case with an infinite number of junctions. Figure 1-3 shows the historic increases in record cell efficiencies to the year 2013. However, it must be noted that some technologies are now close to their theoretical limits and that these increases in efficiency cannot continue indefinitely.

Unlike PV technology, ST technology does not directly produce electricity, and residentially it is usually used only as a way to provide hot water (see Figure 1-2A). However, ST power stations use large mirrors or lenses to concentrate solar energy for the purpose of vaporising a fluid, often water, to drive power generating turbines ST power stations utilising a liquid fluoride salt heat transfer material, operating at temperatures between 700°C and 850°C are expected to a provide heat to electricity conversion efficiency of up to 50% [24].

Organic photovoltaic, OPV, is one of the cheapest PV technologies, which utilises conductive polymers as the light harvesting/charge producing medium. The advantage of OPV is its very low cost. Unfortunately, OPV also suffers from low efficiencies and short lifetimes, degrading more rapidly than inorganic materials. In the work of Gevorgyan *et al.* [25], a roll-to-roll module consisting of P3HT:PCBM was measured to have an ~10% drop in performance after 10000 hours outside exposure in Denmark. However, the authors did note that other modules in other locations around the world decayed faster, in some cases much faster, with degradation to 80% of their original efficiency occurring in under 300hours. The 2012 record efficiency for an organic solar cell reached 9.2% under one sun and was produced by Mitsubishi Chemical [26], with record module efficiencies being somewhat lower. Other promising examples of low cost PVs include crystalline silicon (and amorphous silicon), CIGS and CdTe cells, with record module efficiencies of 18.5±0.4%, 15.7±0.6% and 15.3±0.5% [27] respectively. Both CIGS and CdTe are thin-film technologies which, rather than referring to the amount of material required rather refers to the high through-put processing techniques that can be used for these materials, that thereby reduce costs.

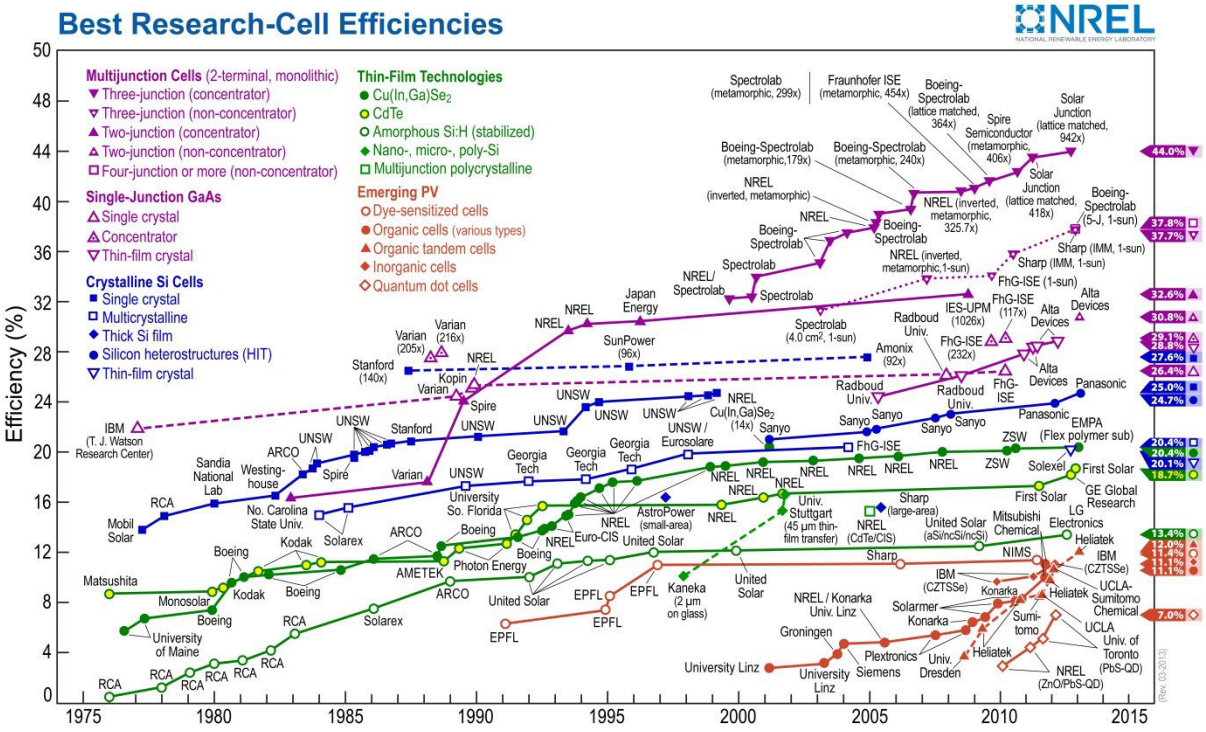


Figure 1-3 Solar cell efficiency chart for the year 2013. Chart produced by the National Renewable Energy Laboratory, NREL (reproduced with permission) [28].

1.3 The Luminescent Solar Concentrator

The LSC was originally conceived of in the 1970s by A. Goetzberger and W. Grebel [29], and separately by H. Weber and J. Lambe [30]. The LSC was proposed as a technology with the potential to reduce the cost of PV generated electricity. The LSC also has the potential to broaden the applicability of PV, for example, in novel building integrated applications, and has the added benefit of improved aesthetics, the ability of harvest direct and indirect irradiance and location versatility when compared to traditional PV modules[31].

The premise of the device is to use a luminescent dopant material homogeneously dispersed within a transparent light guide. The luminescent dopant is used to absorb light from part of the incident solar spectrum, exciting the dopant material to a higher energy level, before

releasing an emitted photon of (of slightly reduced energy) upon relaxation to the ground state. TIR within the LSC then guides a significant portion of the emitted photons to the narrow edges of the transparent light guide, in-order to concentrate light on to PV cell(s) coupled on one or more of these edges. Relative to the size of these PV cell(s), see Figure 1-4, the LSC has a significantly larger top surface area capable of harvesting both the direct and indirect components of the incident light. As a result, the LSCs top surface gathers light over a large area when compared to that of the LSCs edges, and as such there can be significant light concentration at the edges of the LSC (see Figure 1-4). An example of the upper values of photon concentration (see chapter 2, section 2.4.3) achievable by the highest power conversion efficiency LSCs to date can be found in the work of Currie *et al.* [32]. Their work featured an LSC with a power conversion efficiency of 6.8% from an LSC with low spectral overlap, which had a calculated photon concentration of 11.

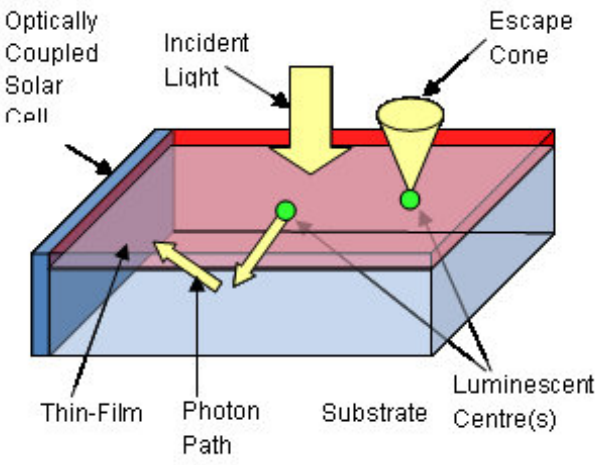


Figure 1-4 Shows the possible fates of photons incident with the surface of an LSC [33].

LSCs come in two general basic geometries, flat plate and cylindrical (see Figure 1-5). Each geometry may be homogeneously doped or have a thin-film configuration (deposited on an appropriate substrate material). A homogeneously doped LSC is typically made from a

solution of PMMA (or some other optically appropriate material) homogenously mixed together with the required luminescent species, the mixture is then poured into a mould and polymerised to form the desired shape.

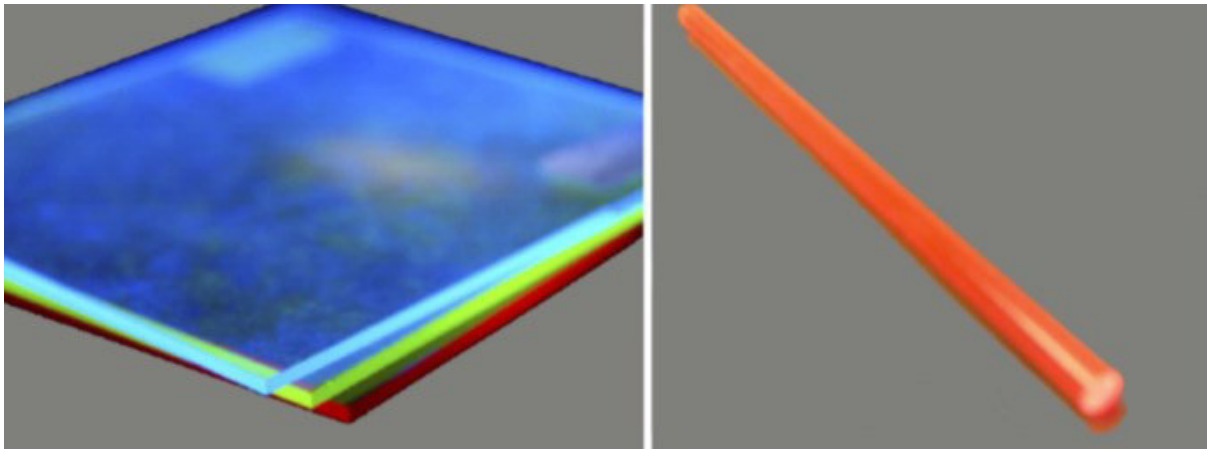


Figure 1-5 Images of cuboidal and cylindrical LSCs, image reproduced with permission from OSA [35].

Thin-film LSCs use a solution similar to that used to produce homogeneously doped LSCs. The solution is applied to an appropriate index matched substrate material such as PMMA or glass, which when dry results in a thin-film, containing luminescent material, on the surface of the substrate. To compensate for the reduced thickness of light absorbing luminescent material, the optical density of the thin-film (typically 10 to 200μm) has to be higher than for a much thicker homogeneously doped LSC (typically 3-5mm thick). However, thin-film, flat plate LSCs do not suffer from an efficiency disadvantage due to the high luminescent material concentrations required for the thin-film, when compared to homogenously doped LSCs [34]. Moreover, for the cylindrical geometry there are efficiency advantages due to a higher trapping efficiency for the coated cylinder [35]. Thin-film coating methods are technologically advanced and this LSC design offers particular advantages in the laboratory where spin coating or wire-bar coating can be easily implemented. Another advantage of

using thin-film LSCs is that glass can be easily used as a substrate material. Glass is generally cheaper than PMMA and is a more ubiquitous building material.

The vast majority of LSCs are flat plate and used as primary concentrators [36], but LSCs have also been utilised as secondary concentrators such as for a power generating window [37]. Both cuboidal and cylindrical LSC geometries have been investigated for this application. It is the inherent versatility of the LSC which allows for new ways of integrating PV and may help support the initiatives to mitigate the effects of climate change through the widespread implementation of renewable power generation. Together with the fact that there are still obstacles to the realisation of the full potential of this technology, that have thus far prevented its commercialisation, these things make the LSC a rewarding subject of study that is further developed in this thesis.

Chapters 2 and 3 of this work explains in detail the underlying theory that underpins the LSC, how it works, its advantages, sources of optical efficiency loss and finally a brief review of a number of promising research areas which may lead to improved LSC efficiency. Chapter 4 develops the methodology employed in this work in order to fabricate test LSCs and fully characterise these samples as well as any PV cells where applicable. Chapter 4 also contains a description of the raytrace computer model used during the course of this thesis, and the method for its use.

The main body of the results of this thesis are presented in chapters 5 to 7. Chapter 5 discusses the results of utilizing vertically aligned CdSe/CdTe core/shell nanorods as the luminescent species for an LSC, with the results proving the advantages of this alignment for LSC operation.

As previously mentioned, LSCs are able to absorb both direct and diffuse (indirect) irradiance which provides the LSC with an advantage over conventional CPV in that no expensive

tracking technology is required to ensure direct solar illumination of the LSC, this means that LSCs are particularly applicable for building integration [31], including being used as power generating windows [37]. For this reason a high Stokes-shifted luminescent species that absorb the short wavelength portion of the solar spectrum to which the eye is not sensitive is characterised in chapter 6 of this work. The LSC also has potential for use in more novel applications such as portable power generation, which is the main focus of chapter 6, in which the potential of large area, portable and flexible LSCs is examined through both experimental and simulation studies.

Chapter 7 discusses the use of LSCs in an entirely new application to boost the efficiency of water splitting via electrolysis with the aim of cost-efficient solar hydrogen production. This, in turn, could support fuel cell development and ultimately help support a future hydrogen economy.

Finally, chapter 8 summarises the conclusions of the results of the studies outlined above, before moving onto potential future work, and lastly describing what advances will be required to move LSCs out of the laboratory and into commercial production.

Chapter 1 References

[1] OECD/IEA, "World Energy Outlook 2012, (2012).
[1] Nordhaus, W., (2006),"Geography and macroeconomics: New data and new findings" Proceedings of the National Academy of Sciences of the United States of America. 103, 10, 3510-3517.
[3] Tol. R., (2009), "The Economic Effects of Climate Change" Journal of Economic Perspectives, 23 ,2, 29-51.
[4] Den Elzen, M., and Meinshaussen, M., (2005). "Meeting the EU 2°C climate target: global and regional emission implications", Netherlands Environmental Assessment.
[5] Global trends 2030: Alternative Worlds, National Intelligence council, (2012).
[6]King Hubbert, M., (2002). "Nuclear Energy And The Fossil Fuels", March 1956
[7] The Economist, "Peak Oil", March 5th 2013. Accessed on (11/11/2013), http://www.economist.com/blogs/graphicdetail/2013/03/focus-0
[8]World energy Group, "Coal: Resources and Future production", (2007).
[9]IEA. "Energy Technology Perspectives 2012". 2012
[10] US National Library of Medicine National Institutes of Health. "Industry Issues: Putting Heat on Gas", environmental Health Perspectives. Accessed (14/1/13).
[11] IAEA Annual Report 2011, IAEA, 2011.
[12] Frankfurt School UNEP Collaborating Centre for Climate & Sustainable Energy finance, Bloomberg New Energy Finance, "Global Trends in Renewable energy Investment 2012" (2012).
[13] McCrone, A., "Wind Farm Operation and Maintenance Costs Plummet" Bloomberg New Energy Finance. 1 November 2012.
[14]"Q3 2012 Clean energy Policy & Market briefing" Bloomberg New Energy Finance. 23 October 2012.
[15] United nations Framework convention on Climate Change. "Kyoto Protocol", http://unfccc.int/kyoto_protocol/items/2830.php . Accessed (8/1/2013).
[16] "Status of Ratification of the Kyoto Protocol", United Nations Framework Convention on Climate Change. Accessed (7/1/2013).
[17]United Nations Framework Convention on Climate Change, "Doha Climate Change Conference-November 2012". Accessed (8/1/2013).
[18] "The EU Climate and Energy Package", European Commission, http://ec.europa.eu/clima/policies/package/index_en.htm . Accessed on (6/8/2013).
[19] Commission of the European Communities, "Commission Staff Working Document: Accompanying Document to the Communication from the Commission to the Council, the European Parliament, the European Economic and Social Committee and the Committee of the Regions: A European Strategic Energy Technology Plan (SET-Plan)", (2007).
[20] Mattos, L., Scully, S., Syfu, M., Olson, E., Yang, L., Ling, C., Kayes, B., and He, G., (2012),"New Module Efficiency Record: 23.5% Under 1-Sun Illumination Using Thin-film Single-Junction GaAs Solar Cells", 38th IEEE Photovoltaic Specialists Conference, Austin, Texas, 3187-3190.

[21] Cnet. “Solar Junction Claims Cell Efficiency record”. http://news.cnet.com/8301-11128_3-20053851-54.html . Accessed (9/1/2013).
[22] Clean Technica. “Sharp Hits Concentrator Solar Cell Efficiency Record, 43.5%” http://cleantechnica.com/2012/05/31/sharp-hits-concentrator-solar-cell-efficiency-record-43-5/ . Accessed 9/1/13.
[23] Green, M., (2001), “Third Generation Photovoltaics: Recent Theoretical Progress” 17th European Photovoltaic Solar Energy Conference and Exhibition, Munich, 14-17.
[24] Forsberg, C., Peterson, P., and Zhao, H., (2007). “High-Temperature Liquid-Fluoride-Salt Closed-Brayton-Cycle Solar Power Towers” Journal of Solar Energy Engineering. 129, 141-146.
[25] Gevorgyan, S., Madse, M., Dam, H., Jørgensen, M., Fell, C., Anderson, K., Duck, B., Mescheloff, A., Katz, E., Elschner, A., Roesch, R., Hoppe, H., Hermenau, M., Riede, M., Krebs, F., (2013), “Interlaboratory outdoor stability studies of flexible roll-to-roll coated organic photovoltaic modules: Stability over 10,000h”, Solar Energy Materials and Solar Cells, 116, p187-196.
[26] Service. R., (2011), “Outlook Brightens for Plastic Solar Cells”, Science, 332(6027):293.
[27] Green, M., Emery, K., Hishikawa, Y., Warta, W., and Dunlop, E., (2012). “Solar Cell Efficiency Tables(Version 40)”, Prog. Photovolt: Res. Appl. 20:606-614.
[28] NREL, “Best Research-Cell Efficiencies”, www.nrel.gov/ncpv/ . Accessed on (31/8/2013).
[29]Goetzberger, A., and Gruebel, W., (1977), “Solar Energy Conversion with Fluorescent Collectors” Applied Physics. 14, 123-139.
[30]Weber. W., . and Lambe. J., (1976), “Luminescent Greenhouse Collector for Solar Radiation” Applied Optics. 15, 10, 2299-2300.
[31] Chemisana, D,. (2011), “Building Integrated Concentrating Photovoltaics: A review”, Renewable and Sustainable Energy reviews, 15, p603-611.
[32] Currie, M., Mapel, J., Heidel, T., Goffri, S., and Baldo, M., (2008). “High-efficiency Organic Solar Concentrators for Photovoltaics”, Science, 321, p226-228.
[33] Fisher. M., Ippen, C., Farrell, D., Walters, R., Gonzalez, M., Trautz, K., Tischler, J., Morseman, J., Buchtemann, A., and Chatten, A., (2012). “Luminescent Solar Concentrators Utilizing Bio-Derived Tandem Fluorophores” 38th IEEE PVSC, Austin, Texas.
[34] Bose, R., Farrell, D., Chatten, A., Pravettoni, M., Buchtemann, A., and Barnham, K., (2007), “Novel Configurations of Luminescent Solar concentrators” , 22nd European photovoltaic Solar Energy Conference, Milan, Italy.
[35]Edelenbosch, O., Fisher, M., Patrignani, L., van Sark, W., and Chatten, A., (2013). “Luminescent solar concentrators with fiber geometry”, Optics Express, 21, S3, pA503-A514.
[36] Bose, R.,Farrell, D., Pardo-Sanchez, C, Pravettoni, M., Mazzer, M.,Chatten, A., and Barnham, K., (2009), “Luminescent Solar Concentrators: Cylindrical Design”, Proc. 24th European Photovoltaic Solar Energy Conferene, (Hamburg, Germany), p332-335.
[37] Chatten, A., Farrell, D., Bose, R., Dixon, A., Poelking, C., Godel, K., Mazzer, M., and Barnham, K., (2011). “Luminescent and Geometric Concentrators for Building Integrated

Photovoltaics", Proc. 37th IEEE Photovoltaic Specialists Conference, (Seattle, USA), p852-857.

Chapter 2

LSC Properties and Operation

2.1 Introduction

This chapter gives a description of the solar emission spectrum, the physical mechanisms involved in LSC operation, the loss mechanisms affecting LSCs, the cost considerations affecting LSCs and alternate LSC geometries. Since the LSC is designed to work with solar cells, to convert the concentrated light into electrical current, this section also includes photovoltaic theory, as well as information related to relevant types of solar cell. Lastly, work in chapter 7 of this thesis has focused on coupling LSCs to photoelectrochemical cells (PECs), and as such an overview of the physics involved with device is also given.

2.2 The Solar Energy Spectrum

The solar spectrum is effectively that of a black body with a temperature matching the Sun's surface temperature, 5760K. As a result of having black body like behaviour, the Sun emits photons with a range of energies determined by the temperature of the Suns surface [1]. Radiation is emitted over the ultra violet (UV), visible (VIS), and infrared (IR), wavelength ranges, with the highest irradiance intensities at wavelengths between 300nm and 800nm, peaking in the blue/green region of the electromagnetic (EM) spectrum. The irradiance of the solar spectrum is a measure of radiant energy received per unit area, per unit time at a specific wavelength or energy.

The solar power density at any point on the surface of the Sun is equal to 62 MW m^{-2} [1], however, due to the distance travelled between the Sun and the Earth (~150 million km), the

intensity is much reduced upon reaching the surface of the Earth's atmosphere, a result of angular dispersion, with a loss proportional to $\frac{1}{r^2}$.

As solar radiation passes through Earth's atmosphere certain wavelengths will be attenuated by the various atmospheric constituent gases and molecules, examples of which include oxygen, carbon dioxide and water vapour. The majority of light in the visible and near infrared (NIR) region of the spectrum is not absorbed when passing through the atmosphere, but severe attenuation occurs over several wavelength bands reducing the intensity to nearly zero at some wavelengths [2]. These bands are due to absorption (or scattering) by specific gaseous elements and molecules within the atmosphere. For example, in the UV part of the solar spectrum, at wavelengths below 300nm incident solar radiation is completely absorbed due to interactions with oxygen and ozone molecules. Particularly broad absorption bands are present in the IR region which is responsible for the majority of the solar irradiance reaching the Earth's surface being at VIS wavelengths, though even VIS wavelengths are broadly attenuated by the atmosphere [2]. It is possible to quantify the attenuation of the solar spectrum as it passes through Earth's atmosphere in terms of the Air Mass (AM) factor [1], see equation 2.1:

$$AM = \frac{l}{L} = cosec(\gamma_s) \qquad 2.1$$

where l is the optical path length to the Sun, L is the optical path length to the Sun when directly overhead and γ_s is the angular elevation of the Sun with respect to the surface of the Earth, see Figure 2-1.

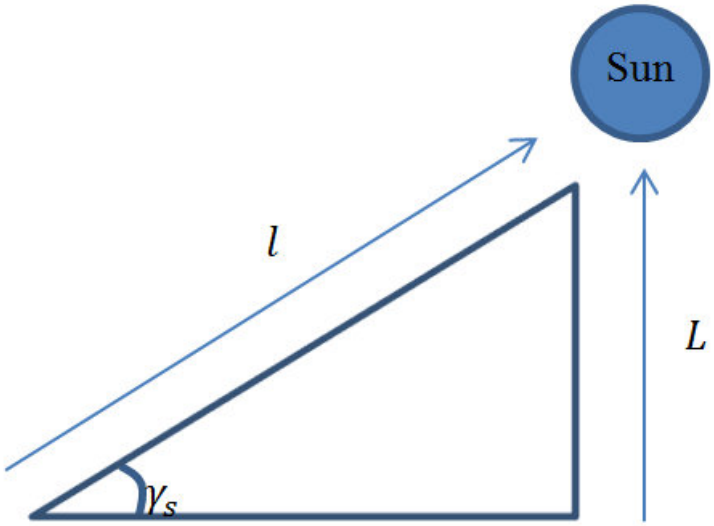


Figure 2-1 Diagram depicting the parameters in equation 2.1, diagram adapted from [*1*].

The Air Mass definition takes the solar spectrum outside of the Earth's atmosphere, the extra-terrestrial space spectrum, and then attenuates it by assuming it passes through an atmosphere which is of known thickness and known chemical composition. The standard solar spectrum assumed (see the ASTM G-173 Reference Solar Spectral Irradiance, NREL [3]) for photovoltaic research is the AM1.5g, see Figure 2-2 (in terms of normalised flux and irradiance power) where the g stands for global, meaning the light collected over a hemisphere i.e. within 2π steradians of the titled plane. The AM1.5g spectrum assumes the Sun is at an elevation of 41.81° [3], and this results in ~900 Wm^{-2} (generally this is normalised to 1000 Wm^{-2}) solar irradiance falling on the Earth. In reality the solar spectrum at the Earth's surface can vary significantly from the AM1.5 spectrum, and is affected by latitude, season, local weather and pollution conditions as well as the time of day.

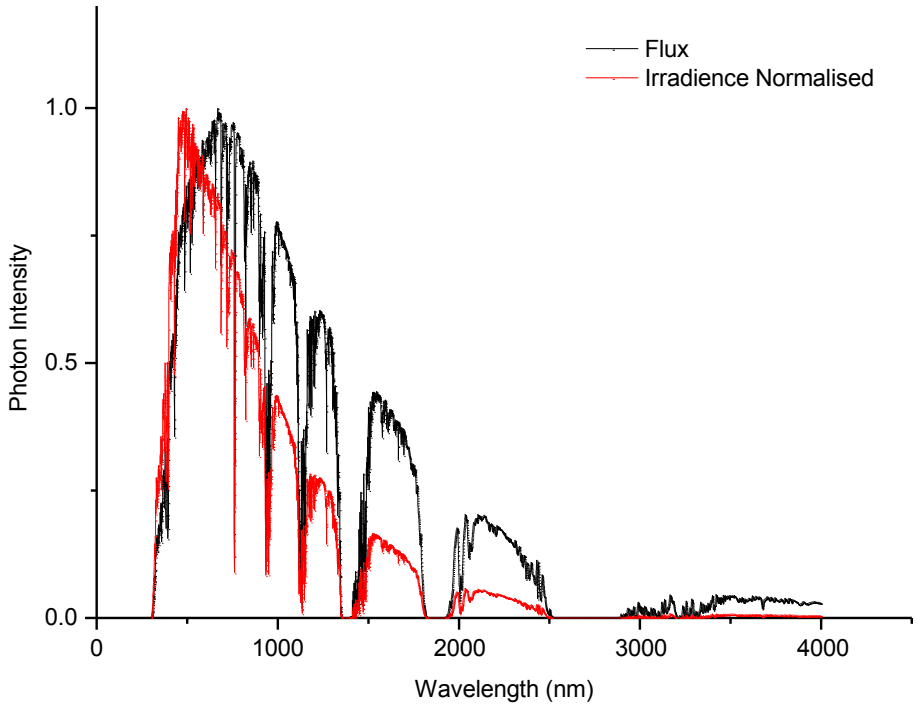


Figure 2-2 Graphs of AM15.g solar spectrum in terms of normalised photon flux and irradiance power.

In addition to absorption effects there are also a number of other more complex effects which will cause small variations in the solar energy spectrum reaching the Earth's surface. These effects include, but are not limited to; solar rotation which occurs over 27 day period, variation in the Earth/Sun distance due to the elliptical nature of Earth's orbit, Sun spots and scattering due to interaction with molecules and particulates in the atmosphere [2].

For the standard clear sky AM1.5g spectrum, scattering of photons as they pass through the atmosphere results in approximately 15% of the Sun's light being diffuse, [1], see Figure 2-3. At higher latitudes there is an even higher percentage of diffuse light due to the angle of elevation of the sun, which increases the photon path length presenting additional opportunities for light scattering. Scattering is also more likely in regions where there is often

cloud cover, and, since LSCs are adept at collecting diffuse light owing to their refractive index, this makes them of particular use in temperate regions such as in the UK, which has an average of 60% diffuse solar irradiation [4]. The work of Goetzberger [5] specifically considers the diffuse portion of the solar spectrum at northern latitudes, and concludes that due to the blue-shifting, and loss of the IR tail in the diffuse solar spectrum, as can be seen in Figure 2-3, a stack of two LSCs utilising appropriate materials would be able to collect most of the diffuse solar spectrum. He went on to show that potentially, two LSC plates could achieve higher optical efficiencies than would be possible if the diffuse spectrum was collected with GaAs and GaP semiconductor solar cells.

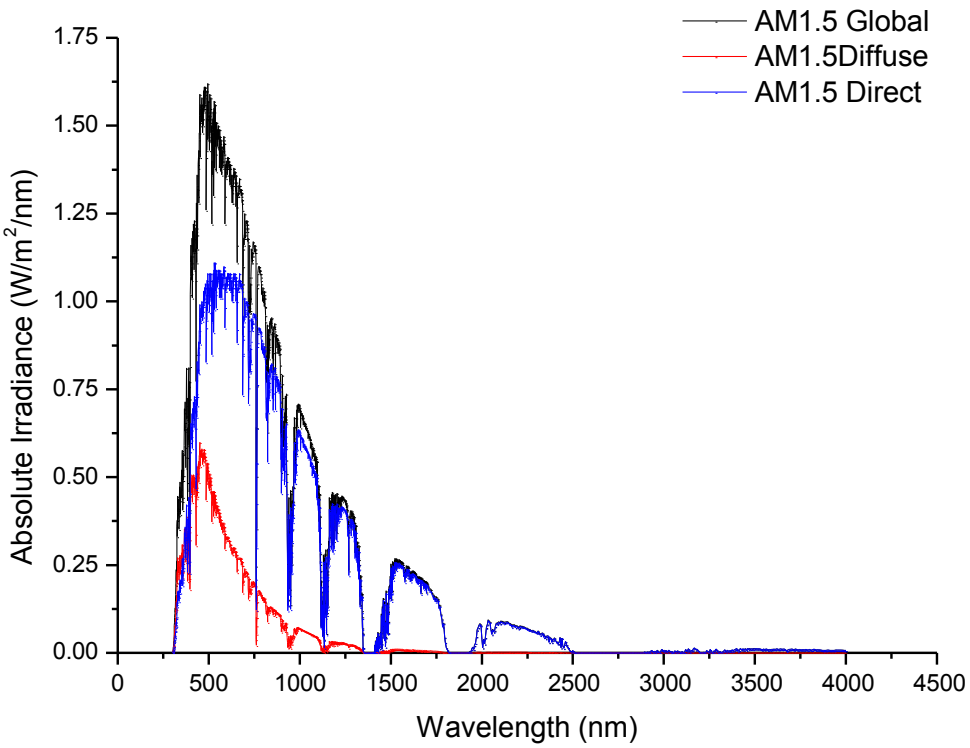


Figure 2-3 Plot of the AM1.5global, direct and diffuse spectra in units of absolute irradiance, data from [6].

2.3 Spectral Units (Flux and Power)

There are two main types of unit used when measuring emission spectra or the spectra of light sources, these are of spectral irradiance (power units) and spectral photon flux units. Figure 2-2 shows what effect each unit has on the shape of the spectrum. Units of power factor in the energy of each photon, which has the result of increasing the intensity of the higher energy region of the spectrum. When working with LSCs, and photovoltaics more generally, it is more appropriate to think of spectra in terms of photon flux, since energy will be lost from photons absorbed by the LSC due to the necessity of having a sufficiently large Stokes-shift (see section 2.6.4 on re-absorption losses). More energy will also be lost due to charge thermalization, a result of energy differences between the bandgap of the solar cell(s) and luminescent emission from the edges of the LSC. However, thermalization losses in the attached solar cells will usually be small, as the emission spectra of the LSC will generally be optimized for the solar cell(s) being used.

2.4 Principal LSC Concepts

The following section outlines some of the key parameters and equations used to determine the performance of a particular LSC, and allow for direct comparisons between different LSCs.

2.4.1 Optical Efficiency

One of the most important parameters of an LSC is its optical efficiency,η_{opt}, see equation 2.2, which is a measure of the total number of photons emitted from its narrow edges, P_E, that will be converted by the attached solar cells, divided by the total number of photons incident on the collection surface of the LSC, P_T.

$$\eta_{opt} = \frac{P_E}{P_T} \qquad 2.2$$

Therefore, by definition the optical efficiency of an LSC is not only influenced by the inherent efficiency of the LSC, but also by the light source to which the LSC is exposed. Often the AM1.5g solar spectrum will be the light source of choice (see section 2.2, Figure 2-2), but this is not always the case, and so all optical efficiencies for LSCs should be given in relation to a specified light source.

2.4.2 Geometric Concentration

The geometric concentration factor, C_G, is defined as the ratio of the area of the luminescent emitting edges of the LSC, to which the solar cells are attached, A_E, divided by the area of the light collection surface, A_S. For the simplest case of a cuboidal LSC, with solar cells attached to all four edges, with matching length (l), and width (w), and a depth(d), we get (equation 2.3):

$$C_G = \frac{A_S}{A_E} = \frac{l^2}{4ld} \qquad 2.3$$

The highest values of C_G are obtained for very thin, large surface area LSCs such as flexible LSCs (see chapter 6).

2.4.3 Photon Concentration

The photon, or optical concentration factor, C_p, is the ratio of the photon flux emitted from the narrow emission edges, ϕ_E, to the photon flux entering the top surface of the LSC, ϕ_S, and is also equal to the product of the geometric concentration and the optical efficiency (see equation 2.4):

$$C_p = \frac{\phi_E}{\phi_S} = C_G \eta_{opt} \qquad 2.4$$

An LSC with a high photon concentration will allow for a substantial reduction in solar cell size. The higher the photon concentration of an LSC the more cost effective the LSC will be in Dollars per Watt ($/W) terms. If an LSC has a photon concentration of 1 that means that the photon flux coming from the narrow converting edges is as high as the photon flux entering the collection surface of the LSC. Theoretical calculations by Smestad *et al.* [7] suggest that photon concentrations from 2-10 may be possible for LSCs that incorporate Lumogen red 300 from BASF as the luminescent species.

2.4.4 Photon Absorption & Waveguiding

When a photon is incident on the front surface of an LSC there are a number of possible outcomes. The photon may be reflected at the interface between the surrounding medium (usually assumed to be air, $n = 1.0003$), and the higher refractive index LSC (typically glass or PMMA, $n \approx 1.49$). Alternatively, the photon may enter the LSC, undergo refraction, as determined by the refractive indices of the different materials, and be absorbed by a luminescent centre, or the host/substrate material. However, the photon could be transmitted through the LSC without interaction with the luminescent material, leaving through the back surface. Lastly, the photon may be scattered due to surface defects or due to local variations in the LSC's refractive index within the host medium.

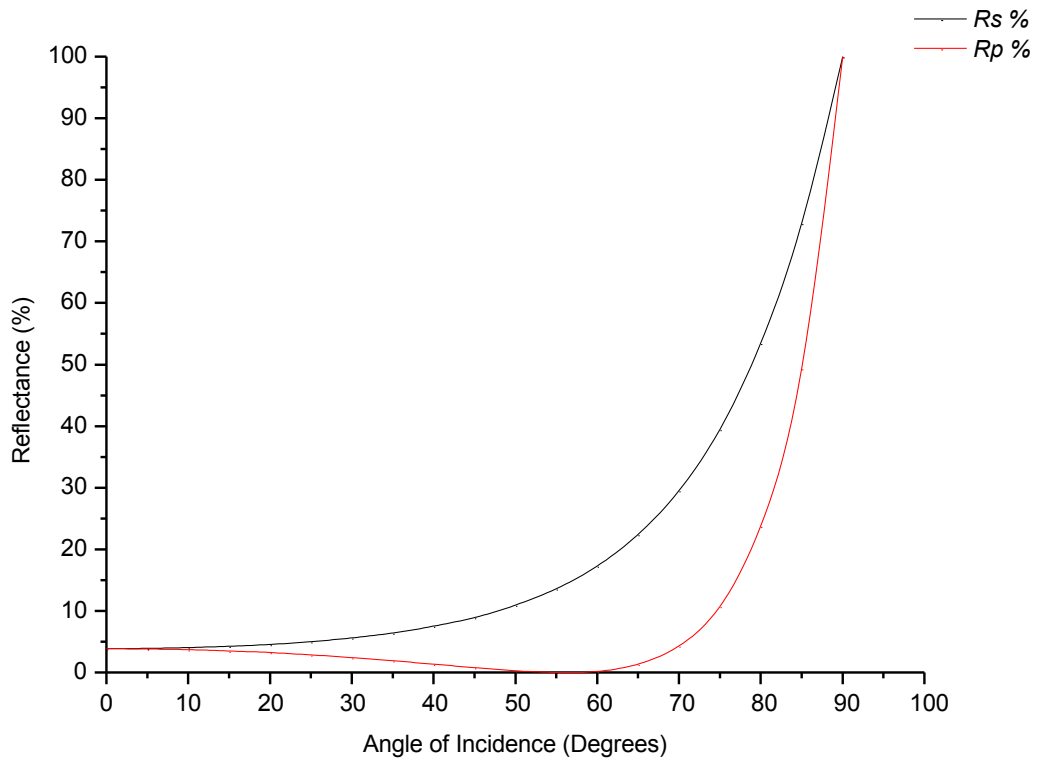


Figure 2-4 Graph showing p and s polarised reflectance for at an air/PMMA interface, calculated using the Fresnel Equations (see equations 2.5 and 2.6).

The reflection occurring when light is incident with a boundary between two materials of different refractive index is described by the Fresnel Equations. The Fresnel equations take into account the refractive indices of the two media as well as the angle of incidence, and they give the fraction of incident light reflected at the boundary. As can be seen from (Figure 2-4), demonstrating an air/PMMA boundary, the angle of incidence has a large effect on the fraction of light reflected at the boundary. Figure 2-4 shows how reflectance also has a polarisation dependence, being divided into *s*-polarised, where the EM component of the incident light is in the same plane as the interface or *p*-polarised, where the EM component is perpendicular to the interface. Equations (2.5 and 2.6) are used to determine the *s*-polarisation, R_s, and *p*-polarisation, R_p, of reflection coefficients respectively.

$$R_s = \left|\frac{n_1 cos\theta_i - n_2 cos\theta_t}{n_1 cos\theta_i + n_2 cos\theta_t}\right|^2 \quad 2.5$$

$$R_p = \left|\frac{n_1 cos\theta_t - n_2 cos\theta_i}{n_1 cos\theta_t + n_2 cos\theta_i}\right|^2 \quad 2.6$$

In the equation above n_1 is refractive index of the material external to the LSC, n_2 is the refractive index of the LSC, θ_i is the angle of incidence and θ_t is the angle of refraction. The angle of the reflected light is equal to the angle of incidence.

The angle of refraction is also determined by the refractive indices of the two media and the angle of incidence of the incoming light through equation 2.7, which defines Snell's Law.

$$\frac{sin\theta_i}{sin\theta_t} = \frac{n_2}{n_1} \quad 2.7$$

Equation 2.7 can be re-arranged to give the critical angle, θ_c, see equation 2.8:

$$\theta_c = sin^{-1}\left(\frac{n_r}{n_i}\right) \quad 2.8$$

where n_r is the refractive index of the refractive medium, and n_i is the refractive index of the incident material.

The velocity light can propagate inside a given material is inversely proportional to the refractive index of the material, as demonstrated by equation 2.9

$$n = \frac{c}{v} \quad 2.9$$

where n is the refractive index of the material, c is the speed of light in a vacuum and v is the velocity of light propagation in the material. This leads to equation 2.10, which relates velocity to the angles of incidence and refraction:

$$\frac{sin\theta_i}{sin\theta_t} = \frac{v_1}{v_2} \qquad 2.10$$

Here v_1 is the velocity in the first medium, and v_2 is the velocity in the second medium.

The transmission (related to absorption) of photons by the luminescent centres within the LSC can be described by the Beer-Lambert Law (equation 2.11):

$$T = \frac{I}{I_0} = e^{-al} \qquad 2.11$$

In equation 2.11 T is the transmission, I is the light intensity of the light transmitted through the LSC and I_0 is the intensity of the light incident on the surface of the LSC, α is the absorption coefficient and l is the sample thickness. For thin-film LSCs, the transmission of the substrate and thin-film layers must be considered separately due to the normally large differences in optical density, OD, of the two parts).

Equation 2.12 links optical density directly to absorption coefficient.

$$\alpha = \frac{OD\ ln10}{l} \qquad 2.12$$

The absorptivity, A, of a sample can be determined by use of equation 2.13, where R is reflectance and S is scatter.

$$A = 1 - T - R - S \qquad 2.13$$

Whether or not a photon is subject to total internal reflection (TIR) (see Figure 2-5 and Figure 2-6) is determined by the boundary refractive index contrast at the wavelength of the photon. Refractive index varies depending on the wavelength of the incident EM radiation, which is known as dispersion but generally does not vary greatly over the wavelength range of the absorption and emission of a typical LSC luminescent species [8] TIR cannot occur at angles less than the critical angle, θ_c,(see Equation 2.8 and Figure 2-5, where the critical angle for PMMA, $n = 1.49$, is ~42°), and therefore, for a given refractive index, a fraction of the emitted light will propagate out from the top and bottom surfaces of the LSC via escape cones. There are also escape cones from the narrow edges of the LSC if the edges are bare, but usually light emitted from the narrow edges will be collected by coupled (index matched) solar cells (see Figure 2-6) or, if not, will be reflected back into the LSC using highly reflective mirror materials. Equations 2.15 and 2.17 show respectively, for a given refractive index and isotropic emission, the fraction of emitted photons that will be lost through the top and bottom surface escape cones, η_{escape}, and the fraction that will remain trapped inside the LSC, η_{trap} is derived from η_{escape}.

$$\Omega_{escape} = \int_0^{2\pi} d\phi \int_0^{\theta_c} sin\theta_c \, d\theta = 2\pi[1 - cos\theta_c] \qquad 2.14$$

$$\eta_{escape} = \frac{2\Omega_{escape}}{\Omega_{total}} = 1 - cos\theta_c \qquad 2.15$$

$$\eta_{trap} = 1 - \eta_{escape} = cos\theta_c \qquad 2.16$$

$$\eta_{trap} = \sqrt{1 - sin^2\theta_c} = \sqrt{1 - \frac{n_1^2}{n_2^2}} \qquad 2.17$$

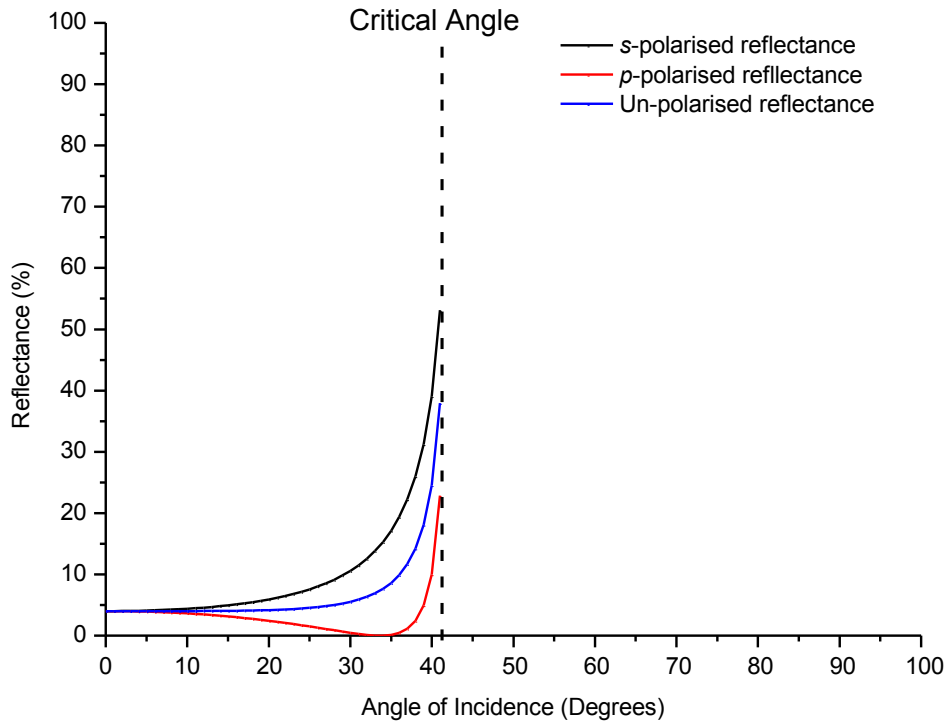


Figure 2-5 Plot of reflection of light propagating out of the LSC, demonstrating TIR at a PMMA/air boundary, refractive indices 1.49 and 1.0003 respectively and a critical angle of ~42°.

In equations 2.14 to 2.17 Ω_{total} is the solid angle of a sphere, 4π, and Ω_{escape} is the solid angle of the escape cone. For an LSC consisting primarily of PMMA, primary emitted light with an isotropic distribution has a trapping efficiency of ~74%.

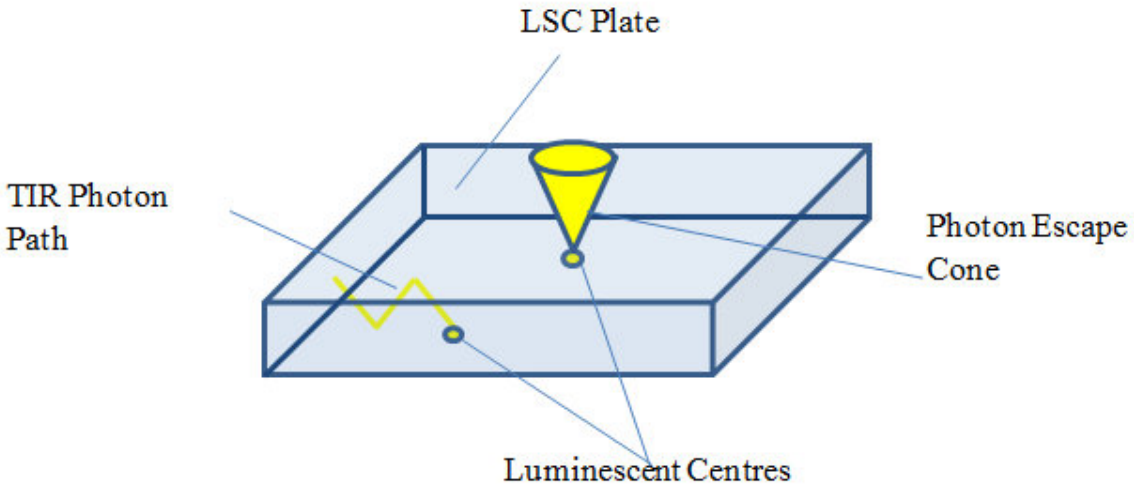


Figure 2-6 Schematic diagram of a LSC diagram illustrating the difference between an emitted photon impinging the LSC top surface at an angle greater than the critical angle (TIR photon), and a photon incident with the surface at an angle less than the critical angle (photon lost via an escape cone).

2.5 Luminescent Centres (Absorption and Emission)

In broad terms, luminescent centres come in two main types: inorganic nanocrystals for example nanorods or quantum dots, and organic based materials such as the perylene based Lumogen dyes from BASF. However, a number of luminescent species exist which have a combination of organic and inorganic constituents, for example nanocrystals, bound to organic ligands, and metal complexes. This next section describes the various physical mechanisms which govern absorption and photoluminescence (PL) in each type of luminescent species.

2.5.1 Absorption and Emission of Inorganic Nanocrystals

Nanocrystals (NCs) such as nanorods (NRs) and quantum dots (QDs) when used in LSCs are essentially individual particles since organic ligands are applied to the surface of these NCs for the purpose of separating them from one another, so as to prevent them from forming a bulk semiconductor and, therefore, to prevent them from losing their unique optical

properties [9]. Since NRs are individual particles they do not have conduction bands, valence bands and bandgaps in the same way as bulk semiconductors do, though they do have energy levels which are somewhat analogous to bulk semiconductors, but still fundamentally different. The energy bands, absorption and emission, are a result of variations in the dimensions of the NCs [12]. For example, an individual QD has quantum confinement in 3 dimensions which produces discrete energy levels [1]. If the QD is part of a large array of similar QDs which have slightly different dimensions, as would be the case in a QD LSC, each with a slightly different set of discrete energy levels, then these discrete energy levels will effectively blend together forming absorption and emission energy bands [1].

In an isolated NC, absorption of a photon will occur if the photons energy is greater than the energy gap between the discrete energy levels present in the NR. Unlike for bulk semiconductors, the size of the NC has an effect on the size of the energy gap (bandgap in the case of bulk semiconductors). This is a phenomenon known as quantum confinement, and it occurs if the exciton Bohr Radius is larger than the NC [14]. NCs have larger energy gaps between their absorption and emission energy levels than the bangaps in corresponding bulk materials, and smaller NCs have a larger difference between their valence and conductance energy levels than larger ones have. Consequently, the absorption spectrum is shifted towards the blue end of the spectrum for small NCs [10].

The emission spectrum from multiple NCs will be centred at an energy which corresponds to the energy gap between the NCs conductance and valence energy states, which means that there will be a Stokes-shift between the emission peak, and the lowest energy absorption peak [10]. Each NC has its own distinct transition energy between the discrete conductance and valence energy levels, which is responsible for producing a near discrete emission [11]. As described above for photon absorption by NCs, if there is a large number of NCs there will also be a range of NR sizes, each with its own energy transition value. In the case of NRs,

variations in the diameter are responsible for the changes in transition energy, rather than variations in the NR length [12]. As a result of the range of NC dimensions, in a typical LSC sample for example, there is a broadening of the previously near discrete emission [13], into a spectrum of emission energies, with the emission intensity across the emission spectrum being determined by the frequency of each size of NC.

NCs can be either homostructures in which the NC are made from a single material, or hetrostructures where the NCs consist of a number of different materials [11].There are two types of NC hetrostructure, where electron/hole relaxation occurs within one material these are referred to as Type-I NCs, when electrons and holes are in two different materials these are call Type-II NCs, for further details see section 3.3.4, chapter 3.

2.5.2 Absorption and Emission for Organic Luminescent Species

In the case of organic materials, including conjugated polymers, there are some differences in terms of their absorption and emission mechanisms, when compared to bulk semiconductors, although they have similarities to NCs. For conjugated polymers and aromatic hydrocarbons (such as the perylene based Lumogen dyes from BASF, see chapters 5, 6 and 7), the band-type behaviour observed for bulk inorganic semiconductors does not exist, instead the electron states and vibrational states are localised, and are bound to specific molecules [14]. The localisation of these states is of vital importance, as it closely links the absorption and emission properties to those of the constituent molecules.

In general if an incident photon of sufficiently high energy is absorbed by an organic luminescent material, then an electron will be provided with enough energy to move from the HOMO (Highest Occupied Molecular Orbital) level to the LUMO (Lowest Unoccupied Molecular Orbital) level, this is the lowest energy electronic transition possible [14]. Above each of these energy levels there exist a number of vibronic energy levels, arising from the

vibration of atoms within the molecule, which form a continuum of additional energy levels above each electronic state of the molecule (this is an example of inhomogeneous broadening). This is illustrated for the ground state (HOMO), and the first excited state (LUMO) in Figure 2-7 [14]. Electrons with sufficient energy can occupy these higher energy vibrational states above the LUMO level (and higher excited states and their manifolds of vibronic levels). However, through a process somewhat akin to phonic decays within inorganics, the excess electron energy is lost non-radiatively, via phonon interactions, which occur much more rapidly than spontaneous emission, until the ground vibrational level is reached, before emitting a photon. Another type of non-radiative relaxation, called intersystem crossing, occurs when there is decay to a triplet state and then either a subsequent phosphorescent emission (see section 2.5.3), or non-radiative decay, to the ground state. A third type of non-radiative relaxation is internal conversion, where energy is transferred from an excited nucleus to an inner shell electron, the electron then escapes taking the excitation energy with it [15].

De-excitation takes the electron back to the HOMO level, but it is likely to occupy one of the higher vibrational states and there will then be further non-radiative decay which returns the electron to the ground vibrational state of the HOMO. The decay through the vibrational energy levels results in the emitted photons being of lower energy than the photons initially absorbed by the material, which consequently creates the Stokes-shift observed in the luminescence from organics. Homogeneous broadening of the molecular emission affects all of the molecules in the same way, unlike inhomogeneous broadening [16]. The finite lifetimes of molecular energy levels may result in homogeneous broadening.

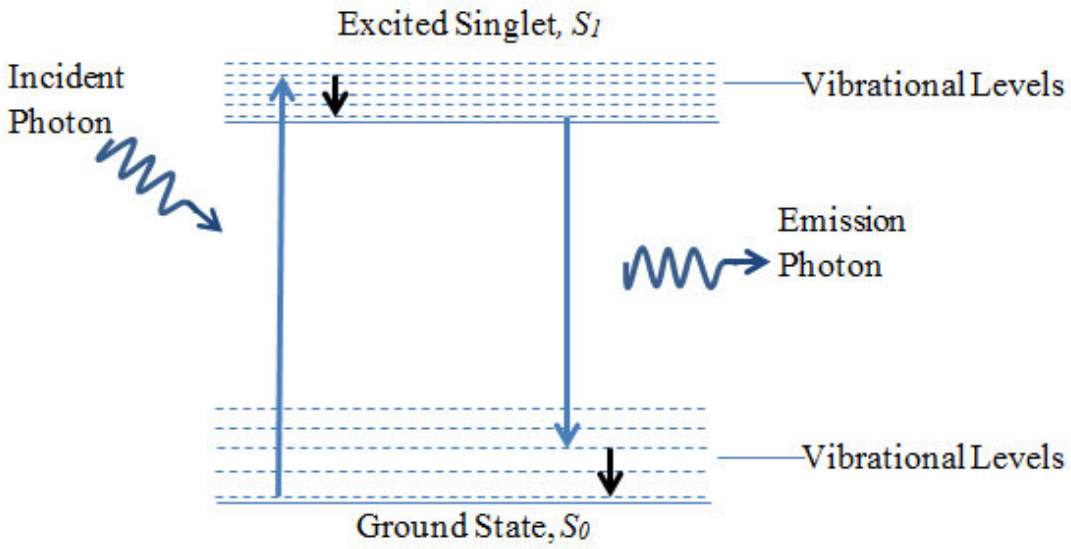


Figure 2-7 Electronic transitions in an organic molecule, adapted from [14].

In conjugated polymers and other molecular semiconductors such as the polycyclic aromatic hydrocarbons and fullerenes such as PCBM, π electrons are delocalised allowing them a large field of movement within the molecule, and effectively reducing confinement [9,14]. Reducing π electron confinement by increasing the size of a molecule allows for more π electron delocalisation, and for the electronic transition energy to be reduced, meaning the absorption and emission wavelengths can be tailored by varying the molecules size such as in anthracene (3 rings), tetracene (4 rings), pentacene (5 rings), or by varying the effective conjugation length in conducting polymers [9,14]. In the work of Izumi *et al.* [17] has shown that in beta-blocked oligothiophenes, the effective conjugation length is up to 96 repeating units of thiophene.

Organic molecules have both singlet (spin paired) and triplet (spin unpaired) states as related to the electron spin states. Typically the strongest photon emission will occur from the spin allowed $S_1 \rightarrow S_0$, transition known as fluorescence, although sometimes the spin forbidden

$T_1 \rightarrow S_0$ transition known as phosphorescence is also a significant emission process and contributes to the photoluminescence (See next section 2.5.3 on phosphorescence).

2.5.3 Phosphorescence

The preceding section (section 2.5.2) is largely concerned with fluorescence which occurs on a timescale on the order of 10^{-9}-10^{-8}s. However, the excited triplet state associated with phosphorescence has a much longer lifetime, typical on the order of 10^{-3}s [18], with the longer phosphorescent lifetime being a result of a low radiative emission probability [14]. Phosphorescence is an example of inter-system crossing in which there is a transition from the first excited singlet, S_1, state to the first of the triplet states, T_1, and subsequently a photon emission from this lowest triplet state to the ground state, $T_1 \rightarrow S_0$, both of which require an electron spin to be reversed. Triplet-triplet annihilation is an additional example of inter-system crossing, in which two molecules in the lowest triplet states interact with one another resulting in a delay in fluorescence [19]. However, quantum mechanics demands that spin must be conserved in an electronic transition this is known as the spin conservation selection rule. Singlet states have spin quantum number S=0, since an electron has S=$\frac{1}{2}$, and the unpaired electrons in singlet excited states are anti-parallel (paired), triplet states have S=1, as the excited unpaired electrons have parallel spin (unpaired). However, although triplet to singlet (and vice versa) transitions are spin forbidden by the selection rule $\Delta S = 0$, in reality these transitions do occur (especially if the vibrational energy levels overlap so there is little or no energy gained or lost in the transition) but, they do happen at a much slower rate and phosphorescence is one of the slowest forms of relaxation [20], (Figure 2-8 Electron energy transition diagram featuring inter-system crossing and phosphorescence, adapted from [14].).

Every singlet state has its own corresponding triplet state, typically of lower energy than the single state, which means phosphorescent emission is generally at lower energy than

fluorescent emission [18]. The lower energies of the triplet state can be explained by Hund's 2nd rule. States which have higher total angular momentum, as is the case for spin-unpaired triplets, relative to spin-paired singlets, will also have the lowest energies since the electron orbits are in the same direction, and as such the electrons do not meet as often and suffer lower repulsive forces. This is when compared to the singlet in which the repulsive forces are higher, which tends to separate the electrons, thereby increasing their potential energy and leading to a higher energy singlet state [21,22]. Phosphorescent materials have been used as a scattering/spectral-down-shifting material to enhance LSC emission output in a recent publication [23]. The phosphorescent layer served to both scatter light outside of its own absorption spectrum, as well as spectrally shifting the wavelengths absorbed by it to more useful wavelengths for the primary luminescent species to absorb. In the work of Currie *et al.* [24] a phosphorescent dye is used as one of the dyes in their 6.8% power conversion efficiency stack LSC, since its high Stokes-shift reduces the chances of reabsorption losses which are discussed in more detail in section 2.6.4.

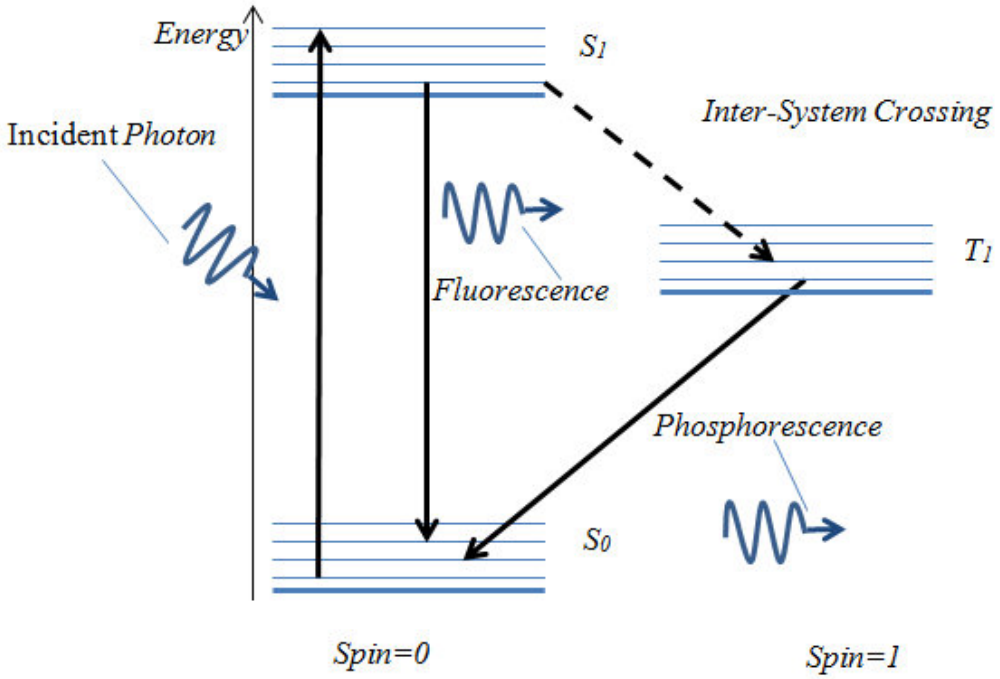


Figure 2-8 Electron energy transition diagram featuring inter-system crossing and phosphorescence, adapted from [14].

2.6 Sources of Optical Efficiency Loss

There exist a number of mechanisms by which LSCs can lose photons before collection by the PV cells, these loss mechanisms lead to a reduction in the optical efficiency of the LSC. The following section gives a summary of key sources of optical efficiency loss in LSCs.

2.6.1 Surface Reflections

Before even entering the LSC, a small fraction of incident photons will be lost to the LSC/PV system due to surface reflections (see section 2.4.4 above). These surface losses are the result of differences in the refractive indices between the different media which make up the reflection boundary and equations 2.5 and 2.6 in section 2.4.4 show how reflection with s and *p* polarisation vary with the angle of the incident light. Often PMMA or glass is used in the fabrication of LSCs. Therefore, for a homogeneously doped LSC made from PMMA, which

has a refractive index of ~1.49, surrounded by air, refractive index 1.0003, approximately 4% of incident photons will be reflected from the top surface of this LSC, assuming the incident photons are at normal incidence to the surface. Figure 2-9 shows how increasing the angle of incidence of incoming photons greatly increases (at large angles) the fraction of photons reflected from the top surface in the case of a non-polarised incident light source, such as the sun, while Figure 2-4 shows how the individual polarisations are differently affected by angle of incidence. For diffuse light isotropic over a hemisphere the appropriate *cos(θ)* weighted angularly averaged reflectivity for an air/PMMA interface is 6.7%. Therefore for an LSC situated at latitude angle to minimise the reflection losses, reflection losses are generally small and only become a major source of loss when the sun is low in the sky around dawn and sunset [9].

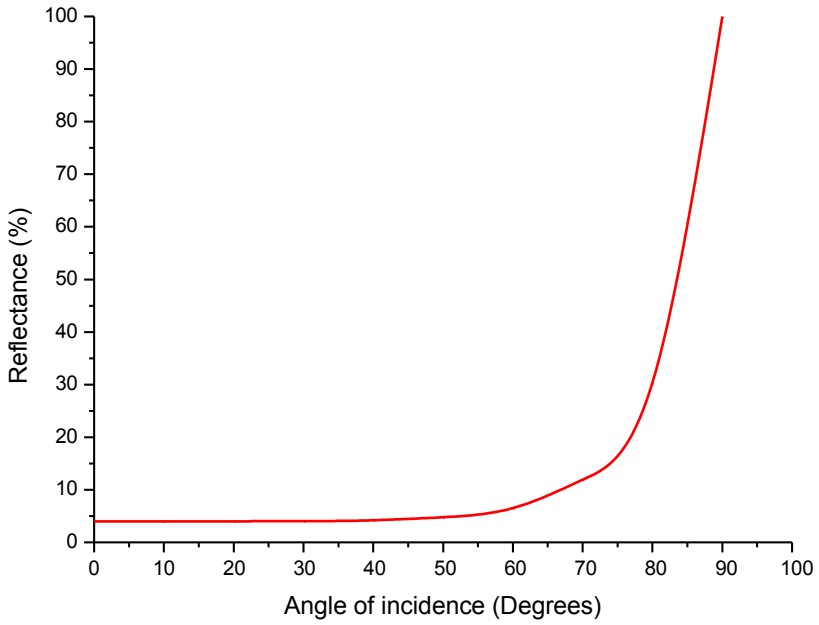


Figure 2-9 Chart illustrating the variation of the fraction of un-polarised light reflected with angle of incidence, for an air/glass boundary where the glass has a refractive index of 1.52.

2.6.2 Non Unity Luminescent Quantum Yield (LQY)

An ideal luminescent species will have a LQY of 1. This means that if a photon of sufficient energy is absorbed by the luminescent centre, and raises an electron to an excited state, when the electron returns to the ground state it will do so radiatively 100% of the time. If the LQY is below 1, a fraction of the incident photons, which are absorbed by the luminescent species and raise an electron to an excited state, will have their energy lost via non-radiative paths. In this latter case the energy is generally dissipated as heat through phonon interactions. Alternatively, an excited atom may lose energy via internal conversion, whereby electromagnetic interactions between the excited atomic nucleus and an inner shell electron results in the energy being transferred to this electron, and the electron is then subsequently ejected from the atom [15].

If an emitted photon from the de-excitation of a non-unity LQY luminescent centre is re-absorbed by another such luminescent centre before leaving the LSC, then the excitation/de-excitation process will occur again, and the LQY of the material will once again determine the likelihood of a radiative event (see section 2.6.4 reabsorption losses). Therefore, samples with large absorption/emission spectral overlap may suffer significant LQY losses, unless the sample has a very high LQY, thereby preventing a large fraction of the absorbed photons ever reaching the attached solar cell(s).

2.6.3 Light Cone/Escape Losses

Individual luminescent centres have a dipolar absorption/emission distribution. Therefore, given an isotropic light field and a large enough number of randomly oriented luminescent centres (randomly oriented transition dipoles), then the emission direction is random, and the emission profile will be exactly spherical. For a PMMA based LSC with n = 1.49 operating under these conditions, the fraction of light trapped in the LSC can be calculated from equation 2.17 to be 74% and thus, in the absence of reabsorption) 26% of the emitted light

will be lost through the escape cones on the top and bottom surfaces (see Figure 2-6). However, in LSC operation the sun does not provide an isotropic light field and so the emission profile will be polarised and dependent on the angle of incidence as has been investigated by Verbunt *et al.* [25] showing that the trapped fraction increases with angle of incidence. For PMMA they calculate the trapped fraction varies from ~71% at normal incidence to ~77% at grazing incidence at 90° to the waveguiding plane. However, these calculations are lengthy, and under isotropic diffuse light illumination equation 2.17 is a good approximation. Additionally, although it does not hold for an LSC illuminated by direct light at a given angle of incidence, it represents an average value that is generally accurate enough to give agreement between simulation (usually accurate to around ±2%) and experiment (usually accurate to around ±5%) [26, 27]. Therefore in the ray-tracing simulations of LSCs, described in detail in the next chapter, the simplifying assumption of isotropic emission is used. It follows therefore that if the dipolar luminescent centres are aligned so as to have the same orientation as one another (transition electric dipoles aligned), then the distribution of emission vectors is determined by the spatial distribution of the luminescent centre(s). Debije's group have also investigated the effect of different types of alignment on LSC operation and this is discussed in detail in section 3.2.5, chapter 3.

2.6.4 Reabsorption Losses

If the Stokes shift between the light absorption spectrum and the light emission spectrum of the LSC is not sufficient to completely prevent spectral overlap between these two spectra, re-absorption of emitted photons may occur (see Figure 2-10). The probability of photon re-absorption is dependent on the extent of the overlap between the spectra, the emission wavelength of the photon(s) in question and the optical density (determined by the concentration) of the luminescent species. Multiple re-absorption events are a debilitating source of energy loss for LSCs; this is due to the probability of other photon loss

mechanisms, such as non-unity LQY (see section 2.6.2) and escape cone losses (see section 2.6.3), being multiplied. For example, as mentioned in section 2.6.2, if LQY is not equal to 1, then there is a percentage chance that an absorbed photon will not be re-emitted, if there multiple re-absorption events due to spectral overlap, energy losses quickly mount.

In the work of Bose *et al.* [28], the detrimental effect of reabsorption losses is shown to provide a practical limit to the upper dimension of an LSC. In their work raytrace simulations of sample utilising Lumogen red 300 (BASF), with a LQY of 95%, showed a clear plateauing of the photon concentration ratio as the sample approached a top surface area of $1m^2$ (where the concentration ration is the ratio of the photon flux leaving the narrow edge coupled to the detector, divided by the photon flux entering the LSC's top surface). The plateauing of the photon concentration ratio was attributed to absorption by the PMMA matrix material (absorption coefficient $2m^{-1}$) and reabsorption losses due to the spectral overlap of the dye. Of course, if the parameters were changed the plateauing would have occurred at different sample dimensions, however, this work clearly demonstrates the diminishing returns of using larger LSCs due to reabsorption losses.

The work of Wilson *et al.* [29] showed that for strip LSC using Lumogen red 305 (BASF) at a concentration of 393ppm and an effective optical density of 86 (as determined by $OD_{eff} = \varepsilon_{peak}\, x\, c\, x\, d\, x\, log(2.71828)$, where ε_{peak} is the peak Naperian absorption coefficient (in this case $0.101ppm^{-1}\ cm^{-1}$), c is the dye concentration (393ppm as described above) and d is the distance or the excitation point from the LSC edge of measurement (5cm). For this case there was only 30% of the emitted photons reaching the edge without first being reabsorbed. It is important to note that Wilson *et al.* were unable to fully measure the absorption tail of the LSC due to sensitivity issues, so reabsorption may have been slightly higher in reality than these results suggest. They go on to conclude that, beyond a certain size

of LSC reabsorption becomes less probable since significant reabsorption losses have already occurred, and the remaining emitted photons are unlikely to have sufficient energy to be reabsorbed again. As described above the level of reabsorption in [29] is also dependent on the LSC parameters.

Calculations by Verbunt *et al.* [25] for a Lumogen red 305 containing LSCs with a polycarbonate matrix showed that their dichroic dye model (which models a dye with dipolar emission even if the dye molecules are randomly oriented overall) had 1.4-1.6 reabsorption and reemission events for every photon, while for their isotropic dye model (randomly oriented dyes are modelled to have isotropic emission, which is how most raytrace models function) had 2 reabsorption and reemission events for each photon.

From examining the 3 examples listed above, the highly detrimental effects of reabsorption losses from absorption and emission spectral overlap cannot be underestimated, and as such a high Stokes-shift material is studied as part of chapter 6 of this thesis.

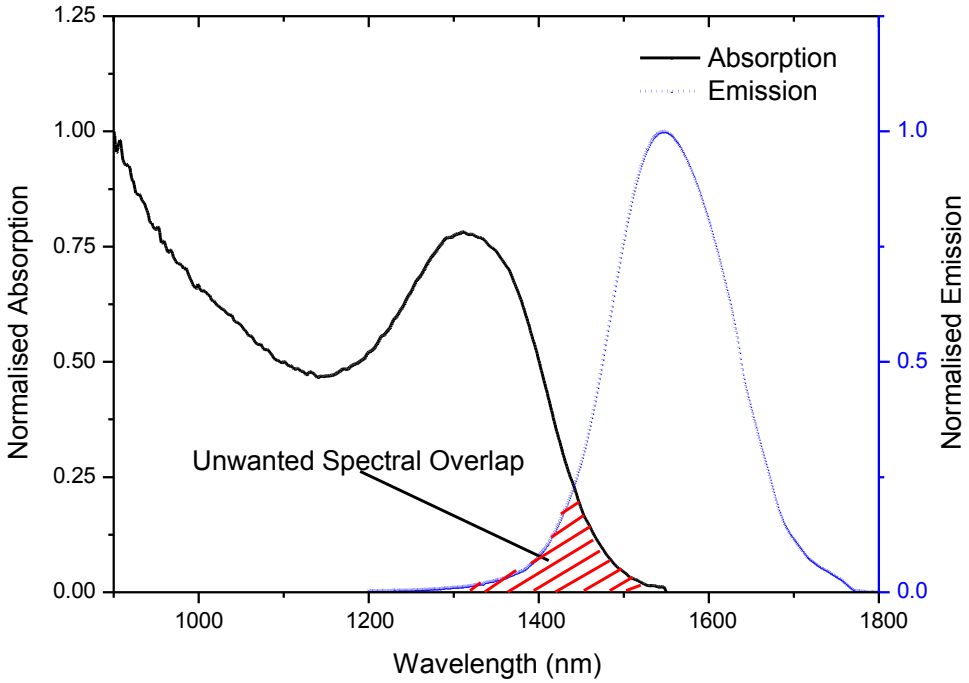


Figure 2-10Graph showing the region of spectral overlap between the absorption and emission spectra for PbSe nanorods. Spectral overlap is an unwanted property since it leads to reabsorption losses.

2.7 Alternate Geometries

Although the majority of LSC research has been performed on traditional planar LSCs, in either homogenous or thin-film varieties, LSCs are not limited to this configuration. In fact recently in the work of Edelenbosch *et al.* [30] it has been shown that cylindrical fibre LSCs, see Figure 2-11, are capable of achieving high optical concentration. Using the AM1.5g spectrum out to 1100nm, the bandgap of silicon, simulations determined that for a 1m length, 1mm radius fibre doped with Lumogen red 305 (BASF), had a photon concentration gain of ~35 times. The authors attribute such a large photon concentration gain to not only the very large incident light absorption area of the LSC fibre, when compared to the very small surface area of the LSC emission edges (high geometric concentration ratio), but also due to

the reabsorption losses occurring over a short distance. Therefore, by further increasing the fibre length, there will be a further increase in geometric concentration but not in reabsorption losses, producing a net gain in photon concentration. In addition, the authors compared coated (doped coating) fibres with homogenously doped fibres (see Figure 2-11) with matching photon absorption, coated fibres were deemed superior as they have a higher trapping efficiency. For example, the trapping probability of a photon emitted at the centre of a cylinder is ~33% compared to ~74% for an emission at the outer edge of the cylinder.

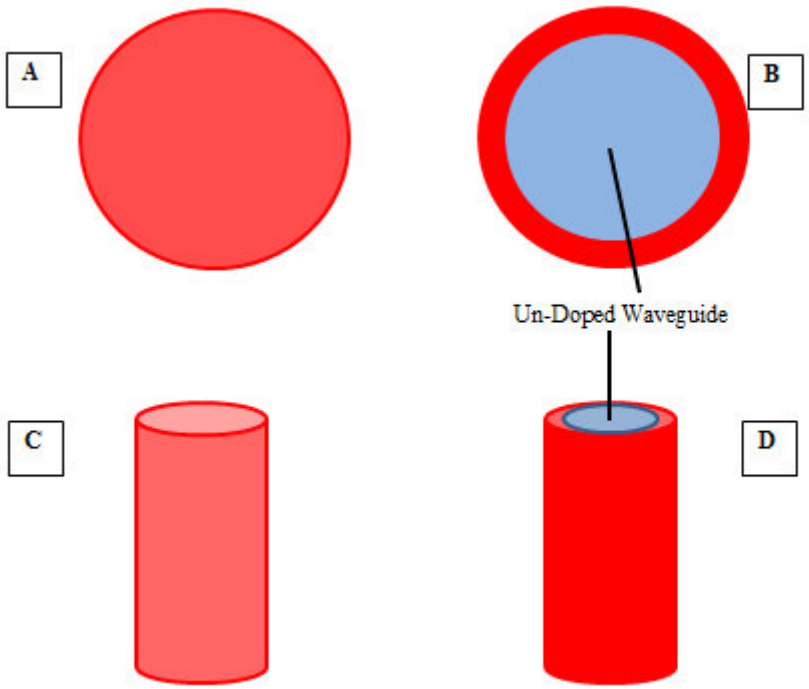


Figure 2-11 A) and B) show emission edges of homogeneously doped and thin-film coated cylindrical LSCs respectively. C) and D) show the long axis view of homogeneously doped and thin-film coated cylindrical LSCs respectively.

Prior to the work of Edelenbosch *et al.* [30] work by McIntosh *et al.* [31] featured raytrace results which suggest that when emission occurs very close to the surface of a cylindrical LSC there may be as much as 1.9 times the photon concentration as for a planar LSC with the same incident light harvesting surface area as a the cylinder. Their work also considered

placing multiple cylindrical LSCs next to one another, in place of a larger single cylinder, for the purpose of reducing reflection losses for incident photons. This resulted in a ~4.5% increase in optical efficiency. Numerous other LSC geometries have been considered, such as the triangular LSCs considered by Goetzberger [32], or the work by Kennedy *et al.* [33]. In the study by Kennedy *et al.* [33], comparing circular, square, triangular and hexagonal geometries, simulations revealed that for a given geometric concentration factor, circular and hexagonal shaped LSCs give the highest photon concentrations. However, for optimum light harvesting the circular geometry should be discounted as it does not tessellate.

Another interesting LSC geometry is considered in the work of Giebink *et al.* [34] to produce a resonance-shifting LSC. In their work they use a typical square shaped, glass substrate with a low index material on the top surface (approximately half of the emission wavelength thick), above this layer the luminescent material was deposited in strips of varying thickness to form cavities with different resonance conditions. The low index material allows many of the emitted photons to enter the substrate, due to its ~0.5 emission wavelength thickness. The photons which enter the substrate do so at quite specific angles, and therefore, after being reflected from the bottom surface of the substrate back to the top of the LSC, the emitted photon will interact with a strip of luminescent material of different thickness from the one it originally came from. Therefore the consequence of the difference in thickness is that the emitted photon will have a near 100% probability of being reflected by this second strip of luminescent material, since it will be non-resonant with the modes which exist within this second cavity. As a result the possibility of reabsorption is greatly reduced. The authors go on to show via simulated results that an ideally patterned resonant shifting LSC may have a photon concentration of 24, and an optical efficiency of 4.8% at a geometric concentration of 500. While a control LSC which is otherwise identical to the resonance-shifting LSC, except that it lacks the spacer layer which is present in the resonance-shifting LSC, may have a

photon concentration of 10 and an optical efficiency of 2% at the same geometric concentration.

2.8 LSC Cost

Since the LSC was originally envisioned as a means to reducing the cost solar power generation, it is important to mention the work that has been done regarding LSC cost considerations. In the 1970s when the LSC was first proposed [5,35] the price of silicon solar cells was far higher than today, and the LSC offered a path to large cost reductions by allowing for significant decrease in the area of silicon solar cells required. Unfortunately, LSC lifetime was hindered by the lifetimes of organic dyes used at this time [36]. However, as the years have passed, the price of solar cells in terms of total expense and cost per Watt terms has dropped dramatically, and this is particularly true for crystalline silicon solar cells as shown in Figure 2-12 [37] As a result the LSC needs to significantly improve in cost per Watt terms to be able to compete with silicon solar cells directly, or (as is more likely in the author's opinion) LSC development should focus on niche applications, for example, building integration, or the applications which are the focus of chapters 6 and 7 of this thesis.

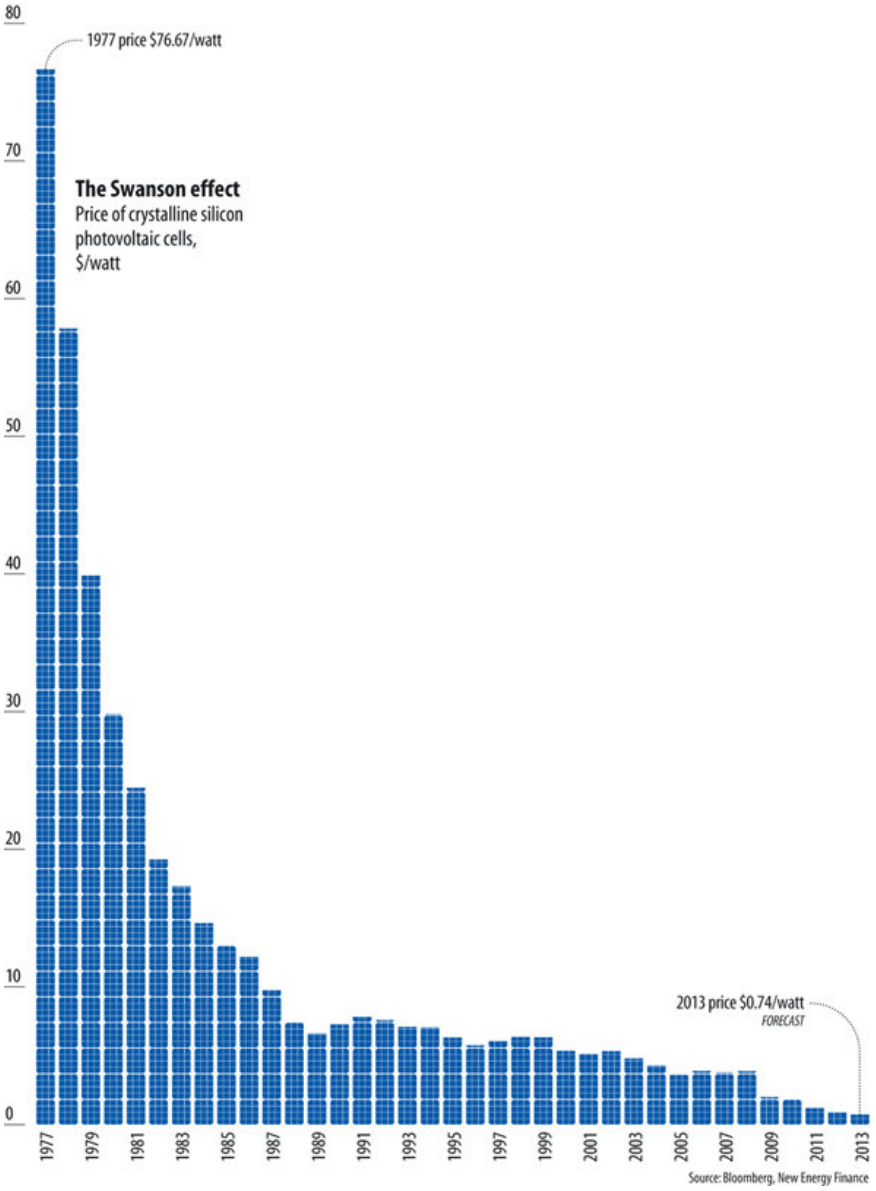


Figure 2-12 Graph showing the dramatic reduction in the price of crystalline silicon solar cells between 1977 and 2013, reproduced with permission from "The Economist" magazine [37].

In the field of solar energy, costing of PV or in this case LSCs is usually considered in terms of cost per Watt, which is the expense of the LSC in terms of materials (including solar cells and optical matching material, etc.), manufacturing and any other associated cost divided by the total power output in units of Watts when illuminated under standard conditions (AM1.5g at normal incidence). When considering published work on the costing considerations of

LSCs, the author feels that it is prudent to consider only the more recent work since the price of solar energy generation changes rapidly, as highlighted in Figure 2-12.

In the work of Farrell and Yoshida [38], the authors split LSC cost considerations between two generations of LSC; Generation-I LSCs which are essentially the standard LSC type that has existed since the 1970s and suffers extensive reabsorption loses and Generation-II LSCs which feature luminescent species/other efficiency enhancing technologies, which in time may allow LSC efficiencies to approach that of the thermodynamic limit calculated in [39]. In [39] a power conversion efficiency of 26.8% is predicted when an ideal LSC is coupled to an ideal silicon solar cell. Farrell and Yoshida [38] calculate the ratio of the cost per Watt of an LSC system (including cells) and the cost per Watt of a PV system, χ, as:

$$\chi = \frac{C_p W_{lsc}}{C_p W_{pv}} = \frac{C_{lsc} P_{pv}}{C_{pv} P_{lsc}(C_g)} \qquad 2.18$$

In equation 2.18 $C_p W_{lsc}$ is the cost per Watt of an LSC system, $C_p W_{pv}$ is the cost per Watt of a PV system, C_{lsc} is the areal cost of the LSC, C_{pv} is the areal cost of PV, P_{pv} is the power from the PV, P_{lsc} is the power from the LSC and C_g is the geometric concentration of the LSC [38]. When $\chi = 1$, the cost per Watt of the of the two systems match, and for values less than 1 the LSC system has the price advantage. Using equation 2.18 [38] they go on to show that if $\chi = 1$, the cost of the LSC plate can afford to be no greater than 11% the cost of a conventional PV system, while if $\chi = 0.5$, the LSC plate must cost less than 0.1% of the equivalent PV, which is clearly impractical.

$$\frac{C_{plate}}{C_{pv}} = \chi \frac{P_{lsc}(C_g)}{P_{pv}} - \frac{1}{C_g} \qquad 2.19$$

In equation 2.19 C_{plate} is cost of the LSC plate minus the cost of the cells and C_{pv} is the cost of the cells [38]. The authors conclude that either higher efficiency, though likely more expensive, generation-II LSCs are required for LSCs to directly replace conventional solar cells, or else generation-I LSCs will serve only for niche applications where cost is less of an issue.

2.9 Photovoltaics

The following section provides a brief introduction to photovoltaic technology. There are of course many types of solar cell available, see section 1.2, introduction chapter 1, and the specific solar cell chosen for use with an LSC is dependent on a number of desired parameters such as cost, efficiency, lifetime and absorption spectrum (a bandgap energy situated close to the onset of the LSC emission spectrum is desirable). The vast majority of LSC publications feature either silicon (Si) or gallium arsenide (GaAs) solar cells, and therefore a brief discussion of each material is included in this section.

In a typical inorganic bulk semiconductor device, after an incident photon has been absorbed, an electron is excited into the conduction band, creating an electron hole pair, and it is here where the primary difference between a photovoltaic device and a luminescent species exists. For a luminescent species to have a high LQY it is necessary for the electron to rapidly return to the ground state via the radiative emission of a photon. However, in the case of photovoltaics, the separation of the electron-hole pair is necessary before they can recombine so that these charge carriers may be collected to produce electrical current; therefore it is desirable for the excited state to have a long lifetime.

Separation of the electron-hole pair is achievable due to the energy gap present in semiconducting materials, and many types of organic molecular materials [1]. This energy gap allows electrons to exist in an excited state for sufficient time for them to be of use, since

cross energy gap decay rates are much longer than the phonon decay rates which occur between continuous energy levels. In inorganic semiconducting materials, after excitation to the conduction band, an electron and its corresponding positively charged hole in the valence band can serve as electrical charge carriers. Bearing this in mind, it is possible to increase the number of charge carriers available within the semiconducting material via the introduction of foreign atoms. These foreign atoms have valence bands containing additional electrons, when compared to the pure semiconductor, and these electrons can be readily excited to the conduction band. The introduction of these dopant atoms has the effect of locally increasing the density of electrons, this is called *n-type* doping, and will locally increase the Fermi energy of the material, see Figure 2-13. Likewise, the opposite can be achieved by doping the intrinsic semiconductor with atoms which have lower numbers of valence band electrons than the pure semiconductor, this increases the number of holes and reduces the Fermi energy, and this process is known as *p-type* doping.

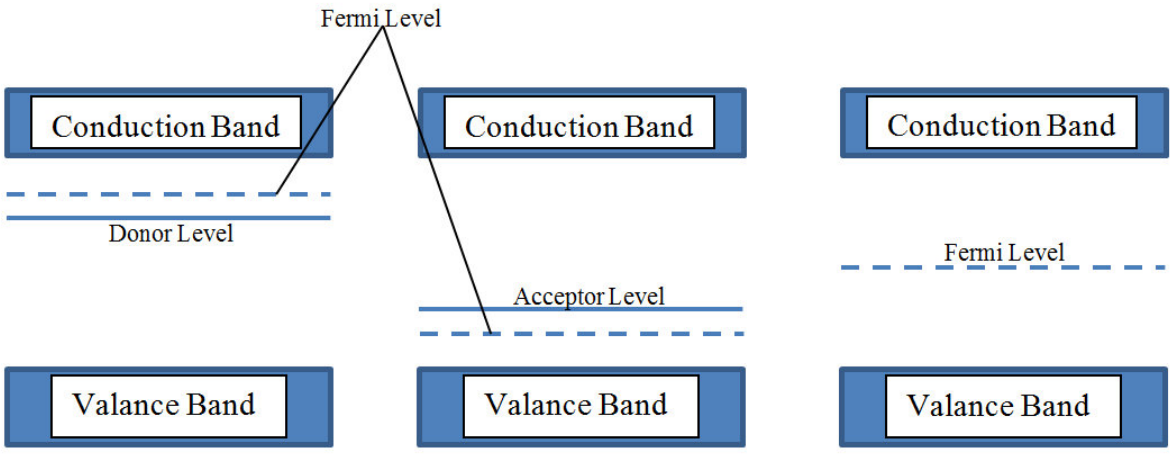


Figure 2-13 Diagrams showing the differences in Fermi level energies for *n-type* doping, *p-type* doping and an intrinsic semiconductor respectively (figure adapted from [*1*]).

When a bulk inorganic semiconductor solar cell is fabricated it is doped in such a way as to produce a *p-n* junction, where the pure semiconducting material is doped on opposite sides

with *p-type* (acceptors) and *n-type* (donors) dopants [1]. The doping leads to a junction being formed between the *n* and *p* regions, and this junction has a potential difference across it. The potential exists because the additional electrons from the *n-type* material diffuse across the junction towards the *p-type* material, while the holes from the *p-type* material diffuse in the opposite direction forming an equilibrium at the junction, but leaving behind ionised *p* and *n-type* dopant atoms at opposite sides of the material. At equilibrium under zero bias the *p* and *n-type* materials have matching Fermi levels, and therefore it is the difference in work functions between these two regions which creates the cell's built-in-bias [1].

In conventional inorganic semiconductor solar cells the *p-n* junction is essential for the device to work, since it separates the electron-hole pairs which are formed by the absorption of an above bandgap energy photon. Without the potential difference formed between the two oppositely doped regions, the excited electron would have sufficient time to recombine with a corresponding hole, and no charge could be extracted from the material.

2.9.1 Silicon (Si) Solar Cells

The main premise of LSCs is to reduce the cost of generating solar power; and therefore, when choosing solar cells to couple to the LSC, it is necessary to choose solar cells which give the best energy conversion efficiencies for the lowest cost. For this reason, Si solar cells are the most commonly used solar cells in conjunction with LSCs, for example [40,41,42] due to the abundance of silicon, and its decades of use in the micro-electronic industries.

The bandgap energy of crystalline silicon is 1.12eV which corresponds to a wavelength of ~1107nm, and it is an indirect bandgap material. Indirect materials have a lower rate of absorption than direct materials [14] as the absorption or emission of a phonon is also required for the transition to occur. A bandgap energy of 1.12eV is not ideal for optimal absorption of the AM1.5g solar spectrum, though this may not be such a large problem when

the cell is used in conjunction with an LSC, since the LSC's emission spectrum can be tailored to the solar cell, either by choosing a different luminescent species or through modification of the existing luminescent species. The ideal bandgap energy for a solar cell under the AM1.5g solar spectrum is 1.4eV, as this corresponds to the peak irradiance of the spectrum [1]. For crystalline silicon, with bandgap energy of 1.12eV, the maximum theoretical power conversion efficiency under the AM1.5g spectrum is 29%. Additionally, it should be noted that since the bandgap is at a wavelength of ~1107nm, which is in the NIR part of the spectrum, crystalline silicon solar cells are ill matched for LSCs, since there are few luminescent species used in LSCs which emit at such a long wavelength. This results in thermalisation losses in the Si cell as the carriers relax to the bandgap energy. It is difficult to find luminescent species that emit efficiently in the NIR as the presence of phonon modes close in energy leads to competing non-radiative relaxation pathways and a low LQY.

Amorphous silicon, α-Si, has a bandgap energy of 1.55eV [43] which corresponds to wavelength of ~800nm, just inside the near infrared part of the spectrum. Therefore, the bandgap of α-Si is more conveniently located for LSCs than in the case of crystalline silicon solar cells. α-Si is also cheaper than monocrystalline silicon as thin-film technologies can be used in production [44]. However, the maximum quantum efficiency for α-Si solar cells (single junction) is lower than that of monocrystalline silicon cells, due to greater lattice disorder introducing additional defects (recombination centres) into the α-Si.

Polycrystalline (or multicrystalline) Si solar cells are also cheap and as such are particularly attractive for LSCs. The downside to using polycrystalline Si cells is the large number of grain boundaries which exist between the crystals, and as a result there is additional charge trapping, when compared to monocrystalline Si, though this effect can be minimised through use of appropriate dopants [45].

2.9.2 Gallium Arsenide Cells

Gallium Arsenide (GaAs), has a bandgap energy of 1.42eV (wavelength ~873nm) making it suitable for high efficiency utilization of the AM1.5g solar spectrum. A single junction GaAs solar cell has a maximum theoretical power conversion efficiency of 31% [1]. Unlike Si, GaAs is a direct bandgap material, therefore, excitation between bands is possible without the requirement for phonons to conserve crystal momentum, and this means that GaAs has a higher absorption coefficient than indirect Si [14]. Despite their advantageous qualities, GaAs cells are currently inappropriate for use in conjunction with LSCs, as a result of their relatively high price compared to Si cells. Therefore GaAs solar cells were commonly used in space and conventional high concentration (>500x) PV array applications before the maturation of multijunction cell technology. GaAs cells are often used in testing LSCs for research purposes, for example [46,47], as their higher bandgap gives a higher voltage and lower thermalisation losses (more efficient conversion) than is achieved with cheaper Si cells.

2.9.3 Solar Cell and Photoelectrochemical Cell (PEC) Characterisation Parameters

In section 2.9 carrier generation in a solar cell was described, it is also important to discuss the opposite phenomenon to carrier generation known as recombination of charge carriers. There are three main types of carrier recombination which occur within solar cells, the first of which is auger recombination. Auger recombination involves the recombination of oppositely charged carriers, the energy released from the recombination is given to an additional carrier, whose energy is eventually lost through thermalisation when the excited carrier returns to the ground state [1]. Auger recombination is more likely to occur in materials with indirect bandgap rather than direct bandgap. A second type of carrier recombination is Shockley-Read-Hall recombination, which occurs when a free charge carrier recombines with an oppositely charged carrier which is currently occupying a trap state located within the bandgap of the semiconductor [1]. The last of the three main recombination types is radiative

recombination where an electron and a hole recombine losing energy in the form of a photon emission.

External quantum efficiency (EQE) is a measure of the probability that an incident photon of a particular wavelength will be absorbed and produce charged carriers which will contribute to the photocurrent of the device (solar cell or PEC working electrode). The EQE is expressed as the ratio of charge carriers collected by the device, over the number of photons of a particular energy incident on the surface of the device. If the energy of the incident photons is less than the devices' bandgap then the EQE will be zero.

The maximum power density P_m of a solar cell is determined by equation 2.20, where J_m is current density and V_m is voltage.

$$P_m = J_m V_m \qquad 2.20$$

The voltage of a solar cell is a result of quasi-Fermi level separation. The voltage is linked to the bandgap, a larger bandgap will result in a larger voltage [1]. The current density of a solar cell is also directly linked to the bandgap. A larger bandgap energy means fewer incident photons will be absorbed by the solar cell, and as a result fewer charge carriers will be generated.

The short circuit current density J_{sc} is the current density at $V = 0$, which occurs when the solar cells' terminals are shorted. J_{sc} is the highest possible current density producible by the solar cell (though obviously no power is being produced by the solar cell at J_{sc}). J_{sc} is defined by equation 2.21 [*1*]:

$$J_{sc} = q \int B_s(E) EQE(E) dE \qquad 2.21$$

where q is the charge of an electron, $B_s(E)$ is the energy dependent incident photon flux density and $EQE(E)$ is the energy dependent external quantum efficiency of the solar cell.

The open circuit voltage V_{oc} occurs when the solar cells' terminals are isolated from one-another, it is the highest possible voltage of the solar cell and occurs when $J_{sc} = 0$. V_{oc} occurs at $J_{sc} - J_{dark} = 0$, where J_{dark} is the dark current of the solar cell, V_{oc} is given by equation 2.22 [*1*].

$$V_{oc} = \frac{kT}{q} ln\left(\frac{J_{sc}}{J_o} + 1\right) \qquad 2.22$$

Where k is the Boltzmann constant, T is the temperature in degrees Kelvin and J_o is the saturation current.

The dark current density J_{dark} comes from the dark current I_{dark}, which is the current generated by the solar cell in the darkness, and flows in the opposite direction to the photocurrent [1]. Equation 2.23 defines the dark current density J_{dark} of a solar cell [1].

$$J_{dark} = J_o(e^{\frac{qV}{kT}} - 1) \qquad 2.23$$

Therefore, the voltage dependent current density $J(V)$ for a solar cell is determined by equation 2.24 [1].

$$J(V) = J_{sc} - J_{dark}(V) \qquad 2.24$$

The fill-factor FF can be used as a way of comparing the quality of different solar cells, it determines the squareness of the JV curve (or IV curve). The closer the fill-factor is to 1, the smaller the carrier recombination and series and shunt resistance, and therefore the higher the quality of the solar cell [1]. The fill-factor is defined by equation 2.25:

$$FF = \frac{J_m V_m}{J_{sc} V_{oc}} \qquad 2.25$$

The overall efficiency η of the solar cell (also known as the power conversion efficiency) is determined by the ratio of the total power density generated by the solar cell under the incident illumination, over the total incident power density (see equation 2.26 [1]).

$$\eta = \frac{J_m V_m}{P_s} = \frac{J_{sc} V_{oc} FF}{P_s} \qquad 2.26$$

where P_s is the power density of the incident light source.

To summarise this section has defined many of the important parameters related to solar cells (and PEC cells) many of which are used throughout this thesis.

2.10 Water Splitting

During the course of this thesis (see chapter 7) LSCs have been investigated in conjunction with photoelectrochemical (PEC) cells for the purpose of splitting water molecules (in this case an aqueous electrolyte which had sodium hydroxide added, so as to give the electrolyte an appropriate pH value, was used) so that gaseous H_2 and O_2 can be extracted. A more correct terminology for the water splitting process occurring in this thesis would be "photoassisted water splitting" [48], since water splitting is not achievable solely by applying light to the Fe_2O_3 working electrode but requires additional potential from PV cells to assist the process. The aims of this research were to cheaply and efficiently extract gaseous

hydrogen and oxygen from an appropriate aqueous electrolyte. Hydrogen is potentially very important in a renewable energy economy because it is a convenient energy storage medium [49] and offers an alternative to using batteries which can be high cost. In addition, hydrogen has the potential to be used as a transportation fuel source, replacing polluting fossil fuels. There are numerous methods which can be employed for hydrogen storage such as compression and cryogenic storage, or storage as a solid chemical fuel through bonding with another appropriate material [50,51]. Improved methods of energy storage will be essential if renewable energy sources are to replace fossil fuels as our primary energy source.

2.10.1 Photoelectrochemical Cell

The PEC cell differs from the standard inorganic photovoltaic solar cell in that there is not a junction between different inorganic semiconducting materials, but rather the semiconducting electrode of the electrochemical cell is in direct contact with an electrolyte which may be either a liquid, a gel or solid organic material [52].

The PEC cell used in this study was a two electrode cell consisting of a metal oxide electrode employed as photoanode and a platinum wire which acts as cathode.

Similar to PV cells a PEC cell functions by converting photons, with energy greater than the bandgap, incident on the semiconducting material of the PEC cell, into electron-hole pairs. However, unlike PV cells, PECs function more like the photosynthetic systems found in plants, with reduction and oxidation (redox) mechanisms occurring [52]. In an ideal semiconductor, for water splitting to occur the electrons in the conduction band need to have a potential which is more negative than the redox potential of proton reduction, H^+/H_2 (0V vs. normal hydrogen electrode (NHE)), while the holes in the valence band need to have a potential more positive than the redox potential of water oxidation, O_2/H_2O (+1.23eV vs. NHE) [53,54]. In effect the oxygen and hydrogen reduction levels must both fall within the

bandgap of the semiconducting electrode, as shown in Figure 2-14, for the two reactions to have enough energy to occur [48]. However, metal oxide semiconductors which act as anode and cathode simultaneously are not known, and at the moment *n-type* and *p-type* semiconductors are commonly employed as photoanodes and photocathodes respectively [54].

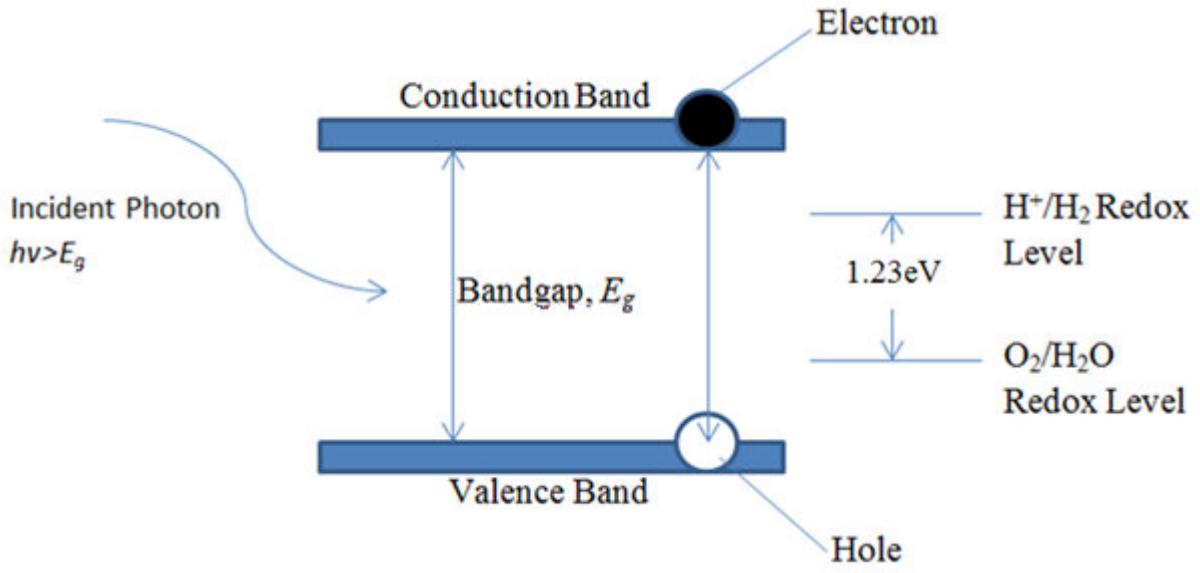


Figure 2-14 Band diagram for an ideal metal oxide semiconductor, adapted from [48].

When an incident photon is absorbed by the semiconducting electrode (working electrode), an electron-hole pair is generated. Four holes are required to oxidise a single H_2O molecule at the semiconductor/electrolyte interface (oxidation reaction), while the electrons move to the counter electrode (helped by the application of a potential difference between working and counter electrodes) where they are able to reduce protons (reduction reaction). Due to the analogy with photosynthesis, PEC cells are often referred to as photosynthetic cells [52]. The oxidation mechanism involves the reaction between holes and water at the interface between the working electrode and the electrolyte. The resulting water oxidation allows molecular oxygen, O_2, to be liberated from the electrolyte material (see equations 2.27 and 2.28 for the

two half reactions, where h^+ is a positively charged hole, and e^- is a negatively charged electron.). The second redox mechanism is reduction, where electrons are supplied to the electrolyte material at the counter electrode/electrolyte interface, resulting in the reduction of the protons to hydrogen gas. However, for there to be any oxidisation or reduction, there must first exist an energy difference of at least 1.23eV between the valence and conduction bands [55]. In practice 1.23eV (which is the theoretical energy required to split water) is insufficient as it does not take losses into account (see section 7.1, chapter 7), and a larger bandgap is required to compensate for thermodynamic and kinetic energy losses in the PEC electrodes [56].

$$2H_2O + 4h^+ \rightarrow O_2 + 4H^+ \qquad (+1.23V\ Vs.NHE) \qquad 2.27$$

$$4H^+ + 4e^- \rightarrow 2H_2 \qquad (0V\ \ Vs.NHE) \qquad 2.28$$

2.10.2 Electrodes

There are a number of parameters which need to be taken into account when selecting appropriate working electrodes for a PEC cell. These parameters include the position of the conduction and valence bands of the working electrode, the chemical stability of the electrodes in conditions where water splitting occurs and cost. The working electrode selected for the work in chapter 7 of this thesis was an Fe_2O_3 thin-film coated on ITO conductive glass. Fe_2O_3 is an *n-type* semiconductor with a bandgap energy of ~2.1eV, which corresponds to a wavelength of ~590nm. This means that the majority of the solar spectrum will not be absorbable by an Fe_2O_3 working electrode, and as a result Fe_2O_3 electrodes are limited to low saturation current densities [57]. However, Fe_2O_3 has the advantage of being highly resistant to oxidation during the redox reactions, and, although the same is also true

for some other high bandgap energy metal oxides such as WO_3 (~2.7ev) and TiO_2 (~3eV) [58,59], these materials have an even worse spectral match to the AM1.5g solar spectrum than Fe_2O_3.

The problem of inappropriate bandgaps is being addressed in two ways, firstly though the use of a second light harvesting electrode, and secondly, by providing protective layers to semiconducting electrodes with more useful band energies. The use of two semiconductors (a tandem device) together allows for more solar spectrum absorption, and has a maximum theoretical efficiency of 41% and a maximum chemical conversion efficiency of 27% (taking in to account photon energy not utilised) [60]. A tandem device is described in the review article of Gratzel [52], in which the device, which consists of a top surface layer of, for example WO_3 or Fe_2O_3, connected in series to a dye sensitised layer of TiO_2 to achieve direct splitting of water by incident light. The holes created in the top layer are used to oxidise water into oxygen, while the electrons from the top layer augment those of the bottom layer to reduce protons into hydrogen. It should be noted that the high solar to hydrogen efficiency quoted for tandem cells, tends to drop off as the electrodes size is increased [54].

The semiconductors being used must have high stability so as to avoid forming thick oxide layers and becoming ineffective as a result of the redox reactions. Stability has been improved by applying protective layers to the surface of the PEC semiconductor electrodes, as shown in the work of Chen *et al.* [61]. In their work they demonstrated that by using atomic layer deposition techniques, a uniform, high quality 2nm thick layer of TiO_2 could be applied to the surface of a Si substrate (used at the working electrode), and a ~3nm layer of iridium catalyst was then applied to the surface of the TiO_2 layer. The protective layer served to protect the surface of the Si from oxidation, and comparisons with an unprotected Si electrode showed that the protected electrode remained current stable in a corrosive

electrolyte environment for in excess of 24 hours, whist the unprotected electrode ceased working within half an hour.

2.10.3 Electrolyte

It is essential to select the correct electrolyte material for the electrodes used within the PEC. A number of electrolyte materials in addition to water have been used in PECs with a range of pH values from acids to neutral pH buffer solutions to base solutions. The importance of the combination of working electrode and electrolyte is clearly shown in the work of Scheuermann *et al.* [62]. In their work, they feature a variety of electrode materials in electrolyte solutions ranging from acids to bases, and differences are seen in the overpotentials for each electrode/electrolyte combination. Overpotential is the difference in potential between, the potential determined thermodynamically for the half reaction, and the potential actually measured at which a redox reaction occurs, they arise from inefficiencies at the working electrode/electrolyte interface [53]. It is desirable to have a lower electrode overpotential, as the overpotential will require the PEC to generate higher potentials to split water. For example, it is shown that for an electrode consisting of a *p*–type silicon substrate, covered by a thin SiO_2 layer (essential to prevent Fermi level pinning), a TiO_2 protective layer, and a 1nm thick Iridium catalyst layer, that the overpotentials recorded in acid, buffer and base solutions are 300mV, 311mV and 340mV respectively [62].

2.10.4 Photoelectrochemical Cell Characterisation Parameters

The following is a description of important PEC specific characterisation terms which are used in chapter 7 of this thesis. Many characterisation terms related to PEC cells such as dark current density are also associated with solar cells and a description of these can be seen in section 2.9.3.

Incident photon to current efficiency (IPCE) is a wavelength dependent measure of the semiconductor working electrodes ability to convert incident photons into current, and is described by equation 2.29.

$$IPCE = 1239.8 \frac{J_{ph}}{P_{mono}\lambda} \qquad 2.29$$

Where J_{ph} is the photocurrent density when a bias is applied, P_{mono} is the power intensity of the incident photons and λ is the wavelength of the incident light.

Chronoamperometry is a measure of the current produced by redox reactions between the electrolyte material and the working electrode after a potential is applied across the electrode and the electrode is illuminated with monochromatic light [63].

To conclude, photoelectrochemical water splitting offers a very promising route to a future low cost hydrogen economy and the development of PEC systems and water splitting reactors is very much an on-going area of research. In chapter 7 of this thesis there is a results chapter in which a PEC cell device is incorporated with LSCs and silicon solar cells, in an attempt to concentrate light of an appropriate wavelength onto the surface of an Fe_2O_3 working electrode to enhance the efficiency of the PEC device.

2.11 Conclusion

This chapter has featured a detailed explanation of how the LSC functions, its merits and its present efficiency shortcomings. This chapter has also taken into account that the LSC is most often used in conjunction with solar cells to generate power, and for this reason a brief overview of the physics of solar cells has been described. Additionally, in this thesis (see chapter 7) LSCs have been used in conjunction with photoelectrochemical cells (PECs). PECs are used for the splitting of water molecules and the collection of H_2 gas. It was of

interest to couple LSCs to these devices for the purpose of concentrating specific wavelengths onto the PEC working electrode, to enhance the devices efficiency. Therefore, a description of the physics of the PEC was also provided in this chapter.

The LSC was first proposed in the 1970s as a way of reducing the costs of generating electricity from solar energy. A simplistic description of an LSC would be as a light harvesting waveguide with the ability to provide low level light concentration at its narrow edges (as well as the ability to absorb diffuse light). This is achieved by using relatively large surface area LSCs to collect incident solar irradiance and to concentrate it onto relatively small surface area solar cells, optically coupled to the narrow edge(s) of the LSC. In these early days of LSC research, LSCs were afflicted by low optical efficiencies and rapidly degrading dyes, and as such LSCs were unable to directly compete with solar cells. Over the past decade and half there has been much renewed interest in LSCs due to the production of superior dyes, such as nanocrystals which offer greater photostability and relatively high LQY, or potentially low cost bio-derived luminescent species (more examples can be seen in chapter 3).

Today, despite better quality dyes being utilised in LSCs, optical efficiencies are still relatively low. In this chapter a thorough description of these efficiency drains is given. Prominent sources of photon losses in LSCs include narrow absorption spectra, non unity LQY and escape cone losses for photons which are not totally internally reflected at the LSC boundary (and thus are lost via the top or bottom surfaces of the LSC). Losses associated with LQY and escape cones are greatly exacerbated by low Stokes-shifts which lead to overlap of the absorption and emission spectral ranges of the luminescent species used within the LSC. As a result of these sources of efficiency loss, a great deal of effort has been expended over the years to mitigate these losses, and chapter 3 has a detailed description of the methods and materials which have been utilised to this end.

This chapter also addressed the various LSC geometries which have been used. Cylindrical LSCs are capable of high photon concentrations due to their large light absorption areas, but very small emission areas, with Edelenbosch *et al.* [30] achieving an ~35 times photon concentration gain with a cylindrical fibre LSC. Other LSC geometries have been considered too, with Kennedy *et al.* [33] showing that the best tessellating shape available, in terms of photon concentration, is the hexagonal LSC. Additionally, Giebink *et al.* [34] were able to produce a resonance-shifting LSC which was capable of far higher photon concentrations than an otherwise equivalent, non-resonant shifting LSC. The results in this thesis focus on the ubiquitous cuboidal LSC shape (although chapter 6 does impart a novel spin on this type of LSC by making the LSC thin and flexible).

Finally, this chapter considers the cost of LSCs. In 1977, approximately the time LSC research first began, silicon solar cells cost $76.67/Watt, but by 2013 this price had fallen to $0.74/W [37]. These dramatic reductions in cost are of course excellent news for the environment, but they have provided a considerable moving goal for LSCs to compete with, in terms of direct competition with, large surface area silicon solar cells. Farrell and Yoshida [38] have suggested that a move to what they refer to as high efficiency second generation LSCs would allow LSCs to compete with conventional solar cells, and detailed descriptions of many second generation materials and concepts can be seen in chapter 3 of this thesis. In the authors opinion though, many second generation technologies will add a not insignificant cost to the price of an LSC, and it is also likely that the price of solar cells will continue to decrease. The author therefore feels that the advantages of the LSC, for example its ability to absorb diffuse light, its ability to allow certain wavelengths of light to be transmitted while absorbing others, its aesthetic qualities, etc., allow the LSC to find extensive use in a range of novel applications (such as building integrated PV). As a result of this, novel LSC applications are the focus of chapters 6 and 7 of this thesis.

Chapter 2 References

[1] Nelson, J., (2003). "The Physics of Solar Cells" London: Imperial College Press.
[2] Salby, M., (1996). "Fundamentals of Atmospheric Physics", San Diego: Academic Press, Inc.
[3] NREL, Reference Solar Spectral Irradiance: ASTM G-173, accessed on (27/9/2013) http://rredc.nrel.gov/solar/spectra/am1.5/ASTMG173/ASTMG173.html .
[4] Mallinson, J, and Landsberg, P., (1977), "Meteorological Effects on Solar Cells", Proc. R. Soc. A. 355, 115.
[5] Goetzberger, A, (1978). "Fluorescent Solar Energy Collectors: Operating Conditions with Diffuse Light", Applied Physics, 16, 399-404.
[6] Farrell, D., (2012), Personal Correspondence, University of Tokyo. Japan
[7] Smestad, G.,Ries,H., Winston, R., and Yablonovitch, E. (1990), "The thermodynamic limits of light concentrators", Solar Energy Materials, 21, p99-111.
[8] Farrell, D,. (2008). "Characterising the Performance of Luminescent Solar Concentrators", PhD Thesis, Imperial College London
[9] Chatten, A., Private correspondence, Imperial College London, UK. (2013).
[10] Schmid, G, (2010). "Nanocrystals: From Theory to Application Second, Completely Revised and Updated Edition", Wiley-VCH, Germany, p28-29.
[11] Krahne, R., Morello, G., Firguerola, A., George, C., Deka, S., and Manna, L., (2011). "Physical properties of elongated inorganic nanoparticles" Physics Reports-review Section of Physics Letters, 501, 3-5, p75-221.
[12] Talaat, H., Abdallah, T., Mohamed, M., Negm, S., El-Sayed, M., "The sensitivity of the energy gap to changes in the dimensions of the CdSe quantum rods at room temperature: SSTM and theoretical studies", Chemical Physics Letters, 473, 4-6, p288-292, (2009).
[13] Efros, A. and Rosen, M., "Band-edge exciton in quantum dots of semiconductors with a degenerate valence band: Dark and bright exciton states", Physical Review B, 54, 7, p4843-4856, (1996).
[14] Fox, M. (2001). Optical Properties of Solids. New York: Oxford University Press Inc.
[15]Loveland, W. (2005). "Modern Nuclear Chemistry", Wiley.
[16] Bass, M., Virendra, M. and Van Stryland, E. (2009). "Handbook of Optics: Design, Fabrication and Testing; Sources and Detectors; Radiometry and Photometry". McGraw Hill Professional.
[17] Izumi, T., Kobashi, S., Takimiya, K., Aso, Y., and Ostubo, T., "Synthesis and Spectroscopic Properties of a Series of β-Blocked Long Oligothiophenes up to the 96-mer: Revaluation of Effective Conjugation Length", Journal of the American Chemical Society", 125, 18, p5286-5287, (2003).
[18] Rendell, D. (1987). "Fluorescence and Phosphorescence". Wiley. Great Britain.
[19] Krishna, V., "Delayed Fluorescence Due to Triplet-Triplet annihilation: A Theoretical Study", The Journal of Chemical Physic, 46, 5, (1967).
[20] Becker, R.(1969). "Theory And Interpretation Of Fluorescence And Phosphorescence". John Wiley & Sons, Inc. United States of America.
[21] Engle, T., and Reid, P., (2006), "Physical Chemistry", Pearson Benjamin-Cummings, p477-479,.
[22] Levine, I, N., (1991) "Quantum Chemistry", Prentice-Hall, 4th edition, p303-304, .
[23] Debije, M., and Dekkers, W., (2012), "Functionalizing the rear scatterer in a luminescent solar concentrator", Journal of Renewable and Sustainable Energy, 4, 013103.

[24] Currie, M., Mapel, J., Heidel, T., Goffri, S., and Baldo, M., (2008) "High-efficiency Organic Solar Concentrators for Photovoltaics", Science, 321, p226-228,.
[25] Verbunt, P., Sanchez-Somolinos, C., Broer, D., and Debije, G., (2013)."Anisotropic light emission in luminescent solar concentrators-isotropic systems", Opticas Express, 21, S3, A485-A493.
[26] Bose, R., (2012)."Raytrace Simulations and Experimental Studies of Luminescent Solar Concentrators", Doctoral Thesis, Imperial College London, (2012).
[27] Bose, R., Chan, N., Xiao, Y., Farrell, D., Chatten, A., Buchtemann, A., Quilitz, J., Fiore, A., Manna, L., Nelson, J., Alivisatos, A., and Barnham, K., (2008). "The Role of Self-absorption in Luminescent Solar Concentrators", Proc. MRS Fall Meeting, Boston, USA.
[28] Bose, R., Farrell, D., Chatten, A., Pravettoni, M., Barnham, K., (2007). "NOVEL CONFIGURATIONS OF LUMINESCENT SOLAR CONCENTRATORS", Proc. 22nd European Photovoltaic Solar Energy Conference, Milan, Italy.
[29] Wilson, L., Rowan, B., Robertson, N., Moudam, O., Jones, A., and Richards, B., (2010). "Characterization and reduction of reabsorption losses in luminescent solar concentrators", Applied Optics, 49, 9.
[30]Edelenbosch, O., Fisher, M., Patrignani, L., van Sark, W., and Chatten, A., (2013). "Luminescent solar concentrators with fiber geometry", Optics Express, 21, S3, pA503-A514.
[31] McIntosh, K., Yamada, N., and Richards, B., (2007). "Theoretical comparison of cylindrical and square-planar luminescent solar concentrators", Applied Physics, B 88,p285-290.
[32] Goetzberger, A., (1978). "Fluorescent Solar Energy Collectors: Operating Conditions with Diffuse Light", Applied Physics, 16, p399-404.
[33] Kennedy M., McCormack, S., Doran, J., and Norton, B., (2007). "Modelling the effect of device geometry on concentration ratios of quantum dot solar concentrators", Proc. ISES World Solar Congress, (Beijing), pp. 1484–1487.
[34] Giebink, N., Wiederrecht, G., and Wasielewski, M., (2011)., "Resonance-shifting to circumvent reabsorption loss in luminescent solar concentrators", Nature Photonics, 5, p694-701.
[35] Weber. W. H. and Lambe. J., (1976). "Luminescent Greenhouse Collector for Solar Radiation" Applied Optics., 15(10), p. 2299-2300.
[36] Batchelder, J., Zewail, A., and Cole, T., (1981). "Luminescent solar concentrators. 2 : Experimental and theoretical analysis of their possible efficiencies", Applied Optics, 20, 21. P3733-3754.
[37] The Economist (cited from Bloomberg New Energy Finance), "Sunny Uplands", http://www.economist.com/news/21566414-alternative-energy-will-no-longer-be-alternative-sunny-uplands , accessed (15/11/2013).
[38] Farrell, D., and Yoshida, M., (2012). "Operating regimes for second generation luminescent solar concentrators", Progress in Photovoltaics: Research and Applications, 20, p93-99.
[39] Markvart, T,. (2006). "Detailed balance method for ideal single-stage fluorescent collector", Journal of Applied Physics, 99, 023101.
[40] Bailey, S., Lokey, G., Hanes, M., Shearer, J., McLafferty, J., Beaumont, G., Baseler, T., Layhue, J., Broussard, D., Zhang, Y,. Wittmershaus, B., (2007) "Optimized excitation energy transfer in a three-dye luminescent solar concentrator", Solar Energy Materials and Solar Cells, 91, p67-75.

[41] Debije, M., Teunissen, J-P., Kastelijin, M., Verbunt, P., and Bastiaansen, C., (2009).“The effect of a scattering layer on the edge output of a luminescent solar concentrator”, Solar Energy Materials and Solar Cells, 93, 8, 1345-1350.
[42] Burgers, A., Sloof, L., Buchtemann, A., Roosmalen, J., (2006). “Performance of Single Layer Luminescent Concentrators with Multiple dyes”, proc. IEEE 4th World Conference on Photovoltaic Energy Conversion, Hawaii, USA, p198-201.
[43] Loferski, J., (1956), “Theoretical Considerations Governing the Choice of the Optimum Semiconductor for Photovoltaic Solar Energy Conversion”. Applied Physics. 27, 777.
[44] Carlson, D., and Wronski, C., (1976). “Amorphous Silicon Solar Cell” Applied Physics Letters. 28 11 671-673.
[45] Green, M., (1995). “Silicon Solar Cells Advanced Principles & Practice”. Centre for Photovoltaic Devices and Systems :Rosebery.
[46] Slooff, L., Bende, E., Burgers, A., Budel, T., Pravettoni, M., Kenny, R., Dunlop, E., and Buchtemann, A., (2008). “A luminescent solar concentrator with 7.1% power conversion efficiency”, Phys. Status Solidi (RRL), 2, p257-259,.
[47] Goldschmidt, J., Peters, M., Dimroth, F., Bett, A., Steidl, L., Zentel, R., Hermle, M., Glunz, S., Willeke, G., (2009).. “Developing Large and Efficient Fluorescent Concentrator Systems”, Proc. 24th European PV Solar Energy Conference and Exhibition, Hamburg, Germany.
[48] Rajeshwar, K, “Hydrogen generation at irradiated oxide semiconductor solution interfaces” Journal of Applied Electrochemistry, 37, 765-787, (2007).
[49] Energy Technology Analysis: Prospects for Hydrogen and Fuel Cells, International Energy Agency, (2005) p70.
[50] Ogden, J., “Developing an infrastructure for hydrogen vehicles: a Southern California case study” International Journal of Hydrogen Energy, 24, 709-730, (1999).
[51] Sakintuna, B, et al., “Metal hydride materials for solid hydrogen storage: A review”, International Journal of Hydrogen Energy, 32, 9, 1121-1140. (2007).
[52] Grätzel, M, “Photoelectrochemical Cells”, Nature, 414, 338-344. (2001).
[53] Bard, A. J, and Faulkner, L, R., (2001). “Electrochemical Methods: Fundamentals and Applications: 2nd Edition”, John Wiley Sons, New York.
[54] Pesci, F., (2013). Personal consultation, Imperial College London, UK.
[55] Fujishima, A and Honda, K, “Electrochemical Photolysis of Water at a Semiconductor Electrode”, Nature, 238, 37-38, (1972).
[56] Brillet, J, et al., “Highly efficient water splitting by a dual-absorber tandem cell”, Nature Photonics, 6, (2012).
[57] Kay, A,. et al. “New benchmark for water photooxidation by nanostructured alpha-Fe2O3 films”, J. Am. Chem. Soc., 128, 15714-15721, (2006).
[58] Miller, E, L., et al., “Optimization of hybrid photoelectrodes for water-splitting”, Electrochemical and Solid-State Letters, 8, 5, A247-A249, (2005)
[59] Pourbaix, M, J, N., Atlas of Electrochemical Equilibria in Aqueous Solutions: 1st Edition, Pergamon Press, (1966).
[60] Bolton, J, et al., “Limiting and realizable efficiencies for solar photolysis of water”, Nature, 316, (1985).
[61] Chen, Y, et al., “Atomic layer-deposited tunnel oxide stabilizes silicon photoanodes for water oxidation”, Nature Materials, (2011).
[62] Sheuermann, A,. et al., “Effects of catalyst material and atomic layer deposited TiO2 oxide thickness on the water oxidation performance ofmetal-insulator-silicon anodes”, Energy Environ. Sci., 6, 2487-2496, (2013).

[63] Kissinger, P., and William, H., (1996). “Laboratory Techniques in Electroanalytical Chemistry, Second Edition, Revised and Expanded, CRC press.

Chapter 3

LSC Efficiency Enhancements and Luminescent Species

3.1 Introduction

The following chapter features a review of the key methods and techniques used to enhance the overall efficiency and practical lifetime of the LSC since it was first proposed in the 1970s. Further, this chapter provides an overview of the prominent types of luminescent species which have been featured in LSCs over the years, including their advantages and disadvantages.

3.2 Methods to Increase LSC Efficiency

There have been many technologies and areas of research pursued with the aim of improving the optical efficiency of LSCs over the years. The following sections examine the main strategies which have been investigated to boost the efficiency of the LSC.

3.2.1 Metallic Mirrors and Scattering Layers

Mirrors can be used in two ways with LSCs, the first, is to apply a the mirror to the back surface of the LSC to give incident light which was not previously absorbed by the LSC another opportunity to interact with, and be absorbed by, the luminescent centres [1] (see Figure 3-1A. Since a metallic mirror will have a refractive index which is greater than that of the LSC, this means that an air gap is needed between the mirror and the LSC to maintain TIR. Maintaining TIR is important due to the reflectivity of aluminium foil (a standard metallic mirror used with LSCs) being 97% across the majority of the visible spectrum [2,3],

while TIR has a reflection probability of nearly 100%, therefore, ensuring TIR prevents unnecessary losses at the LSC/mirror interface.

Back surface mirrors do suffer from some disadvantages, however, such as preventing any light from passing through the LSC, making a mirror inappropriate if the desire is to still have certain wavelengths of light pass through the LSC. The second disadvantage is that back surface mirrors, being specular reflectors, have limited ability to reduce losses from bottom surface escape cones, since the angle of reflectance is equal to the angle of incidence, the escape cone photon will be lost from the top surface instead, unless of course this reflected emission photon is reabsorbed by a luminescent centre.

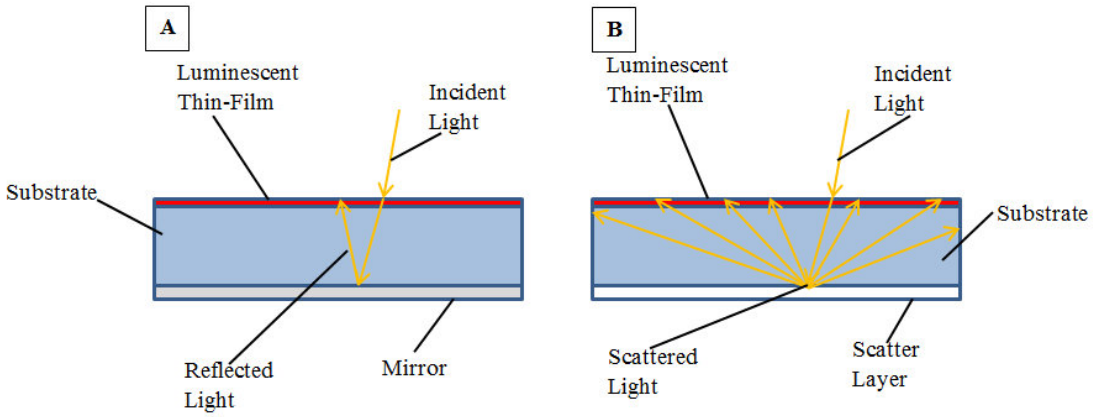


Figure 3-1Side diagrams of LSCs utilising A) a bottom surface reflective mirror, and B) a bottom surface scatter layer.

Metallic mirrors can also be used on the narrow edges of the LSCs replacing some of solar cells attached to the edges, with the ultimate intention of reducing the cost per Watt of the LSC [4]. This is done as the attached solar cells are often the most expensive components in the LSC/solar cell device. However, this is not always the case as, for example, some luminescent species can be quite expensive (e.g. luminescent species containing rare Earth elements are particularly expensive). The mirrors are intended to guide emission photons,

from the edges without solar cells, into the solar cell(s) attached to the LSC. The disadvantages of this method are the increase in reabsorption losses due to an increase in path length, therefore replacing solar cells with mirrors in highly doped LSCs or in LSCs which have luminescent species with significant spectral overlap, will lead to greater reabsorption losses.

Alternatively, instead of using a metallic mirror with specular reflection (see Figure 3-1B), it is preferable to instead use a white diffuse reflector material (Lambertian), such as PTFE, on the back surface of the LSC. The white scattering layer will reflect light with a random direction, potentially allowing for longer pathlengths for unabsorbed incident light than a specular reflecting mirror can offer, increasing the chance of absorption on a second pass. Additionally, incident photons which are not absorbed by the luminescent species, and which are incident with the scattering layer close to the edges of the LSC, may be scattered into the attached solar cell(s). However, a back reflector (either a specular reflector of a scattering reflector) with an air gap separating it from the LSC, is incapable of re-entering the LSC at an angle outside of which fall within the escape cone, up to and including an angle of 90° (with respect to the normal) for the reflected photon, as described by Snell's law. This of course means that if the photon is not absorbed by a luminescent centre as it moves back through the LSC, it will be lost via a top surface escape cone. As was the case for the metallic mirror, adding a diffuse scattering layer to the back surface of the LSC will also prevent the LSC from transmitting any visible light, and as such using a back scatter is not appropriate for some LSC applications, for example LSC windows.

For a Lambertian reflector, the diffuse nature of the reflection is due to absorption and scattering of light beneath the surface of the material [5]. Since light of different wavelengths will be absorbed and scattered by the material, and since the light maybe scattered multiple times within the material, light leaving the scattering material will do so with an isotropic

distribution. The distribution of the scattered light is typically modelled by Lambert's Cosine Law (see equation 3.1), though some have suggested that properties of the specific material should also be taken into account [6]:

$$I_{ref} \propto I_{inc}cos(\theta) \qquad 3.1$$

where I_{ref} is the reflected light intensity and I_{inc} is the incident light intensity. Applying a diffuse scattering layer to the bottom surface of an LSC is a fairly common practice [7-15] since it allows for an efficiency enhancement, and scattering materials such as PTFE (Teflon), matt white paint on card or titanium oxide are used as they are generally quite cheap and easy to work with. In [15] comparisons are made between scattering layers on the back surface of LSC, with and without air gaps. It was found that for LSCs with edges in excess of 5cm in length an air gap, or other low index material, between the scattering layer and LSC provides an efficiency enhancement, though this enhancement tends to decrease with increasing distance and dye concentration. For LSCs with edge length below 5cm, the scattering layer attached without an air gap gives the greatest enhancement, though this can be attributed to incident light being directly scattered out of the narrow edges [15]. As mentioned previously in section 3.2.1, chapter 3 the approach of Debije and Dekkers in [7] is particularly interesting as it makes use of a phosphorescent scattering layer which serves both as a scattering layer and a spectral downshifter to enhance overall light absorption, with emission energy increases of between 4% and 40%, reported, depending on LSC dye concentrations, when compared to traditional scatterers.

Non-fluorescent, flat plate solar concentrators which utilize an attached white diffuse layer, with an air gap, on the back surface, have been investigated in the work of Slooff *et al.* [16], and shown to have a power conversion efficiency of 4.4%, though this work was limited to

simulations only, and limited to dimensions of 5cm by 5cm by 0.5cm. However, Bose [17], deemed the work of Sloof *et al.* [16] to be unreliable since it assumed isotropic reflections from the back reflector. Bose [17] referred to the work of Grabowski [18] to explain that for a flat reflection surface, isotropic reflection is dependent on the angle of incidence of the incident photon. However, since these devices fall outside of the scope of this thesis, they shall not be discussed in greater depth.

In the work of Slooff *et al.* [3] an LSC record power conversion efficiency of 7.1% was achieved. This result was confirmed by measurements at the European Commission Joint Research Centre and used raytrace modelling to interpret the efficiency of a 5cm by 5cm by 0.5cm LSC, doped with Lumogen red 305 (BASF) and Fluorescent Yellow CRS040 (Radiant Color), with a diffuse back reflector layer and a GaAs solar cell on each narrow edge (geometric gain of 2.5). Due to the small size of the LSC and the diffuse scattering layer, a sizeable contribution to the power conversion efficiency was due to direct scattering of the incident light source into the solar cells, which can be seen in their plot of external quantum efficiency as a measured contribution at wavelengths beyond the absorption spectrum of either dye. However, for a larger LSC, this component would contribute a much smaller fraction to the overall power.

3.2.2 Reducing Escape Cone Losses

For an LSC made from glass or PMMA with a refractive index of approximately 1.5, surrounded by air, the trapping probability for isotropic emission is approximately 74%, (see equation 2.15). Therefore, for the above example, there is an approximately 26% probability that an emitted photon will not be subject to TIR, and will be lost from either the top or bottom surfaces of the LSC, and, as was mentioned in section 2.6.3 these losses are known as escape cone losses. The escape cone losses result in large reductions in LSC optical efficiency, losses which are dramatically increased if there is large spectral overlap leading to

significant reabsorption, see section 2.6.4. Any technology which significantly mitigates escape cone losses is potentially very useful, and a review of promising technologies follows.

3.2.3 Wavelength Selective Mirrors

One area of research which is focused on preventing escape cone losses is the wavelength selective mirror as illustrated in Figure 3-2. For an ideal wavelength selective mirror it is necessary for it to allow all wavelengths of light pass which can be absorbed by the LSC's luminescent species, but to prevent the escape of, wavelengths of light which correspond to the luminescent species emission spectrum. There have been several technologies studied for this purpose, and these are discussed in the following sections.

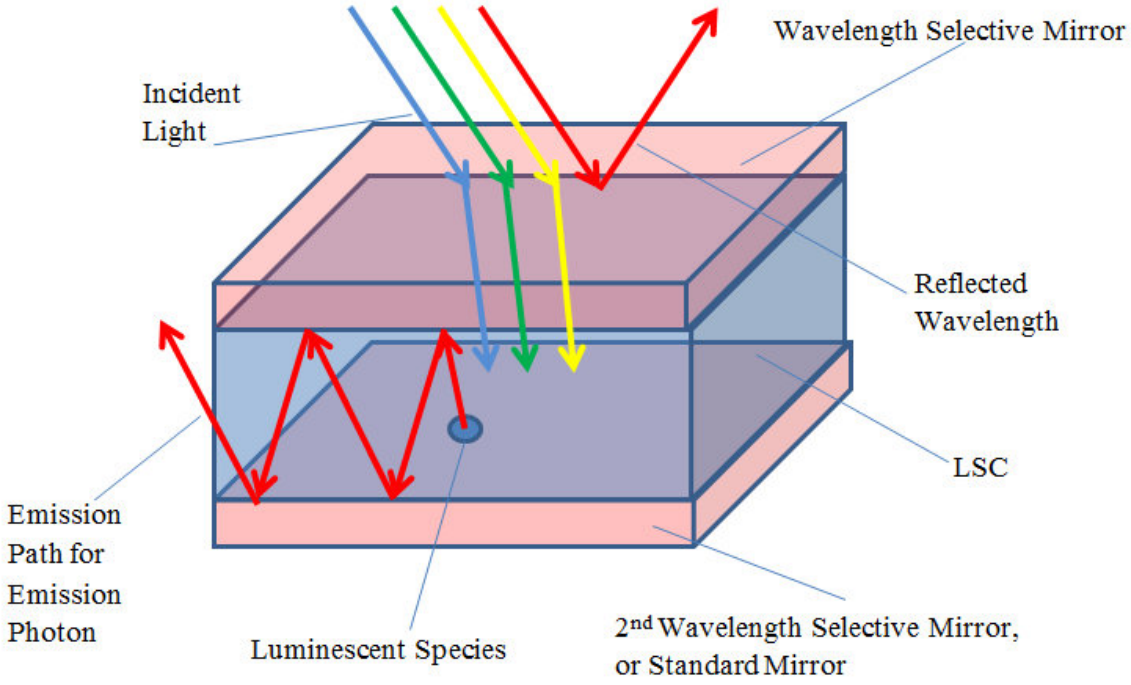


Figure 3-2 Schematic diagram of an LSC utilising a wavelength selective mirror on its top surface. It can be seen that the wavelength selective mirror prevents an emitted photon, impinging on the LSC surface with an angle lower than the critical angle from escaping.

3.2.3.1 Cholesteric Mirrors

One example of a wavelength selective mirror is the cholesteric mirror, where cholesteric refers to a particular type of liquid crystal. Such mirrors have featured in a number of LSC

publications [19-24,26]. Debije *et al.* [24] investigated cholesteric liquid crystal layers with a chiral nematic phase, which were tuneable to reflect light over a specific range of the EM spectrum. In the nematic phase there exists a long range orientational order, and although the molecules have no positional order, they self-align to have long-range directional order with their long axes roughly parallel. The overall direction of the liquid crystals is known as the director [25]. Due to orientational ordering of nematic phase liquid crystals, they often tend to form helixes of one particular handedness giving rise to the chiral nematic phase. This is often known as the cholesteric phase as it was first observed in cholesterol. The helices have a specific pitch, where the pitch is equal to the distance required for the liquid crystals to experience a full 360° rotation. If the pitch length of the liquid crystal helixes happens to share a similar length to that of visible light, the liquid crystals will reflect that wavelength of light, and this will result in the liquid crystals taking on the colour of the light which they are reflecting. Therefore, by controlling the pitch length of the liquid crystals it is possible to control the reflected wavelengths.

Debije *et al.* [24] used liquid crystals arranged in a chiral nematic phase applied to the top and bottom surface of a half-waveplate, which was then positioned on the top surface of the LSC. Liquid crystal layers of opposite handedness (dextrorotatory and levorotatory) were applied by spin-coating onto the half-waveplate so as to allow for the reflection of both polarisations of light An air gap was present between the cholesteric mirror and the LSC to compensate for the higher refractive index of the liquid crystals when compared to that of the LSC. Despite significant angular variation of the reflection band, which caused the reflection band to broaden and shift to lower wavelengths as the angle of incidence was increased, thereby making it impossible to optimise the cholesteric mirror for emission at all angles, they ultimately achieved a 35% increase in light emitted from the edges of the LSC by applying the cholesteric mirror.

More recent work by Verbunt *et al.* [26] has shown using a theoretical matrix based approach that it is possible to reflect back up to 91% of Lumogen red 305 emission by use of a 400nm range wavelength selective mirror, and this approach could potentially boost the LSCs efficiency by up to 66%. Experimental results could not match the level of improvement identified by the theoretical work, with only 5% improvements in edge efficiency being measured for LSCs with an absorbance of ~1 at the peak. However, they found that by reducing the peak absorbance to less than 0.1, they were able to measure an improvement of nearly 30% in LSC efficiency. The improvement for the lower peak absorbance measurement was attributed to lower reabsorption losses.

3.2.3.2 Distributed Bragg Reflectors (DBR), and Dichroic Mirrors

Another type of wavelength selective mirror/filter is the DBR, which makes use of multiple layers of thin-films with alternating high and low refractive index. These layers typically have a thickness equal to a ¼ of the target wavelength to be reflected. In the event that a reflection takes place at a boundary between two of these thin-films, where the light wave moves from a lower refractive index film, to a film of higher refractive index, the light wave experiences a 180° phase shift at the film boundary [27]. Due to the number of alternating boundaries, when the light wave reflections from each of the boundaries return to the initial reflection surface they will all be in phase and will experience constructive interference (see Figure 3-3, where $\eta_0 < \eta_{low} < \eta_{high}$).

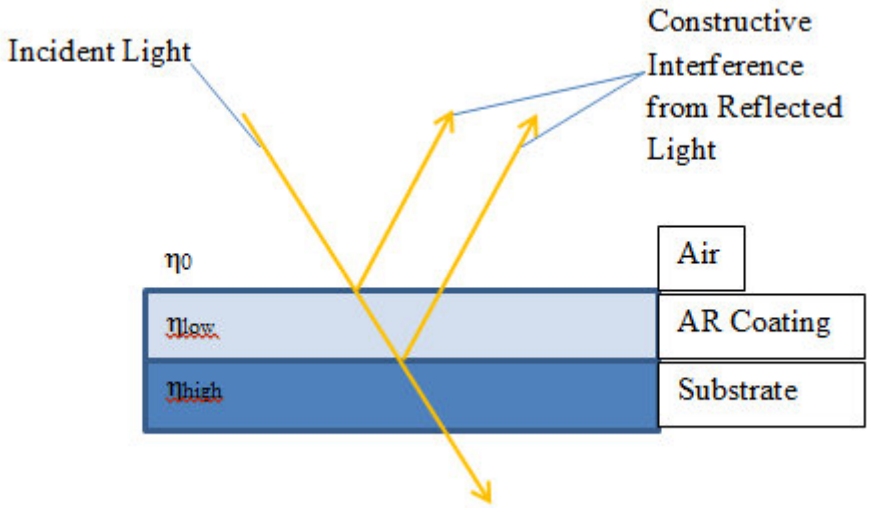


Figure 3-3 Diagram of constructive interference from an anti-reflection coating (diagram adapted from [27]).

For normal incidence the DBR's reflectivity, R, is approximately given by:

$$R = \left[\frac{n_0(n_2)^{2N} - n_s(n_1)^{2N}}{n_0(n_2)^{2N} + n_s(n_1)^{2N}}\right]^2 \qquad 3.2$$

where n_0, n_1, n_2 and $n_s$are the refractive indices of the originating medium, the two alternating materials, and the terminating medium. N is the number of repeated pairs of layers of low/high refractive index material.

The bandwidth $\Delta\lambda_0$ of the stop-band can be calculated from:

$$\Delta\lambda_0 = \frac{4\lambda_0}{\pi} arcsin\left(\frac{n_2 - n_1}{n_2 + n_1}\right) \qquad 3.3$$

where λ_0 is the central wavelength of the band.

From the equations 3.2 and 3.3, above, it can be seen that increasing the number of layers in a DBR increases the mirror reflectivity and increasing the refractive index contrast between the

materials in the Bragg pairs increases both the reflectivity and the bandwidth. Farrell [28] has theoretically investigated the efficacy of DBRs based on the cheap and readily available materials alumina (Al_20_3 n = 1.62) and silica (Si_20_3 n = 1.46) for improving LSC output. Farrell [28] used a matrix method to calculate the properties of the DBR and ray-trace simulations to model the LSC output. He concluded that the significant side lobes that cause unwanted reflection of incident light that could otherwise be absorbed in the LSC prevents the increase in trapping from increasing the overall output. He comments that this is the case even at normal incidence, which represents an upper limit on performance enhancement, and goes on to show that at increasing angles of incidence or under diffuse light the output of the LSC is actually reduced. In addition to the problem of the side lobes, and like in the case for the cholesteric coatings considered above which are themselves another type of thin-film inference coating, the stop-band shifts in position with angle of incidence so again it is hard to optimize a DBR over the full angular range of the emission [28].

Dichroic or "hot" mirrors are similar to DBRs in having multiple thin layers of differing optical properties. By varying the number and thickness of the layers the stop-band can be tuned to be as broad as required. Matrix methods are required to calculate the properties of these more complex structures and there are no simple analytical expressions such as those above for DBRs [29]. Although expensive, dichroic mirrors are manufactured commercially and find application in architecture and theatre lighting. Richards *et al.* [30] first investigated the application of hot mirrors to the LSC. In this work a dichroic mirror is applied to the top surface of an LSC stack, while the back surface features a rear specularly reflective layer. Computer modelled results for a 3 layer stack, each stack being 3mm thick, LSC with a bottom surface specular reflector and in two configurations; with and without top hot mirror, show that the LSC stack is capable of a 25% increase in optical efficiency when the hot mirror matched to the emission peak wavelength is used. This work was followed by an

experimental investigation of applying a dichroic mirror to a single layer Lumogen Red 305 doped LSC [31]. In agreement with [30], for light at normal incidence, a 25% increase in external quantum efficiency of the LSC was observed over the wavelength range for which the dye absorbs. However, as mentioned above this represents an upper limit on the performance increase and, given their cost, dichroic mirrors are not likely to be a cost effective solution for increasing the efficiency of the LSC.

A Rugate filter is more similar to a DBR than a dichroic mirror. The main difference between it and a DBR is the continuously varying nature of the Rugate filter's refractive index compared to the discretely changing index of a DBR. The benefit of a Rugate filter over a DBR is the suppression of the side bands which otherwise cause unwanted reflection of incident light that could otherwise be harvested by the LSC as discussed above. The refractive index of the layers varies with a sinusoidal characteristic in the Rugate filter [32] and, in the work of Goldschmidt *et al.* [33], was used to prevent escape cone losses over the emission wavelength ranges of their luminescent species. This resulted in a 20% overall improvement in the LSCs efficiency when the filter was used. As with the other interference filters considered, a major drawback to the use of Rugate/DBR filters is their angular dependence. In addition to the problem of optimising the stop-band for the whole angular range of the emission, they will also reflect more of the useful incident light, that could be harvested by the LSC, at higher angles of incidence as the stop band blue-shifts [28], which will limit the LSCs otherwise high diffuse light collection [34].

DBRs and Rugate filters are examples of 1D photonic structures, and opals which are 3D photonic structures are considered in [34]. 3D photonic structures are of interest as they have a potentially lower angular dependent response than 1D structures, since the diffraction of light by the opals can allow light even close to 90°, because of the materials diffractive properties, to the normal to be coupled to the sample. Additionally, by varying the size of the

3D structures it is possible to control the reflection wavelength. The opal films had an effective refractive index of 1.37, lower than that of the PMMA substrates of the LSCs, which led to some blue shifting of the reflection peak into the absorption spectrum of the luminescent species, a phenomenon they claim would prevent the LSC from collecting particularly diffuse light. Higher index 3D photonic structures could be used, but in the authors opinion the costs of such materials, for example diamond, would render such structures as inappropriate for use on LSCs.

3.2.4 Plasmonics

In recent years there has been interest in the use of plasmonic materials in LSCs for the purpose of enhancing absorption and PL emission from LSCs. A surface plasmon (SP) is a coherent oscillation of electrons which can occur at the interface between two materials when the real part of the dielectric function changes sign, as is the case at a dielectric-metal interface [35]. When an SP couples with a photon it becomes a surface plasmon polariton (SPP) which can propagate along the surface of a metal, due to interactions with free electrons. SPs and SPPs can also occur in other conducting materials [35]. SPs have very limited effective ranges since their intensity decays with the square of the electric field. This problem has been overcome by reducing the size of the metallic conductors responsible for the surface plasmons to nanoscale dimensions. It can be advantageous to place a luminescent species within range of the nanoscale metallic structures since these structures enhance the intensity of the EM field in their immediate vicinity [36]. As such, a luminescent species positioned within the region of the enhanced EM field may be subject to increased absorption and emission through increased rates of excitation and de-excitation [37]. The work of Zhang *et al.* [38] demonstrated that when silver nanoparticles are in close vicinity to a perylene based dye on a glass substrate, an enhancement in the PL emission from this sample when

compared to a control, without silver nanonparticles, was measured to have twice the emission.

The use of plasmonics with LSCs is a relatively new field though there are a few instances of the use of plasmonics in relation to LSCs [37,39,40]. It has been suggested that the use of plasmonic materials will also allow for luminescent species that have previously been rejected as being unsuitable for use in LSCs, to be used again in the future due to potential performance enhancements offered by plasmonic materials [41]. In [39] and [40] the approach is to utilise plasmonic effects to enhance the absorption of the solar cells to which the LSCs are in contact with, whereas in the work of Chandra *et al.* [37] gold nanoparticles are incorporated into the LSC waveguide itself. Their work featured LSCs which used CdSe/ZnS quantum dots as the luminescent species and tested a variety of different concentrations of gold nanoparticles for the purpose of producing surface plasmons. At nanoparticle concentrations of 2ppm a maximum emission increase of 53% was measured, when compared to a control. The increase in measured emission was attributed to an increased rate of excitation in the QDs and possibly also an increase in the rate of emission.

3.2.5 Alignment

The ability to align luminescent centres within an LSC is an important step towards improving the LSCs optical efficiency, as it can allow for the emission of a luminescent centre to be directed, which can result in a reduction in light lost from escape cones [42]. Alignment of a luminescent species must be somewhat of a compromise, if the electronic dipole alignment is perpendicular (homeotropic) in relation to the substrate material, there will be minimal light absorption (at normal incidence), but also minimal losses from escape cones, whereas if the alignment is parallel (homogeneous) to the substrate absorption (at normal incidence) will be maximised but so will escape cone losses as illustrated in Figure 3-4.

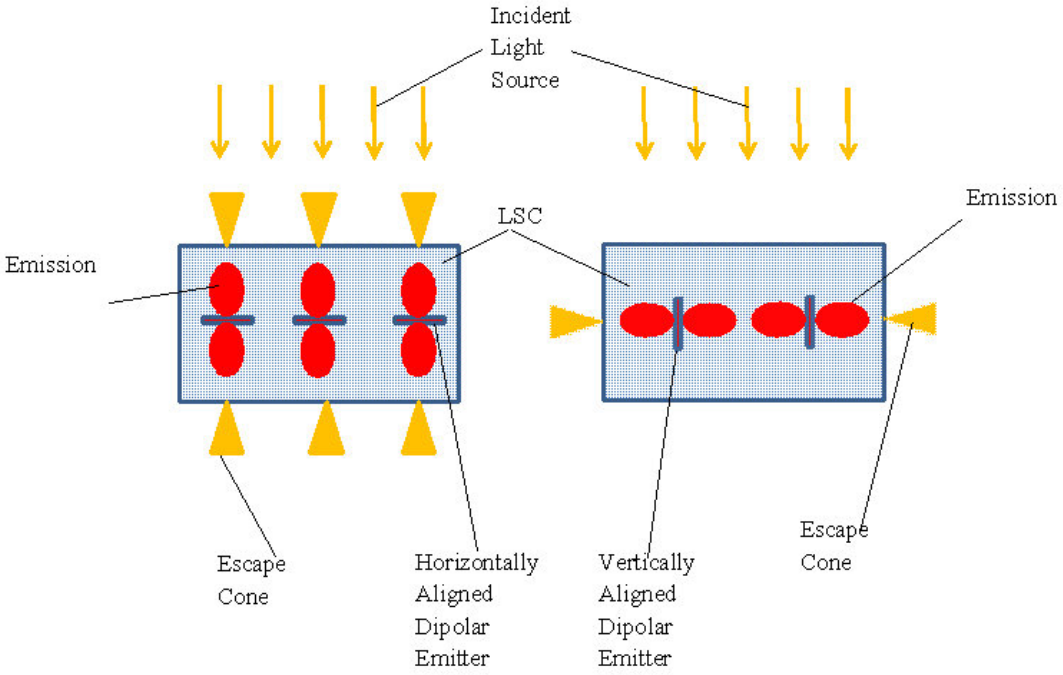


Figure 3-4 Side-view diagrams of horizontally and vertically aligned dipolar emitters respectively. Horizontal alignment has strong incident light absorption, but high top and bottom surface escape cone losses, whilst the opposite is true for the vertically aligned sample.

There have been a number of examples of the use of liquid crystals in LSCs for the purpose of providing alignment of the luminescent species being used [43,44,45]. Verbunt *et al.*[45] [46] have used fluorescent dyes mixed with liquid crystals to provide directionality to their emitted light. To do this they used a polyimide derived material in addition to liquid crystals within an alignment level, when rubbed using a cloth this caused the liquid crystals to align in a desired orientation. In [45] their results showed that dye molecule alignment resulted in a 30% increase in light output from the LSC edges which were oriented perpendicularly to the direction of the dye molecules, as compared to the edges parallel to the dye molecules. In [46] they again compare an isotropically oriented dye, to samples with the dye aligned homeotropically and homogeneously, but also consider the benefits of using a tilted dye alignment of 45-60°, again using liquid crystals to align the samples. As expected the

homeotropic sample had reduced light absorption but also had lower than 5% surface losses. However, this sample did not output more edge photons than the homogeneous sample. They attribute this to more reabsorption losses occurring in the homeotropic sample due to the lateral direction of emission and the higher refractive index of the dye layer, compared to that of the substrate, trapping emission photons in the higher optical density dye film layer (this is clearly observable by the larger red-shifting of this sample's edge emission).

Verbunt *et al.* [46] go on to speculate that a tilted alignment may be able to provide a compromise between the properties exhibited for the homeotropic and homogenous alignment. This means better incident light absorption and less reabsorption losses than the homeotropic sample, but superior light trapping compared to the homogenous sample, however, results for tilted alignment were not featured in this paper. A 2012 review article by the same group [41], explains that tilted alignment over a sufficiently large area is difficult to achieve due to defects, and that research continues on tilted LSCs.

Alignment of nanorods is of particular interest and is the subject of chapter 5 of this thesis, because nanorods possess all the benefits of quantum dots (see section 3.3.4.1) in addition to reduced spectral overlap [47]. Furthermore, there are a number of examples of both nanorod self-alignment [48,49] (or [50] specifically for carbon nanotubes) and induced alignment [51,52] (by application of an electric field) in the literature. A technique for nanorod self-alignment is discussed in the work of Zanella *et al.* [48]. In their work they were able to achieve vertical, self-alignment of CdSe/CdS core/shell nanorods, on a variety of substrates, including glass. The self-alignment did not require the substrates to be prepared in any special way, and was achieved by drop casting a xylene/nanorod (high concentration) solution on to a substrate, and then allowing the solvent to slowly evaporate in a xylene saturated atmosphere. X-ray diffraction measurements were used to determine that areas of approximately $1cm^2$ at the centre of the sample had 89±5% vertical alignment. There was a

reduction in vertical alignment for regions towards the edges of the samples which the authors attributed to more rapid evaporation at the edges of the sample [48].

A further example of nanorod alignment using an electric field to align the nanorods is described in the work of Ryan *et al.* [53]. They used a DC electric field to align CdS nanorods suspended in toluene; this resulted in nanorods moving into a 90° orientation with respect to the sample substrate (vertical alignment). As the toluene evaporated the nanorods became more closely spaced to each other. In the absence of the application of an electric field, it was found that the nanorods at the centre of the substrate still aligned in a perpendicular orientation with respect to the substrate. However, for nanorods further away from the centre of the samples, this perpendicular orientation was slowly lost and nanorods at the edge of the substrate were oriented parallel to the substrate [53].

It is also possible to align luminescent centres by doping an appropriate polymer solution with them to create a film. The doped film can then be heated and drawn, which has the effect providing alignment to the luminescent centres within. This has been demonstrated for organic photoluminescent materials in [54] and for nanorods in [55]. Unfortunately it results in horizontal alignment which is not beneficial to LSC operation.

3.2.6 Multiple LSC Stacks

The possibility of operating LSCs in stacks so as to absorb as much of the solar spectrum as possible was first considered by Goetzberger and Greubel in 1977 [56]. There are a number of benefits to using LSC stacks, rather than single LSCs, including achieving a broader absorption range since additional luminescent species can be used. The stack allows for a more efficient use of the solar spectrum since the emission from each LSC plate can be matched to the bandgap of the solar cell(s) coupled to the edges of that particular LSC plate, therefore reducing thermalization losses. A reduction in escape cone losses is also possible as

some of the escaping photons from the bottom surface of upper LSCs may be absorbed by LSCs lower in the stack (see Figure 3-5). Lastly, using individual luminescent species in conjunction with their own waveguides will result in lower reabsorption losses when compared to using multiple dyes, which will likely have overlapping absorption and emission spectra, within the same LSC. There are of course also drawbacks to the stacked LSC, such as additional costs due to use of more materials, a bulkier device, and most importantly, the cost of the additional solar cells.

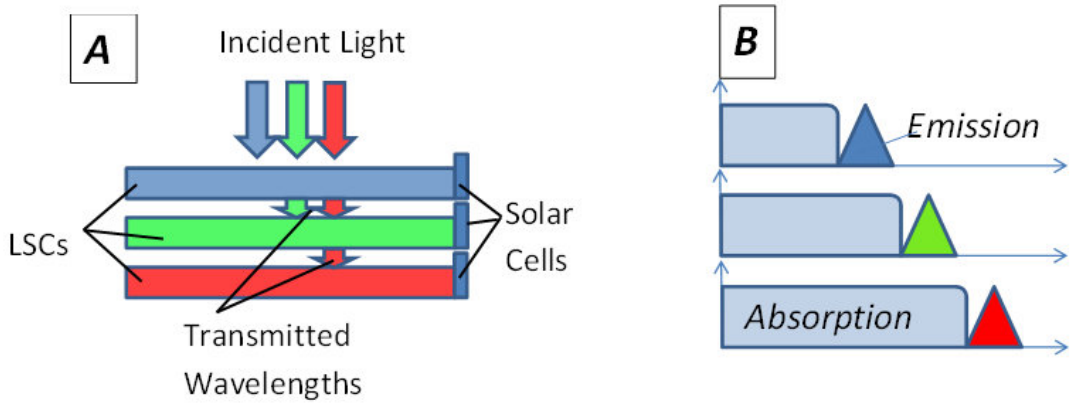


Figure 3-5 Diagram of A) a 3 stack LSC with solar cells affixed, B) the corresponding absorption and emission spectra for the 3 plates (figure adapted from [57].

There are numerous examples of multiple LSC stacks in the literature [10,33,56,58,59]. For example in the work of Goldschmidt *et al.* [33], a two LSC stack was fabricated, in which each LSC featured a different fluorescent dye. A system efficiency, including cells, of 6.7%, was obtained compared to 5.1% for a similar single LSC system. It is important to note, however, that these system efficiencies were achieved using GaInP solar cells, which are currently relatively expansive and therefore impractical for large scale LSC use. Additionally, GaInP cells were used for both LSC plates, meaning that one of the two plate's emission spectra was not ideally matched to the bandgap of the cell and as a result there would have been some thermalization losses.

Currie *et al.* [58] also discuss a two stack LSC in their work, which featured a rubrene based LSC at the top of the stack, which collected the blue and green regions of the EM spectrum, and a platinum based phosphorescent dye in the lower LSC to collect the longer wavelengths. A power conversion efficiency of 6.8% was determined for this tandem LSC stack under an AM1.5G spectrum, with the top LSC emission being coupled into GaInP solar cells and the bottom LSC emission into GaAs solar cells. It is important to note that the two LSCs used in this stack were of limited size, only 25 by 25 by 2mm each and had a geometric gain of only 3, which meant there were no significant reabsorption losses. However, the authors claim that due to the low spectral overlap of their materials the high efficiency should be maintained even up to high geometric gain. They predict that the power conversion efficiency would only be reduced to 6.1% at a geometric gain of 45 [58].

3.2.7 Multiple Dyes

The use of multiple luminescent species in one LSC is an alternative method to stacking LSCs in order to extend the absorption range. The use of multiple dyes can be significantly cheaper than using multiple LSCs, since fewer solar cells and LSC plates are required. For a multiple dye LSC to be efficient, the absorption and emission spectra of each luminescent centre must be carefully considered. An ideal situation would involve the emission from one dye being completely absorbed by the second dye and so on, which would allow for efficient energy transfer from one dye to the next, potentially a large Stokes-shift (depending on the concentrations of the component dyes), and a broader absorption spectral range owing to the multiple dyes being used. It is desirable for the energy transfer between dyes to occur non-radiatively, in order to avoid escape cone losses, via Förster resonant energy transfer (FRET) which occurs only if the spacing between luminescent centres is sufficiently small. FRET is the non-radiative energy transfer between luminescent molecules via long range dipole-dipole coupling, with the excited molecule being known as the acceptor and the molecule where de-

excitation occurs being known as the donor [60]. The distance between, and therefore the concentration of, the luminescent molecules is very important because the efficiency of FRET in solution is proportional to $\frac{1}{R^6}$, where R is the molecular spacing between the donor and acceptor species. Equation 3.4 is used to calculate the efficiency, E_{FRET}, of FRET [12]:

$$E_{FRET} = \frac{R_0^6}{R_0^6 + R^6} \qquad 3.4$$

where R_0 is the Förster radius, the distance between donor and acceptor molecules required for an FRET efficiency of 0.5, and R is the distance between the two types of molecule.

An example of the use of multiple dyes in LSCs can be in the work of Swartz *et al.* [61], featuring an LSC consisting of a Coumarin 6 dye and a Rhodamine dye at concentrations of ~10^{-4}M. In this work the authors identified that a relatively strong emission peak from the Rhodamine donor was evidence of FRET, though they went on to clarify that they would expect little FRET at dye concentrations as low as ~10^{-4}M. However, the authors of [12] question whether there truly was any FRET, having suspicions that due to the long path length the emission from the donor dye would have been absorbed by the acceptor dye before reaching the edges of the LSC, and they say this is the reason why the edge featured no emission from the donor dye.

The work of Bailey *et al.* [12] used a thin-film LSCs with three dyes, all variations of a BODIPY® dye from Molecular Probes, Inc., at a concentration of $1x10^{-2}$±0.2M. Their work tested LSC plates using different combinations of dye pairs in addition to the three dye LSC. The optical densities chosen for the dyes were sufficient for high light absorption at their respective peaks, however, they were chosen for convenience rather than efficiency optimisation. By using the least-squares fitting rule to deconvolve the emission spectrum

from the three dyes it was determined that 98±0.5% of the emission came from dye C, the acceptor, while dyes A and B both contributed 1±0.5% each, which shows that FRET was very efficient, nearly 100% (see Figure 3-6). The authors believe that the energy transfer between dyes is due to FRET because, for dyes A, B and C in individual LSC plates at high dye concentration ($1x10^{-2}$M), there is little discernible polarisation of the edge PL. They reason that since FRET will randomise the polarisation of fluorescent emission, and since they use dyes A, B and C at the same high dye concentration when in the multiple dye LSC, that FRET is likely to be occurring in their multi dye LSC. Furthermore, the authors go on to state that spectral overlap between the absorption and emission in the first two donor dyes is not important, and neither is the LQY, since the coupling is by FRET and is not optical absorption and emission. However, for the acceptor dye the normal LSC rules of low overlap and high LQY apply. Ultimately, they achieved an increase in photocurrent from the edges of the three dye LSC, compared to the one dye LSC, in the range of 45 to 170% [12].

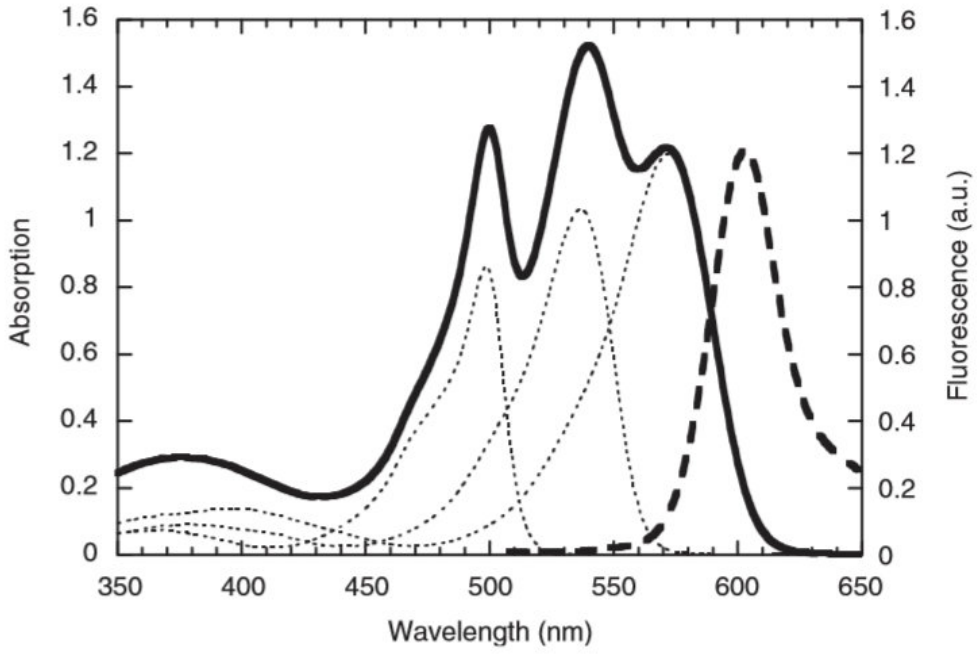


Figure 3-6 Graph from Bailey *et al.* [12] (reproduced with permission from Elsevier Limited) showing the combined absorption spectrum of their three dyes (—), the absorption spectrums of the 3 individual dyes (----), and the emission spectrum the combined dyes (---).

Another example of multiple dyes used in LSCs can be seen in the work of Richards and McIntosh [62], who used ray-trace simulations for a 5 dye homogenous LSC plate. The dyes included, Lumogen Violet, Yellow and Orange from BASF, as well as a NIR dye and achieved a maximum efficiency of 4.4%. LQY was required to be high for all dyes since the dyes were transferring energy optically instead of via FRET. Further examples of multiple dye LSCs can be found in references [30,63,64].

3.3 Types of Luminescent Centres

A number of specific types of luminescent species are currently, or have been previously, researched to determine their suitability for use in high efficiency LSCs. Desirable traits for these luminescent species include: a high LQY (see section 2.6.2), a broad absorption spectrum, and a large Stokes-shift, sufficient to prevent overlap between the absorption and emission. If the attached solar cells are carefully chosen so that their absorption spectra match the emission spectra of the LSCs, then energy losses from very large Stokes-shifts are not a significant concern as the total number of emitted photons is more important than the energy of these emitted photons. Appropriate absorption and emission bands must also be considered and this is highly dependent on the purpose of the LSC. For example it may be more appropriate for an LSC window to absorb light in the UV region of the spectrum. It is also important to note that the highest irradiance and photon flux intensities of the AM1.5g spectrum are in the visible region (see Figure 2-2, chapter 2). Lastly, the luminescent centre must be stable enough to allow the LSC to have a lifetime of the required length. For a commercial product a lifetime of over 15 years would need to be guaranteed. This condition is relaxed for research purposes as it is likely that species that do not show the required stability in solution or in PMMA could either be protected in a commercial product by the use of additional protective coating layers or that more stable variants could be synthesised. An overview of all types of luminescent species which are potentially of use in LSC follows:

3.3.1 Conjugated Polymers

Conjugated polymers (also known as conductive polymers) are a type of polymer which have alternating double and single bonds along the polymer backbone [65]. They are of interest due to their natural conductivity, which is due to the delocalisation of electrons, which have the freedom to move around within the polymer [66]. More specifically the delocalised electrons are the valence π electrons [67]. Short length conjugated materials (which have only a few repeat units and so have sufficiently low dimensions so as to have quantum confinement) may be of particular use in LSCs owing to their wavelength tuneability, which is achieved by varying their length, and thus their level of confinement [65]. A more detailed description or the luminescent properties of conjugated polymers can be found in section 2.5.2.

There are numerous types of conjugated polymers which have been shown to exhibit photoluminescent properties, one such material is polyindinofluorene (PIF). PIF emits blue light and in the work of Jeong *et al*. [68], PIF was measured to have a LQY value of ~80%, in conjunction with additional attached polymers. Jeong *et al*. believed that the LQY value measured was largely due to PIF, as the additional polymers were only present in relatively small quantities. With the addition of various polymers to the PIF backbone, it was found that it was possible to broaden the absorption spectrum or the emission spectrum of this conjugated polymer.

In the work of Kim *et al.* [69] a PIF based conjugated polymer was used for the purpose of producing broadband absorbing organic solar cells. Two types of PIF copolymers were used, poly(6,6',12,12'-tetraoctylindeno[fluorine-co-4,7-bis(2-thienyl)-2,1,3-benzothiadiazole) (PIF-DBT)- and poly(6,6',12,12'-tetraoctylindeno[1,2-b]fluorine-co-5,7-dithien-2-yl-thieno[3,4-b]pyrazine (PIF-DTP) which have absorption energy gaps of ~1.9eV and ~1.6eV respectively, and absorb over the wavelength ranges 300-650nm and 300-800nm

respectively. Such broad absorption spectra, and absorption in the UV/blue part of the EM spectrum shows that these particular conjugated polymers have the potential to be effective luminescent centres within LSCs if they have high LQYs.

Direct use of a conjugated polymer in an LSC was shown in the work of Sholin *et al.* [70], in which the commercial polymer Red F was used as the luminescent species within the LSC. Measurements of the LQY of Red F in solution and at low concentration, to minimise reabsorption losses, determined that Red F had a LQY of 67%. The low overlap between the absorption and emission of this polymer (due to changes in the structure when a polymer has been excited), which minimises reabsorption losses, led to a high optical efficiency of 3.4% for light being collected from a single edge of a 1 inch by 1 inch heavily doped sample (the remaining 3 edges were painted black and incident light source was an un-specified solar simulator).

3.3.2 Organic Dyes

There are many examples of luminescent organic dyes featuring in LSC publications, a number of which are discussed throughout this chapter. The review paper by Debije *et al.* [41] provides a good overview of their use in the field of LSCs. The organic dyes which are most often used in LSCs are rhodamine, coumarin or perylene based. The rhodamine and coumarin based dyes were first used in the early days of LSC research, but were limited by their low stability. The work of Batchelder *et al.* [71] for example, used rhodamine and coumarin based dyes in some of their LSC plates and found that although degradation rates varied between the different varieties of rhodamine and coumarin based dyes, the degradation rates were rapid in all cases, with lifetimes of the order of only a few days.

As can be seen in many of the references in this chapter, organic dyes are heavily used as luminescent species in LSCs. More recently perylene based dyes have been chosen as the

preferred type of organic dye to be used in LSCs [72-74]. The use of perylene based dyes has a number of advantages, such as their high LQY values which were measured in the work of Wilson and Richards [73] as being in the high 90 per cent range to approximately 100% (Lumogen dyes from BASF). This is in agreement with the datasheets from BASF that claim a >85% LQY for their violet dye increasing to >95% LQY for their red dye [75]. Furthermore, in the work of Slooff *et al.* [74] a 250 day continuous illumination of an LSC plate consisting of Lumogen red 305 (BASF) by a UV filtered white light source (up to 1100nm) which had an intensity of $\frac{1}{3}$ that of the Sun resulted in an EQE loss of only 20%. They also mention that for outdoor aging studies that there was some regeneration of the dye during the lower solar intensity of winter.

3.3.3 Phycobilisomes

Phycobilisomes are a type of light harvesting pigment found within some species of red algae and cyanobacteria, which fulfil a similar role to that of chlorophyll in green plants [76]. Since phycobilisomes are present in a number of different species they therefore exist in a number of different forms, which are well adapted to the particular environment in which their host organism lives [77]. These adaptations are a useful trait when considering phycobilisomes as a potential luminescent species for LSCs since different phycobilisomes are better adapted to utilising different wavelengths of the EM spectrum.

Phycobilisomes consist of biliproteins which are subdivided into 3 groups referred to by their bilin energies [77]. The first of these groups (see Figure 3-7) are called phycoerythrins which absorb the highest energy photons in the phycobilisome absorption spectrum. After a photon has been absorbed by the phycoerythrins, the excitation energy is transferred to the biliprotein with the next bilin energy level which are known as phycocyanins, which provide the

intermediate level of the 3 bilin energies. Finally, the excitation energy moves into the biliprotein with the lowest bilin energy level, which are known as allophycocyanins.

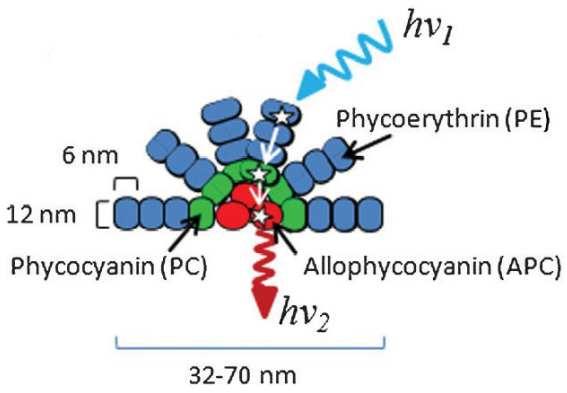


Figure 3-7 Image reproduced with permission from John Wiley and Sons [78] showing the different proteins and the energy transfer mechanism within a phycobilisome.

The 3 different bilin energies found within the biliproteins allow for efficient energy transfer by FRET from the point of absorption to the point of emission, and, an important outcome of this energy transfer is that phycobilisomes have relatively large Stokes-shifts [77] to minimise reabsorption losses. Mulder *et al.* [78] discovered that the energy transfer efficiency for phycobilisomes was up to 95% (when in algae), and the individual LQY for the separate bilin proteins was found to be 98%, 51% and 68% for phycoerythrin, phycocyanin and allophycocyanin respectively, when the phycobilisomes were separated from algae [79].

In the work of González *et al.* [80] an attempt was made to reduce the spectral overlap between the absorption and emission spectra, by modification of the phycobilisomes, to remove secondary peaks which featured in the absorption and emission spectra. Although the secondary peaks were removed, the Stokes-shift between the primary absorption and emission peaks was reduced, and so spectral overlap was not improved. In the work of Fisher *et al.* [81], which is described in more depth in chapter 6 a tandem fluorophore consisting of R-phycoerythrin and rhodamine-B was investigated. R-phycoerythrin has the highest of the

bilin energies within the phycobilisome (see Figure 3-7 and discussion above) and was chosen due to R-phycoerythrin's high LQY (see above). The tandem with rhodamine-B was originally chosen by Columbia Biosciences to broaden the absorption spectrum and to reduce spectral overlap. The first aim is somewhat strange since the absorption spectrum of R-phycoerythrin is broader than that of rhodamine-B, the second aim of broadening the Stokes-shift was achieved though (see section 6.2.1, chapter 6). Ultimately a LQY of only 53% was found for thin-film samples containing this particular tandem fluorophore [81].

In conclusion, large Stokes-shifts and the ability to grow phycobilisomes in large quantities, which should lead to low cost, have made phycobilisomes an attractive luminescent centre for use in LSCs.

3.3.4 Nanocrystals

Colloidal semiconductor nanocrystals are of particular interest for use in LSCs, for example [48,86,88,90,91]due to their absorption and emission spectral tuneability, their high stability and their broad absorption spectra. However, they are quite expensive. Quantum dots (QDs) and nanorods have been used in LSCs but tetrahedrons can also be grown and some material systems produce cubes, triangles etc. [82]. In section 2.5.1, there is an explanation of the excitation and de-excitation mechanisms present in nanocrystals.

Due to their large surface area to volume ratios nanocrystals suffer from significant surface losses due to surface defects and the subsequent recombination events which occur. Therefore, nanocrystals are often grown in core/shell configurations with the shell layer serving to reduce surface defects which would otherwise reduce the LQY of the nanocrystals as well as conferring greater stability [83]. Core shell nanocrystals can be classified as type-I, type-I reversed or type-II. In type-I nanocrystals the energy gap of the shell material is higher than that of the core, this results in both electrons and holes being confined to the nanocrystal

core as a result (an example of type-I nanocrystals would be CdSe/ZnS) [83,84]. In reverse type-I nanocrystals the energy gap present in the shell material will be less than that of the core, the dimension of the shell will then determine whether or not electrons will be completely or only partially limited to the shell. Therefore, it is possible to change the emission wavelength by varying the shell thickness (an example of reverse type-I nanocrystals would be CdS/CdSe) [83]. For type-II nanocrystals either the valence energy level or the conduction energy level of the shell material falls within the energy gap of the core material, which allows for separation of the electrons and holes, with one charge carrier in the core while the other is in the shell layer. An interesting consequence of this is that for type-II nanocrystals, the emission spectrum is from this lowest energy exciton, which can be significantly red-shifted from the energy of the core and helps to explain the shape of the absorption and emission spectra in type-II nanocrstals (an example of type-II nanocrystals would be CdTe/CdSe [83]) [85].

3.3.4.1 Quantum Dots (Nanocrystals)

In the past decade and a half the idea of using QDs as luminescent centres in LSCs has attracted attention, due to them possessing the benefits of nanocrystals discussed in the previous section. QDs were the first type of semiconductor nanocrystal to be widely researched and were thus the first type identified for use in LSCs by Barnham *et al.* [86]. Core shell QDs can also provide high LQYs and a LQY in excess of 80% has been reported [87]. Chatten *et al.* [88] have shown that a broader QD size distribution results in lower overlap between the absorption and emission and therefore lower reabsorption losses

As outlined in section 3.2.4 in the work of Chandra *et al.* [37] gold nanocrystals were used in conjunction with CdSe/ZnS core/shell QDs, this resulted in an increase in QD emission due to the plasmonic effects of the gold nanocrystals.

3.3.4.2 Nanorods

Like QDs nanorods are nanoscale, wavelength tuneable (controlled by the rod dimension, i.e. the level of quantum confinement see section 2.5.1), inorganic materials, and as such they enjoy similar advantages, such as good stability and narrow emission spectra. Additionally, it is possible to align nanorods so that arrays with the same orientation can be produced. This is of value since the transmission dipole within the nanorods is parallel to that of the length axis of the nanorod, therefore, the emission is at maximum intensity in a direction perpendicular to the direction of the nanorods' length axis.

Measurements have shown CdSe/CdS core/shell nanorods to have a reasonable high LQY of 70%, as measured by Carbone *et al.* [89]. It was also noted in their work that the LQY is highly dependent on the aspect ratio of the nanorods, with the lowest aspect ratio rods having the highest LQYs, this was attributed to lower number of defects at the boundary between the core and shell of the nanorods. Their nanorods were grown using a seeding method, and high emission intensities were measured from these nanorods. By varying the dimensions of the nanorods the absorption energy threshold was tuned, and they were able to produce nanorods with emission spectra from the green part of the EM spectrum to the red.

Zanella *et al.* [48] have shown that it is possible to create samples of self-aligned CdSe/CdS core/shell nanorods, where the rods are vertically aligned. Furthermore, they have shown that they are able to achieve vertical alignment on a variety of substrate materials, without special preparation of these substrates beforehand. X-ray diffraction was used to reveal that for approximately $1cm^2$ central regions on these samples, 89±5% of the nanorods were vertically aligned [48]. A LQY value of 70±5% was measured by Carbone *et al.* [89] for CdSe/CdS core/shell nanorods similar to those used in the work of Zanella *et al.* [48]. Realising self-alignment of luminescent species, which have dipolar emission distributions, is an important

achievement because, as discussed in section 3.2.5, alignment has the potential to greatly increase the optical efficiency of LSCs.

Bose *et al.* [90,91] have used CdSe/CdS core shell nanorods as the luminescent species within homogenously doped, and thin-film LSCs. They were able to show, by means of computational raytrace modelling, that the nanorods being tested did not suffer such significant reabsorption losses as suffered by comparable QD doped LSCs.

3.3.5 Rare Earth/Metal Complexes

Rare Earth elements (REEs) have been considered for use as luminescent species for LSCs, since very large Stokes-shifts are possible when an appropriate ligand material is bound to the REE. However, REEs tend to be expensive as large concentrated deposits are rare, although the elements themselves are not uncommon in the Earth's crust [92]. In addition, there is a very high demand for these materials for use in a great variety of modern electronic devices. When considering REEs for use in LSCs, potentially large scale use, it should not be forgotten that there are political issues to contend with as well. A 2010 report by the Centre For Strategic & International Studies claims that China alone was responsible for the production and refinement of 97% of the world's supply of rare Earth elements [93]. Due to the limited diversity in the supply line, it is not unheard of for disputes to lead to a reduction in supply as has occurred between Japan and China [94]. More recently, new supplies have begun to be introduced globally such as at the Mountain Pass mine in the US and at Mt. Weld in Australia [92], potentially leading to reductions in price that may allow for larger scale use of REEs in LSCs.

Price and supply issues aside, there are has been some work featuring REEs as luminescent species for LSCs. In the work of Moudam *et al.* [95] Europium complexes were used as luminescent centres. However, since Europium has a relatively poor absorption coefficient,

the addition of light absorbing antenna ligands is necessary to enhance light absorption, thus creating a Europium complex [95]. The addition of organic ligands to Europium atoms provides an additional bonus in the form of a large Stokes-shift; a result of efficient non-radiative energy transfer within the ligand/europium complex [96]. The work by Moudam *et al.* [95] reports that they obtained a very high luminescent quantum yield of 85% in PMMA for one of their ligand/europium complexes.

More recently the work of Wang. *et al.* [97] discussed a $Eu(TTA)_3(TPPO)_2$, europium tris(2-thenoyl trifluoro acetonate)-di(triphenylphosphine oxide)), europium complex. This complex has an exceptionally high Stokes-shift, and as a result there is no spectral overlap at all between the absorption and emission spectra. Their work showed that for position dependent measurements using a monochromatic light source, the short circuit current density in an attached/adjacent silicon solar cell decreased one order of magnitude more slowly for the Eu complex doped LSC as the point of excitation was moved away from the cell than that for a control sample which employed the standard fluorescent dye. The fluorescent dye is rather cryptically stated as a dye used in the work of Goldschmidt *et al.* [11], this work incidentally featured several dyes (which had some spectral overlap).

3.4 Conclusion

This chapter has focused on methods and materials which have been used to improve the optical efficiencies of the LSC, in response to the efficiency drains identified in chapter 2. Additionally, this chapter includes detail descriptions of prominent luminescent species which have been used in LSCs, as well as their advantages and disadvantages.

The chapter starts by identifying a variety of mirrors and scattering materials which have been used to reduce losses from escape cones (photons which are transmitted through the LSC), such as specular mirrors and white diffuse scattering materials. These mirrors and

scatterers reflect or scatter photons lost from the bottom surface, or the edges of the LSC which are not covered by solar cells, back into the LSC giving the photons an additional chance to be absorbed, and/or collected by an attached solar cell. More complex wavelength selective mirrors such as cholesteric mirrors, DBRs and dichroic mirrors have been used to selectively reflect ranges of wavelengths which correspond to the emission spectral range. These mirrors effectively prevent top surface escape cone losses, though all of these mirrors have some level of angular dependence.

Other important techniques such as alignment of fluorescent dipoles, multiple LSC stacks and multiple dye LSCs are also described in this chapter. The alignment of dipolar emitters is potentially of great importance as ideally aligned dipoles may provide strong light absorption properties, and relatively low escape cone losses, when there is large scale tilted dipole alignment (vertically aligned nanorods are the subject of chapter 5 of this thesis).

Multiple LSC stacks are an interesting area of research since they allow for broader absorption of the AM1.5g solar spectrum, and thus potentially higher overall device efficiencies, they also potentially suffer less from reabsorption losses than multiple dye LSCs. However, multiple LSCs also means a multiplication of the resources which are required to make the device, with additional solar cells adding significantly to the costs of the device. As a result of the additional solar cells, multiple LSC stacks cost considerably more than single LSCs. Multiple dye LSCs will be cheaper than LSC stacks, but they require very careful dye selection so as to allow the emission spectrum of one dye to be largely (or ideally) completely absorbed by the next dye, effectively broadening the absorption spectrum and providing efficient energy transfer. Additionally, if the different dye concentrations are high enough FRET will occur, significantly improving efficiency as escape cone and LQY losses of the donor dyes can be avoided.

A broad range of luminescent species have been considered for use in LSCs, and this chapter has attempted to identify the advantages and disadvantages of the prominent species. Nanocrystals such as nanorods and quantum dots have featured in a number of LSC papers. They have relatively high LQYs, good photostability and wavelength tuneability (nanorods also lend themselves well to various alignment techniques and are the subject of chapter 5 of this thesis).However, currently nanocrystals tend to be quite expensive. Organic dyes tend to have high LQY, but suffer from relatively low Stokes-shifts, while rare-earth complexes have been shown to have very high Stokes-shifts (some feature no spectral overlap), but have to contend with high prices and low availability. Bio-derived luminescent species such as the phycoblisomes, featured in chapter 6, are potentially very cheap and available in large quantities, but have been shown to have relatively low LQYs. So as with the efficiency enhancing techniques described in this chapter, the advantages of an LSC's luminescent species has to be balanced against their disadvantages. Furthermore, careful consideration must be given to the particular use of the LSC in which the luminescent species is to be used, for example chapter 6 of this thesis develops and characterises large, thin flexible LSCs, an LSC for which a high Stokes-shift is essential.

Chapter 3 References

[1] Chatten, A, (2007)Thermodynamic Modelling of Luminescent Solar Concentrators with Reduced Top-Surface Losses", Proceedings 22nd European Potovaoltaic Solar Energy Conference, Munich, Germany, p349-353.
[2] Bose, R., (2012)."Raytrace Simulations and Experimental Studies of Luminescent Solar Concentrators", Doctoral Thesis, Imperial College London, (2012).
[3] Slooff, L., Bende, E., Burgers, A., Budel, T., Pravettoni, M., Kenny, R., Dunlop, E., and Buchtemann, A., (2008). "A luminescent solar concentrator with 7.1% power conversion efficiency", Phys. Status Solidi (RRL), 2, p257-259,.
[4] Goetzberger, A, (1978). "Fluorescent Solar Energy Collectors: Operating Conditions with Diffuse Light", Applied Physics, 16, 399-404.
[5] Kortum, G., (1969), "Reflectance Spectroscopy", Springer-Verlag, Berlin.
[6] Hanrahan, P., and Krueger, W., (1993), "Reflection from layered surfaces due to subsurface scattering" "Proceedings of the 20th annual conference on computer graphic and interactive techniques –SIG-GRAPH '93. P165-174.
[7] Debije, M., and Dekkers, W., (2012), "Functionalizing the rear scatterer in a luminescent solar concentrator", Journal of Renewable and Sustainable Energy, 4, 013103.
[8] Heidler, K., (1981), "Efficiency and concentration ratio measurements of fluorescent solar concentrators using a xenon measurement system", Applied Optics, 20, 5, p773-777.
[9] Mugnier, J., Dordet, Y., Pouget, J., and Valeur, B., (1987). "A photometric approach of fluorescent solar concentrators. Role of diffuse reflectors and spectral sensitivity of solar cells", Rev. phys. Appl.,22, p89-100.
[10] Earp, A., Smith, G., Franklin, J., and Swift, P., (2004) "Optimization of a three-colour luminescent concentrator daylighting system", Sol. Energy Mater. Sol. Cells, 84, p411-426.
[11] Goldschmidt, J, (2009). "Increasing the efficiency of fluorescent concentrator systems", Sol. Energy Mater. Sol. Cells, 93, p176-182.
[12] Bailey, S., Lokey, G., Hanes, M., Shearer, J., McLafferty, J., Beaumont, G., Baseler, T., Layhue, J., Broussard, D., Zhang, Y,. Wittmershaus, B., (2007) "Optimized excitation energy transfer in a three-dye luminescent solar concentrator", Solar Energy Materials and Solar Cells, 91, p67-75.
[13] Tsoi, S., Broer, D., Bastiaansen, C., Debije, M., (2013) "Using Lenses to Improve the Output of a Patterned Luminescent Solar Concentrator", Advanced Energy Materials, 3, 3, p337-341.
[14] Debije, M., Van, M-P., Verbunt, P., Kastelijin, M., Van der Bloom, R., Broer, D., and Bastiaansen, C., (2010) "Effect on the output of a luminescent solar concentrator on application of organic wavelength-selective mirrors", Applied Optics, 49, 4, p745-751.
[15] Debije, M., Teunissen, J-P., Kastelijin, M., Verbunt, P., and Bastiaansen, C., (2009)."The effect of a scattering layer on the edge output of a luminescent solar concentrator", Solar Energy Materials and Solar Cells, 93, 8, 1345-1350.
[16] Slooff, L., Bende, E., and Budel, T., (2009) "THE NON-FLUORESCENT FLAT PLATE SOLAR CONCENTRATOR", Proceeding of the 24th European Photovoltaic Solar Energy Conference and Exhibition, Hamburg, Germany.
[17] Bose, R., (2012). "Raytrace Simulations and Experimental Studies of Luminescent Solar Concentrators", Doctoral Thesis, Imperial College London.
[18] Grabowski, L., (1914) "On the Theoretical Photometry of Diffuse Reflection", The Astrophysical Jouranl, 39, p299-306.

[19] De Boer, D., Broer, D., Debije, G., Keur, W., Meijerink, A., Ronda, C., and Verbunt, P., (2012), "Progress in phosphors and filters for luminescent solar concentrators", Optics Express, 20, 10, pA395-A405.
[20] Verbunt, P., Debije, M., Broer, D., Bastiaansen, C., and Broer, D.,(2012), "Organic wavelength selective mirrors for luminescent solar concentrators", Photonics for Solar Energy Systems, 8438.
[21] de Boer, D., Lin, C-W., Giesbers, M., Cornelissen, H., Debije, M., Verbunt, P., and Broer, D., (2011). "Polarization-independent filter for luminescent solar concentrators", Applied Physics Letters, 98, 021111.
[22] Slooff, L., Burgers, A., and Debije, M., (2008). "Reduction of escape cone losses in luminescent solar concentrators with cholesteric mirrors", Proceedings of the Society of Photo-Optical Instrumentation Engineers (SPIE), 7043, 704306, San Diego.
[23] de Boer, D., Ronda, C., Keur, W., and Meijerink, A., (2011). "New luminescent materials and filters for Luminescent Solar Concentrators", Conference on High and Low Concentrator Systems for Solar Electric Applications VI, 8108, 81080E.
[24] Debije, M.. Van, M-P., Verbunt, P., Kastelijn, M., van der Blom, R., Broer, D., Bastiaansen, C., (2010) "Effect on the Output of a Luminescent Solar Concentrator on Application of Organic Wavelength-Selective Mirrors". Applied Optics. 49 4 745-751.
[25] Hamley, I., (2000)."Introduction to Soft Matter: Polymers, Colloids, Amphiphiles and Liquid Crystals)", Chichester: John Wiley and Sons, Ltd.
[26] Verbunt, P., Tsoi, S., Debije, M., Boer, D., Bastiaansen., Lin, C-W., and de Boer, D., (2012).. "Increased efficiency of luminescent solar concentrators after application of organic wavelength selective mirrors". Optics Express. Vol. 20.
[27] Angus Macleod, H., (2001). "Thin-Film Optical Filters", Third Edition. London: The Institute of Physics.
[28] Farrell, D,. (2008). "Characterising the Performance of Luminescent Solar Concentrators", PhD Thesis, Imperial College London
[29] Chatten, A., Private correspondence, Imperial College London, UK. (2013).
[30] Richards, B., Shalav, A., and Corkish, P., (2004)."A Low Escape-Cone-Loss Luminescent Solar Concentrator", Proc. 19th European Photovoltaic Solar Energy Conference, Paris, France.
[31]van Sark, W., Barnham, K., Sloof, L., Chatten, A., Buchtemann, A., Meyer, A., McCormack, S., Koole, R., Farrell, D., Bose, R., Bende, E., Burgers, A., Budel, R., Quilitz, J., Kennedy, M., Meyer, T., Donega, C., Meijerink, A., and Vanmaekelbergh, D., (2008). "Luminescent Solar Concentrators - A review of recent results", Optics Express, **16**, 26, p21773-21792].
[32] Goldschmidt, J., Peters, M., Dimroth, F., Bett, A., Steidl, L., Zentel, R., Hermle, M., Glunz, S., Willeke, G., (2009).. "Developing Large and Efficient Fluorescent Concentrator Systems", Proc. 24th European PV Solar Energy Conference and Exhibition, Hamburg, Germany.
[33] Goldschmidt, J., Peters, M., Bosch, A., Helmers, H., Dimroth, F., Glunz, S., and Willke, G., (2009). "Increasing the efficiency of fluorescent solar concentrator systems", Solar Energy Materials and Solar Cells. 93, 2 176-182.
[34] Goldscmidt, J., Peters, M., Pronneke, L., Steidl, L., Zentel, R., Blasi, B., Gombert, A., Glunz, S., Willeke, G., and Rau, U., (2008). "Theoretical and experimental analysis of photonic structures for fluorescent concentrators with increased efficiencies" Physica Status Solidi, 205, 12, p2811-2821.
[35] Barnes, W., Dereux, A., Ebbesen, T., (2003). "Surface plasmons subwavelength optics", Nature, 424, p824-830.

[36] Calander, N., and Willander, M., (2002). “Theory of surface-plasmon resonance optical-field enhancement at prolate spheroids”, Journal of Applied Physics, 92, 4878.
[37] Chandra, S., Doran, J., McCormack, S., Kennedy, M., and Chatten, A., (2012).“Enhanced quantum dot emission for luminescent solar concentrators using plasmonic interaction”, Solar Energy and Materials & Solar Cells, 98, p385-390.
[38] Zhang, Y., Aslan, K., Previte, M., and Geddes, C., (2007). “Metal-enhanced fluorescence: Surface plasmons can radiate a fluorophore’s structured emission”, Applied Physics Letters, 90, 053107.
[39] Wang, SY., Borca-Tasciuc, D-A., Kaminski, D., (2011). “Spectral coupling of fluorescent solar concentrators to plasmonic solar cells”, Journal of Applied Physics, 109, 7, 074910.
[40] Wang, R., Wang, X., Zhou, Z., (2012). “Photocurrent enhancement in plasmonic solar cells attached to luminescent solar concentrators”, High and Low Concnetrator Systems for Solar Electric Applications VII, 8468, 84680B.
[41] Debije, M., and Verbunt, P., (2012). “Thirty Years of Luminescent Solar Concentrator Research: Solar energy for the Built Environment”, Advanced Energy Materials, 2, p12-35.
[42] Macqueen, R., Cheng, Y., Clady, R., and Schmidt, W., (2010).“Towards an aligned Luminophore Solar Concentrator”. Optics Express. 18 A161.
[43] Mulder, C., Reusswig, P., Velazquez, A., Rotschild, K., and Baldo, M., (2010). “Dye alignment in luminescent solar concentrators: I. Vertical alignment for improved waveguide coupling”, Optics Express, 18, 8, pA79-A90.
[44] Mulder, C., Reusswig, P., Beyler, A., Kim, H., Rotschild, K., and Baldo, M., (2010).. “Dye alignment in luminescent solar concentrators: II. Horiontal alignment for energy harvesting in linear polarizers”, Optics Express. 18, 9, pA91-A99.
[45] Verbunt, P., Kaiser, A., Hermans, K., Bastiaansen, C., Broer, D., Debije, M., (2009). “Controlling Light Emission in Luminescent Solar Concentrators Through use of Dye Molecules Aligned in a Planar Manner by Liquid Crystals”, Advanced Functional Materials, 19, 2714-2719.
[46] Verbunt, P., Bastiansen, C., Broer, D., and Debije., (2009). “The Effect of Dyes Aligned by Liquid Crystals on Luminescent Solar Concentrator Performance”, Proc. 24th European Photovoltaic Solar Energy Conference, p381-384, Hamburg, Germany.
[47] Bose, R., Farrell, D., Chatten, A., Pravettoni, M., Buchtemann, A., Quilitz, J., Fiore, A., Manna, L., and Barnham, K., (2008). “Luminescent Solar Concentrators: Nanorods and Raytrace Modeling”, Proc. 33rd IEEE Photovoltaics Specialists Conference, San Diego, California, USA.
[48] Zanella, M., Gomes, R., Pavia, M., Giannini, C., Zhang, Y., Riskin, A., Van Bael, M., Hens, Z., and Manna, L., (2011). “Self-Assembled Multilayers of Vertically Aligned Semiconductor Nanorods on Device-Scale Areas”. Advanced Materials. 23, 2205-2209.
[49] Thiemann, S., Gruber, M., Lokteva, I., Hirschmann, J., Halik, M., Zaumseil, J., (2013). “High-Mobility ZnO Nanorod Field-Effect Transistors by Self-Alignment and Electrolyte-Gating”, Applied Materials & Interfaces, 5, p1656-1662.
[50] Engel, M., Small, J., Steiner, M., Freitag, M., Green, A., Hersam, M., and Avouris, P., (2008). “Thin Film Nanotube Transistors Based on Self-Assembled, Aligned, Semiconducting Carbon Nanotube Arrays”, ACS Nano, 2, 12, p2445-2452.
[51] Singh, A., English, N., and Ryan, K., (2013). “Highly Ordered Nanorod Assemblies Extending over Device Scale Areas and in Controlled Multilayers by Electrophoretic Deposition”, Journal of Physical Chemistry, 117, p1608-1615.

[52]Zhou, M., Zhu, H., Wang, X., Xu, Y., Tao, Y., Hark, S., Xiao, X., and Li, Q., (2010)," Cdse Nanotube Arrays on ITO Via Aligned ZnO Nanorods Templating",Chemistry of Material Article, Advanced Functional Materials, 22 p64-69.
[53] Ryan, K., Mastroianni, A., Stancil, K., Liu, H., and Alivisatos, A., (2006), "Electric-Field-Assisted Assembly of Perpendicularly Oriented Nanorod Superlattices", Nano Letters, 6 7 1479-1482.
[54] Montali, A., Bastiaansen, C., Smith, P., and Weder, C., (1998)."Polarizing energy transfer in photoluminescent materials for display applications", Nature, 392, 6673, p261-264.
[55] Talapin, D., Koeppe, R., Gotzinger, S., Kornowski, A., Lupton, J., Rogach, A., Benson, O., Feldmnn, J., nd Weller, H., (2003)."Highly Emissive Colloidal CdSe/CdS Hetrostructures of Mixed Dimensionality", Nano Letters, 3, 12, P1677-1681.
[56] Goetzberger, A., And Gruebel, W., (1977), "Solar Energy Conversion with Fluorescent Collectors" Applied Physics. 14, p123-139.
[57] Argonne National Laboratory, "Physics Division Research Highlight: Luminescent solar concentrators",Us Department of Energy, Accessed on (14/10/2013). http://www.phy.anl.gov/research/Solar_concentrators.html
[58] Currie, M., Mapel, J., Heidel, T., Goffri, S., and Baldo, M., (2008) "High-efficiency Organic Solar Concentrators for Photovoltaics", Science, 321, p226-228,.
[59] Drake, J., Lesiecki, M., Sansregret, J., and Thomas, W., (1982). "Organic dyes in PMMA in a planar luminescent solar collector: a performance evaluation", Applied Optics, 21, 16, p2945-2952.
[60] Helms, V., (2008). "Principles of Computational Cell biology: From Protein Complexes to Cellular Networks", published by Wiley-VCH, p202.
[61] Swartz, B., Cole, T., and Zewail, A., (1977). "Photon trapping and energy transfer in multiple-dye plastic matrices: an efficient energy concentrator", Optics Letters, 1, 2, p73-75.
[62] Richards, B., and McIntosh, K., (2006). "Ray-Tracing Simulations of Luminescent Solar Concentrators Containing Multiple Luminescent Species", Proc. 21st European Photovoltaic Solar Energy Conference, Dresden, Germany.
[63] Burgers, A., Sloof, L., Buchtemann, A., Roosmalen, J., (2006). "Performance of Single Layer Luminescent Concentrators with Multiple dyes", proc. IEEE 4th World Conference on Photovoltaic Energy Conversion, Hawaii, USA, p198-201.
[64] Swartz, B., Cole, T., and Zewail, A., (1977). "Photon trapping and energy transfer in multiple-dye plastic matrices: an efficient solar-energy concentrator", Optics Letters, 1, 2, p73-75.
[65] Fox, M. (2001). Optical Properties of Solids. New York: Oxford University Press Inc.
[66] Inzelt, G., & Scholz, F., (2008). "Conducting Polymers: A New Era in Electrochemistry", Springer-Verlag. Berlin, Heidelberg, P 2.
[67] Barford, W., (2005). "Electronic and optical Properties of Conjugated Polymers", Oxford Science Publications. Oxford University Press, P 1.
[68] Jeong, E., Kim, S-H., Jung, I-H., Xia, Y., Lee, K., Suh, H., Shim, H-K., and Woo, H-Y., (2009). "Synthesis and Characterization of Indeno[1,2-b]fluorene-Based White Light-Emitting Copolymer". Journal of Polymer Science Part A: Polymer Chemistry. 47, 14, 3467-3479.
[69] Kim, J., Kim, S-H., Jung, I-H., Jeong, E., Xia, Y., Cho, S., Hwang, I-W., Lee, K., Suh, H., Shim, H-K., and Woo, H-Y., (2010). "Synthesis and characterization of indeno[1,2-b]fluorene-based low bandgap copolymers for photovoltaic cells". Journal of Materials Chemistry, 20, 8, p1577-1586.

[70] Sholin, V., Olsen, J., and Carter, S., (2007). "Semiconducting polymers and quantum dots in luminescent solar concentrators for solar energy harvesting", Journal of Applied Physics, 101, 123114.
[71] Batchelder, J., Zewail, A., and Cole, T., (1981). "Luminescent solar concentrators. 2 : Experimental and theoretical analysis of their possible efficiencies", Applied Optics, 20, 21. P3733-3754.
[72] Seybold, G., and Wagenblast, G., (1989). "New Perylene and Violanthrone Dyes Stuffs for Fluorescent Collectors", Dyes and Pigments, 11, p303-317.
[73] Wilson, L., and Richards, B., (2009). "Measurement method for photoluminescent quantum yields of fluorescent organic dyes in polymethyl methacrylate for luminescent solar concentrators", Applied Optics, 48, 2.
[74] Sloof, L., Budel, T., Burgers, A., Bakker, N., Buchtemann, A., Danz, R., Meyer, T., Meyer, A., (2007). "The Luminescent Concentrator: Stability Issues", Proc. 22nd European Photovoltaic Solar Energy Conference, Milan, Italy.
[75] BASF, "Lumogen F: Technical Information", Accessed on (29/10/2013), www2.basf.us/additives/pdfs/p3201e.pdf
[76] Gantt, E., (1981)."Phycobilisomes". Annual Review Plant Physiol. 32, p327-34.
[77] MacColl, R., (1998). "Cyanobacterial Phycobilisomes". Journal of Structural Biology. 124, p311-334.
[78] Mulder C., Theogarajan, L., Currie, M., Mapel, J., Baldo, M., Vaughn, M., Willard, P., Bruce, B., Moss, M., McLain, C., and Morseman, J., (2009). "Luminescent Solar Concentrators Employing Phycobilisomes", Advanced Materials, 21, 1.
[79] Grabowski, J, and Gantt, E., (1978). "Excitation-Energy Migration in Phycobilisomes – comparison of experimental Results and Theortical Predictions" Photochemistry and Photobiology, 28, 1, p47-54.
[80] González, M., Bose, R., Fisher, M., Farrell, D., Chatten, A., Morseman, J., Moss, M., McLain, C., Buchtemann, A., Jenkins, P., and Walters, R., (2010)., "Bio-derived Luminescent Solar Concentrators Using Phycobilisomes" , WCPEC-5, Valencia, Spain.
[81] Fisher, M., Ippen, C., Farrell, D., Walters, R., González, M., Trautz, K., Tischler, J., Morseman, J., and Chatten, A.,. (2012). "Flexible Luminescent Solar Concentrators Utilizing Bio-derived Tandem fluorophores", Proc. 38th IEEE Photovoltaic Specialists Conference, (Austin, USA), P3333-3338.
[82] Xia, Y., Xiong, Y., Byungkwon, L., and Skrabalak, S., (2009), "Shape-Controlled Synthesis of Metal Nanocrystals: Simple Chemistry Meets Complex Physics", Angew Int. Ed. 48, 1, p60-103.
[83] Reiss, P., Protiere and Li L., (2009),"Core/Shell Semiconductor Nanocrystals", Small, 5, 2, p154-168.
[84] Kim, S., Fisher, B., Eisler, H-J., and Bawendi, M., (2003), "Type-II Quantum Dots: CdTe/CdSe(Core/Shell) and CdSe/ZnTe(Core/Shell) Heterostructures", American Chemical Society, 125, 38, p11466-11467.
[85] Krahne, R., Morello, G., Firguerola, A., George, C., Deka, S., and Manna, L., (2011). "Physical properties of elongated inorganic nanoparticles" Physics Reports-review Section of Physics Letters, 501, 3-5, p75-221.
[86] Barnham, K., Marques, J-L., Hassard, J., and O'Brien, P., (200). "Quantum-dot concentrator and thermodynamic model for the global redshift". Applied Physics Letters. 76, 1197.
[87] Alivisatos, A., (1998), "Electrical Studies of Semiconductor-Nanocrystal Colloids", MRS Bulletin,.

[88] Chatten, A. J., Barnham, K., Buxton, B., Ekins-Daukes, N., and Malik, M., (2003). “The Quantum Dot Concentrator: Theory and Results”. 3rd World Conference on Photovoltaic Energy Conversion., Osaka, Japan.
[89] Carbone, L., Nobile, C., De Giorgi, M., Sala, F., Morello, G., Pompa, P., Hytch, M., Snoeck, E., Fiore, A., Franchini, I., Nadasan, M., Silvestre, A., Chiodo, L., Kudera, S., Cingolani, R., Krahne, R., and Manna, L., (2007). “Synthesis and Micrometer-Scale Assembly of Colloidal CdSe/CdS Nanorods Prepared by a Seeded Growth Approach”. Nano Letters. 7, 10, 2942-2950.
[90] Bose, R., Farrell, D., Chatten, A., Pravettoni, M., Buechtemann, A., Quilitz, J., Fiore, A., Manna, L., Nelson, J., Alivisatos, P., and Barnham, K., (2008). "The Effect of Size and Dopant Concentration on the Performance of Nanorod Luminescent Solar Concentrators" in Proceedings of the 23rd European Photovoltaic Solar Energy Conference, G. Willeke, H. Ossenbrink, P. Helm, eds. (WIP-Renewable Energies, Munich, Germany), pp. 552-555.
[91] Bose, R., Chatten, A., Pravettoni, M., Buchtemann, A., Quilitz, J., Fiore, A., Manna, L., and Barnham, K., (2008). “Luminescent Solar Concentrators: Nanorods and Raytrace Modelling” Proc. 33rd IEEE Photovoltaic Specialists Conference.
[92] Humphries, M., (2010). “Rare Earth Elements: The Global Supply Chain” Congressional Research Service.
[93] Livergood, R., (2010), “Rare Earth Elements: A Wrench in the Supply Chain”. Centre for Strategic and International Studies.
[94] Bradsher, K., (29/10/2010). “After China’s Rare Earth Embargo, a New Calculus”. The New York Times. http://www.nytimes.com/2010/10/30/business/global/30rare.html?_r=1
[95] Moudam, O., Rowan, B., Alamiry, M., Richardson, P., Richards, B., Jones, A., and Robertson, N., (2009). “Europium Complexes with High Total Photoluminescence Quantum Yields in Solution and in PMMA” Chemistry Communication. 6649-6651.
[96] Yang, Y., Li, J., Liu, X., Zhang, S., Driessen, K., Nockemann, P., and Binnemans, K., (2008). “Listening to Lanthanide Complexes: Determination of the Intrinsic Luminescence Quantum Yield by Nonradiaitve Relaxation”. ChemPhysChem. 9, 4 600-606.
[97] Wang, T., Zhang, J., Ma, W., Luo, Y., Wang, L., Hu, Z., Wu, W., Wang, X., Zou, G., and Zhang, Q., (2011). “Luminescent solar concentrator employing rare earth complex with zero self-absorption loss”. 85, 11, P2571-2579.

Chapter 4

Experimental, Fabrication & Computational Methodologies

4.1 Introduction

The majority of the work described in this thesis has been experimental in nature, and therefore, in this chapter, detailed descriptions of the methodologies for experiments commonly performed throughout the course of this study are provided. Unique experiments are described as required in the relevant sections of the results chapters. This chapter also gives detailed descriptions of the sample fabrication methods employed during this work; from the preparation of luminescent dye solutions, to the application of doped thin-films to substrates. Samples made for the author by collaborators or unique sample fabrication methods are again described in the relevant results chapters. Finally, an overview of the PVtrace raytrace program (written by former group member Dr Daniel Farrell) used to perform computational simulations during the course of this thesis is given, as well as a description of how different input parameters can be introduced to the program.

4.2 The Solar Simulator Spectrum

During this work the Steuernagel Lichttechnik solar simulator is used as an incident light source for many of the experiments performed, therefore, some explanation of the solar simulator light source is needed. The lamp used in this solar simulator was a metal halide HMI 575W/SEL XS.

Since the Ocean Optics USB2000 used to measure the solar simulator spectrum uses a silicon CCD array to detect incident photons. The manufacturer describes the useful range of this

spectrometer as being up to 1000nm [1]. At wavelengths close to the bandgap of silicon (~1100nm) there is significantly more noise associated with the spectrum being measured, and it is for this reason that the solar simulator spectrum in Figure 4-1, has been cut-off at ~1050nm, as beyond this point there is very high noise, with the flux oscillating between positive and negative intensities.

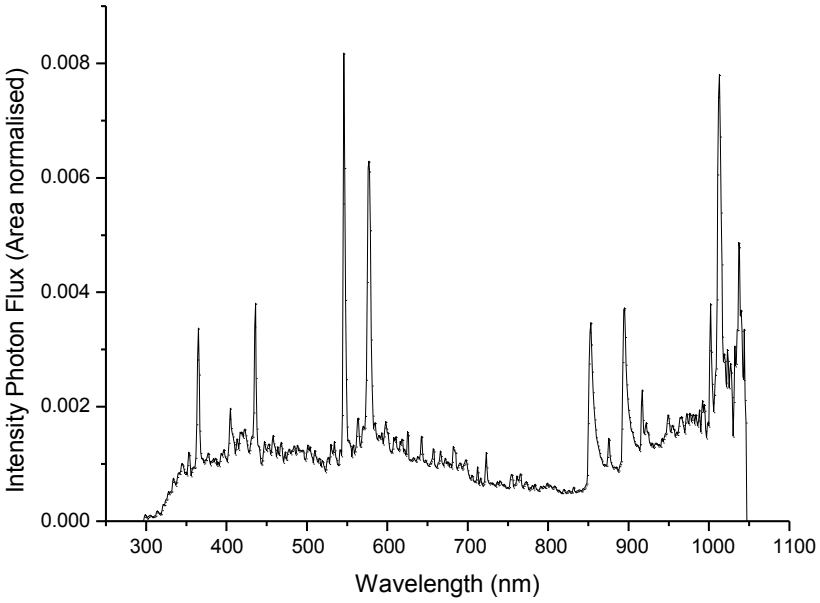


Figure 4-1Steuernagel Lichttechnik solar simulator spectrum (no UV filter).

The reason for the rising measured intensity between ~850nm and ~1050nm., is likely due the age solar simulators lamp, which apparently needed to be replaced during the writing up time of this thesis (after the author had finished all experiments). However, since this is the same spectrum used for the experimental and computational results, the rising of intensity is of less importance than the ~1050nm cut-off point. As a result of this cut-off, the solar simulator spectrum used in simulations (see section 4.14) is shorter than the actual spectrum used in the optical efficiency experiments (see section 4.9). This meant that simulations

artificially limit the range of the incident wavelengths possible for incident photons. However, this shortening of the solar simulator spectrum is unlikely to have greatly affected the optical efficiency of simulated results. This is because the incident and edge emitted photon flux is also measured by a silicon photodetector, in this case a silicon solar cell, which itself will not be able to absorb photons beyond ~1100nm.

Ultimately, because of the reasons stated above, any direct comparison between simulated and measured optical efficiency's will have some inaccuracy since the simulated data will most likely have slightly higher optical efficiencies due to the artificial shortening of the incident solar simulator spectrum.

4.3 Experimental Methods

This section of the chapter outlines the experimental methodologies which were commonly utilised to characterise the various LSC samples, solar cells and photoelectrochemical cells (PEC) cells featured in the following results chapters of this thesis.

4.4 Transmission/Absorption

The following section describes the experimental methods used for measuring the transmission of light through LSC samples (and how the transmission was converted into absorptivity and/or absorption coefficient). Conversion of transmission to absorptivity or absorption coefficient is important as it reveals the quantity of light the LSC is able to absorb, and at what wavelengths.

4.4.1 Transmission Measurements Using UV-Vis

During this study two different experimental setups were used to perform transmission measurements, the first method used a Shimadzu UV-2550 UV-Vis spectrometer, which includes a collimated monochromatic beam passed through a diffraction grating (1200 lines/mm) to produce a continuous spectrum of wavelengths. This UV-Vis system provides

high quality, low noise transmittance spectra. However, it has a sample chamber with a limited size, and the photodetector sensitivity is low. As a result the UV-Vis is limited to being used with small samples (~5cm by 5cm), and lower optical density (~1) samples. A sample is placed inside the UV-Vis between the light source (the light source consists of a 50Wdeuterium lamp between 190nm-350nm and halogen lamp between 330nm-1100nm), and 2 photodetectors (photomultiplier R-928). As the beam of light is scanned over a pre-set range of wavelengths, the luminescent species within the sample may absorb specific wavelengths, depending on whether the absorption spectrum of the sample falls within the range of the spectrometers light source, and if the sample's optical density is sufficiently high.

The UV-Vis sample chamber consists of a sample holder and a reference holder (see Figure 4-2), and the incident beam is split using a beam splitter. The reference holder was always left empty during this work, taking the chamber air as a reference media; all samples and additional references (such as substrates) were placed in the sample holder. All measurements performed using this equipment were for light transmission through the sample. It is possible to set this system to measure in terms of absorptivity but transmission allows more freedom in later processing of the results.

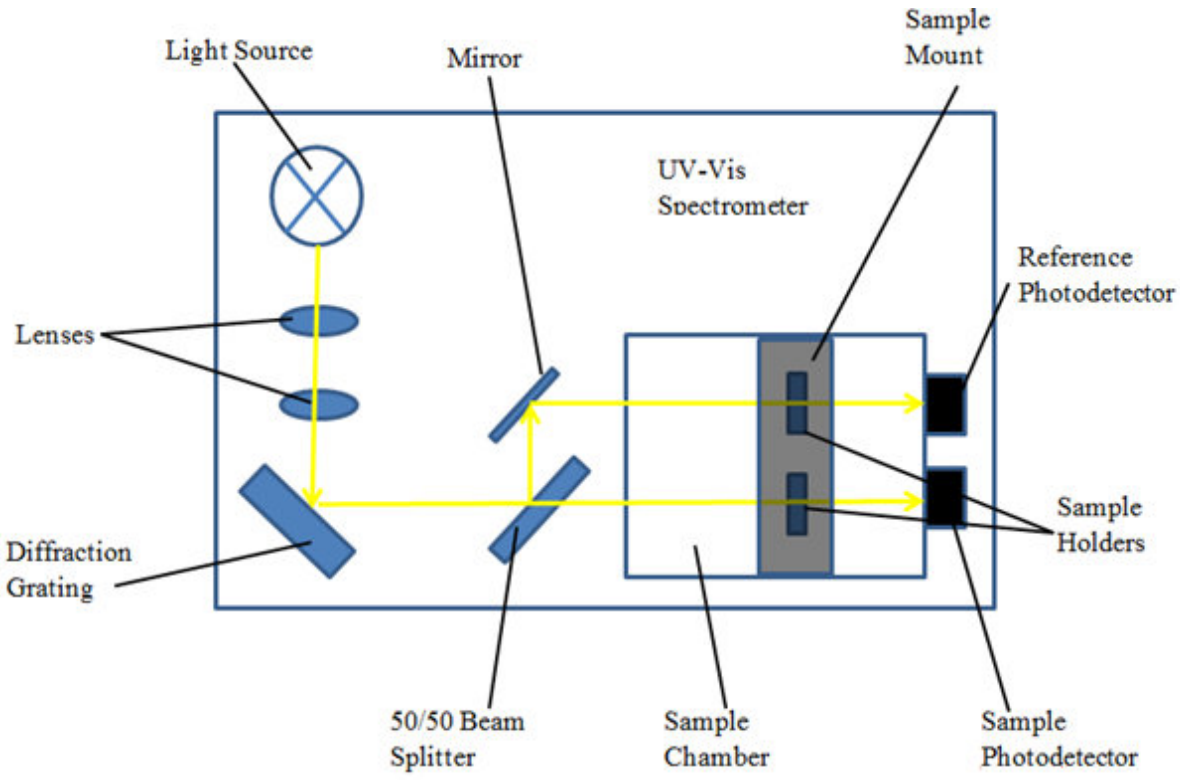


Figure 4-2 Top-down view of a transmission measurement performed using a UV-Vis spectrometer.

In addition to the sample being measured, appropriate reference measurements are also required. In all experiments, a baseline (background) measurement is performed first, which is effectively an air reference (where both the sample mount and reference mount are empty), and after this a substrate/matrix material reference was taken. If a thin-film sample was being used this means using a substrate which had identical properties to the substrate used for the LSC sample, i.e. matching material and dimensions. It was also necessary to apply a thin-film of the matrix material to the substrate, minus the luminescent material, and match thickness of this film to that of the LSC sample being tested. By correcting for the reference transmission measurements it was possible to process out much of the background absorption, due to the substrate and matrix materials, and to remove much of the surface reflection and scattering loses. By using equations 2.11 and 2.13, in chapter 2, the

transmission and absorptivity for the LSC sample and the reference material(s) could be determined and absorptivity of the substrate and matrix material could be removed from the LSC sample, leaving just the absorptivity due to the luminescent species. This could then be used for raytrace simulations (see section 4.14).

For some luminescent materials it was useful to measure their spectral properties whilst they were dissolved in an appropriate solvent, (since matrix materials may affect the spectral properties of the luminescent material) within a cuvette transparent to the desired wavelengths. References were taken in the same way as mentioned above for thin-film samples, but instead of coating a substrate in matrix material, it was necessary instead to take a reference of the cuvette filled with the solvent alone.

4.4.2 Transmission Measurements Utilising an Ocean Optics Fibre Spectrometer

An alternative method used in this thesis for measuring the transmission spectrum of an LSC sample, used an optics bench set up including a Steuernagel Lichttechnik solar simulator (ses section 4.2), and an Ocean Optics USB2000 fibre spectrometer (OOS) used to detect the light transmitted through the sample. This experimental method was often used when the optical density of the LSC sample(s) being measured was too high for the UV-Vis spectrometer described in the section above. However, due to the OOS having a silicon CCD array detector, the transmissions measurements tended to have a noisier signal, when compared to the UV-Vis spectrometer mention in section 4.4.1, which has a photomultiplier tube as a photodetector.

Optics posts were used to mount LSC samples with horizontal orientation, underneath the solar simulator aperture. Below the sample an optical fibre with a 200µm aperture, which was connected at the opposite end to the OOS, was clamped in place facing the solar simulator's aperture, with the LSC sample positioned in-between (see Figure 4-3). Prior to performing

measurements the OOS was calibrated using the accompanying Spectrasuite software, subsequently providing a calibrated spectrum in units of power (μW/cm/nm). The calibration is performed by setting up the apparatus as shown in Figure 4-3 only, with the LSC sample removed and then by running the calibration option in the Spectrasuite software. Specifically, the calibration process makes use of a calibration file which allows the measured signal to accurately correspond with actual wavelengths of the light being measured. Additionally, the calibration process has a signal optimisation component which takes into account the aperture size of the OOS fibre, it varies the integration time to prevent signal saturation (it is possible to adjust this manually), it subtracts a dark (background signal) from the recorded count and converts from photon count to units of power. By making this calibration when the incident spectrum is maximised, it was ensured that the subsequent measurements were accurate (i.e. were not saturated).

Two measurements were performed during a transmission measurement, the first was taken with the sample in place (see Figure 4-3), allowing the OOS to collect the photons which are not absorbed, reflected or scattered by the sample and which instead are transmitted through it, identified by the intensity (I). A second measurement was then performed by removing the sample, and measuring the intensity of the light without the sample blocking the fibre aperture, identified as the incident intensity (I_0). It is from these two measurements that wavelength dependent transmission can be ascertained (see equation 2.11, chapter 2). By using the transmission measured for the LSC sample, it is possible to calculate both the absorption coefficient (which also requires the thin-film/LSC thickness) and the absorptivity (which requires knowledge of the reflectivity and surface scattering of the sample).

As described above in section 4.4.1 for transmission measurements performed using a UV-Vis spectrometer, it was again necessary to take reference measurements for the substrate and matrix material (without the luminescent species being present) with dimensions and

materials matching those of the LSC sample. By correcting for the reference transmission measurements, it was possible to process out much of the background absorption due to the substrate and matrix materials, and to remove much of the surface reflection and scattering loses.

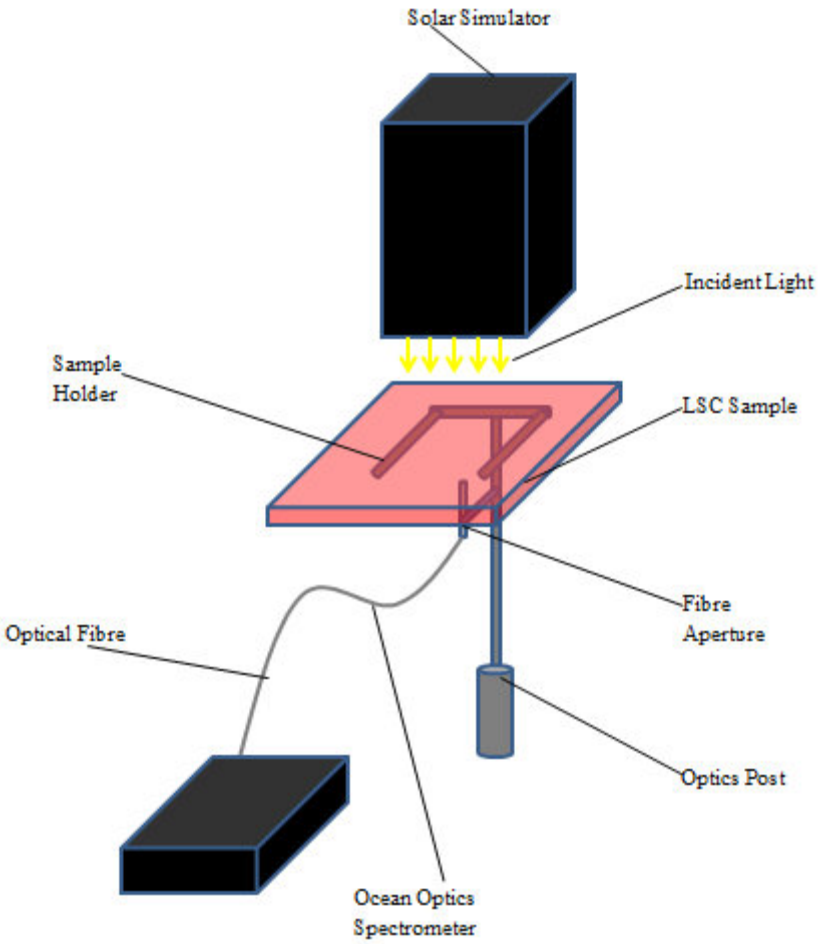


Figure 4-3 Diagram of experimental setup for a transmission measurement using an Ocean Optic spectrometer and a solar simulator light source.

4.5 Photoluminescence Measurements

This section identifies and explains the importance of the two different methods used to measure photoluminescent (PL) emission from LSC samples. Top surface PL emission and edge PL emission were measured. PL measurements are essential as they provide valuable

spectral information about the luminescent species, such as the range and energy of the emission. When shown in conjunction with absorptivity measurements (or by comparing the amount of red-shifting of the edge emission spectrum when compared to the top surface PL measurements), they reveal the quantity of spectral overlap which provides information regarding the probability of reabsorption losses (see section 2.6.4, chapter 2). Edge PL measurements are also vital for determining how much light is being emitted from the LSC's edges, in terms of optical efficiency or power (see sections 4.9 and 4.10)

4.5.1 Top Surface Emission Measurements (Fluoromax)

Top surface emission measurements were performed using a Horiba Jobin Yvon Fluoromax 3. The Fluoromax consists of a 150W Ozone-free xenon arc lamp light source, focusing optics, a diffraction grating (1200 groves per mm) allowing discrete wavelengths to be separated from the light source spectrum, a sample chamber and an R928P photon counting photomultiplier tube (185nm to 850nm) for photon detection [2].

An LSC sample was fixed inside a rotating sample mount within the sample chamber at a 60° angle to the incident beam as shown in Figure 4-4. The sample chamber provides an upper limit for the size of the sample of approximately 10cm by 10cm by 0.5cm. Although the sample can be positioned at different angles with respect to the incident beam, 60° was chosen as it allows a large quantity of the top surface emission photons to be collected by the photodetector, without reflecting the incident beam into the photodetector, as would be the case at angles close to 45°. All top surface measurements featured in the results chapters of this thesis were taken at a 60° angle, thus allowing for some level of comparison between samples, and allowing some repeatability to measurements.

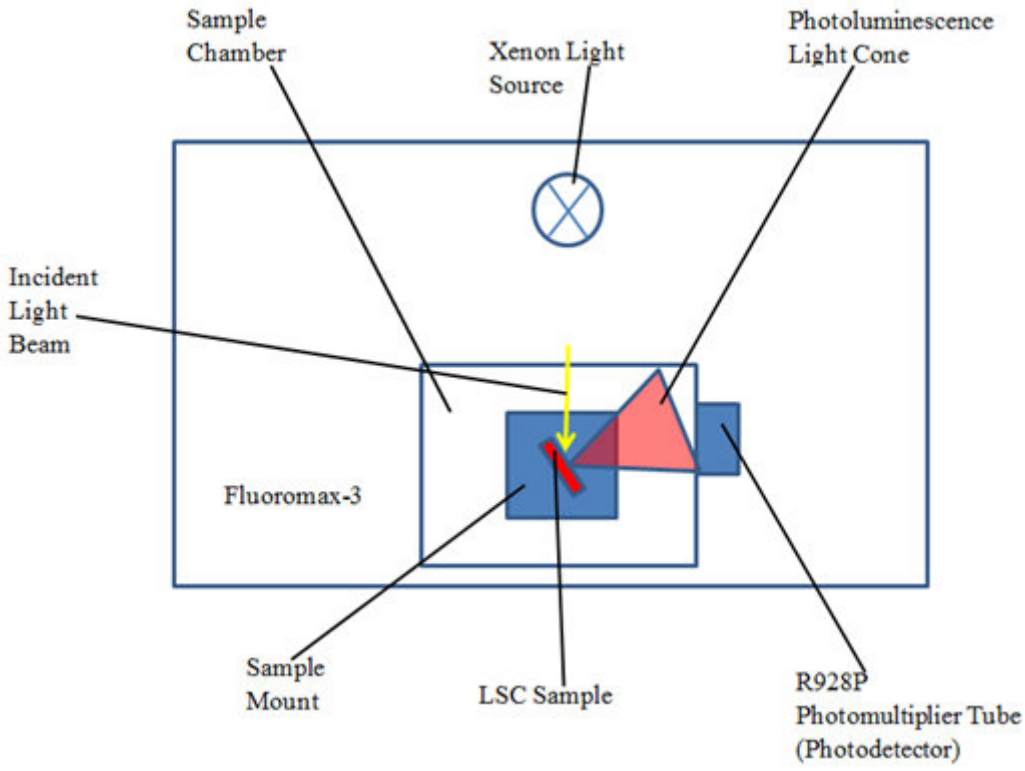


Figure 4-4 Top-down view of top surface emission measurement inside a fluoromax 3 system.

The accompanying software was set to performing an emission acquisition, for which a scan range, step size (for the scan range), integration time, excitation wavelength, entrance and exit slit width were set. Generally, the slits were both set to 1nm (as this provided good resolution and a reasonably high incident light signal), the integration time was set to half a second (allowing sufficient time to produce a low noise signal) and the step size to 1nm. Taken together these settings usually provided for a good signal to noise ratio. The scan range entered varied from sample to sample, and for top surface emission measurements, it was set to encompass the complete emission spectrum of the sample (or where the emission spectrum was expected, if the emission range was unknown). Likewise, the excitation wavelength also varied between samples as it was often desirable to set the excitation wavelength to match that of the absorption peak(s) found from the transmittance data obtained for the sample (see

section 4.4.1), as this will produce high intensity emission peaks. However, there are times when it is useful to excite the sample away from the absorption peak(s), e.g. to determine the emission intensity for different parts of the absorption spectrum which relate to individual components within the luminescent species.

The intensity of the top surface emission spectra were measured in units of counts per second. It is important to have top surface emission spectra (and in terms of photon flux) for use in raytrace simulations (see section 4.14.1), as very little of the top surface emission has been lost due to reabsorption (see section 2.6.4, chapter 2). Top surface emission measurements are the result of a localised point on the top surface of the LSC sample being excited, and therefore re-absorption loses are kept to a minimum, meaning there is negligible red-shifting of the collected emission spectrum. Having these "fundamental" non red-shifted emission spectra allows for more realistic simulations to be performed.

4.5.2 Edge Emission Measurements (Using Ocean Optics Fibre Spectrometer)

Edge emission measurements were performed using a Steuernagel Lichttechnik solar simulator, and an optics bench setup similar to the one used for the optics bench mounted transmittance measurements (see Figure 4-3, section 4.4.2). The sample was again mounted horizontally beneath the solar simulator, while the optical fibre aperture (connected to the OOS) was coupled to one of the narrow edges of the LSC sample as shown in Figure 4-5. The Spectrasuite software which accompanies the OOS, was calibrated (see calibration and signal optimisation in section 4.4.2) to measure the low signal intensity from the edge emission of the sample. For this experiment calibration of the OOS was performed by coupling the OOS fibre to the edge of interest on the LSC sample, inputting this data to the Spectrasuite software, to give the emission in units of power. However, it does not give the absolute power of the emission, it is more accurate to say that it gives the proportional power over the emission spectrum, due to the limited angular acceptance of the 200μm fibre

aperture. Essentially, the conversion to power units is a by-product of the calibration and optimisation process. After calibration, the edge emission spectrum was measured. Since the emission was from the edge of the sample, there was often considerable spectral red-shifting when compared to the top surface emission spectrum.

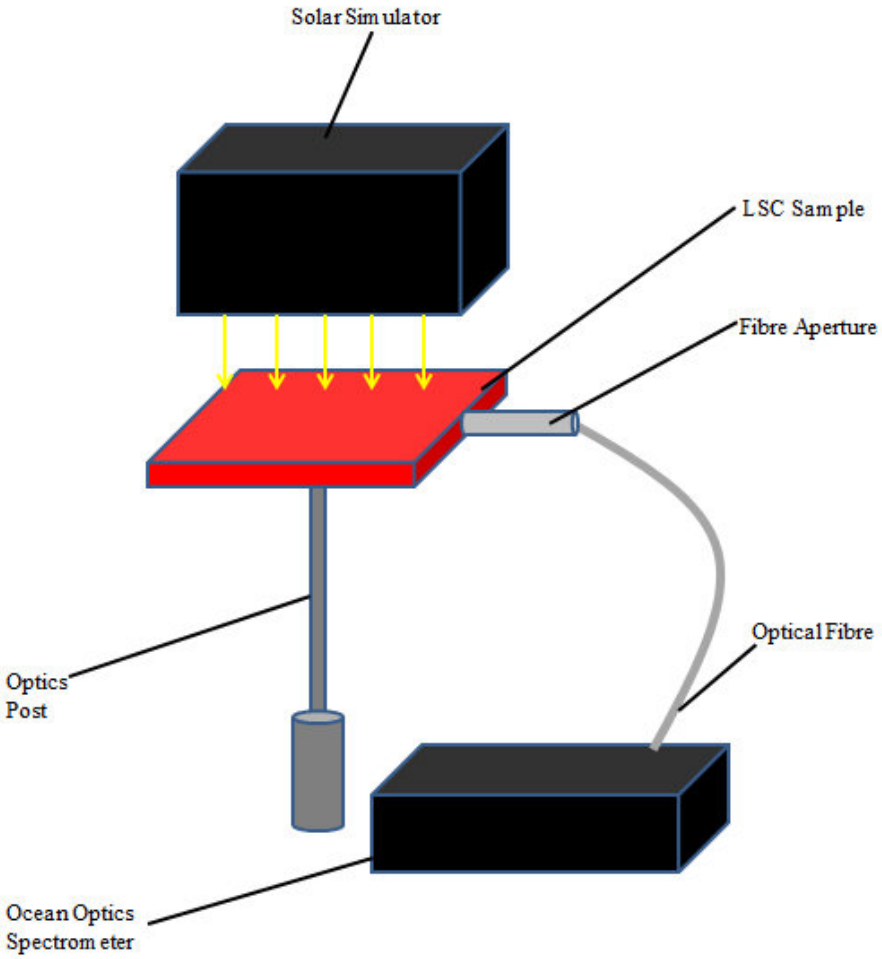


Figure 4-5 Diagram of the edge emission PL setup, utilising an Ocean Optics fibre spectrometer and a solar simulator light source.

4.6 Photoluminescent Efficiency (PLE)

PLE measurements were again performed using a Horiba Jobin Yvon Fluoromax 3, as described in section 4.5.1. PLE measurements are used to detect PL emission intensity (in terms of photon flux) at a specific emission wavelength. The emission wavelength chosen is

often a position of interest on the LSC sample's emission spectrum, for example the wavelength of peak emission intensity. Concurrently, the software is set to scan an excitation beam onto the surface of the sample with a specific range set by the experimenter (usually chosen to encompass the absorption spectral range of the luminescent species used within the LSC). As the diffraction grating inside the Fluoromax 3 system moves to produce the wavelengths in this pre-set range, the emission intensity at the emission wavelength of interest, which was previously set (see above) varies. If the LQY does not vary with excitation wavelength this effectively produces an absorption spectrum as the PL emission intensity at the chosen wavelength is directly proportional to the absorptivity.

PLE measurements can be useful in determining the absorption spectrum of a sample which has low light transmission, which would otherwise be problematic to measure using transmission measurement experiments. PLE can also be used to compare the relative luminescent efficiency of a sample by comparing the PLE spectrum to the absorption spectrum of the sample measured using a transmission experiment (see section 4.4.1). If the relative peak heights differ in these two spectra then the way that the LQY varies with wavelength can be deduced.

To run a PLE scan, a sample is placed inside the Fluoromax-3 sample chamber, and mounted on the rotating sample mount at a 60° angle to the incident beam (see Figure 4-4 for top surface emission measurements), and the chamber is then closed. Using the accompanying software, the experiment type is set to emission acquisition, a scan range, step size, integration time and slit size is then set and the scan is then collected (further details can be found in section 4.5.1).

4.7 Luminescent Quantum Yield (LQY)

Luminescent quantum yield (LQY) measurements are used to determine how efficient the radiative emission is for a given luminescent species (see chapter 2 section 2.6.2 on LQY).

The primary method used to measure LQY in this work is the method outlined by De Mello [3]. This method makes use of a PTFE integrating sphere as shown in Figure 4-6, which due to its dimensions, limits an LSC sample for testing to approximately 25mm by 25mm by 1mm in size. The integrating sphere was used inside the sample chamber of a Horiba Jobin Yvon Fluoromax 3 (see sections 4.5.1 and 4.6 for further details), and it was substituted for the LSC sample and sample mount seen in Figure 4-4.

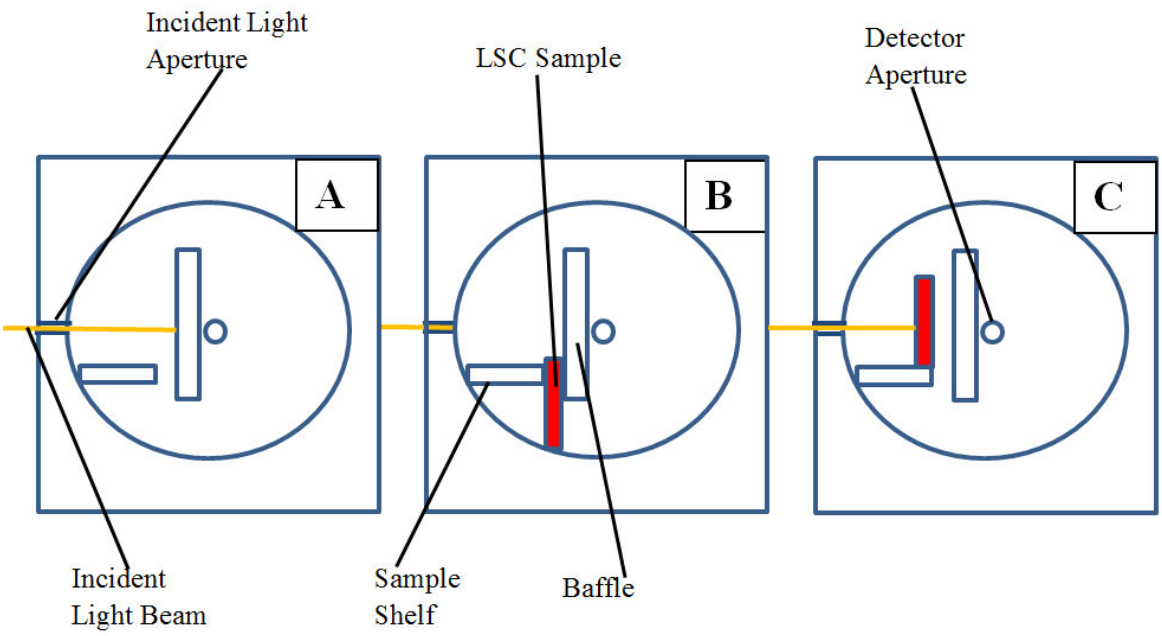


Figure 4-6 Diagram showing side-view cross sections of the integrating sphere used in the LQY experiments. A) Corresponds to experiment A with no LSC sample B) Illustrates experiment B with the incident light beam indirectly illuminating the sample. C) Corresponds to experiment C where the incident light is targeted directly onto the sample.

There were 3 parts to the LQY experimental method, the first part, experiment A, was to place the empty integrating sphere inside the Fluoromax sample chamber, and setting the

accompanying software in the same way as described in the top surface emission method (see section 4.5.1). However, this time the acquisition range must be set to include the excitation peak, as well as the emission peak. This first measurement does not have an emission spectrum since it was performed without an LSC sample (see Figure 4-6A), but it does allow for the total incident number of photons to be calculated by integration.

The second experiment, experiment B, was performed in the way same as for experiment A, but on this occasion the LSC sample to be measured was placed inside the integration sphere in a position so as to avoid direct contact with the incident beam (see Figure 4-6B). This measurement has a limited emission peak, and is used to determine the scattering loses which result from having the sample in the integrating sphere, on this occasion the areas under both the excitation peak and emission spectrum are determined by integration.

The third experiment, experiment C was performed with the sample positioned inside the integrating sphere directly in front of the entrance aperture (see Figure 4-6C), exposing the sample directly to the incident beam and allowing for the greatest emission intensity of the three experiments. The three experiments produce three graphs (see Figure 4-7 to Figure 4-9), and from these three graphs the areas under the 5 curves, incident light peak A ,L_A, incident light peak B ,L_B, incident light peak C ,L_C, emission peak B ,P_B,, and emission peak C ,P_C, were integrated in terms of counts per second. Prior to integration, the data in the three graphs was multiplied by a correction factor (measured by Dr Colin Belton [4]) which takes the wavelength dependent reflection of the integrating sphere into account.

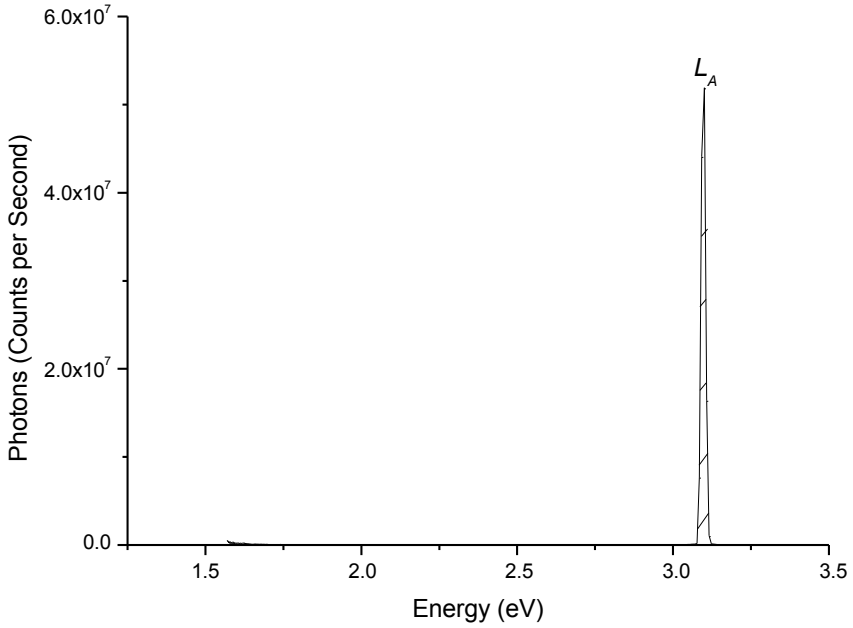


Figure 4-7 Plot of the excitation peak, L_A, used to stimulate photoluminescence in an LSC sample. This graph corresponds to experiment A

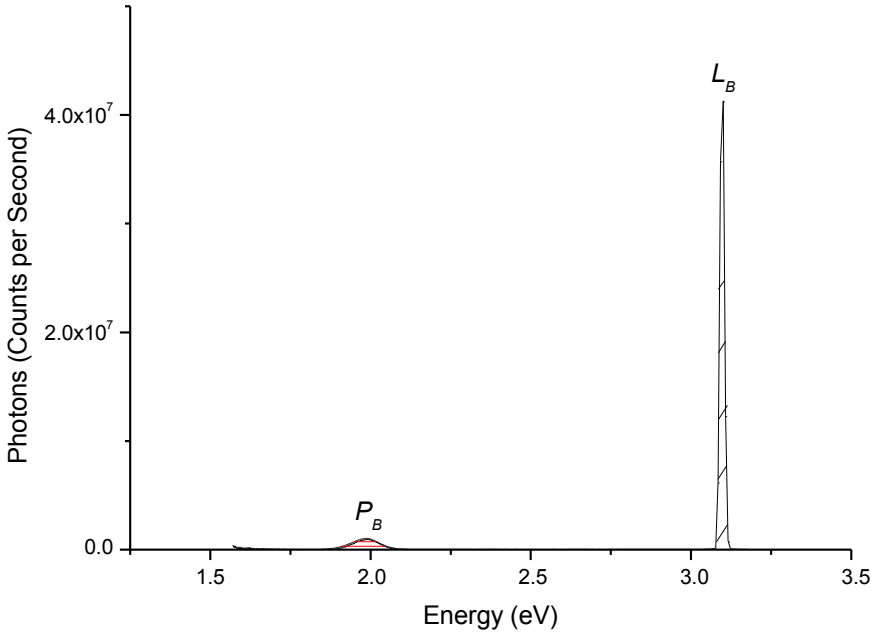


Figure 4-8 Plot of the excitation, L_B, and emission peaks, P_B, of an LSC for experiment B (indirect sample illumination).

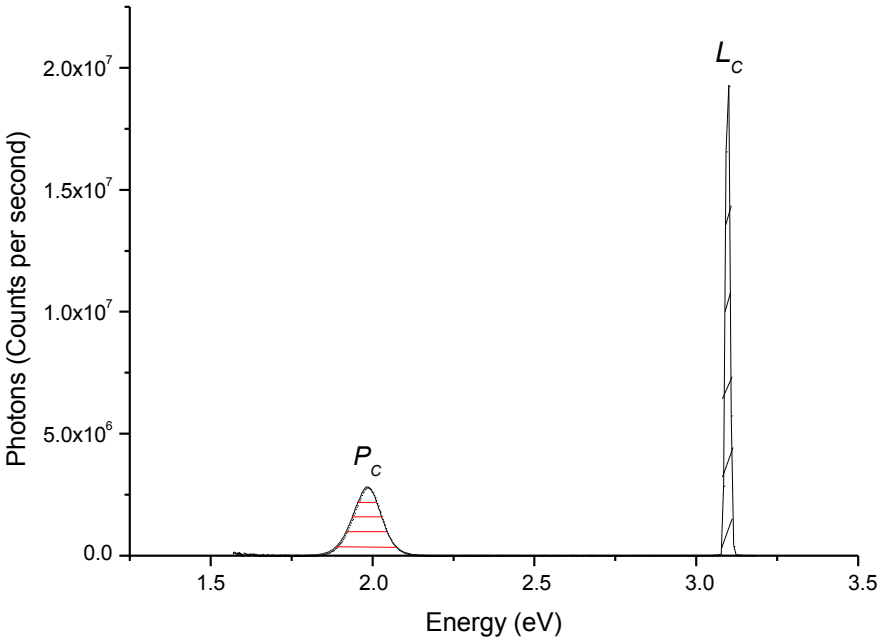


Figure 4-9 Plot of the excitation, L_C, and emission peaks, P_C, of an LSC for experiment C (direct sample illumination).

The following equations were used to determine the LQY of the sample (using integrated data from Figure 4-7 to Figure 4-9), equation 4.1 was used to ascertain the absorptivity, A, of the sample, and equation 4.2 was used to calculate the LQY percentage efficiency, η, of the sample.

$$A = \left(1 - \frac{L_C}{L_B}\right) \qquad 4.1$$

$$\eta = \left(\frac{P_C - (1 - A)P_B}{L_A A}\right) x100 \qquad 4.2$$

4.8 External Quantum Efficiency (EQE)

External quantum efficiency, EQE measurements are taken for solar cells to determine (per wavelength), the ratio of charge carriers extracted over the total number of photons incident on the solar cell (see equation 4.3). A description of EQE can be found in section 2.9.3, chapter 2, it is important to note that knowledge of the solar cells EQE is necessary when calculating the optical efficiency of an LSC sample. This is because the proportion of edge emitted photons from the LSC converted to charge by the attached solar cell is determined by the solar cells EQE (see section 4.9). The measurements were performed using an optics bench setup which makes use of a 100W halogen lamp, an optical chopper, a Bentham TMc300 monochromator, a digital lock-in amplifier, optics (fibre couple) and a Newport 818 UV Si photodetector as shown in Figure 4-10.

$$EQE(\%) = \frac{N_q}{P_{Tot}} x100 \qquad 4.3$$

where N_q is the total number of charge carriers and P_{Tot} is the total number of incident photons on the surface of the solar cell.

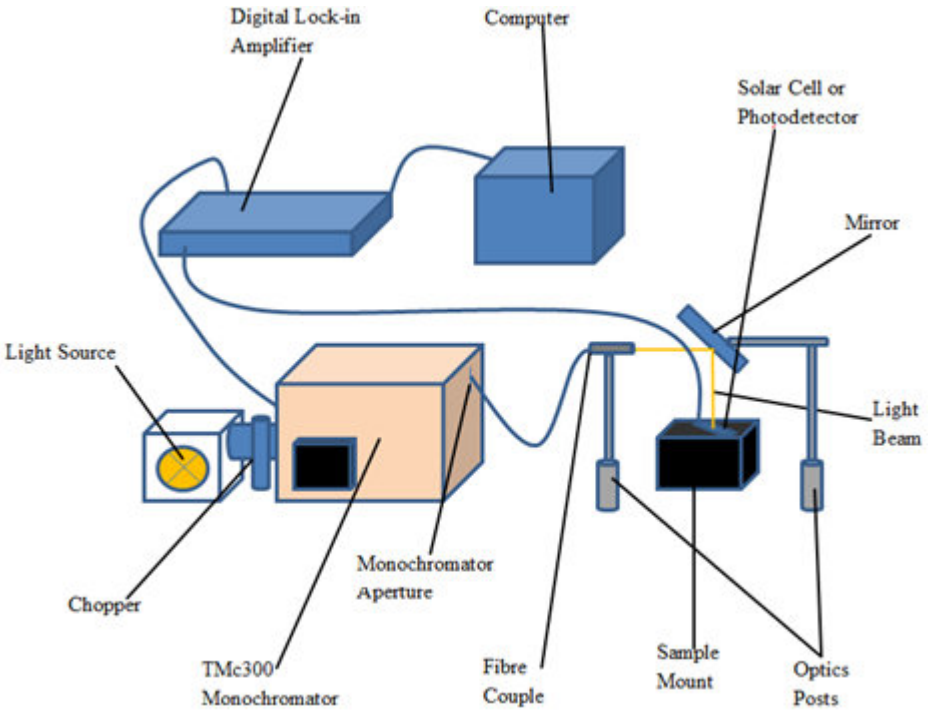


Figure 4-10 Diagram of the EQE experimental setup. The photodetetector and solar cell are interchangeable depending on whether a reference or a measurement are being taken respectively.

As can be seen in Figure 4-10, the light from the halogen lamp enters the monochromator after being chopped by an optical chopper to a frequency which avoids sources of noise in the laboratory (e.g. mains), while a computer controlled diffraction grating (1200 lines per mm) splits the light source into individual wavelengths. A fibre coupler is used to collimate and focus the light as it leaves the monochromator, a 45° angled mirror then focuses light onto either the calibrated silicon reference photodetector, or a solar cell, depending on whether a reference or solar cell measurement was being taken respectively.

The reference measurement is used to determine the total number of photons incident on the surface of the solar cell, per wavelength, and is performed by connecting the silicon photodetector to channel B of the lock-in amplifier and setting it to measure photocurrent. The photodetector is then placed under the focused light beam (see Figure 4-10). Using the

accompanying photocurrent acquisition software (programed by another group member, Kan-Hua Lee [5]), the monchromator was set to move its diffraction grating to provide a range of wavelengths, sufficient to cover the absorption range of the photodetector. A step size must then be chosen for the wavelength range (choosing a step size is a compromise between experiment speed and spectral resolution). Typically, the auto range function is used on the digital lock-in amplifier to prevent overloading. The photocurrent software and the lock-in amplifier software were both set to record data from channel B and a bias voltage of zero was set across the photodetector. Lastly, the photocurrent for the incident beam was collected and was plotted against wavelength.

For the solar cell measurement, the solar cell is connected to the lock-in amplifier in place of the silicon photodetector, and the cell is positioned under the focused monochromatic beam in the same way as the silicon photodetector had been previously. The photocurrent acquisition software, and the lock-in amplifier software were set up as described above for the reference photodetector. In the photocurrent software the wavelength range, the step size, and range are set to match that of the previous reference. Again a bias voltage of zero is set for the solar cell (short circuit).

An EQE plot is output by the photocurrent software by selecting the solar cell data, dividing it through with the reference data, and multiplying this ratio by an accompanying calibration file for the silicon photodetector.

4.9 Short Circuit Current

Short circuit current measurements were performed using an optics bench setup. This measurement was performed so as to determine the photon flux entering the LSCs top surface, and the photon flux(es) exiting the narrow edges of the LSC, thus allowing the

optical efficiency for the sample under a given light source (in this work usually a Steuernagel Lichttechnik solar simulator, see section 4.2) to be determined.

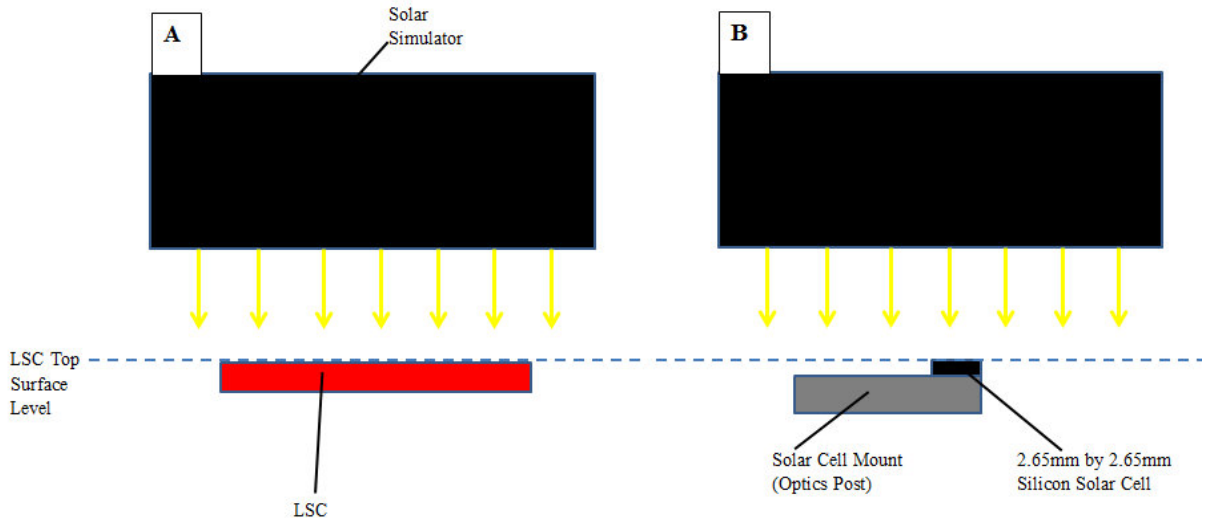


Figure 4-11 Side-view diagrams of the experimental setup used to measure incident photon flux. A) features the setup with the LSC in place, while B) shows the LSC removed.

The LSC sample was horizontally mounted underneath the aperture of a Steuernagel Lichttechnik solar simulator. A 2.65mm by 2.65mm silicon solar cell, of known EQE (see section 4.8), was connected to a Keithley 224 current source meter measure unit. The solar cell was carefully positioned so as to be at exactly the same level as the top surface of the LSC sample when it is being measured (see also Figure 4-12), facing the light source, as shown in Figure 4-11. The LSC sample was removed from its mount and the silicon solar cell was moved to where the corners of the LSC had previously been, as well as to where the centre of the LSC had previously been as illustrated in Figure 4-12, and photocurrent measurements were taken. These measurements made it possible to determine an average of the incident photocurrent over the surface of the LSC by averaging the photocurrents from the measurements. The average photocurrent was divided by the area of the cell to give the average photocurrent density. The EQE of the Si solar cell was measured (see section 4.8) as

well as the spectral shape of the solar simulator spectrum using the OOS (as for PL measurements see section 4.5.2), The measured solar simulator spectrum was converted from a signal proportional to the incident power to one proportional to the photon flux. Scaling the incident spectrum and convolving this with the known EQE spectrum of the cell enabled a short circuit current density to be calculated by integrating the convolved spectra and multiplying by the charge on an electron. The scaling factor was then varied until the calculated short circuit current density matched the average value measured over the top surface of the plane occupied by the LSC. In this way both the spectrum and absolute photon flux density on the top surface of the LSC are known.

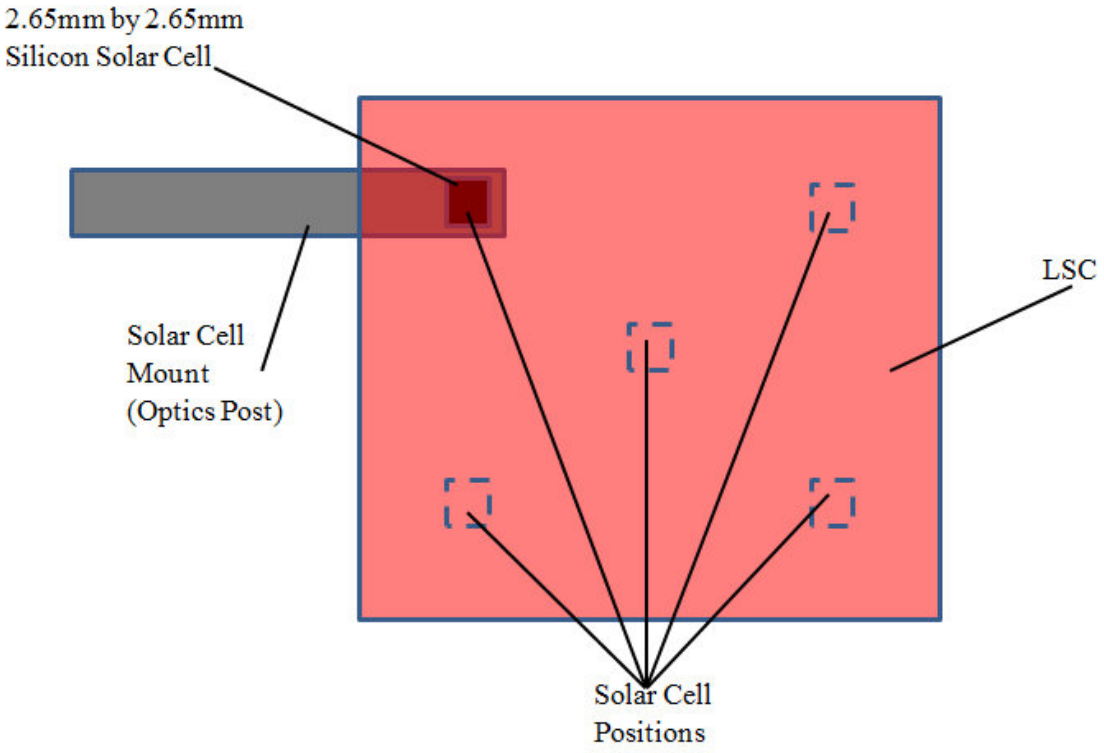


Figure 4-12 Diagram of top-down view of incident photon flux measurements.

The LSC sample was returned to the sample mount and the silicon solar cell was coupled to the narrow edges of the LSC (see Figure 4-13) using optical matching fluid, refractive index

1.4917 (Cargille), this method was performed throughout this thesis allowing the optical efficiencies of different LSC samples to be compared. The author felt the use of matching fluid, which eliminated the air gap between the LSC and the solar cell preventing TIR at the LSCs narrow edges, was appropriate as it gave a more accurate measure of the internal brightness of the LSC. Which is to say that if an air gap were present it would have artificially reduced the optical efficiency compared to what would be seen by solar cells if they were bonded to the edges of the LSC. Furthermore, rather than applying angular correction factors (which would likely have had to be different when measuring the aligned nanorod sample in chapter 5, compared to the rest of the thesis), it was decided that a standard experimental value would be used to determine optical efficiency. This may slightly add to any differences between experimental and simulated data, but wouldn't have fundamentally changed any conclusions. Ultimately, the optical efficiency results measured within this thesis are internally consistent with one-another.

Measurements were taken at 3 locations along length of each narrow edge of the LSC (see Figure 4-14), and multiple repeat measurements were made at each position, on each edge, to obtain an average. Due to the 2.65mm by 2.65mm dimension of the Si solar cell, it was often necessary to mask off parts of the solar cell which did not come into contact with the narrow edges of the LSC (this unfortunately introduces fairly significant uncertainty in measurements). For example, many thin-film LSC samples were fabricated on 1mm thick substrates, and so the solar cell over-hung the edges of the LSC. Additionally, there are LSCs with substrates thicker than 2.65mm, and in these cases it was necessary to use the solar cell to measure the edge of the LSC, starting either at the top or the bottom, and then moving the cell and measuring again for the remaining part of the LSC, masking if required (the photocurrent from multiple measurements of this type is then summed).

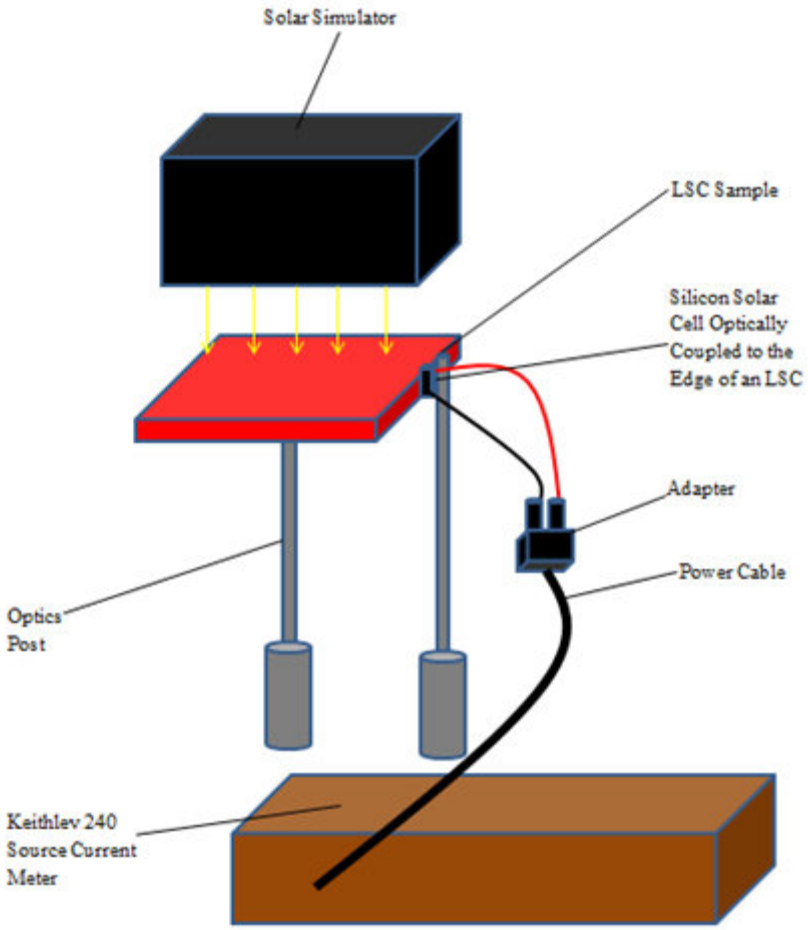


Figure 4-13 Diagram illustrating the short circuit current measurement experimental setup (part of the measurements required to determine the edge emission photon flux).

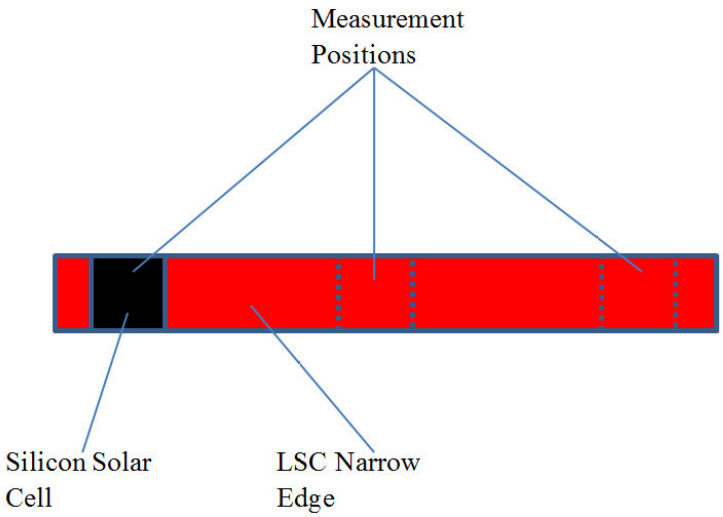


Figure 4-14 Side-view of the photon flux measurement locations on the edge of an LSC.

The average edge photocurrent was divided by the area of the measurement to give the average photocurrent density. Again knowing the EQE of the Si cell (see section 4.8) as well as the spectral shape of the edge emission spectra (each edge may have slightly differently red-shifted spectra if the LSC sample is not square) from measurements using the OOS (as in section 4.5.2 again with the spectra converted into units proportional to photon flux). Similar to calculating the incident photon flux density, the edge PL spectra were scaled and convolved with the known EQE spectrum of the cell again enabling a short circuit current density to be calculated by integrating the convolved spectra and multiplying by the charge on an electron. Again the scaling factor was then varied until the calculated short circuit current density matched the value(s) measured for the edge(s) of the LSC. In this way both the PL spectrum and absolute photon flux densities emitted from the edge(s) of the LSC are known.

Knowing the photon flux density incident on the top surface and the photon flux densities (or single density if the LSC is square when all the edges are equivalent) emitted from the edges of the LSC, the appropriate photon flux densities can be multiplied by the area of the top surface of the LSC and edge area(s) in order to calculate the total photons incident on the top surface of the LSC and the total photons emitted from the edges. Then the optical efficiency of the LSC can be calculated using equation 2.2, chapter 2.

4.10 Light and Dark IV

A very similar method to the one described above in section 4.9 can be used to determine the power conversion efficiency of an LSC if solar cells are attached to its edge(s), and if the dark current density (see section 2.9.3, chapter 2) of this solar cell(s) is known (see method in section 4.10). If the short circuit current density is known, and the dark current density is

known, then equation 2.24 in chapter 2 can be used to calculate the current density generated (per the applied bias) by the solar cell and the light source (whether an incident light source like a solar simulator or the emission from the edge(s) of an LSC). If this data is plotted against voltage, it produces a light *IV* graph. By multiplying the applied bias (from dark current density measurement) by the voltage dependent current density, a graph of power density against voltage can be produced, the max power point on this graph is equivalent to the operating power density of the solar cell. This can be converted into power by multiplying the power density by the area of the solar cell. Lastly, (assuming the power of the incident light source on the surface of the solar cell has also been measured) the power conversion efficiency of device can be calculated by dividing the power output by the device by the power of the incident light source as per equation 2.26, chapter 2.

Light and dark IV (current/voltage) measurements were performed on solar cells, (see chapters 6 and 7, and also see chapter 7 for IV measurements on a photoelectrochemical cell (PEC cell)). Dark IV measurements are used to determine the dark current of a solar cell; with higher dark current reducing the overall solar cell efficiency. The dark current measurement involved connecting the solar cell to a Keithley 2400 source meter, which was in-turn connected to a computer with appropriate software. This measurement was performed in a dark room with blacked out windows. The software controlled the source meter, and was used to supply the solar cell with an appropriate bias for the solar cell being tested. The software also allowed the voltage step size (for resolution) and current limit (to prevent solar cell damage) to be set.

Light IV measurements were performed in a similar way as the dark IV measurements, only this time the solar cell had to be illuminated by an appropriate light source, i.e. a light source with a wavelength range appropriate to solar cell's absorption spectrum. In this work the light source of interest was typically the edge emission spectrum from whichever LSC had been

selected for use with the solar cell being measured. The LSC itself was illuminated by an appropriate broad band light source, typically a solar simulator (see sections 4.4.2 and 4.5.2) as shown in Figure 4-15.

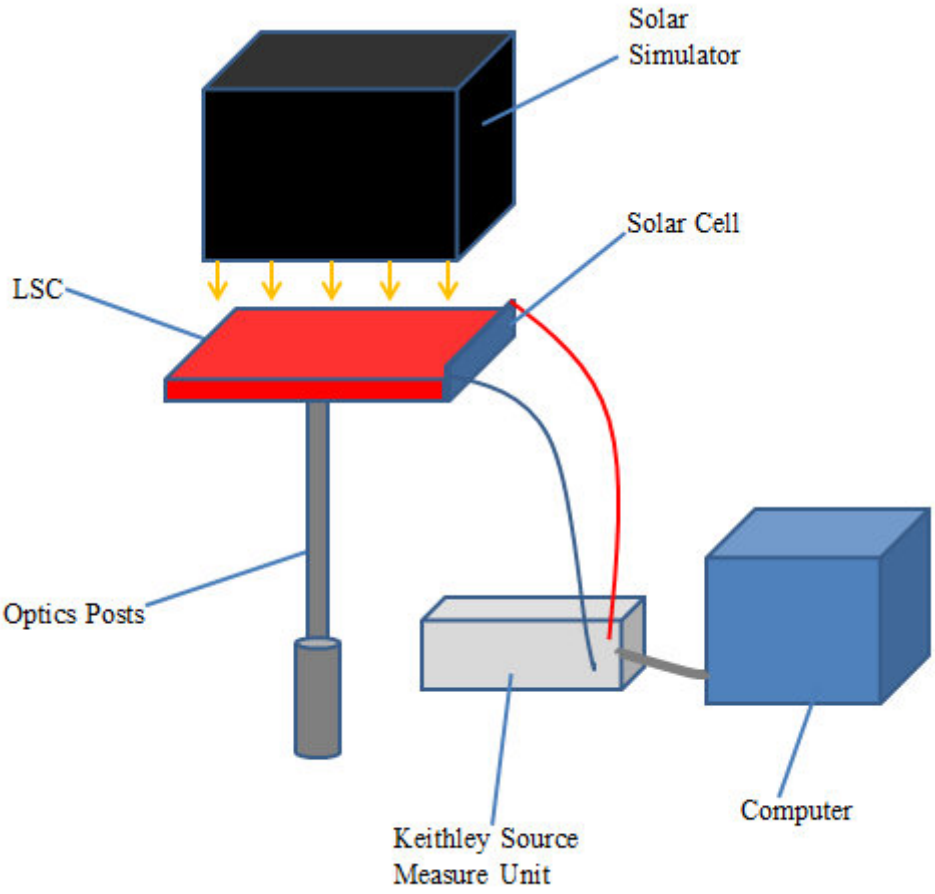


Figure 4-15 Diagram illustrating the light IV experimental setup.

4.11 Angular Dependent Measurements

The following section describes the methods used when performing angular dependent transmission measurements and angular dependent reflectance/surface scatter measurements. Both measurements are used only in chapter 5 and were used to determine the angular dependent absorptivity of nanorod samples.

4.11.1 Angular Dependent Transmission

Angular dependent transmission measurements were performed on a nanorod and a control sample at locations of interest, the locations chosen, and the reason why they were chosen is explained in chapter 5, section 5.5.2. The experimental setup used for these measurements is featured in Figure 4-16. This experiment required the mounting of a 473nm CW (linearly polarised) laser on an optics rail, which was in-turn mounted on a rotating stage (with adjustable x, y and z components). The laser beam was focused on the thin-film surface of the LSC sample (which was suspended over the centre of rotation of the rotating stage) at the position of interest. Behind the LSC a Newport 818 UV-Vis silicon photodectector (connected to a power meter) was mounted to the optics rail, to collect the laser light which had been transmitted through the sample (note: all measurements were performed in a dark room without windows).

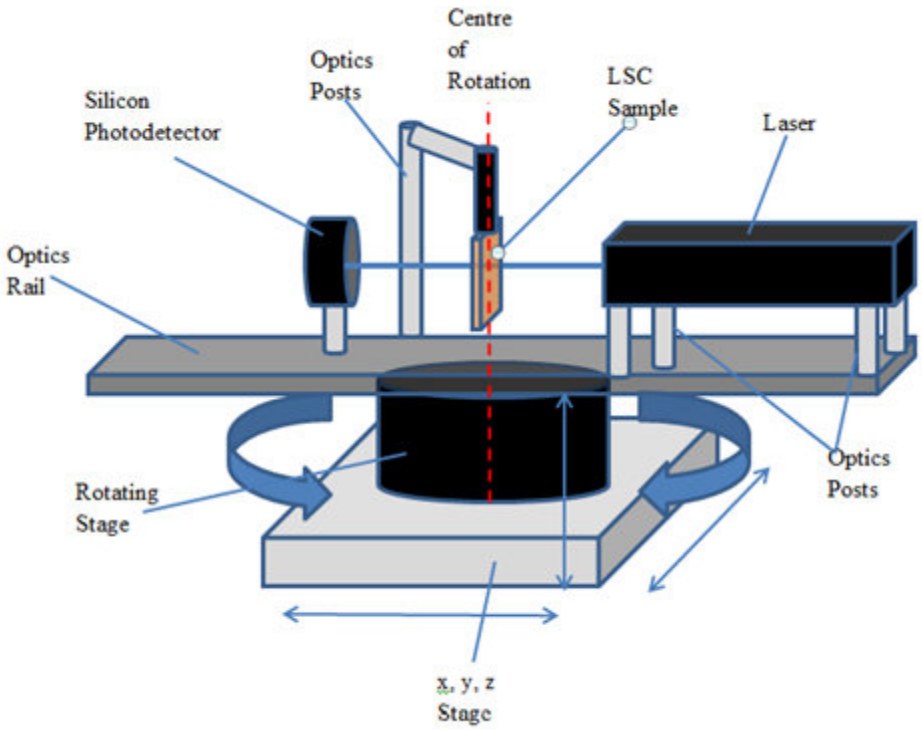


Figure 4-16 Diagram of angular dependent transmission experimental setup.

The experiment started with a measure of the incident laser power, with the sample temporarily positioned to one side so as to avoid obstructing the beam, this was a measurement of the incident intensity I_0 (see section 4.4.2). The sample was then repositioned so as to be in the path of the incident beam, making absolutely certain that the location chosen for measurement on the surface of the thin-film was positioned at the centre of rotation of the rotating stage (this prevented drifting of the laser beam across the samples surface at higher incident angles). Transmission measurements were performed over a range of angles from -60° to +60°(relative to normal incidence), with 2° step sizes (multiple repeats were performed and averages were taken).

4.11.2 Angular Dependent Reflectance and Surface Scatter Measurement

Combined measurements of surface scatter and reflectance were collected using a carefully aligned setup utilizing a 473nm CW laser as the light source directed at the surface of the LSC sample. This was the same laser as was used in the transmission/absorptivity results (see section 4.11.1). The sample was mounted on a motorised, double rotation stage (see Figure 4-18). The scattered/reflected laser light from the surface of both the nanorod and the control samples left the samples with an approximately conical distribution, which made it possible to focus this light into a Newport 818 UV-Vis Silicon photodetector, by using a pair of lenses. The sample was rotated through a range of angles on a motorised stage controlled by computer software (-60° to +60° to match the transmission experiment, see section 4.11.1), concurrently another motorised stage positioned beneath the stage on which the sample was mounted also rotated. This second motorized stage also had the two focusing lenses and the photodetector mounted on it, which allowed the reflected/scattered light to remain focused on the photodetector as the sample was rotated with respect to the incident laser beam. The focal length of the lenses was ~5cm, and the lens closest to the sample was of larger diameter than the lens closest the detector. Figure 4-17 shows a diagram of the cone shaped

reflectance/scatter coming from the samples surface. Prior to taking the reflectance/scatter measurements, the photodetector was placed at normal incidence to the incident laser to collect the total incident power (the measurement was repeated again after the reflectance/scatter measurement to obtain an average). By using this power measurement, and the subsequent reflectance/scatter measurements, the percentage of light reflected/scattered was calculated as a function of angle.

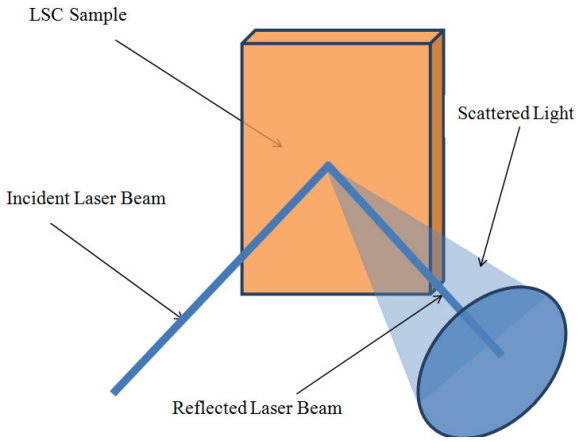


Figure 4-17 Diagram showing the conical laser scatter distribution and reflected laser beam from the surface of an LSC sample.

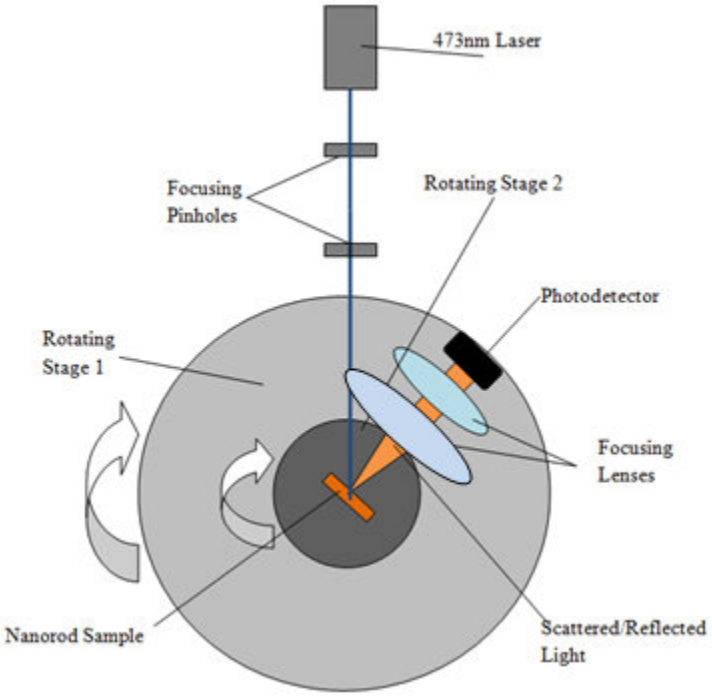


Figure 4-18 Top-down diagram of the reflection/scatter experimental setup.

Since this particular experiment was performed in conjunction with the angular dependent transmission measurement described in section 4.11.1, it was essential to measure the LSC sample(s) at the same positions for both measurements (see chapter 5, section 5.5.2 for specific information regarding these positions).

4.12 Measuring Thin-Film Thicknesses

Thin-film thickness measurements were performed in two different ways in this thesis, the first method, which was used for small LSC samples (useful for samples up to ~50mm by 50mm by 2mm), and was capable of highly accurate thin-film measurements (accurate to ±5nm). This method made use of a Tencor Alpha-Step-200 Profilometer. The alpha step consists of an adjustable sample stage (adjustable in x, y and z directions, as well as a rotating stage), a mechanically controlled stylus, which was scanned across the surface of the samples and was capable of accurately measuring very small variations in height (as described above),

and lastly, a monitor which displayed a high resolution video image of the sample (see Figure 4-19).

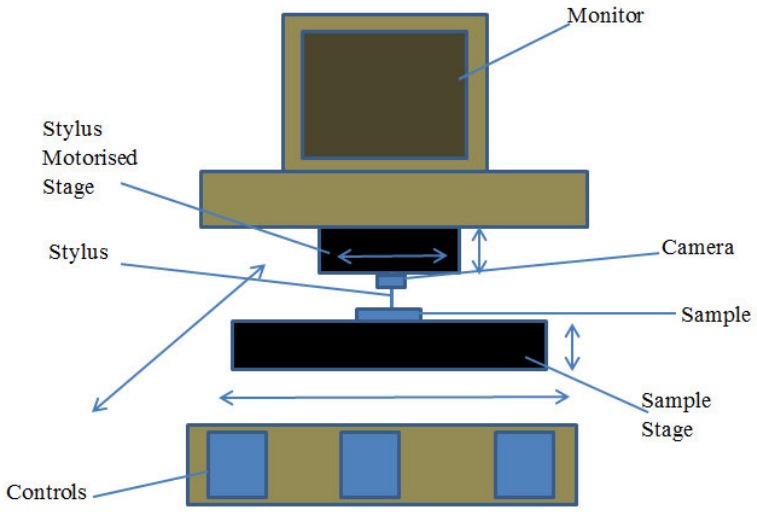


Figure 4-19 Diagram of alpha-step profilometer with sample. Stylus and sample sizes enlarged for clarity.

Prior to measuring the thickness of a samples thin-film layer, it was necessary to score the thin-film at the location at which the thin-films thickness was to be measured. A scalpel was used to score the sample. Great care was taken to make sure the sample was scored deeply enough to clear all of the desired thin-film material, but not so deep as to score the LSC substrate, both of these situations needed to be avoided to have any confidence in the thin-film thicknesses measured. After the sample had been scored at the desired location(s), excess material lifted up by the scoring process was carefully wiped off the surface of the sample using a disposable non-fibrous cloth. This step was important as the edges of the scalpel scored regions tended to lift away from the substrate, artificially increasing the thickness of the measurement.

The thickness measurements were performed by placing the sample on the sample stage, then by adjusting the sample stage position so that the region of interest (slightly to one side of the score line at the position where the thin-film measurement was to take place) on the samples surface, lined up with the styluses position. Once the stylus was in the desired position the stylus was lowered into direct contact with the sample. This alignment process was made possible by using the video image from a high resolution camera positioned above the stylus. After the stylus had been moved to the desired start position, the alpha-steps software was set to scan across the score mark. The software was adjusted to vary the scan range and the scan speed, slower scan speeds were usually chosen since they provided measurements of greater accuracy (scan times were typically a few seconds depending on the scan range chosen). A scan range sufficient to move the stylus from one side of the scratch to the other was chosen, and the difference in height between the surface of the thin-film and the lowest point of the score mark (see Figure 4-20) was taken as the thin-film thickness at that point (repeat measurements were used to enhance confidence in the validity of the measurement).

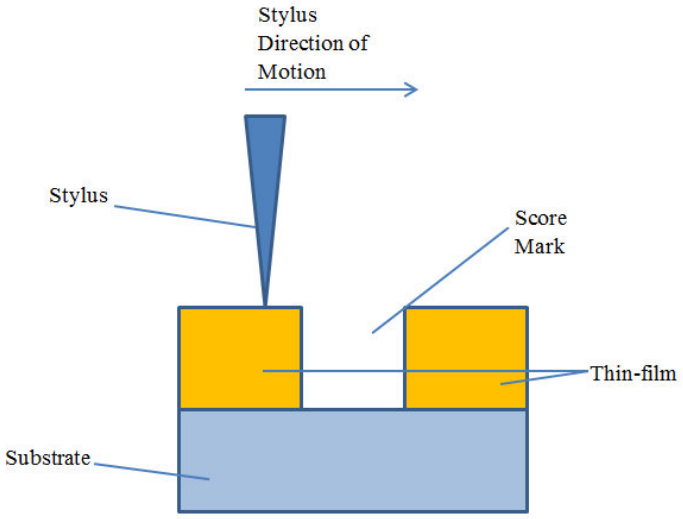


Figure 4-20 Diagram of scored thin-film and the stylus just prior to the start of a measurement.

An alternate method for measuring thin-film thickness, which was used for measuring large area, thick LSCs (LSCs too large to be measured using the alpha-step setup, see above) used digital callipers. The use of digital callipers was not an ideal choice as they lacked the same level of accuracy as the alpha-step system (the callipers used were accurate to ±10μm), and where limited to measurements of a maximum of ~2.5cm from the LSC's edges. However, for larger LSC samples with reasonably thick "thin"-films (e.g. greater than a few 10's of μm's), and with multiple measurements performed at different locations around their various edges, it was possible to get a reasonable approximation of the LSC's thin-film thickness.

4.13 Fabrication Methods

The following section describes the different fabrication techniques used to produce many of the LSC samples investigated in this work. For samples featured in this work which were not made by the author, a description of the sample and fabrication method used is given in the appropriate results chapter. A list of all the samples studied in this thesis is included in section 4.15 at the end of this chapter.

4.13.1 Thin-Film Solution Production Methods

Throughout this work, a large number of thin-film LSC samples were produced using a variety of luminescent species. To fabricate a thin-film LSC, a matrix solution doped with the luminescent species of choice, must first be prepared. Although the constituent parts of the solution vary, the general method for producing a thin-film solution throughout this work varies very little.

For the majority of the samples a glass vial was first cleaned using acetone, and then isopropanol, before being allowed to dry. The required quantity of PMMA crystals (from Sigma Aldrich), refractive index 1.49, was weighed out (depending on the quantity and dye concentration required) using a micro balance (four decimal place accuracy) and a measuring

spatula and added to the vial. During the course of this study it was ascertained that thin-films prepared using a PMMA / solvent /luminescent species mixture do not produce durable thin-films. These thin-films have a tendency to separate from their glass substrates after a period of only a few days (due to evaporation of the solvent and contraction of the thin-film), resulting in the peeling of the thin-film and ultimately rendering the LSC useless. To avoid this degradation, a quantity of poly(lauryl methacrylate) (PLMA) (from Sigma) refractive index 1.445, was added to the majority of thin-film LSCs studied in this work which were prepared by the author (exceptions to this rule can be seen in the list of samples in section 4.15), and was factored in as part of the weight of the PMMA matrix material [6]. PMMA is brittle and, according to the Dow chemical company [7] PLMA as a copolymer adds durability and internal plasticisation. Experimentation revealed that 15wt% of PLMA, in relation to the mass of PMMA used as the matrix material, was sufficient to add considerable lifetime to the fabricated thin-films, but without dramatically altering the optical properties of the LSC thin-film.

A quantity of the desired luminescent dye was measured and added to the PMMA/PLMA in the glass vial. Dye concentrations are recorded in terms of weight percentage in relation to the weight of the matrix material, (which was typically PMMA/PLMA unless otherwise stated). For example, a sample with a 1wt% concentration of Lumogen Red 305 in a matrix of PMMA/PLMA, might have a combined weight of 1g of PMMA/PLMA and 0.01g of Lumogen Red 305 dye. The luminescent species and matrix material needed to be dissolved to form the thin-film solution. Therefore, a solvent capable of dissolving both the polymer crystals, and the luminescent material was added to the glass vial, and 2-3 days were typically required for the polymers to fully dissolve. For larger quantities of thin-film solution, magnetic stirrers and a hot plate (at temperatures up to 80°C) (hotplate use and temperature

depended on the properties of the luminescent material and solvent being used), were occasionally used to expedite the dissolution.

The quantity of the solvent used for dissolving the matrix materials and luminescent species is assumed to ultimately have a negligible effect on the concentration of the luminescent species in the thin-film layer, due to the evaporation of the solvent once the thin-film solution had been applied to the substrate and had fully dried. Therefore, the quantity of solvent was chosen to optimise the viscosity of the thin-film solution, which was necessary primarily for varying the depth of the thin-film being fabricated. However, it must also be noted that viscosity is of fundamental importance when performing spin-coating or wire bar coating, as it plays a major role in determining the quality of the thin-film e.g. the coverage of the substrate (see sections 4.13.2 and 4.13.3).

4.13.2 Spin-Coating Methodology

One of the two methods utilised by the author for fabricating thin-film LSCs involved the use of spin-coater machines. Spin-coaters are adept at producing very thin-film, small area LSC samples, as shown in Figure 3-15, which are useful for a number of characterisation measurement techniques. For example, due to size constraints imposed by the limited dimensions of the integrating sphere used in the LQY measurements (see section 4.7), small samples are required. Alternatively, in the case of transmission measurements utilising a UV-Vis setup (see section 4.4.1), a lower optical density is required to compensate for the low sensitivity of the photomultiplier tube photodetectors used in the UV-Vis machine, and spin coating proves to be very effective at producing good quality thin-films.

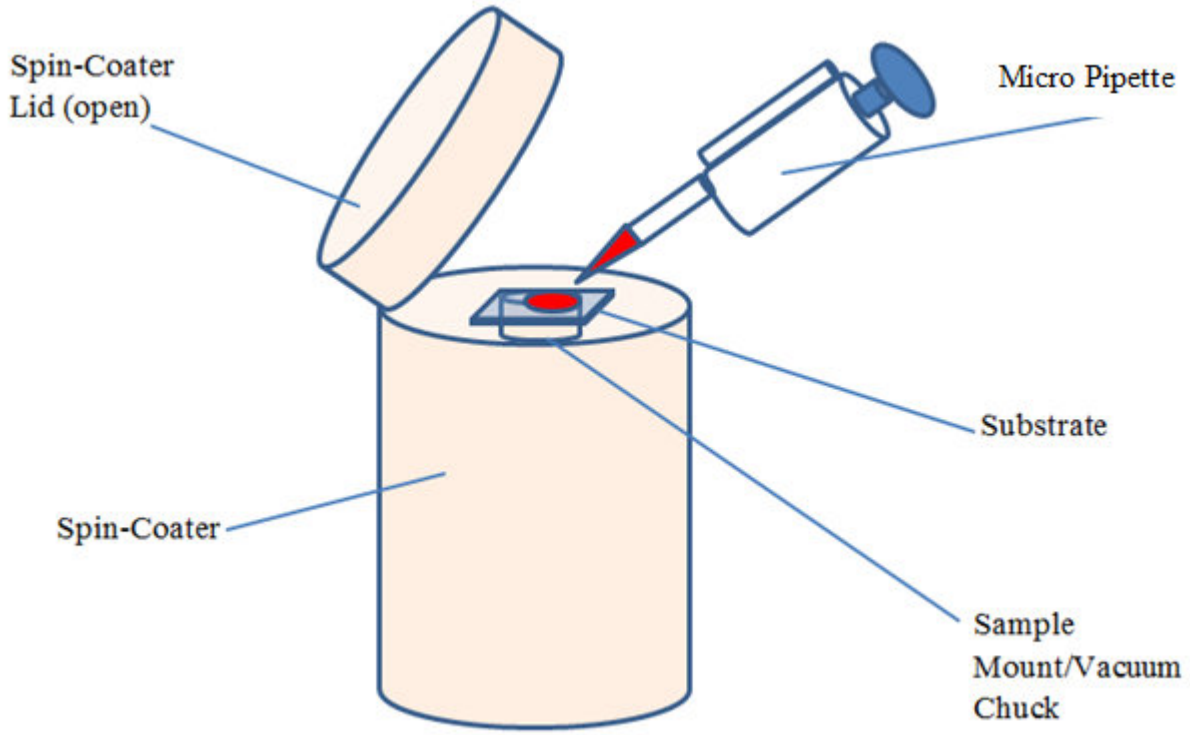


Figure 4-21 Diagram featuring the spin-coater sample fabrication setup.

The spin coater (see Figure 4-21) used in this work are subject to a number of limitations, foremost of which are a limited surface area due to the dimensions of the machine and the force the sample is subjected to at high rpm (revolutions per minute). Secondly, the viscosity of the thin-film solution (see section 4.13.1) has to be relatively low when compared to the range which can be used with a wire-bar coater (see section 4.13.3) in order to produce a thin-film which can cover the top surface of the substrate. Thirdly, spin-coating does not provide thin-films of entirely uniform thickness, with the edges of the samples often being considerably thicker than the central region due to build-up of material there due to surface tension. However, this may not be a large issue depending on how the sample is due to be characterised. Lastly, due to the high rpm substrates are subjected to, spin-coaters are not practical for use with flexible LSC substrates (as used extensively for the studies reported in chapter 6) as the edges of the substrate flex upwards under high rpm.

Advantages and disadvantages considered, the use of a spin-coater is quite simple. Since the spin coated samples which feature in the results section of this work were produced for specific characterisation methods (as explained above), they were not required to be very thick. To produce a LSC thin-film only a few μm thick, the spin coater (which was used in a clean room) was typically programed to run for one minute, at a speed of 3000rpm and an acceleration of 800 revolutions per s^2. The substrate chosen for use in a new LSC sample was cleaned thoroughly prior to coating using acetone, then isopropanol and lastly drying with compressed nitrogen. This last step removes the "water marks" due to the evaporation of the cleaning solvents.

The cleansed substrate was held inside the spin coater by vacuum suction, and an adjustable micro pipette was used to measure out and apply a quantity of thin-film solution (see Figure 4-21). Better quality, more even, thin-films were obtained by using larger amounts of material and spreading it across the surface of the substrate prior to spin-coater activation. Total substrate coverage often did not occur if this step was neglected. After spin-coating, excess material (thin dry strands of PMMA/PLMA) overhanging the edges of the sample were removed by hand, and then more carefully by using chlorobenzene and non–fibrous cloth to thoroughly clean the sample edges. It was imperative when cleaning the edges of the newly fabricated sample that the chlorobenzene did not come in contact with the top surface, to avoid damaging the thin-film.

4.13.3 Wire Bar Coater Methodology

The wire bar coater (WBC) (RK Control Coater from RK Printcoat Instruments) is capable of producing large area LSCs (also flexible LSCs) with thin-film coatings from a few μm in thickness, to a few hundred μm thickness (although surface variations in film thickness across the surface of the sample were often more significant than those observed for spin-coated samples). The disadvantages to using a WBC are its requirement for large amounts of

excess material, which is wasted and requires extensive cleaning, and, it also requires more skill than a spin coater to use it effectively (in terms of finding the correct solution viscosity, bar height, bar speed, temperature of heated bed etc.).

A substrate used on a WBC has to first be cleaned using acetone and isopropanol. The cleaned substrate is then placed on the WBC bed and surrounded with other pieces of substrate of the same thickness (often microscope slides). This is not usually necessary for substrates less than 1 mm thick, but for thicker substrates provides a starting point for the thin-film level in height with the LSC substrate. This technique allows the thin-film to be spread from a point before the start of the substrate, thus providing for a thin-film of (near) uniform thickness (see Figure 4-22).

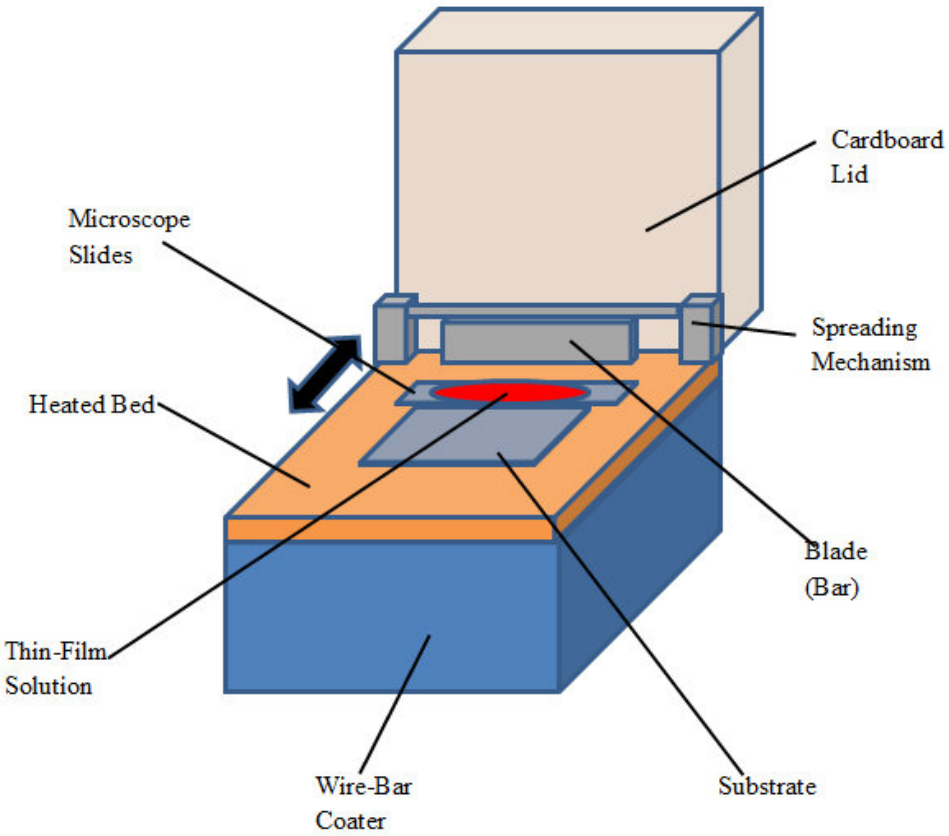


Figure 4-22 Diagram of wire-bar coater sample fabrication setup.

The WBC has a number of bars of different diameters to produce films of different thicknesses. However, the adjustable blade (Micrometre Adjustable Applicator blade from RK Printcoat Instruments) is far more versatile, allowing for a large range of heights to be set. Furthermore, it was also easier to maintain than the grooved bars, since the grooves on the wire bars tend to trap PMMA/PLMA, making them extremely difficult to clean. Micrometre callipers (attached to the blade) were used to set the blade height.

Large quantities of thin-film solution had to be applied during coating (several times the desired volume of the thin-film), this was primarily due to the spreading action of the WBC causing the thin-film to narrow as the WBC blade moves away from the start position (forming a trapezium shaped thin-film when viewed from above). The blade's spreading motion leads to a good coverage on a central strip of the substrate, but often leaves the edges of the substrate with little film coverage. Therefore, starting with an excess of thin-film solution allowed for more even thin-film coverage over the substrate.

During the coating it was found that covering the WBC bed area with a hood, built-in house, provides for a more even film. Prior to its use, ripples often appeared in the surface of thicker films, with the ripples being caused by the flow of air inside the fume hood in which the WBC was operated, due to the use of chlorinated solvents.

4.14 Computational Methods

The bulk of the computational modelling performed during the course of this work made use of a raytracing program, called PVtrace, written in the Python programming language by Dr Daniel Farrell (a former group member) [8]. The program uses geometric optics and Monte Carlo simulations to model the interactions of photons with an LSC.

It is possible to write scripts which instruct the PVtrace program to simulate a great variety of LSCs, including different geometries, incident light sources, absorption and emission spectra,

dimensions, LQYs refractive indices, as well as different mirror configurations and index matching (as for an attached solar cell) or air gap (as for mirrors) conditions at the LSC surfaces. What follows is an overview of the program.

A specific LSC can be modelled by writing a script which tells PVtrace to model the LSC's shape e.g. cuboid or cylindrical and its dimensions. More complex LSCs can be also be modelled, such as thin-film LSCs or cylindrical LSCs with an un-doped central core and a doped outer cylinder. An incident light source can be simulated by entering the desired light source's spectrum, position, whether it is a planar or a point source and the number of photons from the light source. Lastly, the material properties of the LSC can be defined; this is done by importing absorption and emission spectral data for luminescent species and defining its LQY and refractive index. The substrate and host matrix materials require similar material information. However, since the substrate materials were usually glass or PMMA, with absorption coefficients that do not vary much over the wavelength range of interest, an absorption spectrum with absorption coefficient of 0.3 m^{-1} for PMMA and 1.0 m^{-1} for glass were usually assumed. A separate piece of code allowed the transmission at the peak absorption wavelength to be set to any percentage desired, which is useful in determining what optical density is required to give the highest efficiency LSC, without saturating the transmission spectrum.

Additional coding instructs the script to save data generated in the simulations to a data file. This data file is then processed by a separate script containing all relevant parameters, for example, the optical efficiency and the photon concentration. Finally, the script can instruct the simulations to be shown in a 3D visualizer program, which can be helpful with de-bugging, and generally aids the modelling process.

4.14.1 Raytrace Methodology

As stated above, PVtrace makes use of geometric optics and Monte Carlo methods to simulate an LSC. To do this, the following processes occur as illustrated schematically in Figure 4-23:

1) Parameters are input including the number of photons, the dimensions and other properties of the LSC (layer thicknesses, mirrors and any index matching are specified), refractive indices, relevant absorption and emission spectra, incident light source spectrum and LQYs as detailed above. The incident light spectrum is turned into a probability distribution function that can be sampled by uniformly distributed random number to reproduce the original data. In this way the wavelengths of the source photons in the simulation are determined. Depending on the properties of the light source (point/planar) further random numbers determine the direction of the photon or its point of origin and whether (and where) it intersects the LSC is determined.
2) Whether or not a photon is absorbed by the LSC (luminescent species or matrix material) is determined by random number generators, spectral data and pertinent equations. For example, the probability a photon will be reflected from the top surface of the LSC is determined by the angle of incidence of the photon, the refractive index of the LSC material, the polarisation of the light source and the reflection coefficient equation (see chapter 2 for relevant equations). The probability of reflection is compared against a random number to determine whether a given photon is reflected. The probability of a non–reflected photon (a photon which enters the LSC) being absorbed by the luminescent species or host matrix is determined by the pathlength through the materials (dependent on the angle of refraction as determined by Snell's law) and their absorption coefficients at the wavelength of the photon. Changing the depth of the LSC region where the luminescent species is present, therefore, affects the number of incident photons

absorbed. For example, for a thin-film LSC simulation, if the depth of the thin-film is increased then the fraction of light being transmitted through the sample will decrease (provided the same input absorption coefficient spectrum is used). As a result raytrace simulations allow extrapolations of experimental data (often collected from small experimental LSCs) to more practical dimensions.

3) A photon that is not absorbed by the LSC will either be reflected at the front surface, or will pass through the LSC, and will be lost (unless there is a reflective material beneath the LSC or there is an additional LSC which is able to absorb the photon). In the event that there is a reflection event, the angle of reflection will need to be calculated, for a specular reflector this angle is equal to the angle of incidence, whereas for a scattering reflector the reflection angle and direction is determined by a random number generator mapped to the 2π solid angle of a hemisphere. Ultimately, if the photon is returned to the original LSC via reflection, or if there is an additional LSC underneath the first, then step 3) will be repeated.
4) If a photon is absorbed by the LSC, the LQY is compared against a random number to determine whether or not the photon is emitted. If a photon is emitted, then the emission wavelength is determined by the probability distribution of the emission spectrum in a manner similar to that of sampling the incident light spectrum described above. However, to comply with the law of energy conservation the emitted photon must be of lower energy (longer wavelength) than the originally absorbed photon.
5) A photon not re-emitted is lost due a non-unity LQY, which counts as a non-radiative relaxation, and results in a photon being permanently lost from the simulation.
6) Emission direction is modelled to be entirely random for isotropic emission (randomly oriented luminescent species), with the co-ordinate vector being determined by a random number mapped to the 4π solid angle of a sphere. However, some simulations have

directional emission due to aligned luminescent species being present (see chapter 5), in these cases dipolar emission probability distributions limit the directions over which photons can be emitted.

7) Total internal reflection (TIR) is determined by Snell's law, the refractive index of the LSC material(s), the boundary material and by the angle of emission determined in 6).

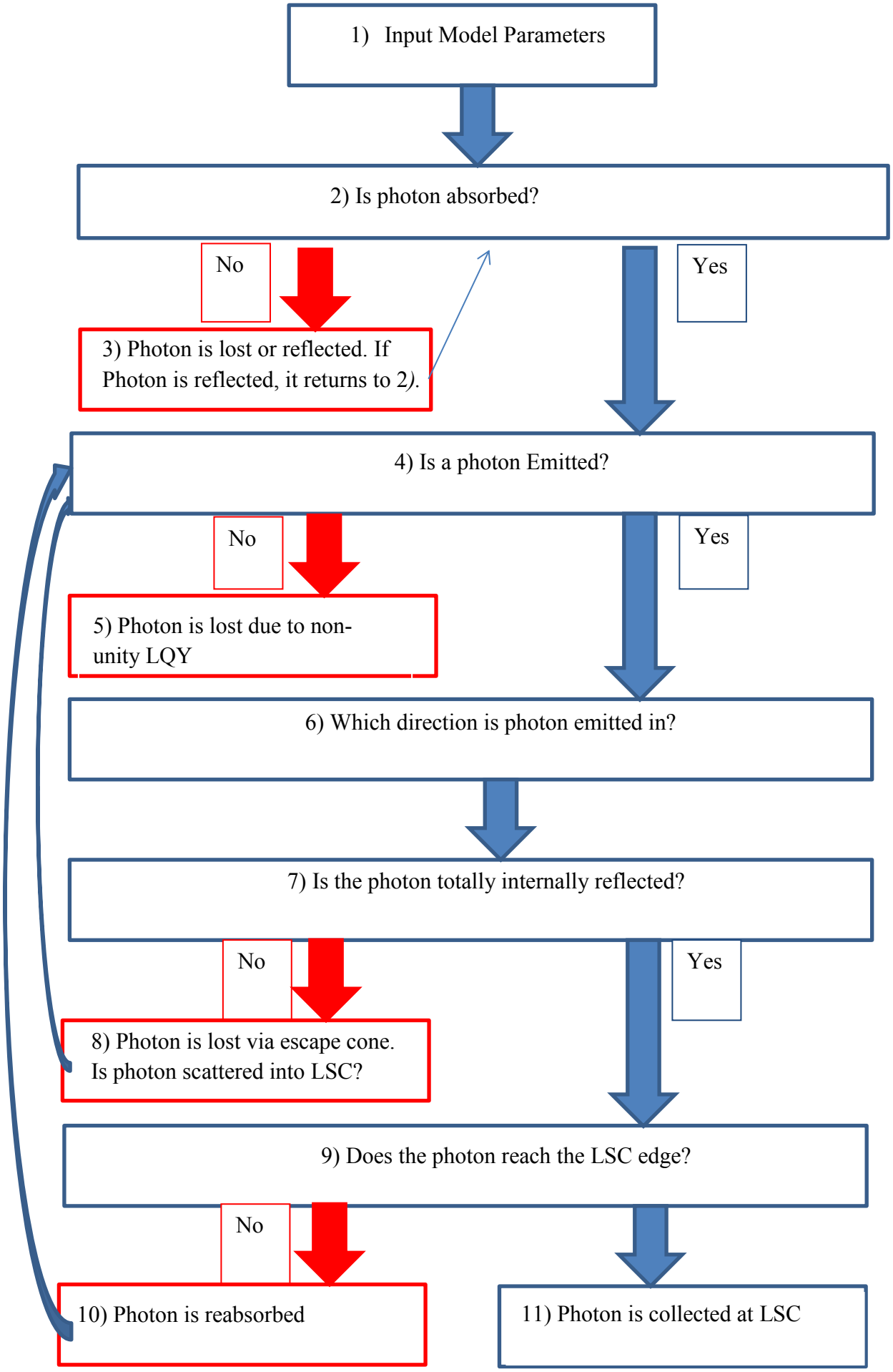
8) If the angle of photon emission is less than the critical angle at the LSC boundary TIR will not occur, and the photon may either be lost from the LSC via an escape cone (see section 2.6.3 chapter 2) or may be reflected back in by Fresnel reflection (as in step 2) above). A reflective layer will allow a lost photon to re-enter the LSC (as determined by comparing a random number with the appropriate reflection coefficient), if so the photon returns to step 4).

9) Each photon is tracked (often through multiple TIR, and other reflection, events) to determine whether it reaches one of the narrow edges before it is either lost from the simulation (via an escape cone or non-radiative relaxation) or is reabsorbed. If it does reach an edge, then the photon is added to any others which emerge from the narrow edge(s), and will be subsequently counted in optical efficiency and photon concentration calculations.

10) Whether a photon is reabsorbed or not is determined after each intersection of the photon by one of the LSC surfaces (assuming it is not lost) by the pathlength, the re-emitted photon's wavelength, which in-turn is determined by the emission spectrum of the luminescent material as described above, and the overlap this has with the absorption spectrum. If re-absorption does occur then the process returns to step 4).

11) The photon is collected at the edge and is manipulated by the raytrace program's output equations accordingly. This is also the case for photons lost through escape cones and by

non-radiative relaxation in order to determine the relative importance of the different loss mechanisms.


1) Input Model Parameters
2) Is photon absorbed?
No
Yes
3) Photon is lost or reflected. If Photon is reflected, it returns to 2).
4) Is a photon Emitted?
No
Yes
5) Photon is lost due to non-unity LQY
6) Which direction is photon emitted in?
7) Is the photon totally internally reflected?
No
Yes
8) Photon is lost via escape cone. Is photon scattered into LSC?
9) Does the photon reach the LSC edge?
No
10) Photon is reabsorbed
11) Photon is collected at LSC

4.15 List of Samples

The following is a complete list, and brief description of, samples which were studied in this work.

Chapter 5

Lumogen Red Control Sample

Description: LSC consisting of randomly oriented Lumogen red 305 0.6 wt% concentration; sample serves as a non-aligned control sample.

Dimensions: Substrate = 2.5cm by 1.25cm by 0.1cm, average thin-film thickness = 9.140μm

Luminescent Species: Lumogen red 305 (perylene based dye from BASF)

Substrate Material: Glass

Matrix Material: 85wt% PMMA + 15wt% PLMA

Nanorod Sample

Description: LSC sample with (partially) vertically aligned arrays of CdSe/CdS core shell nanorods.

Dimensions: Substrate = 2.5cm by 1.25cm by 0.1cm, average thin-film thickness = 285nm

Luminescent Species: CdSe/CdS core/shell nanorods

Substrate Material: Glass

Matrix Material: N/A (nanorod's organic ligands effectively serve as a matrix material)

Chapter 6

Second Generation Phycobilisomes

Description: LSC thin-film sample containing modified Phycobilisome molecules as luminescent species. Phycobilisomes were modified in an attempt to reduce absorption/emission spectral overlap due to secondary peaks.

Dimensions: Substrate = Substrate = 6cm by 6cm by 0.7mm, average thin-film thickness 28μm

Luminescent Species: Modified Phycobilisomes

Substrate Material: Glass

Matrix Material: Starch, sucrose, trehalose and buffer solution

PE-610

Description: LSC thin-film sample incorporating a tandem dye from Columbia Biosciences consisting of R-Phycoerythrin (a protein from Phycobilisomes) and Rhodamine dye. The tandem dye is intended to increase the Stokes-shift and absorption efficiency.

Dimensions: Substrate = 6cm by 6cm by 0.7mm, thin-film average thickness =108μm

Luminescent Species: R-Phycoerythrin and Rhodamine dye.

Substrate Material: Glass

Matrix Material: Starch, sucrose, trehalose and buffer solution

0.51mg/ml, 0.703mg/ml and 1.405mg/ml PE-610

Description: 0.51mg/ml, 0.703mg/ml and 1.405mg/ml quantities of PE-610 dye in buffer solution.

Dimensions: 1mm pathlength cuvette

Luminescent Species: R-Phycoerythrin and Rhodamine dye

Substrate Material: Quartz

Matrix Material: Phosphate buffer solution (pH7.4)

ADS065BE (0.1, 0.5, 1, 2 and 4wt%)

Description: A series of LSCs containing an electrophosphorescent metal complex dye from American Dye Source. Dye concentrations used were 0.1. 0.5, 1, 2 and 4 wt%.

Dimensions: Substrate = 2.5cm by 2.5 cm by 0.1cm, thin-film thicknesses of 5.523 to 6.793µm

Luminescent Species: ADS065BE, an electrophosphorescent meatl complex consisting of iridium (III) bis(2-(4, 6-difluorephenyl)pyridinato-N,C^2)

Substrate Material: Quartz

Matrix Material: 85wt% PMMA + 15wt% PLMA

First Generation Flexible LSC

Description: A flexible LSC prototype sample, featuring Lumogen red 300 as the luminescent species, at a concentration of 1 wt%.

Dimensions: Substrate = 6.0cm by 6.0 cm by (2x0.25mm), thin-film 180µm

Luminescent Species: Lumogen red 300 (BASF)

Substrate Material: 2X0.25mm PLEXIGLAS Film clear 99524 from Evonik Industries (in a sandwich configuration above and below the thin-film)

Matrix Material: Photoinitiated lacquer of unknown composition supplied by collaborators at Microsharp Corporation Limited.

Second Generation Flexible LSC

Description: A flexible LSC prototype sample, featuring Lumogen red 305 as the luminescent species, at a concentration of 1 wt%.

Dimensions: Substrate = 9.0cm by 5.9 cm by 0.5mm, thin-film 110µm

Luminescent Species: Lumogen red 305 (BASF)

Substrate Material: 0.5mm PLEXIGLAS Film clear 99524 from Evonik Industries

Matrix Material: PLEXIGLAS Film clear 99524 from Evonik Industries (dissolved in chlorobnzene).

Chapter 7

Red LSC

Description: An LSC with a thin-film consisting of Lumogen red 305 (BASF). This sample was coupled to silicon solar cells which were in turn connected in series with a photoelectrochemical cell, for the purpose of applying additional potential for water splitting reactions.

Dimensions: Substrate = 10cm by 10cm by 0.5cm, thin-film thickness = 107.5µm.

Luminescent Species: Lumogen red 305 (BASF) 3wt% concentration

Substrate Material: Glass

Matrix Material: 85wt% PMMA + PLMA 15wt%

Violet LSC

Description: An LSC with a thin-film consisting of Fluorescent violet (Kremer). This sample was coupled to a photoelectrochemical cell, which was in turn connected in series to silicon solar cells, for the purpose of generating potential for water splitting reactions.

Dimensions: Substrate = 10cm by 10cm by 0.5cm, thin-film thickness = 55µm.

Luminescent Species: Fluorescent violet (Kremer) 2.5 wt% concentration

Substrate Material: Glass

Matrix Material: 85wt% PMMA + PLMA 15wt%

Photoelectrochemical Cell

Description: Photoelectrochemical (PEC) cell uses incident photons to generate potential to split water (electrolyte molecules) to liberate hydrogen gas. PEC, connected in series with silicon solar cells to increase potential difference and allow for electrolyte splitting.

Dimensions: 10cm by 0.5 cm Fe_2O_3 working electrode. Platinum counter electrode with a 0.5mm diameter.

Working Electrode: Fe_2O_3 coating on ITO conductive glass, with dimensions of 10cm by 0.5cm.

Counter Electrode: Platinum wire immersed in electrolyte solution.

Electrolyte: pH13, sodium hydroxide, 0.1 molar solution.

Chapter 4 References

[1] Ocean Optics, Accessed on (15/9/2013), http://www.oceanoptics.com/products/usb2000+precon.asp .
[2] Horiba Scientific. Fluoromax-3. Accessed on (3/10/2013). http://www.horiba.com/us/en/scientific/products/fluorescence-spectroscopy/steady-state/fluoromax/fluoromax-compact-spectrofluorometer-524/ .
[3] De Mello, J., Felix Wittmann, H., and Friend, r., (1997). ., "An Improved Experimental Determination of External Photoluminescence Quantum Efficiency", Advanced Materials, 9, 3.
[4] Belton, C. (2012) Personal correspondence, Imperial College. London, UK.
[5] Lee, K-H, (2012). "EQE program written", Imperial College London, UK.
[6] Buchtemann A,. (2012), Private Correspondence, Fraunhofer IAP, Germany.
[7] Dow, "RcocrylTM 320 Lauryl Methacrylate (LMA). Accessed on (6/11/2013). http://www.dow.com/products/market/construction/product-line/rocryl-alkyl-esters/product/rocryl-320-lauryl-methacrylate-(lma)/]
[8] Farrell, D.J, (2013), "pvtrace: optical ray tracing for photovoltaic devices and luminescent materials", http://github.com/danieljfarrell/pvtrace

Chapter 5

Utilising Vertically Aligned CdSe/CdS Nanorods Within an LSC

5.1 Introduction

This chapter focuses on self-aligned CdSe/CdS nanorods, and includes experimental results from their characterisation as well as simulated results comparing ideally aligned nanorod samples with randomly oriented nanorods. In addition to characterising the CdSe/CdS nanorods, a thorough investigation of the aligned nanorod sample, made by a collaborator at the Istituto Italiano di Tecnologia (the Italian Institute of Technology), was performed to determine the validity of this method for LSCs.

Nanorods are an obvious choice for use as a luminescent species within LSCs since they are wavelength tuneable through their diameter, allowing for their absorption and emission spectral ranges to be adjusted, and they have relatively high LQYs (approximately 70% for CdSe/CdS nanorods in the work of Carbone *et al.* [1]. Like quantum dots they largely consist of inorganic materials, though they usually have organic surface ligands to prevent agglomeration (the ligand on the nanorods used in this chapter was octadecylphonic acid). The strong covalent bonding in the crystal lattice makes them far more stable than organic dyes [2]. It is also possible to create aligned arrays of nanorods through self-alignment techniques [3], which since nanorods are dipolar emitters, allows for directionality of the emitted photons, which has the potential to reduce escape cone losses [4]. Chapter 3, section 3.2.5 explains in some detail the potential importance of aligned emission from a luminescent species and the impact this might have on an LSC's optical efficiency.

This chapter details experimental and theoretical results for a sample consisting of a 25mm by 12.5mm by 1mm glass substrate, with a CdSe/CdS nanorod thin-film featuring small regional variations in its thickness (see section 5.5.2). The sample was fabricated by Dr Marco Zanella at the Istituto Italiano di Tecnologia. In addition, results from an approximately 25mm by 12.5mm by 1mm control sample, with a thin-film consisting of Lumogen red 305 (BASF) in a matrix of PMMA and PLMA (Sigma-Aldrich) spin coated on the surface, are discussed. This control sample serves as an isotropically emitting comparison to the aligned, directionally emitting, nanorod sample.

5.2 SEM Images of Nanorod Samples

Figure 5-1A and Figure 5-1B demonstrate the top-down and edge-on SEM images of CdSe/CdS core/shell nanorods. These images were taken by a collaborator, Dr Marco Zanella, and are of samples grown using a method identical to one used to manufacture the nanorod sample characterised in this chapter. An overview of the self-alignment method used for this nanorod sample can be found in section 3.2.5 of chapter 3, and a more detailed explanation is given in [3].

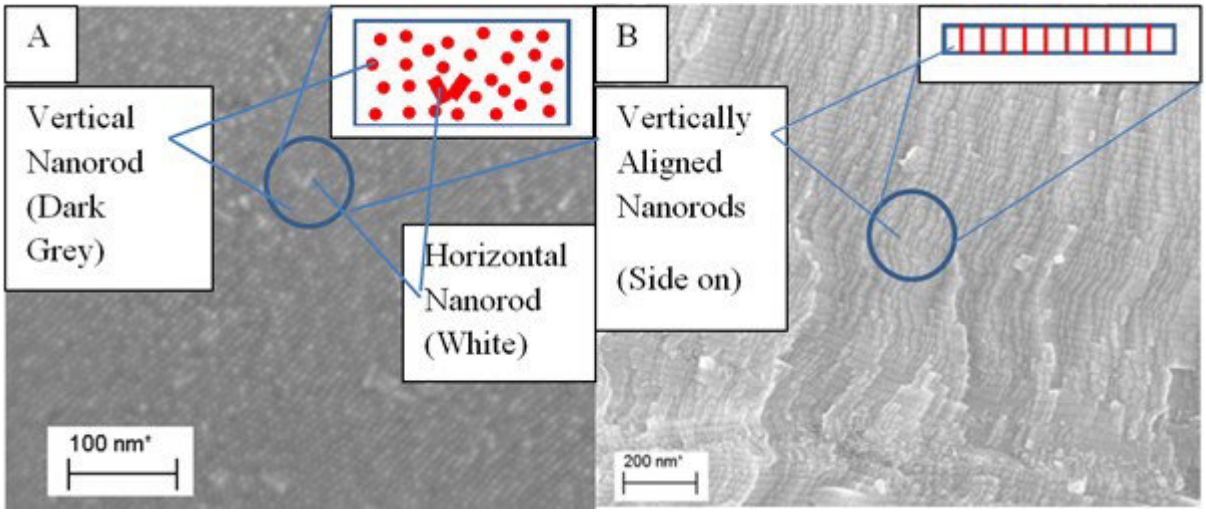


Figure 5-1 A) SEM top-down image of largely vertically aligned nanorods and B) SEM side-view of vertically aligned nanorods, figures courtesy of [5].

Despite the low resolution of Figure 5-1A and Figure 5-1B, it is possible to make out the vertical alignment of the nanorods. It is important to note the scales which accompany the figures in these images, as these images only cover a very limited region of the nanorod thin-film. However, these SEM scans coupled with the other results discussed in [3], which was fabricated using an identical method, and by the same person, as produced the sample characterised here, therefore provide reasonable starting evidence to suggest that the nanorod sample did indeed consist of vertical, self-aligned nanorods.

5.3 Dipole Behaviour

The luminescent species used in LSCs are generally anisotropic emitters, i.e. their emission (and absorption) has a dipolar radiation pattern. However, LSCs employing randomly oriented luminescent species are usually considered isotropic emitters (and computationally modelled as such), with the exception of the recent work by Verbunt *et al.* [6]. In the specific case of nanorods, the transition dipole will be oriented parallel to the long axis of the nanorod, therefore, emission (and absorption) will be maximal at right angles to the nanorod long axis [1]. In this chapter vertically aligned arrays of CdSe/CdS nanorods are studied, and as a result, unlike randomly oriented luminescent species, they must be thought of as anisotropic emitter/absorbers, as an assumption of isotropic behaviour would be inappropriate and inaccurate. This being the case, in this section, the radiation distribution of an anisotropic material is described. The anisotropic nature of an emitter can be derived from Fermi's Golden Rule [7] as:

$$\Gamma_{lk} = \frac{2\pi}{\hbar} g(E_k) \, |H'_{kl}|^2 \qquad 5.1$$

where $g(E_k)$ is the density of states and $|H'_{kl}|^2$ is a transition matrix element. Since this thesis is concerned with angular emission rate of in terms of power, a full derivation of the

probability of the transition distribution for a dipole, from first principles, is beyond the remit of this work, and the reader is advised to see [7] and similar materials for further information. Equation 5.2 from [8], starts from the average power radiated per unit solid angle $\frac{d\bar{P}}{d\Omega}$:

$$\frac{d\bar{P}}{d\Omega} = \left(\frac{1}{4\pi\epsilon_0}\right)\frac{ck^4|P_0|^2}{8\pi}sin^2\theta \qquad 5.2$$

where ϵ_0 is permittivity of free space, $\left(\frac{1}{4\pi\epsilon_0}\right)$ is the Coulomb force constant, c is the speed of light, k is the wavenumber, P_0 is a polarisation vector and θ is the angle between the nanorod dipole moment and the direction of emission. Equation 5.2 can be simplified to equation 5.3:

$$\frac{d\bar{P}}{d\Omega} = \alpha sin^2(\theta) \qquad 5.3$$

where:

$$\alpha = \left(\frac{1}{4\pi\epsilon_0}\right)\frac{ck^4|P_0|^2}{8\pi} \qquad 5.4$$

Equation 5.5 gives the total power of a dipolar distribution:

$$\bar{P} = \int d\Omega \, \frac{d\bar{P}}{d\Omega} \qquad 5.5$$

The solid angle $d\Omega$ in equation 5.5 can be converted into spherical co-ordinates as shown by equation 5.6, where φ is the angle of the photon emission in the plane perpendicular to the dipole moment direction:

$$d\Omega = sin(\theta)\, d\theta d\varphi \qquad 5.6$$

Finally, equations 5.3 and 5.6 can be substituted into equation 5.5 to produce equation 5.7:

$$\bar{P} = \alpha \int_0^{2\pi} d\varphi \int_0^{\pi} d\theta sin^3\theta \qquad 5.7$$

These equations are important because they describe the angular emission distribution from a dipolar emitter, and they are later used in the computational model which is the subject of section 5.8.

5.4 Basic Characterisation (Ensemble Absorptivity, Top Surface Emission and LQY)

This section addresses the nanorods' specific characteristics, to determine if the CdSe/CdS core/shell nanorods in the sample featured in this work are indeed of value for use in LSCs, regardless of their self-alignment properties. Even if perfect luminescent species self-alignment across the entirety of the LSC sample were possible, it would have little value if the luminescent species itself was inappropriate for LSC use. Therefore, this section details the measurements of the sample's ensemble absorptivity spectrum (an important distinction as will be seen in section 5.5), its top surface emission (to avoid reabsorption losses) and the LQY of the nanorods.

5.4.1 Absorption & Emission Spectra

Figure 5-2 shows the absorption and emission spectra for the CdSe/CdS nanorods (hereafter referred to as the nanorod sample). The absorption spectrum is in terms of absorptivity, with the incident beam at normal incidence to the surface of the sample. The absorptivity is corrected for absorption by the substrate using a glass reference slide identical to that used as the substrate for the nanorod sample (which explains the decrease in absorptivity at wavelengths less than 340nm). It can be seen that the absorption spectrum is relatively broad for an LSC luminescent species, and extends from ~650nm down into the UV region of the

solar spectrum. Unfortunately, the peak absorption doesn't coincide with the peak intensity of the AM1.5g solar spectrum (see Figure 2-2, chapter two), which will limit the ultimate efficiency of the LSC. However, as stated above in section 5.1, the absorption and emission spectral position for nanorods can be tuned by varying the nanorods' dimensions, thereby moving the absorption spectrum into a more ideal wavelength range.

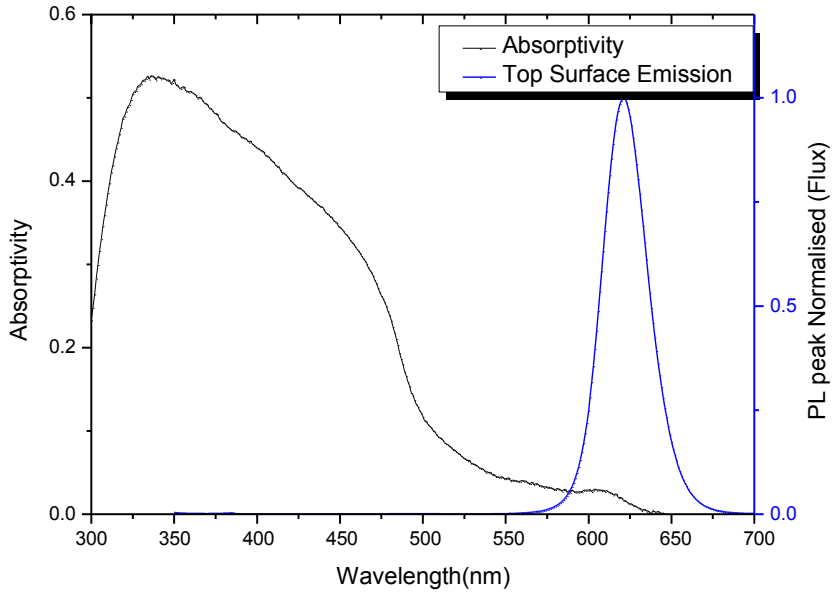


Figure 5-2 Absorptivity and top surface emission spectra of the nanorod sample.

Figure 5-2 shows the emission spectrum is relatively narrow compared to the absorption spectrum. A narrower emission spectrum has the advantage of potentially having the majority of emitted photons being at wavelengths close to the band edge of an appropriately chosen solar cell, and, as a result less of the energy from photons in the emission peak will be lost due to thermalisation in the attached solar cell(s). However, the emission spectrum is broad when compared to that of a single nanoparticle (which tends to form discrete emission lines see section 2.5.1, chapter 2); the increase in width is a result of variations in the nanorods dimensions, since the nanorod sample consists of many nanorods [1]. Instead of having a

discrete excitation state like is the case for a single atom, or a near discrete excitation energy state as per the case of a single nanorod, a large number of nanorods with varying dimensions tends to have a near continuous range of energy levels.

Figure 5-2 also shows that the spectral overlap between the absorption and emission spectrum is not insignificant, although the absorptivity intensity in the overlapping region is relatively low. A consequence of the spectral overlap observed in Figure 5-2, is that although reabsorption is possible across most of the emission's spectral range, the probability of an emitted photon being reabsorbed at a given wavelength/energy is relatively low in the case of small samples. However, for larger LSCs and or high optical density LSCs utilising these particular CdSe/CdS core/shell nanorods, reabsorption losses are likely to be high and will greatly limit the LSC's optical efficiency.

5.4.2 Luminescent Quantum Yield

In the work of Carbone *et al.* [1], experimental results for the CdSe/CdS core/shell nanorods, in solution revealed that they had a LQY in the range 70-75%. Their work also revealed that the LQY is heavily dependent on the aspect ratio of the nanorods, with a LQY of only 10% being measured for their highest aspect ratio rods. As the nanorods featured in this chapter were produced by their group, assuming a LQY in the 70-75% range is not unreasonable, but as noted above, the aspect ratio needs to be considered. As stated previously, the nanorod sample used in this chapter was produced by Marco Zanella using the method described in Zanella *et al.* [3]. In this paper it is stated that it is possible to align nanorods with aspect ratios of between 3.5 and 10. Zanella did not provide the author with lengths of the nanorods used in the nanorod sample. However, he did state that the nanorods used to make the sample were intended to have a LQY of 70-75% [5], taking this and the aspect ratio work done by Carbone *et al.* [1] into account, it would suggest that the intended average aspect ratio of the nanorods was ~4. With this knowledge, and the observed broad emission spectrum (see

section 5.4.1) it is likley that the nanorods in this sample did not all have aspect ratios of ~4, and instead had a range of sizes (and range of aspect ratios), which would affect the average LQY. Furthermore, the high nanorod densities required for vertical self-alignment may have a detrimental effect on the LQY due to aggregation, potentially leading to emission quenching.

Using the LQY experimental method described in chapter 4 section 4.7, which is derived from the method described in reference [9], the LQY of the nanorod sample was measured as 51.9±0.5%. This measurement was performed whilst the nanorods were in a thin-film, and was taken within a month of the samples' initial fabrication. This measurement is obviously significantly different from the values of 70-75% quoted in the work of Carbone *et al.* [1]. However, as the LQY was measured for the film rather than for a dilute sample in solution there will have been some reduction in the experimental LQY due to reabsorption, although this is expected to be small as the sample's absorptivity is low in the region of spectral overlap. Also, as mentioned above, emission quenching due to aggregation or a different aspect ratio (or range of aspect ratios) may be the cause of the lower LQY measured for this sample.

It should be noted that some of the angular dependent absorptivity measurements, which are reported in section 5.6, were performed approximately a year after the LQY measurements. No special methods were employed when storing the sample during this period. The sample was kept in a laboratory cupboard (often dark conditions), in standard air and temperatures. Therefore it is possible that over this year the LQY may have declined possibly due to oxidation.

To summarise this section, it can be said that in addition to virtues possessed by nanorods such as high stability, wavelength tuneability etc., as described in section 5.1, these

CdSe/CdS core/shell nanorods have a relatively broad absorption spectrum, and a relatively narrow emission spectrum which will reduce thermalisation losses. It must also be noted that there is reasonably high spectral overlap between the absorption and emission spectrum that would lead to considerable reabsorption losses in a large or high optical density sample. Lastly, an LQY value of 51.9±0.5% was measured which, although lower than the 70-75% quoted in the work of Carbone *et al.* [1] for the same type of nanorods, could likely be improved by tuning the growth process. As size variations and LQY can potentially be limited in the future by optimising the growth process the CdSe/CdS nanorods have enough positive attributes to make them worthy of study as a possible luminescent species for an aligned LSC.

5.5 Spectroscopic Signatures of Nanorod Alignment: Surface Mapping

In this section absorptivity measurements are taken across the surface of the sample, creating a surface map of the sample in terms of absorptivity, to determine if there is nanorod alignment present, and if so to what extent. In a commercially practical LSC, any alignment would need to exist over the entire surface of the LSC. Furthermore, the nanorod film thickness measurements are also discussed, in order to clarify whether the changes in absorptivity are due to variations in thickness, or variations in alignment.

5.5.1 Absorptivity Map

Figure 5-3 shows a map of light absorptivity for the nanorod sample. This spectroscopic mapping technique allows the entirety of the nanorod LSC's top surface to be probed. This is something which is not practical with techniques such as SEM. SEM can provide great detail over a small scale, as can be seen in Figure 5-1, but, such an approach is not practical for determining the quality of alignment over a large area. A good degree of alignment over the surface of a large scale LSC would be essential, and the spectroscopic method used here

provides a relatively quick way to determine the level of nanorod order/disorder over the entirety of the LSC's top surface.

The incident light source used was a 473nm continuous wave (CW) laser, which impinged on the nanorod sample's surface at normal incidence. As can be seen there is significant variation in measured absorptivity across the surface of the sample, with the absorptivity at regions at the extreme edges of the sample being approximately twice that of the absorptivity over the central region. This suggests that there is either a substantial increase in the thickness of the nanorod film at the edges of the sample (this is later investigated, see section 5.5.2), or that the increase in light absorptivity with increased distance from the centre may be a result of increasing disorder further from the centre of the sample (or perhaps a combination of the two). Vertically aligned nanorods targeted by a direct light source, such as a laser at normal incidence to the LSC surface, would be expected to have lower absorptivity than other orientations of nanorods, due to the direction of their transition dipole. This being the case, Figure 5-3 may be showing evidence of a region of vertical nanorod alignment over the central region of the sample (see dark blue/purple region).

Increasing disorder of the nanorods will likely have resulted from the more rapid evaporation rates at the edges of the sample due to increased surface area [5]. With increased disorder, there will be less and less vertical alignment at greater distances from the centre. At normal incidence, vertically aligned nanorods will have the weakest absorption and, therefore, with increased disorder absorptivity will be increased as non-vertical rods have a higher absorption coefficient due to the increased light absorption perpendicular to the nanorods' long axis [1]. This loss of order towards the edges may be being shown in Figure 5-3 by the red regions in particular.

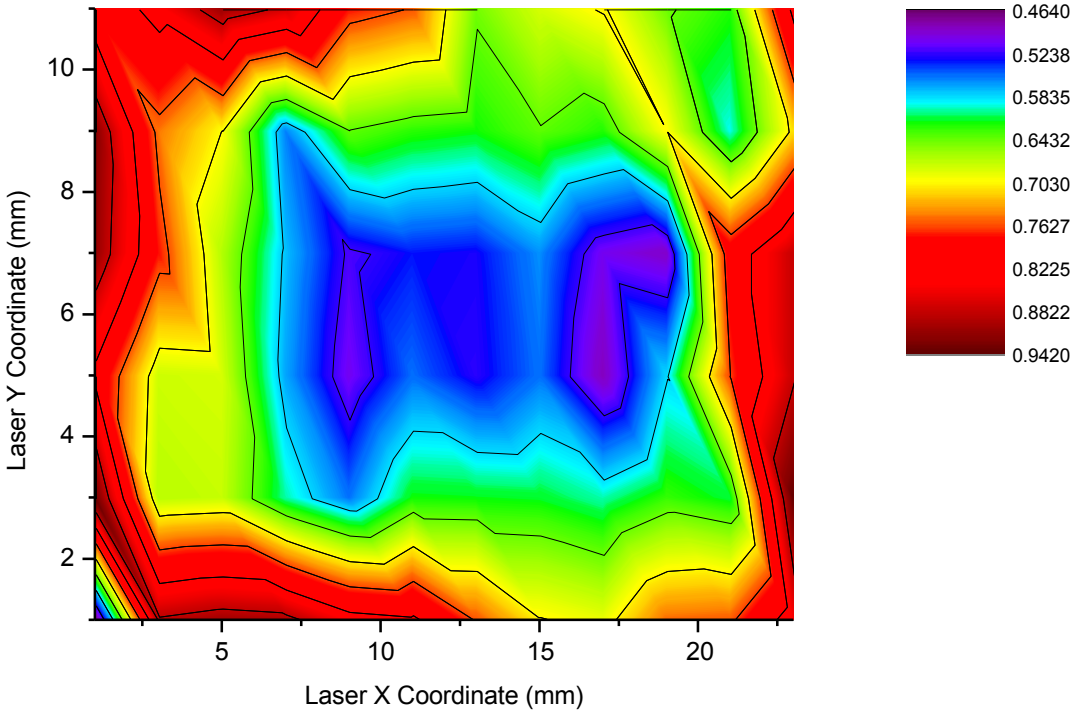


Figure 5-3 A position dependant absorptivity map of the nanorod sample using a 473nm laser as a light source.

Since the variations in absorptivity may be due to regional variations in thickness rather than alignment, the thickness of the nanorod thin-film was also investigated in an attempt to eliminate this as the cause of absorptivity variation.

5.5.2 Thin-Film Thickness Measurements

This subsection details the thickness measurements taken on the nanorod thin-film layer (as well as the thin-film layer on a Lumogen red 305 (BASF) control discussed in section 5.6). There were two motivations for determining the thickness of the thin-film layers. The first, as discussed above, was to get location specific thickness measurements so as to ascertain whether or not variations in thin-film thickness or alignment were responsible for the variations in absorptivity. The second motivation was to collect accurate thin-film thickness

measurements at 3 locations of interest (as determined from Figure 5-3), which were then used in section 5.6, to accurately calculate the absorption coefficient, and thus the angular dependent absorptivity at these 3 positions of interest. These positions of interest referenced by the X and Y coordinates of Figure 5-3, were (X,Y) = (12.5,6.25), (18.5,6.25) and (21.5,6.25), and will henceforth be referred to as 12.5mm, 18.5mm and 21.5mm respectively. Obviously for these positions to be of use in later experiments it was essential to always know which edge was which. In practice this was relatively easy due to easily recognisable features around the sample's edges, and by storing the sample with the same orientation after each experiment.

The three locations of interest are illustrated in Figure 5-4 and were chosen in the hope that if significant differences in the level of vertical nanorod alignment existed at the edges, when compared to the sample's centre, (as suggested in the work of Zanella *et al.* [5] and further indicated by Figure 5-3 above) that the extent of variation between the centre and the edges and across the film could be determined. Angular dependent absorptivity measurements were deemed counterproductive at positions even closer to the edge than position 21.5mm, since areas of incomplete thin-film coverage at the extreme edges of the sample increased the possibility of erroneous results.

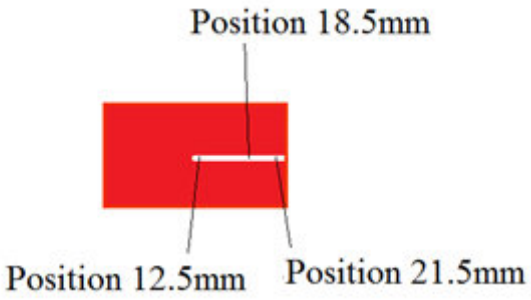


Figure 5-4 Diagram showing the general locations of the thin-film thickness measurements.

Table 5-1 and Table 5-2 show the measured thin-film thicknesses for the control sample and nanorod sample respectively, while Table 5-2 also contains the corresponding absorption coefficient, calculated using equations 2.11 (Beer's law) and 2.13 (absorptivity) from chapter 2 (with transmission being extracted from Figure 5-3 data). The thicknesses were measured by scoring the thin-film down to the substrate and measurements of the change in height between the substrate and surrounding thin-film were performed using an Alpha step profilometer scanned across the score mark (see section 4.12, chapter 4 for full method). It is interesting to note that even though the control sample was fabricated by a spin-coating method (see chapter 4 section 4.13.2), the data in Table 4-1 show that the thickness of the thin-film is relatively uniform with a variation of around 1.5% and without a build-up of material at the LSC edges. As a result of relatively even thin-film thickness the absorption coefficient is also relatively constant across the control sample's surface.

Position Measured	Film Thickness (µm)±0.01
12.5mm (central)	9.10
18.5mm	9.24
21.5mm (edge)	9.09

Table 5-1 Measurements of the thin-film thickness of the control sample at the 3 positions coinciding with the angular dependent absorption measurements (see section 5.6).

Table 5-2 shows the extent of the variations in the measured thickness of the nanorod sample's thin-film, with the thickness measured at position 21.5mm, i.e. nearest to the edge being slightly thicker than the measurements closer to the centre. However, the difference is less than 3% whereas Table 5-2 shows a large difference between the absorption coefficients calculated for the 3 positions, with the measurement at the edge (position 21.5mm) being

$5.01\pm0.25\text{x}10^{6}$ m^{-1}, which is approximately twice that measured at the centre (position 12.5mm) of $2.65\pm0.13\text{x}10^{6}$ m^{-1}. Therefore, the variations observed in Figure 5-3, are likely only minimally related to the small variations in thickness across the thin-film of the nanorod sample. If thickness variations are not the main cause of the substantial variations in absorptivity shown in Figure 5-3, then it seems likely that the differences are due to vertical nanorod alignment near to the centre of the sample (low absorptivity dark blue regions), and non-vertical nanorod alignment closer to the edges (high absorptivity red regions).

In retrospect, additional measurements at different positions across the surface of the nanorod sample would have been useful, so as to gain a greater understanding into the level of thin-film thickness variations across the sample as a whole. If possible additional measurements closer to the sample's edge would have been particularly useful (position 21.5mm is 2.5mm away from the edge) since this region has the highest absorptivity and should also be the most disordered [3] as well as potentially the thickest due to increased surface tension. However, as mentioned above, Alpha-step measurements are very destructive and it was decided to limit the damage in order to be able to usefully perform further measurements on the nanorod sample at a later time if required. The results in Table 4-2 also suggest that by position 18.5mm, which is approximately halfway to the edge, that the alignment has already dropped off somewhat because, although the measured thickness is almost exactly the same, the absorption coefficient has increased by around 15%.

Position Measured	Film Thickness (nm)±10	Absorption Coefficient (m^{-1}) (Error ±5%)
12.5mm (central)	282	$2.65x10^6$
18.5mm	283	$3.09x10^6$
21.5mm (edge)	290	$5.01x10^6$

Table 5-2 Measurements of the thin-film thickness of the nanorod sample at the 3 positions measured during angular dependent absorption measurements.

To summarise, this section has strongly suggested that there is nanorod alignment limited to a region of the nanorod thin-film located close to the centre of the sample. Figure 5-3 shows significantly lower absorptivity at the centre of the sample compared to the edges, and thickness measurements have quite conclusively shown that the variation in absorptivity cannot be accounted for by changes in the film thickness alone. Therefore, Figure 5-3, together with the thickness measurements, suggests that the nanorod alignment is limited to the centre of the sample, and that the nanorods do not have order over the entirety of the film. However, long range order would be required for a commercially viable LSC.

5.6 Spectroscopic Signatures of Nanorod Alignment: Angular Absorption Profiling

In this section angular dependent measurements carried out in order to determine the angular dependent absorptivity of the nanorod sample at different locations on its top surface are discussed. These measurements, which included angular dependent transmission, reflection and scattering, were used in an attempt to further evaluate the degree of self-alignment of the nanorod sample (see chapter 4, section 4.11 for experimental methods). In section 5.5.1, the absorption map clearly showed that absorptivity is weakest at the centre of the nanorod sample, but is much stronger towards the edges. Section 5.5.2 revealed the changes in thin-

film thickness cannot be solely responsible for the position dependent variation in absorptivity. However, even taken together these facts cannot definitively confirm the presence of aligned nanorods in the sample. Therefore angular dependent absorptivity measurements were performed, since these measurements are capable of identifying aligned dipoles, as isotropic and dipolar absorbers have different angular signatures as discussed below in section 5.6.3. Furthermore, the model described in section 5.6.3 identifies a parameter, β, which indicates the level of alignment which exists at a specific location.

The angular dependent absorptivity measurements were also used to determine how rapidly alignment was being lost (at increased distance from the centre of the sample), which is essential knowledge which will be needed if larger LSCs are to be made with this self-alignment technique in the future. Lastly, the angular dependent absorptivity response is compared to an isotropic luminescent control sample. The specific locations of interest in these measurements were 12.5mm, 18.5mm and 21.5mm as identified above. In addition, since the refractive index of these samples was unknown, calculations were performed to the determine the effective refractive index of the nanorod thin-film, since this is essential for calculating theoretical angular absorptivity values, and for later ray-trace simulations (see section 5.8).

5.6.1 Theoretical Absorptivity: Nanorod and Control Samples

The following describes how theoretical angular dependent absorptivity values were calculated. These calculations were important as they show how the absorptivity as a function of incident angle differs between a sample with directional absorption when compared to an isotropically absorbing sample. By fitting the experimental data with the angular absorptivity model it is possible to estimate the fraction of dipoles that are aligned.

5.6.1.1 Reflectance

When calculating and plotting angular dependent theoretical absorptivity values for samples with dipolar absorption or samples with isotropic absorption, it was necessary to determine realistic values for both reflectivity and transmission. Both the nanorod and the control samples consisted of multiple boundaries between different materials, each having its own refractive index (see section 5.6.4 for the nanorods' refractive index). In the case of the nanorod sample, there existed boundaries of air/optical matching fluid, optical matching fluid/nanorods, nanorods/glass and glass/ air as illustrated in Figure 5-5. The matching fluid was left over from a previous experiment, and, since it would have damaged the sample to remove it, it was not removed which may have meant that the surface was not quite planar. The control sample featured a similar range of materials, but with a Lumogen red 305 rather than a nanorod layer. The geometry of the incident laser with respect to the sample surface resulted in *p* polarised light and therefore equation 2.6, chapter 2, was used to calculate the reflection at each boundary. The sum of the calculated reflectances at each interface was used to determine the total theoretical reflection value from the nanorod sample's surface, and was then used for the theoretical absorptivity calculations.

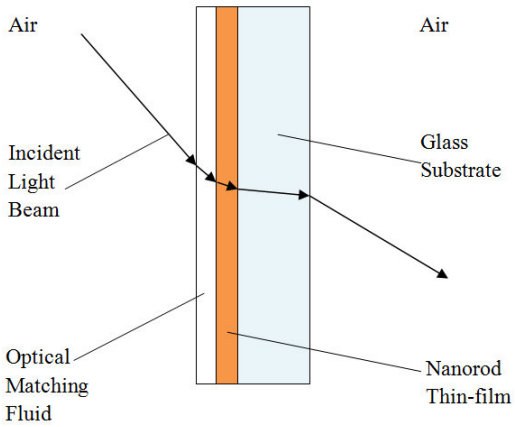


Figure 5-5 Diagram showing a side-view of the different material boundaries (each of which with a different refractive index) present in the nanorod sample.

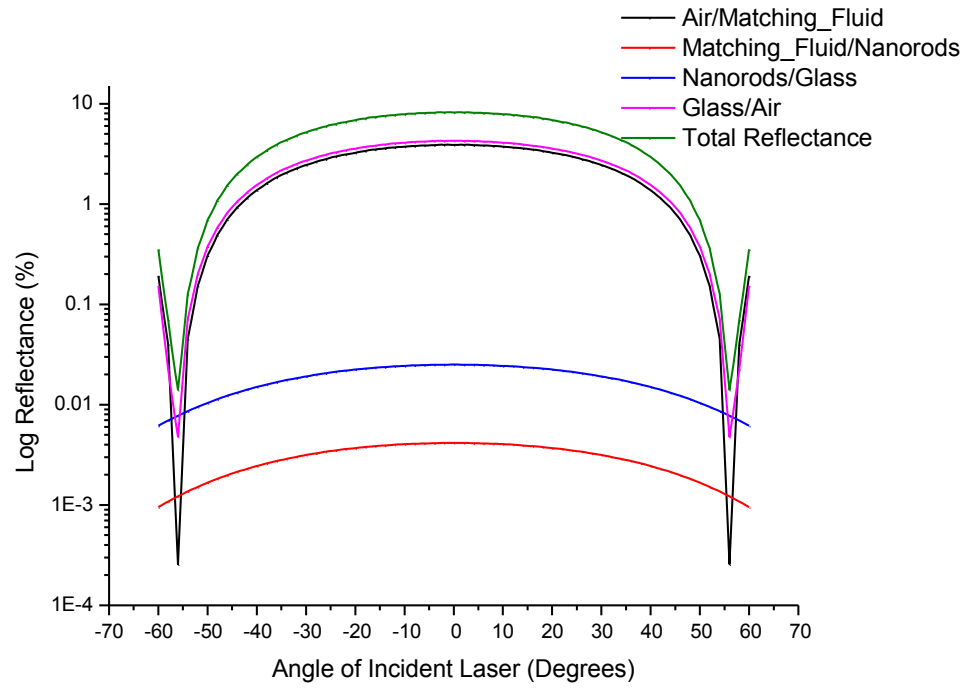


Figure 5-6 Logarithmic graph of the percentage reflectance loss between each of the boundaries present in the nanorod sample, as a function of incident laser angle.

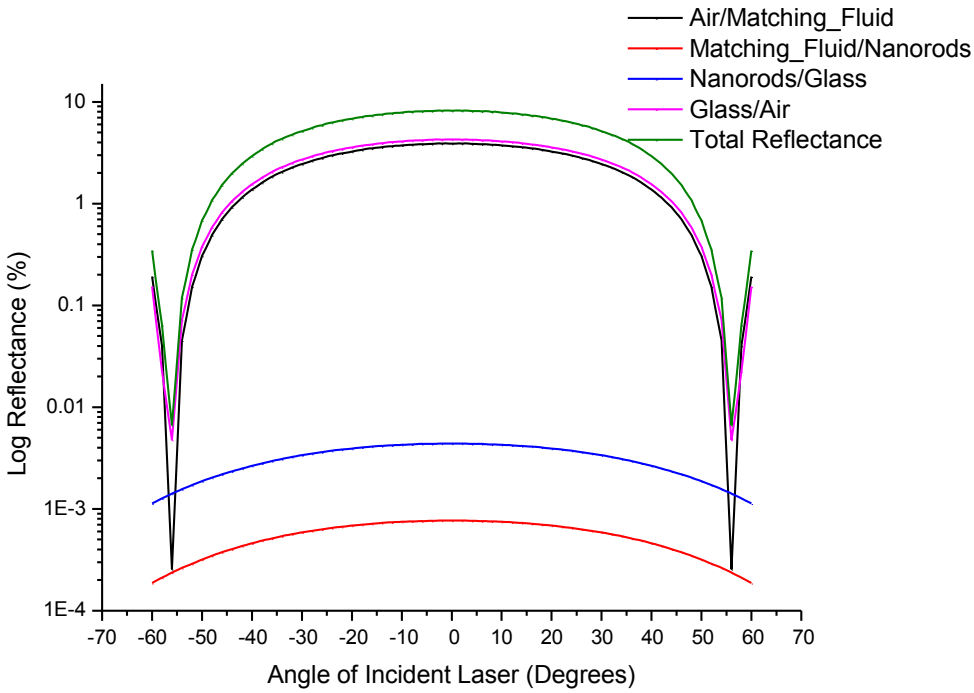


Figure 5-7 Logarithmic graph of the percentage reflectance loss between each of the boundaries present in the control red 305 sample, as a function of incident laser angle.

Figure 5-6 and Figure 5-7 show the log percentage reflectance losses at each material boundary within the nanorod and control samples respectively. An effective medium calculation is used for the nanorod refractive index, and is described in section 5.6.4. Unsurprisingly, for both samples the majority of reflection losses occur at the air/matching fluid and glass/air boundaries, which is due to the large refractive differences between air, n=1.0003, and matching fluid, n=1.4917, and air and glass, n=1.52. The differences between the refractive indices of two different materials in contact with one another cause a change in the velocity of the photons as they move from one material to the next. The velocity change between materials also changes the refraction angle as the photon moves between the two media. It can be seen from Figure 5-8 and Figure 5-9 how significantly the angle of incidence is changed, due to refraction, from the external angle when compared to the internal angle. The internal angle never exceeds ±40° despite the fact the incident laser beam moves up to ±60° with respect to the surface of the sample.

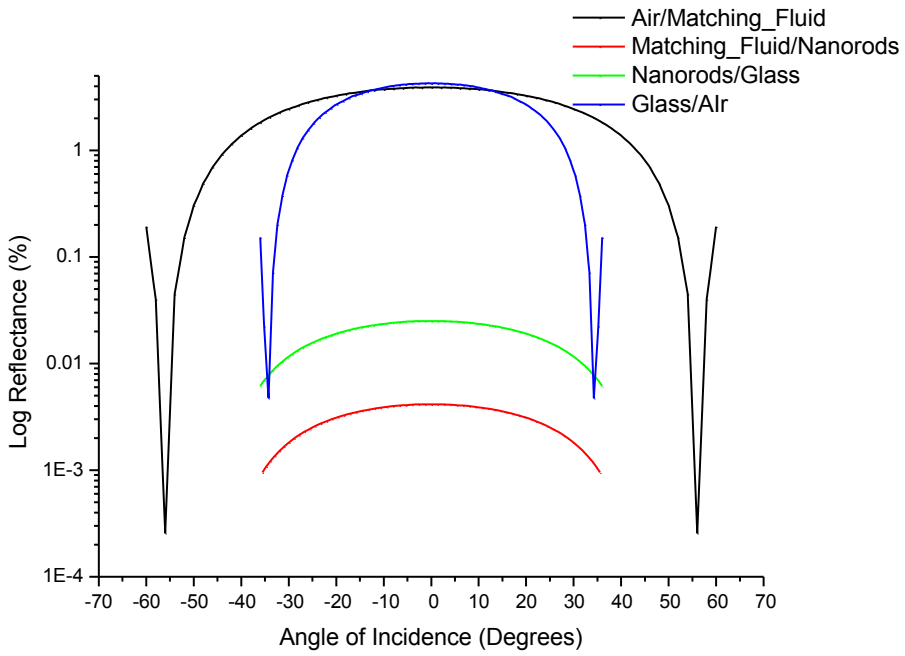


Figure 5-8 Logarithmic graph of the percentage reflectance loss between each of the boundaries present in the nanorod sample, as a function of internal/external angle.

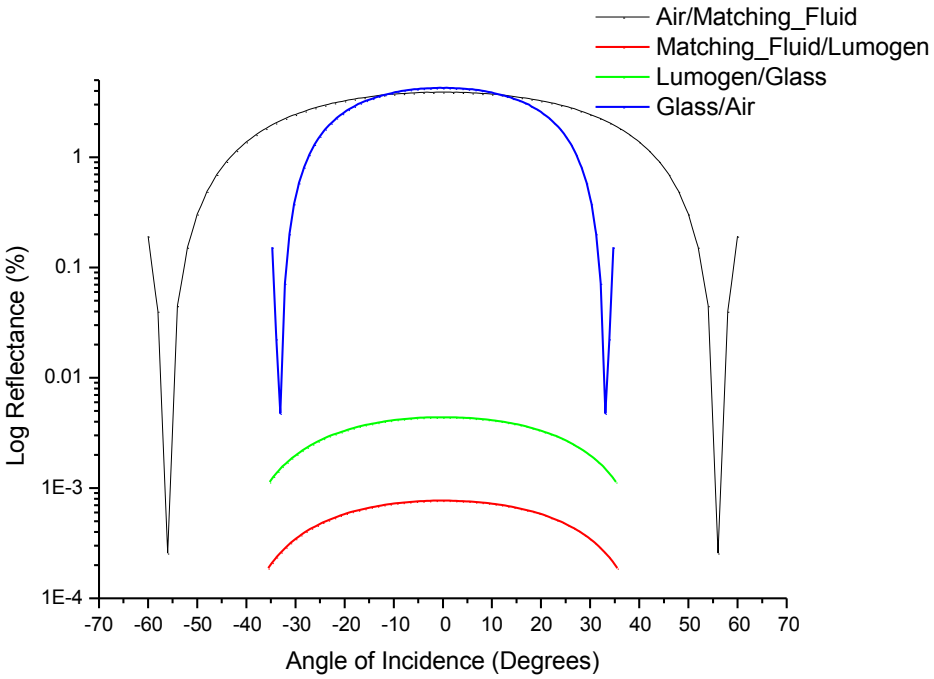


Figure 5-9 Logarithmic graph of the percentage reflectance loss between each of the boundaries present in the control sample, as a function of internal/external angle.

5.6.1.2 Theoretical Transmission Values

Theoretical transmission values were obtained by taking a transmission measurement (using the 473nm laser, and the silicon photodetector) at normal incidence, at the position of interest (corresponding to one of the 3 positions shown in Figure 5-4). The transmission value measured at the chosen position, along with a measurement of the thin-film thickness (see section 5.5.2) at this position, were input into the Beer-Lambert equation (see sections 4.11, 4.12, chapter 4, for angular transmission and thickness measurement methods respectively) to calculate the absorption coefficient at normal incidence, at the chosen position. The path-length through the thin-film for the incident light varies as a function of incident angle and therefore the Beer-Lambert equation was modified to include an angularly dependent path-length.

Equations 5.8, 5.9 and 5.10 were used to calculate the theoretical absorptivity values:

$$A(\theta) = 1 - \big(1 - R(\theta) - S(\theta)\big)e^{-\alpha f(\theta)x(\theta)} - R(\theta) - S(\theta) \qquad 5.8$$

In equation 5.8 $A(\theta)$ is the angular dependent absorptivity, $R(\theta)$ is the angular dependent reflection (see section 5.6.1.1), $S(\theta)$ is the angular dependent surface scatter, α denotes the absorption coefficient (normal incidence), $f(\theta)$ is the angular dependent function describing the degree of alignment and $x(\theta)$ is the angular dependent optical path-length in the thin-film. For an isotropic absorber/emitter all angles have the same absorption strength, therefore,

$$f(\theta) = 1 \qquad 5.9$$

For dipolar emitters, the angular distribution follows a $sin^3(\theta)$ distribution as defined in section 5.3, equation 5.7. However, the dipole absorption follows a $cos^2(\theta)$ distribution as shown in equation 5.10. The $cos^2(\theta)$ dependence is due to the light absorption probability of a dipole being proportional to the square of the cosine of the angle being between that of the polarisation vector of the incident light, and the nanorod's transition dipole moment [10] (the power 2 dependence arises from Fermi's Golden Rule, see equation 5.1).

$$f(\theta) = \beta C cos^2(\theta) + (1 - \beta) \qquad 5.10$$

In equation 5.10 β is a linear interpolation parameter which describes the level of alignment of the emitting species, ranging from 0 for completely isotropic to 1 for perfectly dipolar. C is a scaling factor which accounts for the apparent increase in absorption coefficient when comparing aligned and isotropic absorbers. For example, if a volume of randomly oriented dipoles is exposed to a unidirectional and linearly polarised light source at normal incidence

to the surface of the volume (i.e. along the z direction, equivalent to the laser beam used in experiments) [11], then a simple geometric argument can be used to explain that the polarisation vector makes a non-zero projection on 1/3 of the dipoles. For a similar situation in which the dipoles are all aligned either along the x or the y directions, then the incident light is able to couple to all of the dipoles. Therefore, this would suggest that a volume with perfectly aligned dipoles would have an absorption coefficient 3 times larger than for a volume containing randomly oriented dipoles. This being the case, for a nanorod film with perfect alignment C=1, whereas for a perfectly randomly oriented nanorod sample C=1/3. C is used as a fitting parameter in the theoretical model described above (see section 5.6.3) and is defined as the ratio of the maximum normal incidence absorptivity for aligned nanorods to the maximum normal incidence absorptivity for an isotropic distribution. θ is the (internal) angle of the incident laser beam (see section 4.11, chapter 4).

5.6.2 Scatter and Reflection Results

Surface scatter and reflection were measured for the nanorod sample and the control sample at the positions 12.5mm, 18.5mm and 21.5mm described in section 5.5.2, and the experimental details are given in section 4.11.2, chapter 4.

Due to the obvious variations in the surface roughness noticeable by both visual inspection and from evidence suggested by the surface absorptivity map in Figure 5-3 the scatter/reflectance measurements were taken at the same three points on the surface of the nanorod sample that the angular dependent absorptivity measurements were taken. The results are illustrated in Figure 5-11. Prior to the scatter/reflection measurements on the control sample, it was visually apparent that there was far less variation in surface roughness across the control sample's surface (the thin-film thickness was also very uniform), as shown in section 5.5.2, than was the case for the nanorod sample. Therefore, the surface

scatter/reflectance was only measured at two separate locations, both of which gave near identical results as can be seen in Figure 5-11.

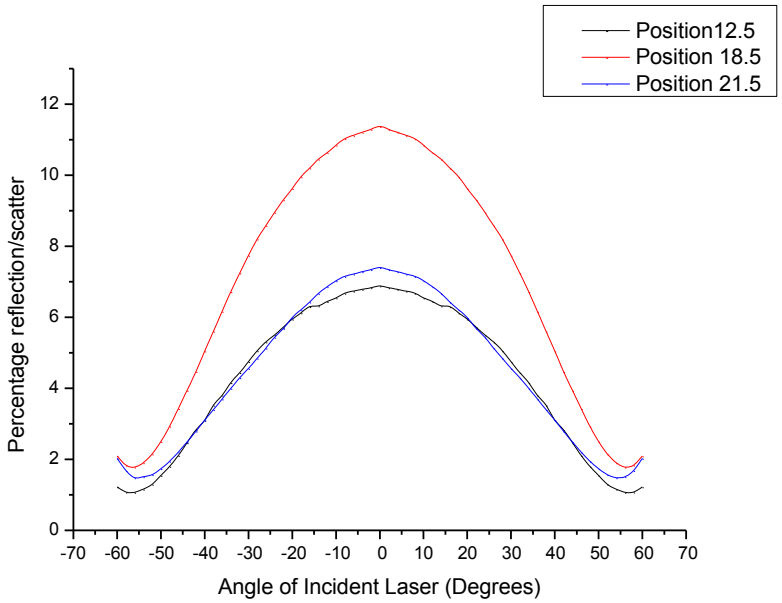


Figure 5-10 Graph of the position dependent percentage scatter/reflectance losses, for the nanorod sample, relative to the angle of incidence of the 473nm laser.

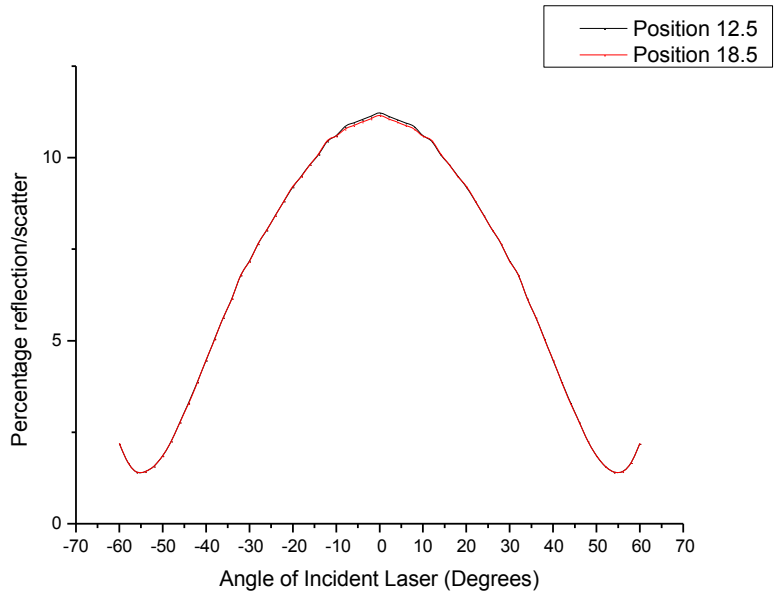


Figure 5-11 Graph of the position dependent percentage scatter/reflectance losses, for the Lumogen red 305 control sample, relative to the angle of incidence of the 473nm laser.

It is interesting to note from Figure 5-10 that for the nanorod sample the combined reflectance/scatter measured for position 18.5mm is considerably higher that that measured at positions 12.5mm and 21.5mm, the centre and edge of the sample respectively, which are relatively similar to one another. The higher reflectance/scatter measured at position 18.5mm coincides with the border location of the low and high absorptivity regions on the nanorod sample, as shown by the absorptivity surface map seen in Figure 5-3. Since it is unlikely that the refractive index would change dramatically across the sample's surface, the difference seen in the reflectance/scatter measurements for the different positions is likely due to scatter. Position 18.5mm may be an area with particularly high thin-film defects formed due to different rates of solvent evaporation, across the thin-film, when the sample was produced. It may be that at position 18.5mm, any verticle alignment present at the centre of the nanorod sample is abruptly lost at position 18.5mm, due to different evaporation rates, and this is instead a region with a higher degree of randomness associated with the nanorods' orientation. If this is indeed the case, it is strange that position 21.5mm (edge) appears to have similar scatter to that of position 12.5mm (centre). This coupled to higher absorptivity measured towards the edges of the nanorod sample (see Figure 5-3), suggests that perhaps there is some level of horizontal nanorod alignment close to the sample's edges, or that the because the sample is slightly thicker at the edge (see Table 5-2) it may have a better surface quality there.

5.6.3 Absorptivity: Measured and Theoretical Comparison

Figure 5-12 to Figure 5-16 show experimental and theoretically calculated results for angular dependent absorptivity for both the nanorod sample and the Lumogen red 305 control sample, at positions 12.5mm, 18.5mm and 21.5mm. In section 5.6.1, there is a thorough description of how the theoretical absorptivity values for both dipolar and isotropic absorber/emitters, at varying angles of incident light source, were calculated. The theoretical results can be

compared with the experimental results in Figure 5-13 and Figure 5-16. The experimental angular dependent absorptivity (see section 4.11, chapter 4 for methods) results depicted in the figures were found using equation 5.11:

$$A(\theta) = 1 - R(\theta) - T(\theta) - S(\theta) \qquad 5.11$$

In equation 5.11 $A(\theta)$ is the angular dependent absorption, $R(\theta)$ is the angular dependent reflection, $S(\theta)$ is the angular dependent scatter (both reflection and scatter were measured in one experiment, see section 5.6.2 and section 4.11, chapter 4 for angular dependent methodologies) and $T(\theta)$ is the angular dependent transmission.

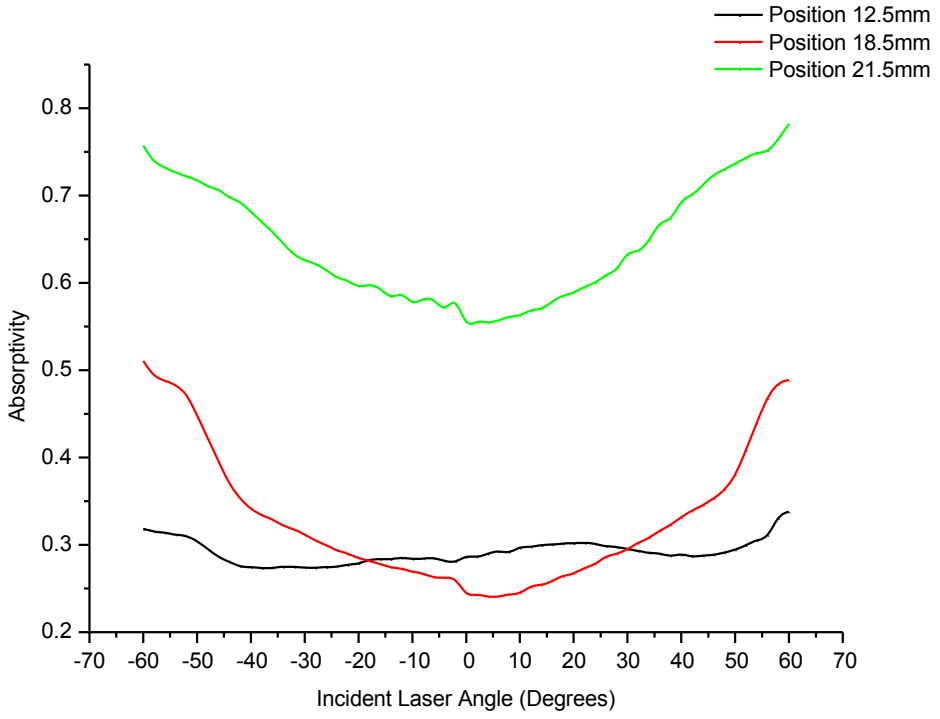


Figure 5-12 Graph of the angular dependent absorptivity at positions 12.5mm, 18.5mm and 21.5mm on the nanorod sample.

From Figure 5-12, that shows the experimental results for the nanorod sample, it can be seen that the results for position 12.5mm (centre of sample) appear much flatter than the results taken at positions away from the centre (which have approximately "U-shaped" absorptivity distributions). This clear difference in angular dependence provides additional evidence of ordered arrays of vertical nanorod alignment at the centre of the nanorod sample. This figure also seems to show that the ordered arrays of vertically aligned nanorods are rapidly lost, since despite the similarly low absorptivity intensities for position 12.5mm and 18.5mm, the angular dependence is clearly different. This may imply that by position 18.5mm, that while a significant portion of the nanorods may be oriented just off vertical; they likely have little long range orientational order. At position 21.5mm, the nanorods likely have completely or near completely random alignment.

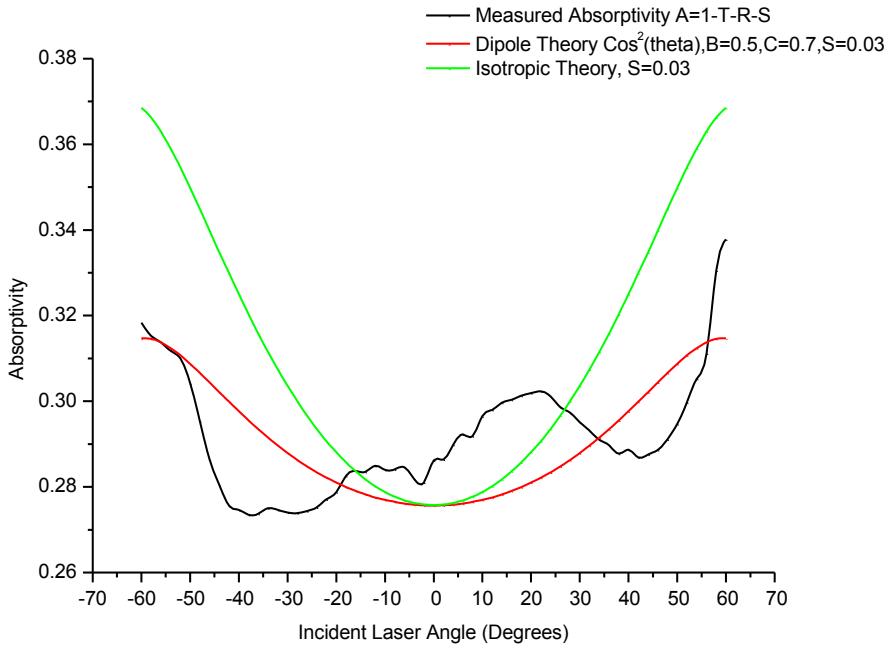


Figure 5-13 Angular dependent absorptivity at position 12.5mm for the nanorod sample, as well as the theoretical dipolar and isotropic angular absorptivity distribution.

In Figure 5-13 the angular dependent absorptivity distribution at position 12.5mm on the nanorod sample is compared with the theoretical distributions. The green line shows the theoretical angular absorption distribution for an isotropic absorption/emission sample (from equation 5.8 and 5.9 and the theoretical data, such as reflection in section 5.6.2). This isotropic distribution was originally slightly offset from the measured value which was rectified by factoring in a theoretical value for scattering losses, S, in this case 3%. However, it is clear to see that an isotropic distribution does not match the shape of the measured angular dependent absorptivity.

The theoretical angular dependent absorptivity distribution in Figure 5-13, which had a $cos^2(\theta)$ dependence (see section 5.6.1.2), was produced using the theoretical values of reflection and angle dependent pathlength, as well as the experimentally measured value of absorption coefficient at position 12.5mm on the nanorod sample. It can be seen that when the constants β and C are equal to 0.5 and 0.7 respectively (constants are explained in section 5.6.1.2), and a scatter value of 0.03 (3%) is used, then a significant match (both shape and absorptivity intensity) exists between the theoretical dipole distribution and the measured angular dependent absorptivity distribution. Since, as described in section 5.6.1.2, a β value of 0 exists for a perfectly isotropic emitting sample, and a value of 1 for a perfectly dipolar sample, therefore, a value of 0.5 (i.e. 50% of dipoles are vertically aligned) suggests dipolar absorption is occurring. The 0.7 value of C, as explained in section 5.6.1.2, implies that there is a reasonable level of nanorod alignment, since the C scaling factor ranges from 1/3 for no alignment, to 1 for perfect alignment. Therefore, taking into account the shape of the theoretical angular dependent absorptivity dipole graph, and the values of β and C, it can be said that there is quite significant nanorod alignment at position 12.5mm (the centre) of the nanorod sample.

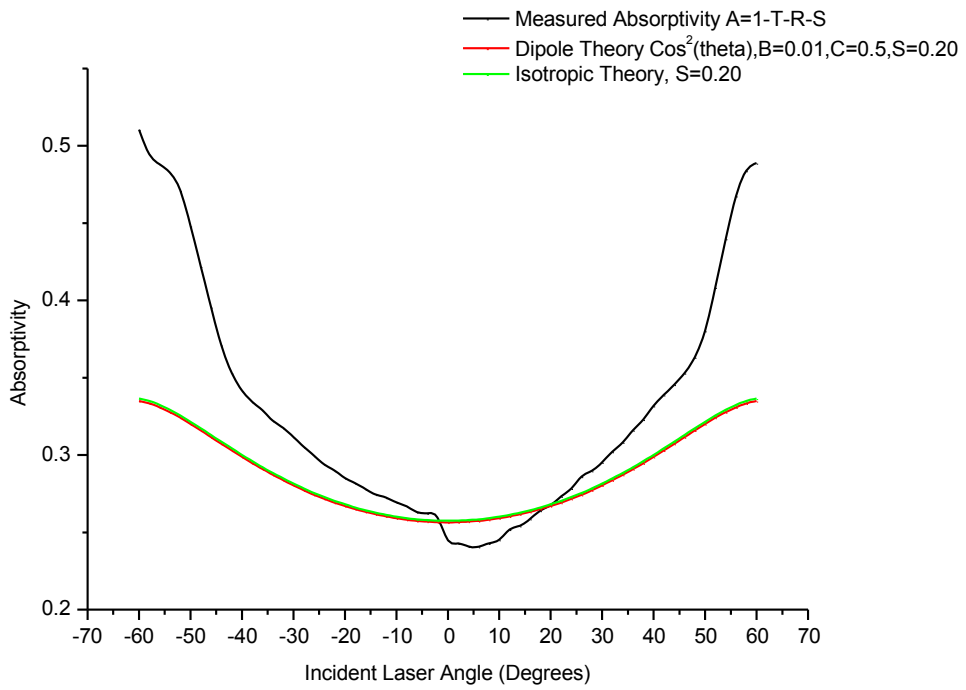


Figure 5-14 Angular dependent absorptivity at position 18.5mm for the nanorod sample, as well as the theoretical dipolar and isotropic angular absorptivity distribution.

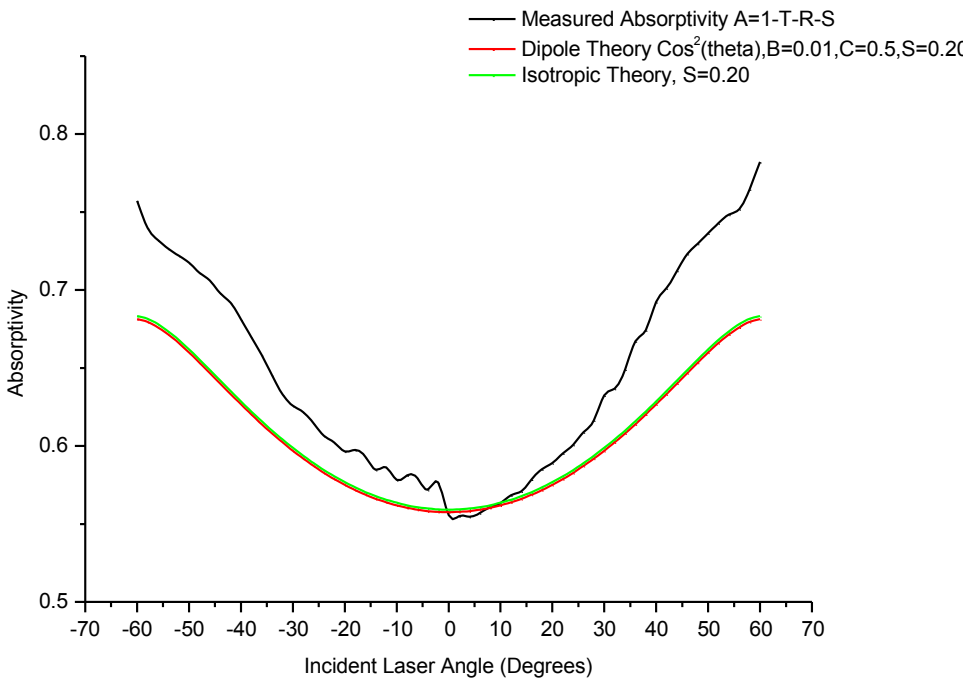


Figure 5-15 Angular dependent absorptivity at position 21.5mm for the nanorod sample, as well as the theoretical dipolar and isotropic angular absorptivity distribution.

Figure 5-14 and Figure 5-15 show the angular dependent absorptivity spectra for positions 18.5mm and 21.5mm, on the nanorod sample, respectively. As was described above for position 12.5mm, an attempt has been made to match the isotropic theory and the dipolar theory with the experimentally measured angular dependent absorptivity. In both Figure 5-14 and Figure 5-15, it can be clearly seen that in order to match the shapes, and absorptivity intensities, of the dipolar theory with the measured absorptivity, the dipolar theory results have essentially become the same as the isotropic theory results. It was only possible to fit the dipole theory to the experiment by using $\beta = 0.01$, $C = 0.5$ and $S = 0.2$ for position 18.5mm, and by using $\beta = 0.01$, $C = 0.5$ and $S = 0.03$ for position 21.5mm. In both cases, such low values of β show that there was essentially no nanorod alignment at either of these positions, and this ultimately implies that the nanorod alignment was lost completely at distances of 6mm or more from the centre of the nanorod sample (and perhaps at distances even closer to the centre of the sample).

Lastly, it should be noted that in Figure 5-14, a scatter value of 0.20 (or 20%) was required to correct for the off-set in absorptivity observed for the isotropic and dipole fits, which is much higher than the values used for either of the other locations. Although it is clear from Figure 5-10 that position 18.5mm has greater surface scatter losses than either position 12.5mm or 21.5mm, the measurements in Figure 5-10 do not suggest the difference should be as significant as is shown in Figure 5-14. An explanation for this may be that there is increased subsurface scattering occurring for absorptivity measurements at position 18.5mm.

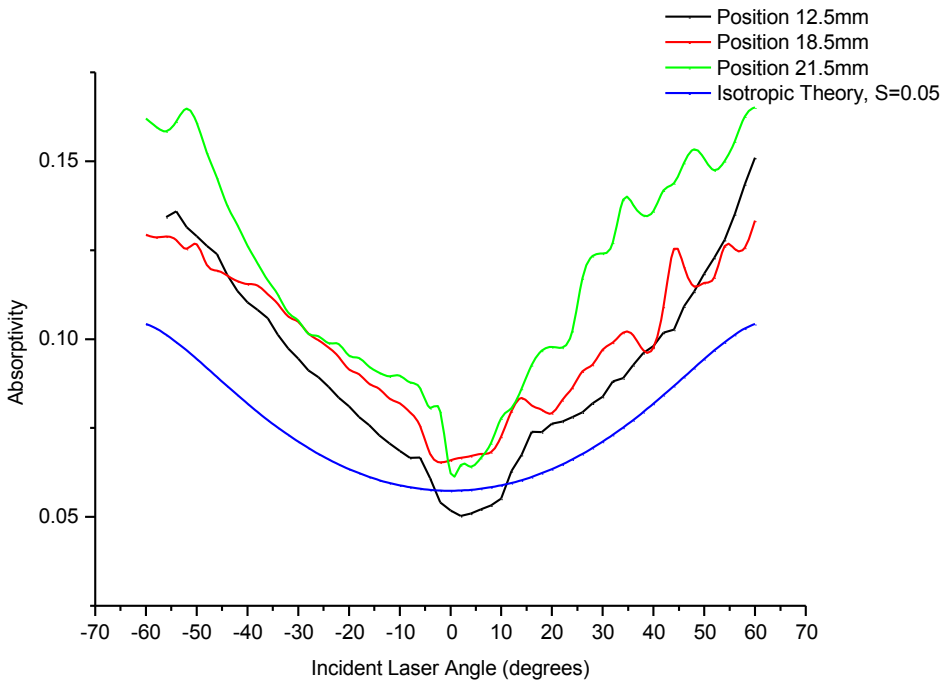


Figure 5-16 Graph of the angular dependent absorptivity at positions 12.5mm, 18.5mm and 21.5mm on the Lumogen red 305 control sample.

Figure 5-16 above shows the theoretical and measured absorptivity results for the Lumogen red 305 control sample. As mentioned in section 5.1, the control sample was chosen because although the individual molecules of the dye are dipolar absorbers/emitters, when in large numbers, and without any special preparation to align the molecules, thin-film LSCs made with Lumogen red 305 serve as isotropic absorbers/emitters. It can be seen in Figure 5-16 that all three measured positions match well to the isotropic theory graph. It should be noted that the difference between the maximum and minimum absorptivities for the 3 experimentally measured positions is larger than for the isotropic theory results, perhaps suggesting angular dependent scatting losses. A theoretical scatter value of 0.05 (5%) was used to correct for an offset that existed between the isotropic theory and the 3 experimental measurements. Unlike for the nanorod sample, at no position does there appear to be evidence for alignment of the luminescent species.

By comparing the measured results for the nanorod sample to those of the control sample, and by considering how the experimental results for position 12.5mm is a good fit for the theoretical dipolar absorptivity, it can be concluded that there is a high probability that a localised region close to the centre of the nanorod sample does indeed have aligned nanorods. As described above, this determination of the nanorod sample's alignment was achieved by an optical approach, and did not require the use of destructive SEM techniques.

The evidence for limited alignment at the centre of the nanorod sample is further supported by the work of Zanella *et al.* [3], who used an x-ray diffraction approach to determine that for a central region of approximately $1cm^2$ the nanorods were vertically aligned. However, their work suggested that the vertical alignment was lost gradually as the distance from the centre of the sample increased. In contrast the results of this work suggest that the nanorods are aligned at the centre, but that this alignment is completely lost by a distance of only 6mm from the sample's centre, i.e. by position 18.5mm. Zanella *et al.* [3] identified variations in the solvent evaporation rate as the probable cause for loss of alignment nearer to the edges, since solvent located nearer to the edge of the sample has a larger surface area and will evaporate more rapidly. Variations in evaporation rate seems to be a plausible explanation, since the nanorod sample investigated here seems to lose alignment rapidly, away from the sample's centre, and it is reasonable to hypothesise that evaporation towards the edges of the sample would be more rapid resulting in a loss of nanorod order.

In conclusion, since the region of alignment is localised in the centre of the nanorod sample, and in a relatively small area, this may reduce the practicality of this particular alignment method for LSCs of any realistic size (i.e. greater than a few cm in size). Therefore, to be effective for use in LSCs, efforts may be needed to make the rate of solvent evaporation across the surface of a drying nanorod sample even. This may be possible by locally controlling the temperature of the sample, but would not be a trivial matter. However,

without further testing it is difficult to be conclusive, since the sample provided was only small and therefore edge effects acting over a cm or so would be particularly pronounced. It may indeed even be the case that a larger proportion of a larger sample would be aligned.

5.6.4 Refractive Index of Nanorod Samples (Effective Medium Theory)

In the field of LSCs, it is of great importance to know, or at least have a reasonable hypothesis of what the refractive indices of the constituent parts of the LSCs are, since both incident reflection and TIR are highly dependent on this parameter (see section 2.4.4, chapter 2). In the case of the CdSe/CdS core/shell nanorods used in the nanorod sample, the refractive index of the thin-film was unknown due to the multiple constituents of which the thin-film consists. These constituents included: Cd, Se, S, air (likely trapped due to the cylindrical shape of the nanorods) and the organic ligands which coat the nanorods (these ligands act to separate the nanorods from one-another). As a consequence, it is necessary for an estimate of the refractive index to be derived from the available information, using a method known as Effective Medium theory and by using equation 5.12, which is an adaptation of the Maxwell-Garnett equation [12], that can be rearranged to give equation 5.13:

$$\frac{n_{eff} - n_H}{n_{eff} + 2n_H} = F_L \frac{n_L - n_H}{n_L + 2n_H} \qquad 5.12$$

$$n_{eff} = n_H \frac{n_L(1 + 2F_L) - n_H(2F_L - 2)}{n_H(2 + F_L) + n_L(1 - F_L)} \qquad 5.13$$

In the equations above n_{eff} is the effective refractive index, n_H is the refractive index of the higher index component, n_L is the refractive index of the lower index component and F_L is

the volume fraction of the lower index material. This particular Effective Medium equation is known as the Maxwell-Garnett Theory [12].

It is believed that the nanorods in these vertically aligned samples are arranged with a triangular period lattice, since it is assumed that the individual nanorods are hard spherocylinders (see Figure 5-1A and Figure 5-17), and this type of arrangement is the result of the high nanorod concentrations required for self-alignment [3]. However, Zanella *et al.* [3], by whom the nanorod sample was fabricated, state that "the rods cannot be completely considered as hard sphereocylinders", due to the soft organic ligands attached to the nanorods and other factors such as Coulomb interactions. However, in order to simplify the effective medium calculations, the nanorods are assumed to be hard sphereocylinders arranged in a hexagonal lattice.

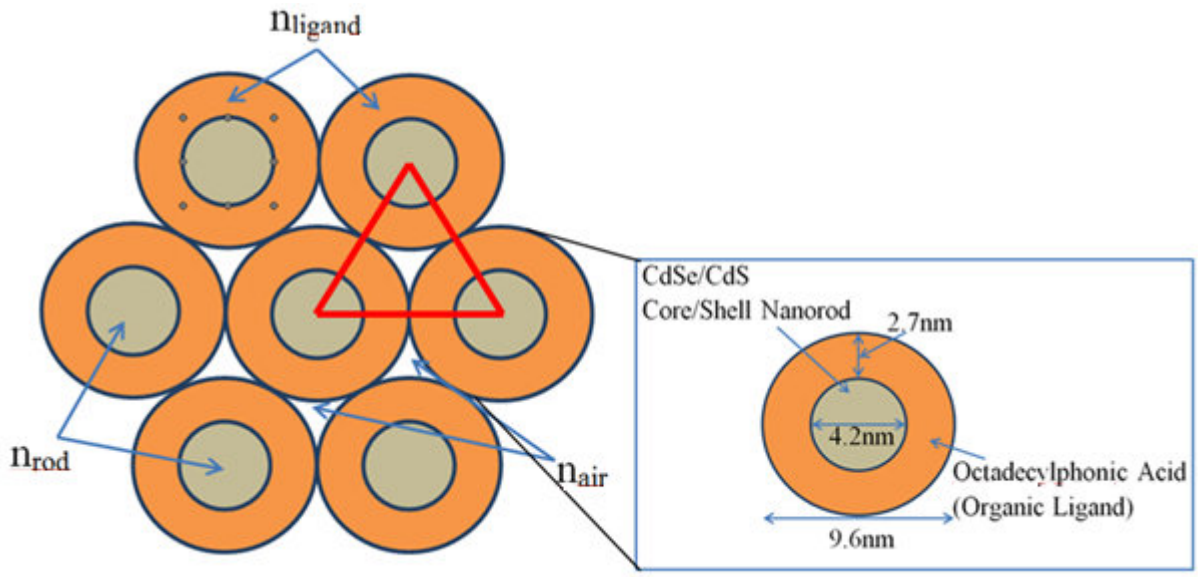


Figure 5-17 Diagram showing a unit cell of vertically aligned nanorods. Diagram highlights the different refractive indices present in the nanorod thin-film.

Some assumptions needed to be made when calculating n_{eff} due to unknown parameters (Figure 5-17, highlights the known nanorod component dimensions). The most significant of these assumptions is related to the thickness of the CdS shell component of the nanorod. Since this thickness is unknown, three logical choices are presented which may be used as the refractive index for the inorganic component of the nanorods. 1) It can be assumed that the majority of the inorganic part of the nanorod is made up of the core material CdSe, and as such the refractive index of bulk CdSe can be used (see Table 5-3). 2) The inorganic part can be assumed to consist mostly of the shell material, CdS, and the refractive index of this material can be used. 3) It is assumed that both the core and the shell components have near equal quantities and the average of the refractive indices for CdSe and CdS can be used.

Figure 5-17 shows the basic structure, as well as the dimensions of a typical nanorod used in the nanorod sample [5]. By knowing the dimensions of each component it was possible to determine the volume (or in this case area) fraction of air in the nanorod thin-film. Figure 5-17 which shows a triangular repeat unit (for any combination of 3 nanorods) in the periodic lattice, shows how the air fraction was calculated. The three semi-circular segments enclosed by the red triangle in this figure were subtracted from the area of the triangle, and this left only the area of air, known as a packing factor [13].

Table 5-3 contains a list of the values of refractive index entered into the equation 5.13, and the effective refractive indices calculated for the material combinations: nanorod/ligand and (nanorod/ligand)/air. Option 3) as described above was assumed in these calculations where an average index of CdSe and CdS was assumed for the nanorods' inorganic core. The two effective refractive indices calculated come from a two-step use of the Maxwell-Garnett Theory, equation 5.13. Two-steps were required since there were more than two components with different refractive indices present in the nanorod thin-film. Although an average index

for CdSe/CdS can be taken for the reasons stated above, the ligands, which are the inorganic component of the nanorod, and the air component all have known volume fractions and refractive indices. This information made it possible to calculate the effective refractive index for the combined organic and inorganic components of the nanorods, and then use this effective index in a second Maxwell-Garnett approximation, which took into account the air trapped in the thin-film, to determine the overall effective refractive index of the thin-film. The final refractive index of the two-step process was calculated to be 1.47261.

Material	Refractive Index
CdSe	2.75184
CdS	2.51496
Ligand	1.465
Air	1.0003
Nanorod/Ligand (first step index)	1.62054
(Nanorod/Ligand)/Air (final refractive index)	1.47261

Table 5-3 Table containing the refractive indices for the different components of the nanorod thin-film layer.

Figure 5-18, below, shows how the refractive index calculated using the effective medium theory, equation 5.13 varies as the volume ratio of the organic ligands to the inorganic rod component changes. More specifically, Figure 5-18 shows the values calculated for the final effective medium calculation which takes into account the refractive indices of the organic, inorganic and air components of the nanorod thin-film layer. As can be seen from Figure 5-18 the refractive index decreases as the organic ligand makes up a larger fraction of the nanorods' total volume. Considering that the organic ligand material has a much lower

refractive index of the inorganic component, such a decline in refractive index is to be expected.

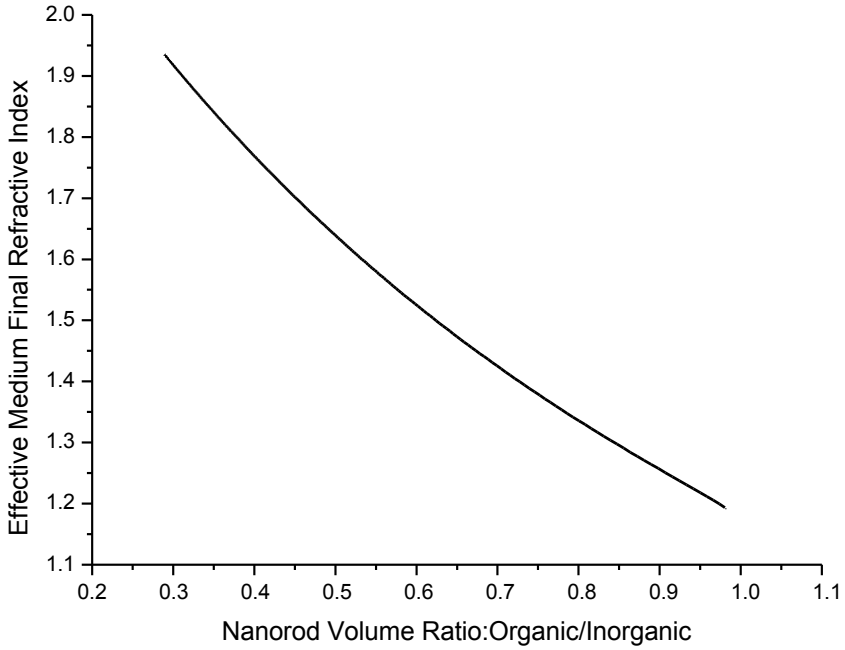


Figure 5-18 Graph showing how the final (second step) effective medium calculation refractive index varies as the volume ratio of the organic and inorganic nanorod components varies. Note the nanorod volume ratio does not contain the air trapped in the thin-film.

.

5.7 Optical Efficiency Results for the Nanorod LSC

In this section the incident photon flux entering the nanorod LSC's top surface, and the photon flux emitted from the LSC's edges are used to determine the optical efficiency of the nanorod LSC. These results are later compared to three ideal computationally modelled nanorod LSCs (with vertical, horizontal and random alignment) in section 5.8. Given the nanorod sample's limited vertical nanorod alignment (at the centre of the sample), it should be possible to determine to which of the 3 idealised simulated situations the real nanorod sample most closely resembles, in terms of optical efficiency.

Table 5-4 gives the average measured optical efficiencies from the two long narrow edges of the nanorod sample, as well as the two short narrow edges and the total optical efficiency for all four edges (see section 4.9, chapter 4 for experimental method).

Edges	Optical Efficiency (%)
2 Long Edges	2.66±0.03
2 Short Edges	1.33±0.01
All Edges	4.00±0.04

Table 5-4 Table shows the optical efficiencies measured from the nanorod sample.

The optical efficiency from all four edges of this sample was 4.00±0.04%, this measurement was performed using a Steuernagel Lichttechnik solar simulator (no UV filter), see Figure 4-1, chapter 4. Since the illumination source has a much shorter wavelength range than the AM1.5g solar spectrum, a larger percentage of the solar simulator generated photons will be absorbed by the nanorod LSC than would be the case for the AM1.5g solar spectrum. This results in a higher experimentally measured optical efficiency than would be achieved under the standard conditions.

5.8 Computational Simulations of Vertically, Horizontally and Isotropically Aligned Nanorod Samples

In the following section, results for ray-trace simulations on nanorod samples featuring vertically, horizontally and randomly aligned nanorods are discussed [14]. These simulations allowed ideal samples to be modelled in which perfect nanorod thin-films were simulated, with long range nanorod alignment extending across the entirety of the sample's surface (in the case of vertical and horizontal alignment samples). For example, in the sample consisting of vertically aligned nanorods, there were no variations in film thickness across the surface of

the sample, and all nanorods were vertically aligned with the long axis of each nanorod being aligned perpendicularly to the substrate. In all cases the simulated samples had substrate dimensions of 2.5 x 1.25 x 0.1cm and thin-films 285nm thick (matching the parameters of the experimental sample) with the LQY (51.9±0.5%.) and the absorption and emission (top surface emission) spectra also matching those of the characterised nanorod sample.

5.8.1 Direct Irradiance

Table 5-5 gives optical efficiencies for simulated samples for random, vertically, and horizontally aligned nanorod samples under direct (normal incidence) irradiance with a spectrum matching that of the Steuernagel Lichttechnik solar simulator light source (UV filter removed) as illustrated in Figure 4-1, chapter 4. It can be seen that under direct normal light illumination, a random nanorod alignment provides the highest optical efficiency, 6.86%, while the horizontal alignment has an optical efficiency of 5.76%, and that for the vertically aligned nanorods is zero. This is explained by the dipolar distribution of the nanorods, which means for a direct normal light source there will be no light absorption for perfectly vertically aligned nanorods. However, in the case of horizontally aligned nanorods a direct normal light source gives optimal incident light absorption, but with the lowest light trapping efficiency. Both alignment cases agree with the experimental results of Verbunt *et al.* [15] (see figure 3.4, chapter 3). The simulated isotropic oriented nanorod sample will have a mix of orientations, which has better incident light absorption than vertically oriented nanorods, as well as better light trapping than horizontally aligned nanorods.

Sample Alignment	Optical Efficiency (%)
Random	6.87
Vertical	N/a
Horizontal	5.76

Table 5-5 Optical efficiencies calculated from computational ray-trace simulations for ideally aligned nanorod samples under direct normal irradiance.

In section 5.7 the optical efficiency of the nanorod sample was measured to be 4.00±0.04% (total light from all 4 edges) when under a Steuernagel Lichttechnik solar simulator light source. The solar simulator used for the experimental measurements can be approximated as a direct light source (though in reality there will be a little angular divergence, 5% in the case of a class B solar simulator [16]) Observations of Table 5-5 show that the isotropically oriented simulated sample has an optical efficiency of efficiency of 6.87%; this is for a sample which has matching dimensions, LQY and spectral properties as the actual nanorod sample characterised in this chapter, and when a direct light source with the same spectrum as the Steuernagel Lichttechnik solar simulator was used. Obviously, ray-trace simulations cannot perfectly match a real sample (i.e. a real sample has variations in its thin-film thickness). However, since the experimentally measured optical efficiency is significantly lower than the optical efficiency of the random sample featured in Table 5-5, and since this table shows that a simulated vertically aligned sample has an optical efficiency of 0%, it is not unreasonable to conclude (when considering the evidence of vertical alignment seen earlier in this chapter) that this shows further evidence of some level of vertical nanorod alignment in the real nanorod sample.

5.8.2 Diffuse Irradiance

Table 5-6 gives optical efficiencies for the same simulated samples with random, vertically, and horizontally (ideally) aligned nanorod samples but now under indirect (diffuse)

irradiance and again with an incident spectrum matching that of the Steuernagel Lichttechnik solar simulator light source (UV filter removed) as seen in Figure 4-1, chapter 4. In these simulations the incident photons were isotropically distributed over a hemisphere.

Sample Alignment	Optical Efficiency (%)
Random	4.31
Vertical	9.15
Horizontal	5.75

Table 5-6 Optical efficiencies calculated from computational raytrace simulations for ideally aligned nanorod samples under diffuse irradiance.

In Table 5-6, it can be seen that for simulated nanorod samples under diffuse illumination, the simulated vertically aligned nanorods give the highest optical efficiency, of 9.15%, followed by the horizontally aligned sample which has an optical efficiency of 5.75%. The diffuse light source used for this simulation produces photons which are incident over a range of angles with the LSC sample; unlike the case for the direct light source featured in section 5.8.1, which simulates incident photons perpendicular to the LSC top surface. As a result of the diffuse light source, the dipoles of the vertically aligned nanorods are able to couple to a significant portion of the incident light, but those photons at normal incidence remain unabsorbed. In addition, since diffuse photons have an angular component, top surface reflection losses will be larger than for direct irradiance, with the angularly averaged value being about 6.7% rather than the 4% for normal incidence. Hence for the vertically aligned nanorods, there now exists a situation where a significant portion of the incident photons are absorbed, but there is also a very high TIR efficiency. This compares with the horizontally aligned nanorod simulation, in which there is still very high absorption of the incident, diffuse, light source, but for which there exists the very low TIR efficiency.

These simulated results suggest that under a diffuse light source, vertical nanorod alignment is preferable than randomly oriented, or horizontally aligned nanorod samples, which is particularly beneficial for LSCs since they do not employ solar tracking devices. It should also be noted that countries located in the temperate regions of the planet experience more diffuse light, with the UK in particular receiving an average of 60% diffuse light over the year [17]. Therefore vertically aligned nanorods would appear to be a good choice. However, as is postulated in the work of Verbunt *et al.* [15], a tilted alignment of dipolar emitters is believed to be superior to either vertical or horizontal alignment for normal incidence. However, in a practical application without tracking the angle of incidence of the direct solar beam would vary throughout the day and, it may well again be the case that vertical alignment, with its optimal trapping efficiency, is preferable although further simulations (which would be location and installation angle dependent) would be required to verify this.

5.9 Conclusions

In this chapter a thin-film sample consisting of vertically aligned CdSe/CdS core/shell nanorods in a thin-film deposited on a glass substrate has been characterised for use as an LSC. Firstly, due to their stability, wavelength tuneability and relatively high LQY of ~70% [1], CdSe/CdS core/shell nanorods make an attractive choice for use in LSCs, although their advantages are tempered by their high costs and limited availability (due to the scarcity of the raw materials).

Optical spectroscopy measurement methods including angular dependent absorptivity were used to determine that the nanorod sample did indeed contained aligned arrays of nanorods, and also to determine the extent to which the alignment covered the sample's surface. These measurements determined that the vertically aligned nanorods existed over a limited region at the centre of the sample, but no evidence of this alignment was seen at locations of more than

6mm from the centre, suggesting that alignment is rapidly lost as the distance from the centre of the sample is increased, as previously shown in [3].

Further proof of partial vertical nanorod alignment was seen in comparisons between optical efficiency measurements performed on the nanorod sample, and the optical efficiencies calculated for simulated samples with identical dimensions, LQY and spectral parameters. Experimentally measured results using a Steuernagel Lichttechnik solar simulator revealed that the nanorod sample had an optical efficiency value (all four narrow edges) of 4.00±0.04%. The isotropic simulated sample also used the spectrum form the Steuernagel Lichttechnik solar simulator light source (direct normal incidence), and had an optical efficiency of 6.87%. The significant difference between the experimentally measured optical efficiency and the simulated isotropic sample, suggested that the nanorod sample was not completely isotropic. Therefore, it seemed likely that since the vertically aligned simulated sample had an optical efficiency of 0% (under direct normal incidence light) that this, taken together with the other evidence seen earlier in this chapter, strongly implied that there was indeed some limited level of vertical nanorod alignment in the real nanorod sample.

Since the results featured in this chapter do show vertical nanorod alignment at the centre of the nanorod sample, albeit very limited in its extent, the question of whether this self-alignment technique is of use for LSCs has to be addressed. Commercially viable LSCs would obviously need to be larger than 2.5 by 1.25 by 0.1cm in size, and yet even on an LSC this size (the sample tested in this work), only a small central region appeared to have aligned nanorods. The author agrees with the assertion in [3] that uneven rates of solvent evaporation, with solvent towards the edges of the sample evaporating more rapidly, is the reason for the disordered observed at the edges of nanorod sample. This being the case, it is perhaps not unreasonable to believe that a larger sample might have a larger central region over which vertical alignment is maintained, though towards the edges the nanorods would still be

disordered. If a large area sample like this was produced, and there was indeed a corresponding large area of aligned nanorods at the centre, then conceivably the edges of the sample with the disordered nanorods could be removed, although this would be very wasteful. Alternatively, a greater area of vertical alignment may be possible if the rate of evaporation across the surface of the sample was carefully controlled. In principle this could conceivably be achieved by varying the temperature of the substrate across the surface of the sample, although in reality this would prove extremely difficult due to the conduction of heat. Ultimately, it may prove more practical to use an alternative method for alignment, for example in the work of Verbunt *et al.* [18] liquid crystals are used to provide alignment to fluorescent dyes.

Lastly, computational modelling has been used to show that, although vertical alignment is completely inappropriate for direct normal sources of light, since a vertically aligned nanorod absorbs and emits light preferentially that is perpendicular to the direction of the nanorods' long axis, under diffuse irradiance vertical alignment has an advantage. For example, the simulations show that if a diffuse light source with a spectral range identical to that of a Steuernagel Lichttechnik solar simulator is used, then for horizontally aligned, vertically aligned and randomly oriented nanorod samples, the optical efficiencies are 4.31%, 9.15% and 5.75% respectively. This makes vertically aligned nanorod LSCs ideal for use in building integration applications where there may be little direct sunlight, or the LSC may be at a fairly large angle to the sun (such as in a window for example). Additionally, at temperate latitudes there tends to be a high percentage of diffuse light due to cloudy conditions which would make vertically aligned nanorods particularly useful.

Chapter 5 References

[1]Carbone, L., Nobile, C., De Giorgi, M., Sala, F., Morello, G., Pompa, P., Hytch, M., Snoeck, E., Fiore, A., Franchini, I., Nadasan, M., Silvestre, A., Chiodo, L., Kudera, S., Cingolani, R., Krahne, R., and Manna, L., (2007). "Synthesis and Micrometer-Scale Assembly of Colloidal CdSe/CdS Nanorods Prepared by a Seeded Growth Approach". Nano Letters. 7, 10, 2942-2950.

[2]Chatten, A. J., Barnham, K., Buxton, B., Ekins-Daukes, N., and Malik, M., (2003). "The Quantum Dot Concentrator: Theory and Results". 3rd World Conference on Photovoltaic Energy Conversion., Osaka, Japan.

[3] Zanella, M., Gomes, R., Povia, M., Giannini, C,. Zhang, Y., Riskin, A., Van Bael, M., Hens, Z., and Manna, L., "Self-Assembled Multilayers of Vertically Aligned Semiconductor Nanorods on Device-Scale Areas". Advanced Materials. 23, 2205-2209.(2011).

[4] Macqueen, R., et al.."Towards an aligned Luminophore Solar Concentrator". Optics Express. 18 A161, (2010).

[5] Zanella, M., Personal correspondence, Istituto Italiano di Tecnologia, (2012).

[6] Verbunt, P., Sanchez-Somolinos, C., Broer, D., and Debije, M., (2013). "Anisotropic light emission in luminescent solar concentrators-isotropic systems", Optics Express, 21, S3, A485-A493.

[7] Liboff, R., (2002), "Introductory Quantum Mechanics (Fourth Edition), Addison Wesley.

[8] Sevgen, A., (2009), "Electric Dipole Radiation". Accessed on (25/10/2013), http://hbar.phys.boun.edu.tr/~sevgena/p202/docs/Electric%20dipole%20radiation.pdf

[9] De Mello, J., Wittmann, H., and Friend, R., (1997). "An Improved Experimental Determination of External Photoluminescence Quantum Efficiency", Advanced Materials, 9, 3.

[10] Fluorophore absorption. Accessed on (3/11/2013) http://www.usbe.cas.cz/people/lazar/celler/absorption.php

[11] Farrell, D.J, Personal Correspondence. RCAST University of Tokyo, Japan, (2013).

[12] Choy, T., (1999), "Effective Medium Theory: Principles and Applications", Clarendon Press, Oxford.

[13] Stavrinou, P., Personal consultations, Imperial College London. (2013).

[14] Farrell, D.J, (2013), "pvtrace: optical ray tracing for photovoltaic devices and luminescent materials", http://github.com/danieljfarrell/pvtrace

[15]Verbunt, P., Bastiansen, C., Broer, D., and Debije. M., (2009). "The Effect of Dyes Aligned by Liquid Crystals on Luminescent Solar Concentrator Performance", Proc. 24th European Photovoltaic Solar Energy Conference, p381-384, Hamburg, Germany.

[16] ASTM E927 – 10, Standard Specifications for Solar Simulation for Terrestrial Photovoltaic Testing, (2010). Accessed (9/11/2013), http://www.astm.org/Standards/E927.htm

[17] Mallinson, J, and Landsberg, P., (1977). "Meteorological Effects on Solar Cells", Proc. R. Soc. A. 355, 115.

[18] Verbunt, P., Kaiser, A., Hermans, K., Bastiaansen, C., Broer, D., Debije, M., (2009). "Controlling Light Emission in Luminescent Solar Concentrators Through use of Dye Molecules Aligned in a Planar Manner by Liquid Crystals", Advanced Functional Materials, 19, 2714-2719.

Chapter 6
Flexible LSCs & Novel Luminescent Species.

6.1 Introduction and Premise

In this chapter the development of a flexible LSC and an associated solar cell holder is reported. Furthermore, a number of promising luminescent species were characterised for potential use within the flexible LSC (and for LSCs in general). The premise for this work was to develop a large area, cheap and flexible LSC for the purpose of being used as a cost effective source of portable power. Aspects of this work were pursued in collaboration with the Naval Research Laboratory in the USA. The work of Yoon *et al.* [1] has previously investigated a flexible LSC concept, though their LSC design is of a somewhat different configuration. Their design used arrays of micro silicon solar cells (capable of absorbing photons via the front, back and side surfaces) embedded within the LSC.

Since this LSC was primarily designed to be easily mobile, the design parameters also required the LSC to be thin enough to allow for easy transport. This meant that the device had to have the ability to be rolled up, and it also had to be light enough so as not to overly encumber a person as they transported the device. Although LSC/solar cell combinations, and particularly large area LSCs, have relatively low power conversion efficiencies when compared to portable silicon solar cells, which are discussed in Trautz *et al.* [2], they do have a number of advantages. These advantages include; lower weight, potentially much lower cost, and higher durability since the LSC can still function even if damaged. Furthermore, the LSC has greater flexibility for deployment and could be used in many different places, for example over a tent or on the ground.

Developing a large area flexible LSC presented a number of challenges, the first of which was to identify an appropriate cheap luminescent species which could be used effectively over a large area device, since large areas make reabsorption losses a particular concern (see section 2.6.4, reabsorption losses, chapter 2). Another issue was how to attach a solar cell to an edge, or edges, of a flexible LSC in a way that not only effectively coupled the solar cell(s), but also protected the cell(s) from damage and allowed for repeated use.

A large surface area LSC will mean that many of the emitted photons will have large distances to travel to reach the edges, and this is further exacerbated by making the LSC thin enough to be flexible, with both characteristics lead to higher reabsorption losses. It has been shown that for many luminescent species, see for example [3-4], that reabsorption limits the useful length and width dimensions of the LSC, to generally less than 1m. Therefore, when considering luminescent materials for flexible LSCs, which it is envisaged would have at least a $1m^2$ top surface area (to be of practical use), it is essential to avoid materials with insufficient Stokes-shifts (see again section 2.6.4, re-absorption losses, chapter 2).

6.2 Luminescent Materials

The following section details the characterisation of a variety of luminescent materials which have an attribute, or attributes, which grant the material great potential for use in large area, flexible LSCs.

6.2.1 PE-610 (Phycobilisome Derived Luminophore)

PE-610 (Columbia Biosciences) is a hybrid material known as a tandem fluorophore (see Figure 6-1 and Figure 6-2), which consisted of R-Phycoerythrin (R-PE), which is a chromophorylated protein removed from phycobilisomes (phycobilisomes are the light harvesting component found in species of red algae [5], see chapter 3, section 3.3.3), coupled to Rhodamine B dye. Due to the abundance of red algae and rapidity of their growth,

phycobilisomes (and proteins derived from them) are a potentially useful luminescent material since the material is likely to be low cost and highly abundant. Due to an existing collaboration, Columbia Biosciences requested that the author incorporated PE-610 material into an LSC, as they believed it to be a promising material for this application. Columbia Biosciences' motivation for coupling the two materials was twofold, firstly, to increase the Stokes-shift between the absorption and emission peaks, and secondly, to enhance the absorption efficiency in the combined material by broadening the absorption spectrum (relative to the individual constituent parts, as shown in Figure 6-3).

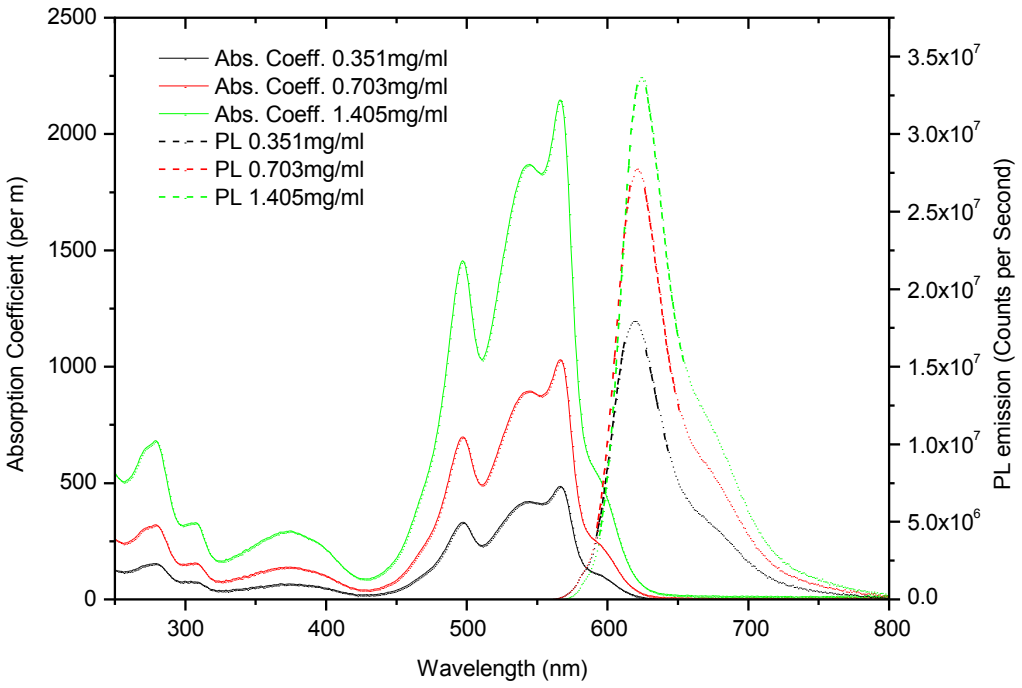


Figure 6-1 Absorption coefficient and top surface PL emission spectra for different concentrations of PE-610 dye solution (in pH neutral buffer solution).

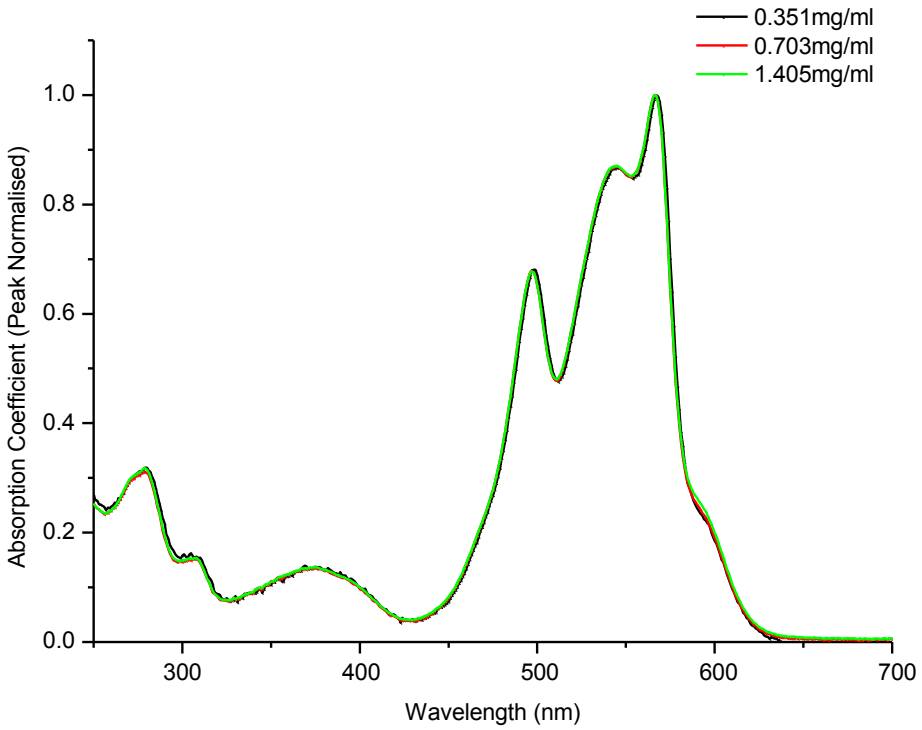


Figure 6-2 Peak normalised absorption spectra for the different concentrations of PE-610 luminescent species.

Figure 6-1 illustrates the absorption coefficient and top surface emission spectra of the PE-610 material when dispersed within a pH neutral buffer solution, and held inside a quartz cuvette, at a number of different concentrations. Figure 6-2 (Figure 6-3 see below) shows the absorption coefficient, peak normalised for each of the 3 PE-610 dye concentrations (0.351mg/ml 0.703mg/ml and 1.405mg/ml in terms of mass of PE-610 per ml of buffer solution). As can be clearly seen, the shapes of the 3 absorption spectra are virtually identical to one another, proving that absorption coefficient linearly scales with dye concentration.

In Figure 6-1, it can be seen that the spectral overlap between the absorption and emission spectra is relatively low, ~57nm, owing to the limited absorption tail on the absorption spectrum, rather than there being a significantly large Stokes-shift. The primary absorption

peak for this material is located at ~567nm, and the primary emission peak is located at ~624nm. The PE-610's peak absorption is therefore a good match for the standard AM1.5g solar spectrum.

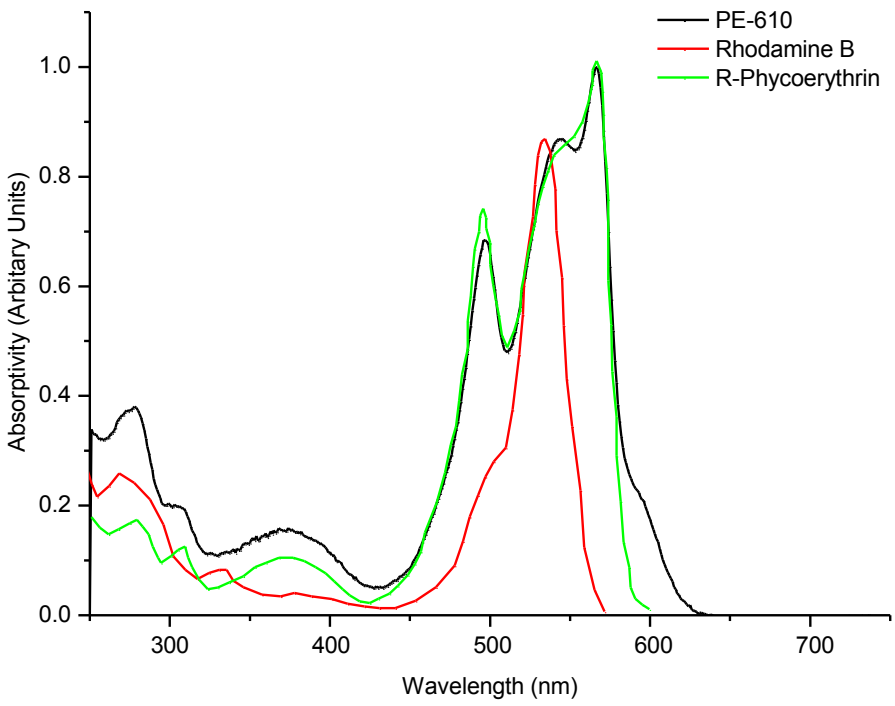


Figure 6-3 Rhodamine B and R-PE absorptivity spectra in relation to the PE-610 tandem dye's spectrum. The Rhodamine B spectrum was produced by extracting data from [6], and the R-PE data was extracted from [7].

Figure 6-3 shows the absorptivity of the Rhodamine B and R-PE components individually and relative to the PE-610's spectrum. From observations of the spectra of the two constituent parts, it is not clear exactly why Columbia Biosciences believed combining these two materials would broaden the absorption range of the R-PE. However, it does appear that combining these two materials has achieved the goal of increasing the Stokes-shift between the absorption and emission spectra. The emission peak of PE-610 appears at ~624nm, while

the emission peaks of Rhodamine B and R-Phocoerythrin appear at ~580nm and ~570nm respectively. The increased Stokes-shift observed for PE-610 may be due to interactions between the Rhodamine B and the R-PE altering the energy levels within the R-PE, and ultimately reducing the energy difference between the ground and excited states. Whether or not this is the case, the net result is positive for the use of PE-610 in LSCs, since it serves to reduce the spectral overlap between the absorption and emission spectra.

Unfortunately, due to the limited dimensions of the integration sphere, available for LQY experiments, it was not possible to measure LQYs for the 3 different PE-610 concentrations, since the PE-610 was in solution and the cuvettes did not fit into the integrating sphere. Therefore, it was assumed that the LQY for each of the 3 different concentrations matched that of PE-610 in a thin-film, of 53.0±0.5%, reported in Fisher *et al.* [12] (the author's work). Individually, Rhodamine B has a reported LQY of 65% in ethanol [8], while the LQY of R-PE is quoted as high as 98% [9], which further brings into question why Rhodamine B was chosen for the PE-610 material, since both its spectral range and LQY are lower than those of R-PE. Furthermore, the LQY measured for the PE-610 is lower than both the constituent parts, suggesting that significant degradation of the materials may have occurred during the processing of the PE-610. However, the additional shoulder shown in the absorption spectrum in Figure 6-3 (6-2) implies other factors beyond simple dye degradation may have been present. Possibly contamination of the material occurred during the production of the dye or during the thin-film fabrication. Another possibility is that interactions between the two materials leads to altered energy levels in the mixture relative to the separate constituents. Furthermore, photodegradation or oxidation may have occurred since no attempt was made to protect the sample from oxygen.

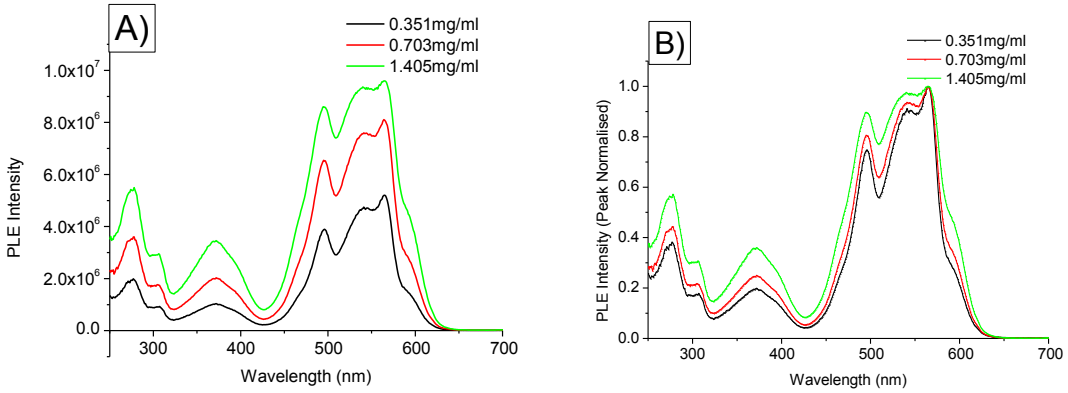


Figure 6-4 A) Photoluminescence efficiency (PLE) against wavelength for different concentrations of PE-610 dye in buffer solution. Reproduced with permission from IEEE [12]. Plot B) peak normalised data.

The photoluminescence excitation (PLE) spectra (see section 4.6 of chapter 4 for method) of the PE-610 are shown in Figure 6-4. As can be seen in Figure 6-4A and B there is a noticeable difference in the shapes of the PLE spectra between the 3 different concentrations of PE-610. In Figure 6-4B (which gives peak normalised PLE data) the differences in the shapes of PLE spectra are particularly noticeable, with the long wavelength peaks (~567nm, ~543nm and ~497nm) becoming less defined, and the short wavelength peaks (~374nm and ~274nm) becoming more defined, as the dye concentration is increased. Figure 6-5 compares the area normalised PLE spectra with the absorption coefficient spectra (at the same dye concentrations), and provides further confirmation of the trait described above seen in Figure 6-4.

Comparing the PLE spectra to the corresponding absorption coefficient spectra reveals that the two spectra do not match one another. There is clearly less PL observed at the long wavelength peaks of the spectrum than would be expected from the absorption data. Likewise there is more PL emission for the short wavelength peaks than would be expected, and these trends are exacerbated as the dye concentration is raised. Essentially, it appears as though the

LQY is lower for the long wavelength region of the absorption spectrum than the short wavelength region, and this trait is exacerbated as the dye concentration is increased.

One last point of interest in Figure 6-3 (as mentioned above) is the absorption shoulder which features on the absorption spectrum between ~600nm and ~630nm. As can be seen from the figure, this part of the spectrum is not due to either Rhodamine B or R-PE, and it is also present in the PLE spectra in Figure 6-5. As noted above, for the unexpectedly large Stokes-shift present in PE-610, it's possible that this shoulder is due to interactions between the Rhodamine B and the R-PE, causing changes in the energy levels. Alternatively, it is possible that it is due to contamination of the PE-610 during production, which doesn't seem unreasonable since R-PE is extracted from phycobilisomes which also consist of other proteins (see section 3.3.3 chapter 3).

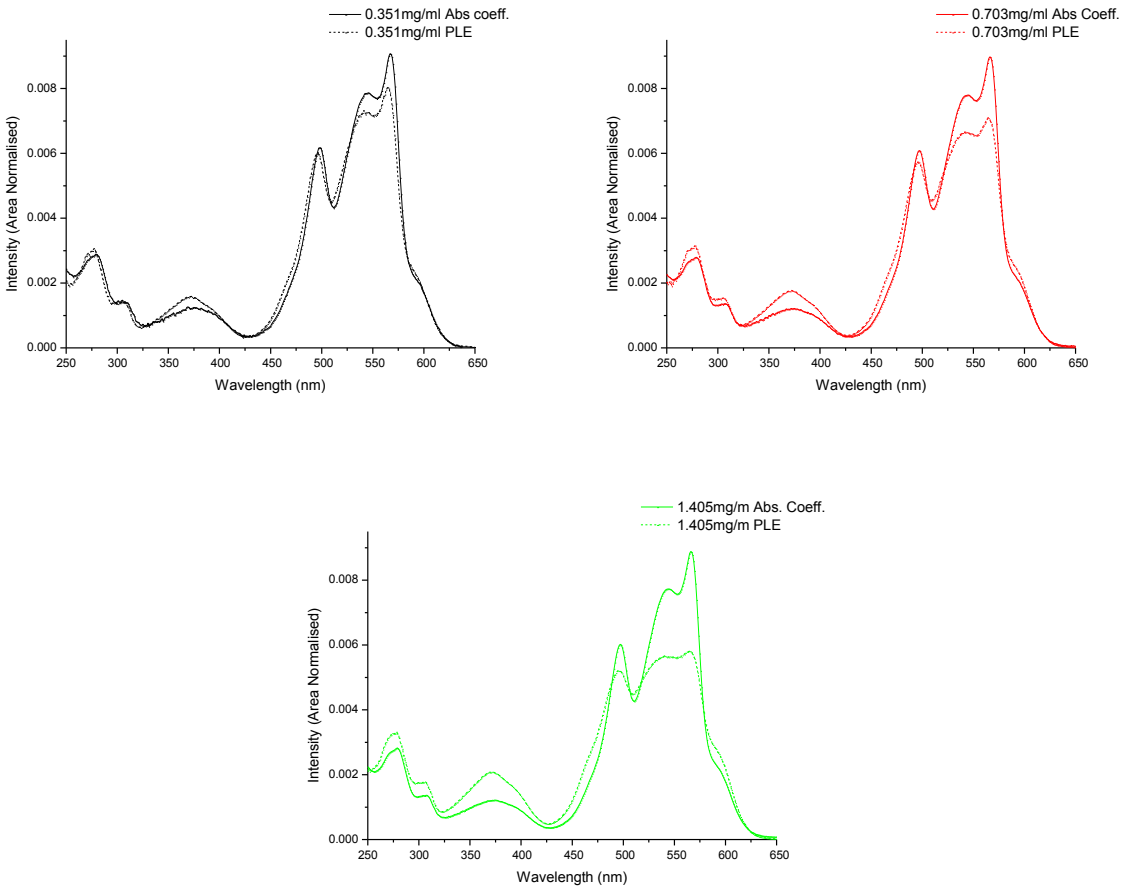


Figure 6-5 Comparisons between absorption coefficient and PLE for different concentrations of PE-610 dye.

The difference between the absorption coefficient spectra and the PLE spectra for each dye concentration featured in Figure 6-5 can be explained by variations in the absorptivity of light, $A(\lambda) = 1 - e^{-\alpha(\lambda)x}$, at different wavelengths, since the absorption coefficient has a wavelength dependence. Essentially, although the absorption coefficient scales linearly across the absorption coefficient spectrum as dye concentration is varied, the fraction of light absorbed does not necessarily do so, which is the case if the absorption coefficient is large, due to the $e^{-\alpha(\lambda)x}$ dependence. For example, if you were to double the absorption coefficient of a material at a particular wavelength, this would not necessarily result in a halving of the amount of light being transmitted through the material.

	0.351mg/ml	0.703mg/ml	1.405mg/ml
Absorption Coefficient per m (at 375nm)	66	140	294
Fraction of Light Absorbed (at 375nm)	0.06	0.13	0.25
Absorption Coefficient per m (at 575nm)	311	662	1388
Fraction of Light Absorbed (at 575nm)	0.27	0.48	0.75

Table 6-1Table containing the dye concentration dependent absorption coefficients and light absorption fractions at 375nm and 575nm.

Table 6-1 gives absorption coefficient values and light absorption fractions for each of the 3 PE-610 dye concentrations at wavelengths of 375nm and 575nm. It can be seen that the absorption coefficient is increasing (approximately) linearly as the dye concentration is increased; this is also the case for the light absorption fraction, as given by $A(\lambda) = 1 - e^{-\alpha(\lambda)x}$, at 375nm. However, at 575nm, although the absorption coefficient is still increasing linearly with increased dye concentration, albeit at much higher absorption coefficients than was the case at 375nm, the light absorption fraction no longer increases linearly. This trait is particularly noticeable between the 0.703mg/ml and 1.305mg/ml samples with absorbed fractions of 0.48 and 0.75 respectively, and is due to exponential function, $e^{-\alpha(\lambda)x}$. Rather than there being any changes in the LQY with concentration, it is, therefore, very likely that the differences in shape witnessed between the PLE and absorption coefficient data in Figure 6-5 are caused by the non-linear relationship between the light absorption fraction and the absorption coefficient. It is therefore also very likely that the increasing differences seen between the PLE and absorption coefficient data as the dye concentration increases, is also the result of the absorption coefficient getting larger leading to greater deviation from the light absorption fraction.

6.2.1.1 PE-610 LSC Optical Efficiency

Table 6-2 shows the optical efficiency obtained for an LSC utilizing PE-610 as the luminescent species within a thin-film LSC, with a substrate consisting of borosilicate glass with dimensions 6cm by 6cm by 0.7mm and a thin-film thickness = 0.108mm. The luminescent species was dispersed in a matrix of starch, sucrose and trehalose, and optical efficiency measurements were performed as described in section 4.9, chapter 4, using the Steuernagel Lichttechnik solar simulator as the incident light source, see figure 4-1, chapter 4.

The initial measurement (referred to as fresh sample in Table 6-2) was performed approximately three days after the sample had been initially fabricated (via spin coating methods by a collaborator) and gave an optical efficiency of 3.2±0.3%. Approximately 10 months later the measurement was repeated (referred to as aged sample in Table 6-2), and the optical efficiency was found to have dropped to 1.1±0.1%. During the interim time the sample was not stored using any special considerations, and was placed in a cupboard in a laboratory and, therefore, exposed to typical indoor air temperature, pressure and humidity, but only limited light.

Sample Quality	Optical Efficiency (%)
Fresh Sample (27/5/12)	3.2±0.3 [12]
Aged Sample (8/4/13)	1.1±0.1

Table 6-2 Table giving the optical efficiency when fresh and when aged, for a thin-film LSC consisting of PE-610 measured using a Steuernagel Lichttechnik solar simulator as the light source.

Taking the surroundings into account, it would seem that the degradation of the sample was likely due to the oxidation of the luminescent species during exposure to the solar simulator

light source. It has previously been shown in the work of Chen *et al.* [10] that R-PE photodegrades fairly rapidly under intense visible light, although its rate of degradation was shown to be 60% slower when encapsulated in a sol-gel matrix. However, from the perspective of use in LSCs, an approximately two thirds reduction in optical efficiency in a period of time of just under a year is a very rapid decline, especially considering that the sample's light exposure in the intervening time was low. Therefore, encapsulation methods should be considered for future iterations of phycobilisome samples, so as to maintain the optical efficiency for a more appreciable length of time.

6.2.1.2 PE-610 Simulations

Table 6-3, below, shows the simulated results obtained for several different dimensions of LSC, each using the experimental data measured for the PE-610 material. In each case the simulated light source was at normal incidence and had a spectrum which matched the full AM1.5g solar spectrum. The absorption spectrum, emission spectrum (top surface) and LQY were all experimentally measured data for the PE-610 in buffer solution. LQY measurements were performed by collaborators at the Fraunhofer Institute for Applied Polymer Research, Germany.

The LQY value for PE-610 dispersed in pH neutral buffer solution was measured to be 53±0.5% using the method outlined in the work of Suzuki *et al.* [11] (excitation wavelengths of 350nm and 560nm were used in the LQY measurement), which is a slight variation on the method described in chapter 4 section 4.7, which is used in other work reported in this thesis. The optical efficiencies presented in Table 6-3 are the average optical efficiencies from 5 separate simulation trials, each trial running a total of 10,000 incident photons. Each simulation was programmed to give 98% absorption at the primary absorption peak. In all simulations the thin-film was modelled as 100μm thick. In addition, the absorption spectral

range of the PE-610 material covers ~9.6% of the AM1.5g spectral range and could potentially absorb a maximum of ~22.8% of the photons in the full AM1.5g spectrum. This needs to be borne in mind when viewing the optical efficiencies featured in Table 6-3. A 98% primary peak absorption was chosen rather than 100% absorption across the entirety of the PE-610 absorption spectrum, due in part to the peak absorption wavelength corresponding with the highest intensity range of the AM1.5g spectrum (see Figure 6-8), and more importantly, to avoid significant re-absorption losses (see Figure 6-1).

LSC Length and Width (mm)	Substrate Depth (mm)	LQY (%)	Optical Efficiency (%)	Photon Concentration
100 by 100	0.5	53.0±0.5	1.0±0.1	0.417±0.042
250 by 250	0.5	53.0±0.5	0.5±0.1	0.521±0.104
250 by 250	3	53.0±0.5	1.2±0.1	0.242±0.020
500 by 500	0.5	53.0±0.5	0.15±0.06	0.313±0.125
500 by 500	3	53.0±0.5	0.51±0.03	0.206±0.012
1000 by 1000	0.5	53.0±0.5	0.05±0.02	0.208±0.083
1000 by 1000	3	53.0±0.5	0.15±0.02	0.121±0.016

Table 6-3 Simulated optical efficiencies using the full AM1.5g solar spectrum as the incident light source as well as the spectral and physical properties of the PE-610 plate, for a number of LSC geometries. Data extracted from [12].

It can be seen from Table 6-3 that the highest optical efficiency was achieved for the 250 by 250 by 3mm LSC, and had a value of 1.2±0.1%, which is significantly higher than for the 250 by 250 by 0.5mm LSC which has a simulated optical efficiency of just 0.5±0.1%. A thicker substrate has the benefit of reducing the photon pathlength within the light absorbing thin-film layer. Emitted photons will have to pass through the highly absorbing thin-film layer as they undergo TIR (generally multiple times) to the narrow edge of the LSC. Therefore, increasing the LSC thickness, and as a result reducing the photon pathlength

through the thin-film, will reduce the opportunities for reabsorption losses [13]. This point is further reinforced by comparing the rate of optical efficiency decline as the sample gets larger. For example, between the 250 by 250 by 0.5mm sample and the 500 by 500 by 0.5mm sample, the optical efficiency declines by 70%. However, compare this to the corresponding samples which had a 3mm thick substrate and it can be seen that the equivalent optical efficiency decrease is 57.5%. Therefore, it is clear that by making the flexible LSC as thick as is reasonable, is essential if higher optical efficiencies are to be achieved. At the same time however, it must be considered that thicker LSCs will be heavier, more expensive and more difficult to roll-up for storage and transport, and will also require larger solar cells.

Lastly, even for the 3mm thick substrate, it can be seen that on increasing the lateral dimensions from 250 by 250mm to 1000 by 1000mm there is an 87.5% decrease in optical efficiency showing that reabsorption is still a problem even in the thicker LSCs. To put these numbers into perspective this means that increasing the top surface area by 16x results in a halving of the photon concentration due to increased reabsorption losses. It is also important to note from Table 6-3 that in all cases the thinner sample had a higher photon concentration, when compared to the thicker sample, with the corresponding length and width dimensions. Furthermore, it can be seen that as the length and width dimensions increased the photon concentration decreased. For this particular application a high optical efficiency is the more important parameter, as being able to produce useful quantities of power is a perquisite of the flexible LSC device.

6.2.2 High Stokes-Shift Luminescent Materials

As discussed in previous sections of this chapter, for a luminescent species which is being used in a large area, flexible LSC, it is of prime importance to have a high Stokes-shift that effectively removes spectral overlap between the absorption and emission spectra. The following sections discuss the characterisation of a novel material, ADS065BE, with its

spectral properties showing good potential for use in LSCs. All high Stokes-shift samples characterised in this work used 2.5 by 2.5 by 0.1cm quartz slides as substrates, and had thin-films (see Table 6-4 for film thicknesses), consisting of a 85% PMMA/15% PLMA matrix, spin-coated on the top surface (see section 4.13, chapter 4 for fabrication methods).

6.2.2.1 ADS065BE

ADS065BE is a commercially available electrophosphorescent metal complex produced by American Dye Source, Inc., its molecular structure consists of iridium (III) bis(2-(4, 6-difluorephenyl)pyridinato-N,C^2) [14]. Its absorption and emission properties are shown in Figure 6-6 and its chemical structure in Figure 6-7. Figure 6-6 reveals that this material has a high Stokes-shift of ~217nm between the primary absorption peak, located at ~292nm, and the primary emission peak, located at ~515nm, for the 4wt% thin-film LSC. The wt% value is in terms of the percentage weight of the luminescent material, in relation to the weight of PMMA/PLMA used to make the thin-film, and it can be seen in figure 6-6 that there is some variation in the peak wavelength positions for the different dye concentrations (dye was dissolved in THF solvent).

An explanation for the concentration specific changes described above may be offered by the work of Lu and Penzkofer [15], where Rhodamine 6G was tested at a number of different concentrations. They observed quite significant changes in the absorption spectrum of Rodamine 6G as the dye concentration increased, which they attributed to interactions giving effectively different sized molecules (in their case dimers, trimers etc.) as the concentration increased, which resulted in a deviation from Beers Law. Furthermore, they note that different solvents can increase the variation in absorption spectra. For example, they found that there was a larger departure from Beers Law at lower concentrations when Rhodamine 6G was in water, when compared to methanol, which they attributed to “stable ground state

dimers" in water [15]. Since there were such significant changes in the shape of the absorption spectra as the concentration was varied, suggesting that the energy levels were altered, this would also explain the observed variation in the emission spectra. The emission spectra for each sample were produced by using an excitation beam with a wavelength equivalent to the peak absorption wavelength, ~292nm. The most important element of Figure 6-6 is that there is only negligible spectral overlap between the absorption and emission spectra, which is ideal for a large area, flexible LSC.

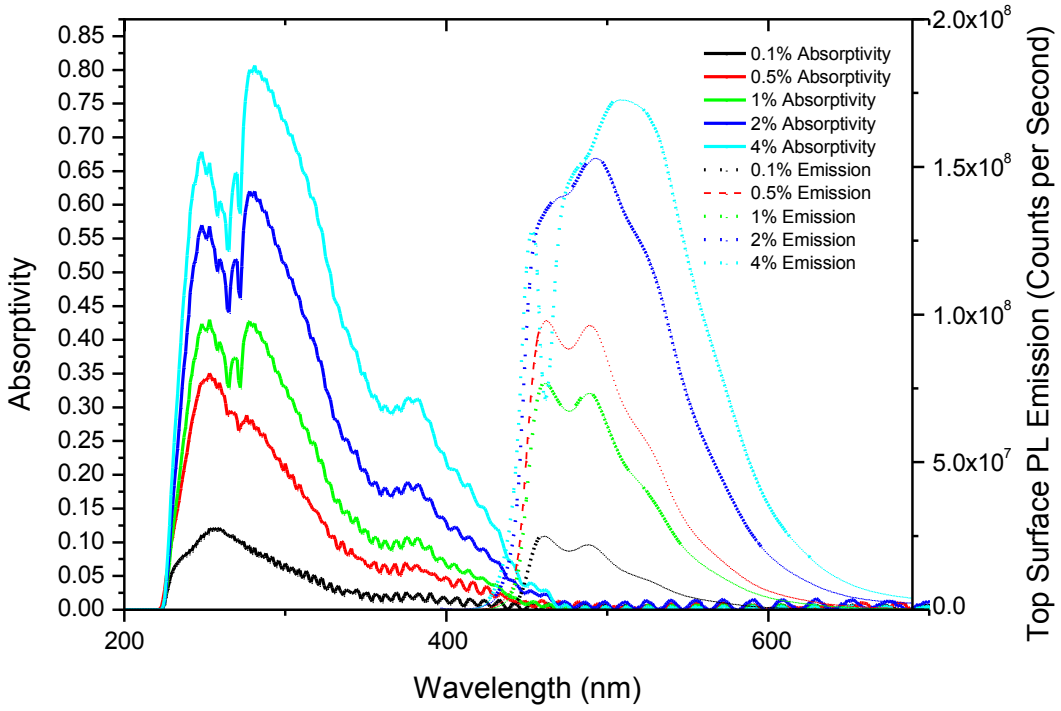


Figure 6-6 Absorptivity and top surface PL spectra for LSC samples utilising ADS065BE at a number of different concentrations.

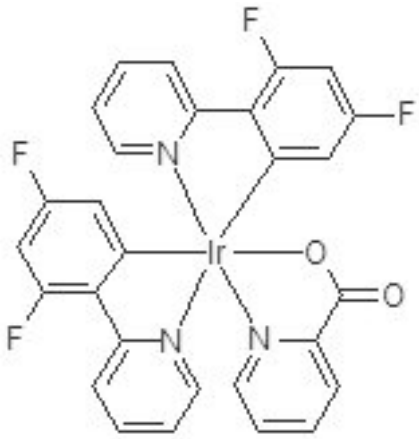


Figure 6-7 Chemical structure of ADS065BE. Reproduced with permission from American Dye Source [14].

Figure 6-8 shows the absorption spectrum for ADS065BE overlaid over part of the AM1.5g solar spectrum, and shows that the material, which has an absorption spectrum peak at ~292nm, does not have an ideal absorption spectrum for absorbing solar photons. Much of the absorption spectrum falls outside of the standard solar spectrum's range, limiting the number of photons which can be collected by an LSC which uses the ADS065BE material, and ultimately reducing the optical efficiency of the device. Indeed, in terms of spectral range overlap between the ADS065BE and the AM1.5g solar spectrum, there is only ~5.3% overlap, and ADS065BE can only absorb a maximum of ~7.4% of the AM1.5g photons. However, this material would still be very useful for a light harvesting window as it absorbs at wavelengths to which the human eye is insensitive.

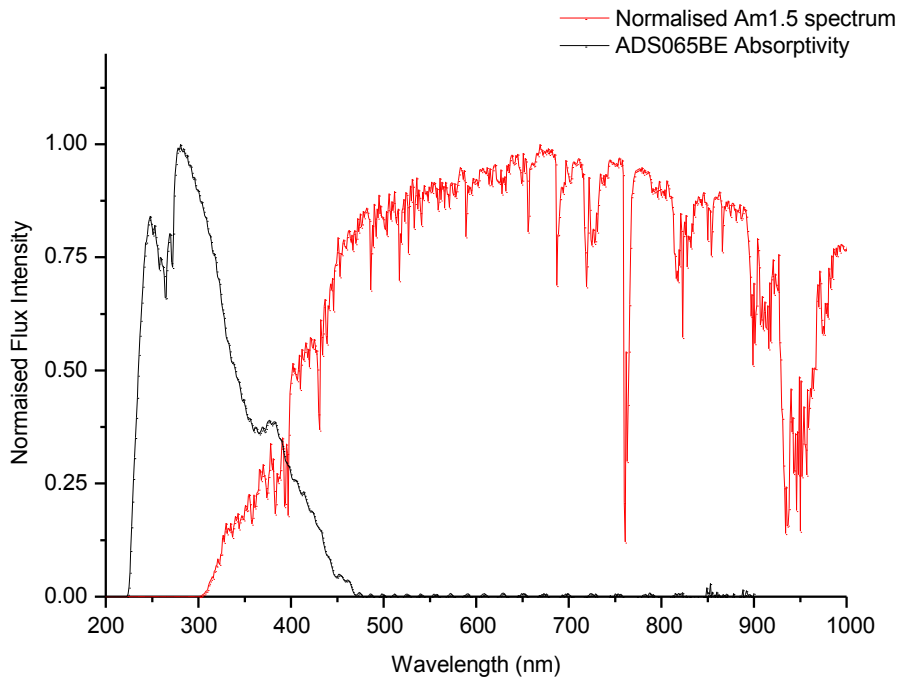


Figure 6-8 Compares the absorption spectrum of ADS065BE with the AM1.5g solar spectrum.

Figure 6-9 is a graphical representation of how the LQY of thin-film samples of ADS065BE varies as the weight percentage of the dye is varied. The general trend of this figure reveals that as the dye concentration is increased, the LQY increases from a low of 46±4.6%, at a dye concentration of 0.1wt%, to a high of 70.7±7.1%, at a dye concentration of 4wt%.

It is important to note at this point, that increasing the dye concentration significantly (as has been done for the ADS065BE samples) would normally be expected to result in a decrease in the LQY due to reabsorption or PL quenching caused by agglomeration, not the increase which is shown in Figure 6-9. A couple of factors may be in action here which result in the observed increase in LQY as the dye concentration increases. Firstly, since the thin-films on all of the ADS065BE samples only range from ~5.5µm to ~6.8µm thick, there would of course be a low probability of absorption and, therefore, only limited emission, some of

which may be obscured by noise. Figure 6-6 shows that for the lower concentration samples, the emission tail is much shorter than for the higher concentration samples, which adds credence to the speculation above regarding the loss of signal in a relatively high noise background. A second possible explanation for the unexpected rise in LQY might be found from the variations in shape of the absorption and emission spectra, observed at different dye concentrations, seen in Figure 6-6. As described above, and shown in the work of Lu and Penzkofer [15], increasing the concentration of the luminescent species can result in interactions between the molecules effectively altering their size, and potentially their energy levels. These interactions between the luminescent molecules, as the concentration gets higher, may perhaps also result in a change in the LQY, and if this is the case, coupled with the changes in the absorption and emission spectra seen in Figure 6-6, this provides further evidence of structural changes caused by molecular interactions.

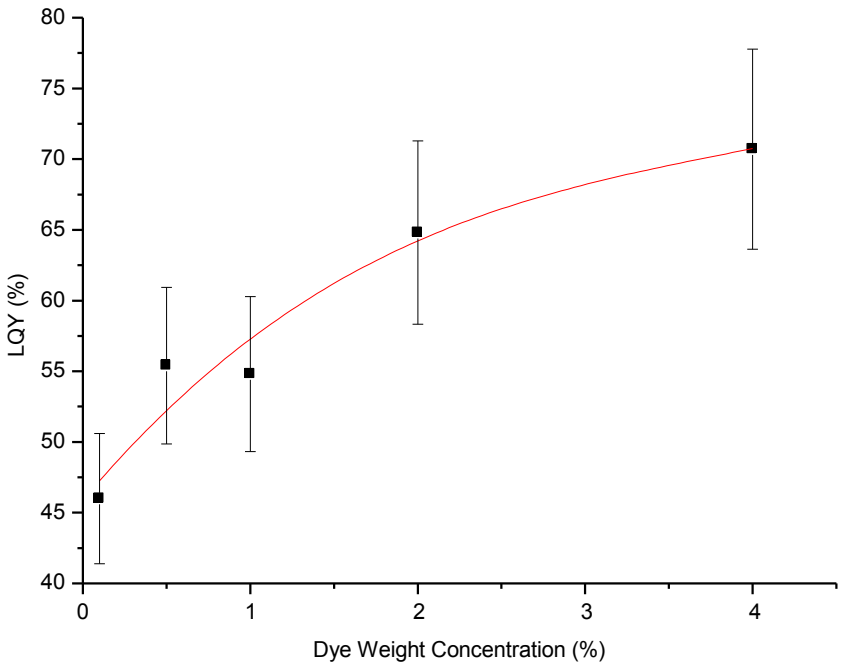


Figure 6-9 Variation of LQY with dye concentration wt% for ADS065BE.

There are insufficient data points in Figure 6-9 to draw a strong conclusion of what the ultimate LQY might be for an LSC sample utilizing ADS065BE, though the relative difference between the LQY measured for 2wt% and 4wt% when compared to the other dye concentrations may suggest that at 4wt% the LQY is starting to plateau. Higher weight percentage concentrations would have provided a better indication of the ultimate LQY of this material, but, due to limited material availability, it was not possible to produce thin-films with higher dye loading.

Further evidence that the 4wt% sample is approaching the maximum LQY value can be seen in Figure 6-10, which shows the excitation peaks and emission curves for the 3 LQY experiments (see section 4.7, chapter 4 for more details on the LQY method). The important details to note in Figure 6-10 are the relative integrated photon fluxes (in terms of photon count per second) of peaks L_A and L_C, these are the incident light beams in experiments A and C respectively. The L_A peak has an integrated photon flux of 1.43×10^7 photons per second, and L_C has an integrated photon flux of 1.76×10^6, therefore, all but 12.3% of the photons from the incident beam have been absorbed. Taking this data into account, it is not unreasonable to speculate that a LQY of 70.7±7.1% is indeed close to the ultimate LQY of the ADS065BE material.

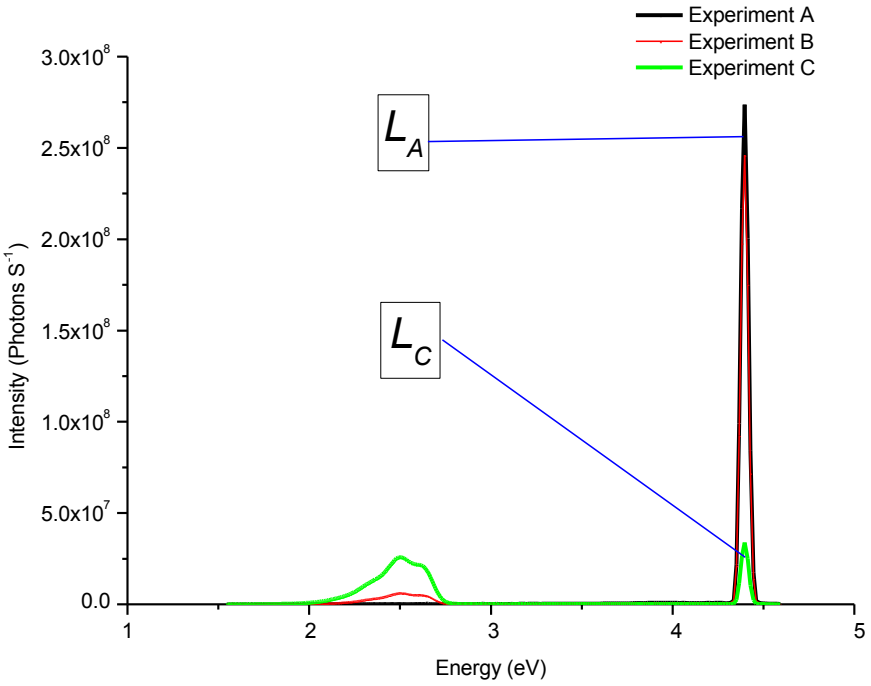


Figure 6-10 Plot showing the respective peaks of the incident light beam, and resulting emission in experiments A, B and B of the LQY measurement on Sample ADS065BE 4wt%.

This material shows a lot of potential for future use in LSCs, but is let down by its absorption spectral range. If it were possible to adjust the absorption threshold but maintain the high Stokes-shift and reasonably high LQY, then ADS065BE would prove to be an ideal luminescent species for LSCs. Being an iridium based material, the price of ADS065BE is high, due to the scarcity of iridium in nature (it is a rare earth material), and so the high price and scarcity of the material would present a substantial obstacle for large sale use of ADS065BE in LSCs. Usefully, since it absorbs at shorter wavelengths, and as mentioned above, this material could be of use for LSC windows, as discussed in the work of Chatten *et al.* [16], since it would allow a large fraction of visible light to pass through the LSC window, but still generate some power. The UV absorption of the glass used would have to be taken into account since this may result in a lowering of the efficiency an LSC window could

generate, and materials such borosilicate glass would be of use here due to its low UV absorption. However, borosilicate is more expensive than more traditional types of glass.

6.2.2.2 Optical Efficiency Measurements for High Stokes-Shift Materials

Table 6-4 details the optical efficiencies of thin-film LSC samples for a number of different concentrations of ADS065BE. All optical efficiencies are the result of the ratio of total edge emission photons and total incident photons (see section 4.9, chapter 4 for methodology). In all cases the incident photon flux was determined from the spectrum seen in section 4.2, chapter 4 produced by the Steuernagel Lichttechnik solar simulator used to illuminate the samples. Note the UV filter was also removed from the solar simulator so as to extend the range into the UV region of the EM spectrum to 300nm, which is a closer match to the AM1.5g spectrum.

Table 6-4 contains the material concentrations, the experimentally derived optical efficiencies of the fabricated test LSCs and the LQYs of the high Stokes-shift material featured in this chapter. Despite the ADS065BE material having a non-ideal absorption spectrum, a 25mm by 25mm by 1mm LSC is still able to attain a reasonable optical efficiency, relative to the input incident light source spectral range. Indeed, ADS065BE 4wt% thin-film LSC has a measured optical efficiency of 5.2±0.5% which can be attributed to the very low reabsorption losses, and the relatively high LQY. Figure 6-11 shows how the optical efficiency of the ADS065BE samples varies as the dye concentration increased.

Sample Name	Optical Efficiency (%)	Average Thin-Film Thickness (µm)	LQY (%)
ADS065BE 0.1%	3.8±0.4	6.8±0.7	46.0±4.6
ADS065BE0.5 %	4.7±0.5	6.63±0.01	55.4±5.5
ADS065BE 1%	4.8±0.5	5.97±0.02	54.8±5.5
ADS065BE 2%	4.6±0.5	5.5±0.2	64.8±6.5
ADS065BE 4%	5.2±0.5	5.7±0.2	70.7±7.1

Table 6-4 Optical efficiencies, average thin-film thicknesses and measured LQY for all the high Stokes-shift samples studied in this chapter.

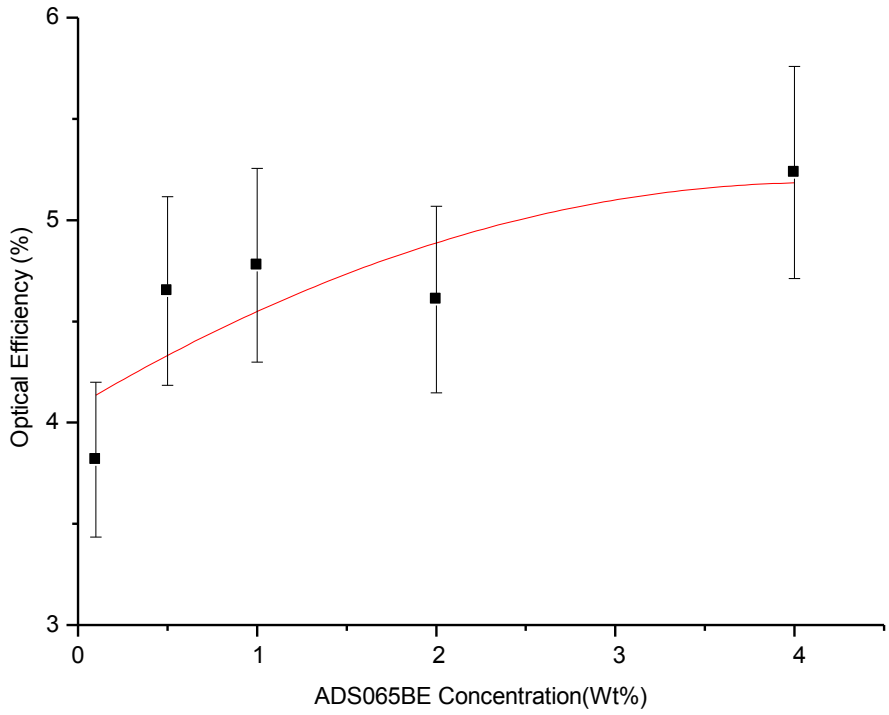


Figure 6-11 Measured optical efficiency against weight percentage concentration for material ADS065BE, includes a second order polynomial trend line as a guide for the eye.

6.2.2.3 ADS065BE Simulations

A number of raytrace simulations (see chapter 4, section 4.12 for methodology) were performed on LSCs featuring the high Stoke-shift material as the luminescent species. These simulations were performed with the intention of extrapolating the experimental results, from the small test LSCs, to more practical LSC dimensions (needed for a large flexible LSC). The simulations were performed for thin-film LSCs, with the thin-films having a depth of 100µm for all simulations. Simulations were run for LSCs with substrate sizes of 100mm by 100mm by 0.5mm (geometric concentration ~41.7, including thin-film depth), 200mm by 200mm by 0.5mm (geometric concentration ~83.3) and 1000mm by 1000mm by 0.5mm (geometric concentration ~416.7). The incident light source chosen for all the simulations was the full AM1.5g solar spectrum at normal incidence, and the optical efficiencies quoted in Table 6-5 were calculated from the incident photon flux on the LSC top surface, divided by the total photon flux emitted from all four edges. The LQY values used for each simulated sample match those shown in Table 6-4, above.

Sample Name	Optical Efficiency (%) 100 by 100 sample	Optical Efficiency (%) 200 by 200 sample	Optical Efficiency (%) 1000 by 1000 sample
ADS065BE 0.1%	0.402±0.090	0.255±0.020	0.077±0.010
ADS065BE0.5 %	0.634±0.088	0.402±0.056	0.047±0.010
ADS065BE 1%	0.673±0.019	0.407±0.020	0.078±0.029
ADS065BE 2%	0.845±0.053	0.568±0.021	0.095±0.048
ADS065BE 4%	1.107±0.052	0.779±0.021	0.138±0.021
Photon Concentration (ADS065BE 4%)	0.461	0.649	0.575

Table 6-5 Optical efficiencies for the raytrace simulations for thin-film LSCs containing the high Stokes-shift luminescent species. Thin-film layer = 100µm, and the incident light source was the full AM1.5g solar spectrum.

Unsurprisingly, given the low spectral overlap exhibited by the ADS065BE material, in Table 6-5 the rate of decline in optical efficiency is relatively low (between the 100 by 100 sample and the 200 by 200 sample), this fact is explored more fully in section 6.3.4, where a comparison between the high Stokes-shift material and the commonly used Lumogen red 305 is made. Lower optical efficiency samples tend to have higher rates of decline in optical efficiency as the sample size is increased, due to proportionally higher background losses in low optical efficiency materials compared to high. It was, therefore, decided that for the ADS065BE samples which have relatively low optical efficiencies, sample sizes of 100 by 100mm and 200 by 200mm should be used instead of 250 by 250mm and 500 by 500mm. This is because the high Stokes-shift materials have relatively low optical efficiencies, and since they are were being characterised for their high Stokes-shift properties it was desirable to compare losses in efficiency, with increased sample size, in terms of reabsorption loss rather than background losses. However, a 1000 by 1000mm sample is still included in the simulations so as to see overall how large flexible LSCs behave.

In Table 6-5 the simulations for ADS065BE 4wt% give the highest optical efficiencies for all the dimensions simulated, with optical efficiencies of 1.107±0.052% for the smallest sample and 0.138±0.021% for the largest. This result is not surprising when considering that this sample had the highest LQY (see Table 6-4), and also the strongest absorptivity and emission spectra (see Figure 6-6) relative to the other ADS065BE samples. Despite the low spectral overlap between the absorption and emission spectra of the ADS065BE material, there is a dramatic decrease in the optical efficiency when the largest dimension simulations are compared to the smallest ones. One explanation for this, as described above, will be background absorption and scattering by the substrate material and the matrix material which had loss coefficients of $1.0m^{-1}$ and $0.3m^{-1}$ respectively. Secondly, it must also be considered that a smaller sample will absorb a greater percentage of photons close to the sample edges than is the case for a larger sample, and therefore a higher percentage of the emitted photons may be collected directly at the edges rather than being lost via escape cones, since TIR may not be required to reach the collection edges in this instance. The absorptivity data in Figure 6-6 suggests that higher optical efficiencies would likely be achieved at higher concentrations since, even at 4wt%, only 80% of the incident light is being absorbed at the peak and light harvesting is therefore far from optimal and could easily be improved by around a quarter. Looking at the results for 4wt% in terms of photon concentration it can be seen that on increasing the lateral dimension from 100 to 200mm the photon concentration increases from 0.461 to 0.649 but on increasing the lateral dimension to 1000mm the photon concentration then falls to 0.575. Therefore, the optimal size of LSC of this thickness comprised of this material lies somewhere between these two sizes. After factoring in the EQE of the Si solar cells, a photon concentration of 0.65 would mean that the flexible LSC coupled to Si solar cells would give a higher output than would be achieved by exposing the cells to the AM1.5g spectrum directly. For an incident spectrum with a higher level of diffuse light, which would

be blue shifted relative to AM1.5g, the light harvesting and photon concentration would be significantly better.

6.3 Flexible LSC Prototype

In this section, the challenges and methodologies involved in fabricating the flexible LSC power producing device, comprising the solar cell holder (with contained solar cell) and the flexible LSC itself (utilising the standard Lumogen red 305 dye), are addressed.

6.3.1 LSC Holder

Figure 6-12 and Figure 6-13 are concept designs for the flexible LSC cell holder. These designs are a product of consultations between the author and collaborators at the NRL, with the final design and assembly of the holder being carried out at the NRL. The design is itself very simple, with the device being made from plastic. The simplicity of the design and the materials used are essential as they will allow large numbers of these devices to be produced cheaply, and simplicity also means there are fewer things which can go wrong in real world use. As can be seen from Figure 6-12, the flexible LSC simply slides into the gap between the clamp and the base of the holder, and then screws at either end of the clamp can be loosely tightened so as to hold the LSC in direct contact with the solar cell(s) within the holder. The prototype LSC holder was capable of holding a 6cm by 0.2cm solar cell, and although 0.2cm is wastefully large for the flexible prototype (see section 6.3.3), this parameter was dictated by solar cell availability, whereas for a commercially utilised LSC holder, the holder and cell dimension could be varied as required.

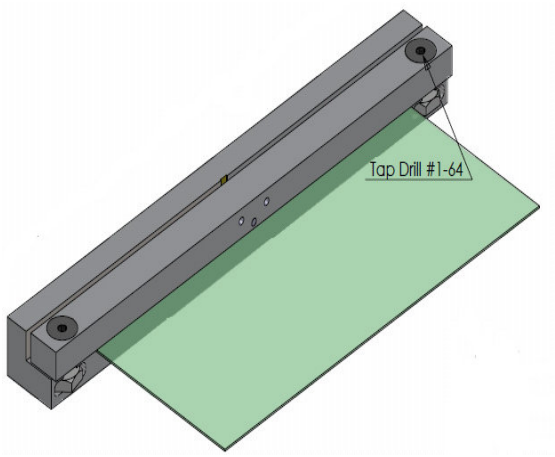


Figure 6-12 Diagram of a flexible LSC attached to the holder. Image reproduced with permission from IEEE [12].

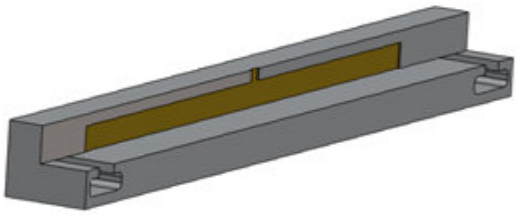


Figure 6-13 Diagram of the open holder without the solar cell, figure supplied by Kelly Trautz (NRL).

Figure 6-13 shows the cell holder with the clamp and screws removed. It can be seen that there is a recess in the back of the holder to fit the dimensions of the solar cells being used. There is also a channel above the recess to allow top and bottom contact wires to be routed to the outside of the LSC holder. This device can easily be scaled up to accommodate LSCs and cells of greater size, without the need for significant design changes. To get the maximum possible photon flux from the edge of the LSC, optical matching fluid between the LSC edge and the cells would be required, and periodic cleaning of the solar cells would also need to be considered in a real world environment.

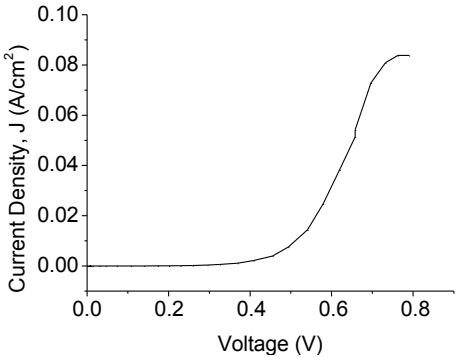


Figure 6-14 Plot of dark IV of the silicon solar cell(s) (Solaronix), measured when mounted in the LSC holder (data extracted from [17]).

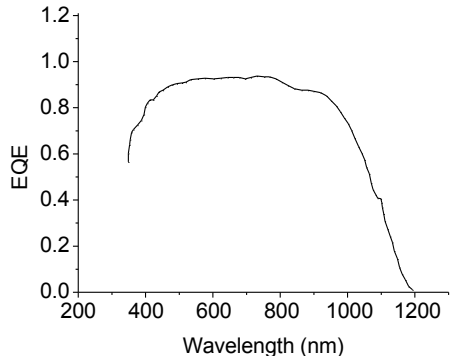


Figure 6-15 Plot of the EQE of the silicon solar cells used in the LSC holder. EQE measurements performed while cell was mounted in the LSC holder (data extracted from [17]).

Figure 6-14 and Figure 6-15 show the dark IV and EQE (measurements performed by NRL collaborators [17]) of the silicon solar cells provided by Solaronix used in the LSC holder. Both the dark IV and the EQE measurements were performed while the solar cells were mounted inside the LSC holder. It can be seen that the EQE of the silicon solar cell is >0.9 over the majority of the Lumogen red 305 emission spectrum (see Figure 6-19), which is a favourable factor for the use of these silicon cells in this flexible LSC prototype device.

6.3.2 First generation Flexible LSC Prototype

An initial flexible LSC was fabricated from 2 sheets of PLEXIGLAS Film clear 99524 from Evonik Industries, with a thin-film containing Lumogen red 300 1wt%, see Figure 6-17B**),** (a now discontinued dye from BASF and the predecessor of Lumogen red 305). The length and width of the LSC were approximately 60mm each, while each of the Plexiglas sheets were 250µm thick, with an ~180µm thin-film layer sandwiched between the two sheets. The thin-film matrix material used was a lacquer provided by Microsharp Ltd, UK, which had similar optical properties to PMMA. This lacquer was made in-house by Microsharp, and details of its precise chemistry were not provided. The lacquer was particular easy to work with, as it

mixed well with the Lumogen dyes, and cured after brief exposure to intense UV irradiation still allowing the thin-film to flex after curing.

A flexible substrate LSC as described above was tested by the author at NRL in the LSC holder and the results are given in Table 6-6 and Figure 6-17. Unfortunately, as can be seen, when tested under the solar simulator at the NRL, rapid photodegradation of the sample occurred, with the sample colour rapidly changing from a luminescent red, to a non-luminescent brown/red. It transpired that the photoinitiator material used to polymerise the lacquer material had two initiation wavelengths, at 255nm and 325nm. Unfortunately, the photoinitaiator was presumably still active after the thin-film had cured, and after being exposed to the class A solar simulator at the NRL, the sample rapidly deteriorated as is demonstrated in Table 6-6 and Figure 6-16. The photodegradation is likely due to the Lumogen red 300 breaking down (there are many π bonds that can easily be broken) on exposure to initiator free radicals generated by exposure to the solar simulator. It should be noted that the solar simulator spectrum used at the NRL in actuality extends beyond the 350nm and 2500nm boundaries shown in Figure 6-17A). These limits were imposed by the photodetector used to measure the spectrum, and as a result of incomplete incident spectral data, computer simulations and indeed power conversion calculations on the first generation flexible LSC would have been inaccurate, and so were not performed.

Time From Initial Illumination (Seconds)	Power Maximum (mW)
0	0.255±0.003
174	0.168±0.002
419	0.172±0.002
716	0.168±0.002
1373	0.136±0.001
2452	0.142±0.001

Table 6-6 Variation in power output over time of the first generation flexible LSC prototype directly coupled to the LSC holder with Si solar cells inside.

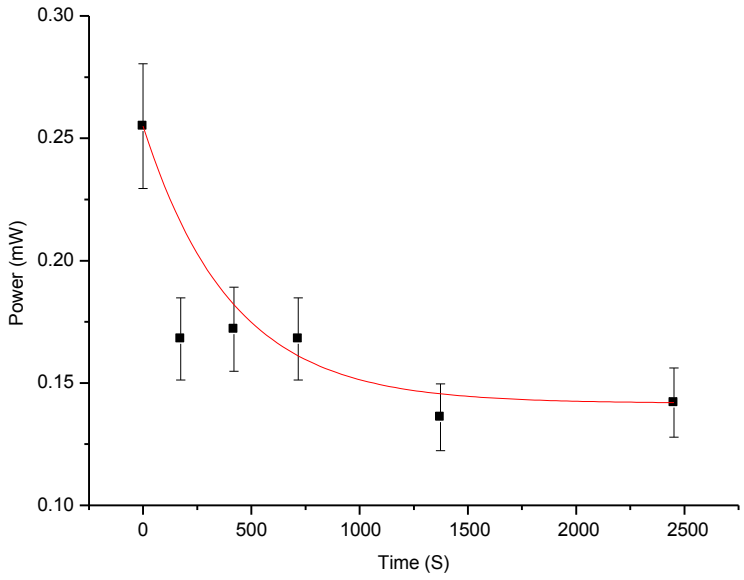


Figure 6-16 Power generated by first generation flexible LSC and LSC holder, containing Si solar cells (Solaronix), against time.

Clearly the rate of photodegradation seen in Table 6-6 and Figure 6-16 is not compatible with an effective LSC, and therefore, alternatives to the Microsharp lacquer were tested, eventually leading to the second generation flexible LSC prototype, discussed in the following section.

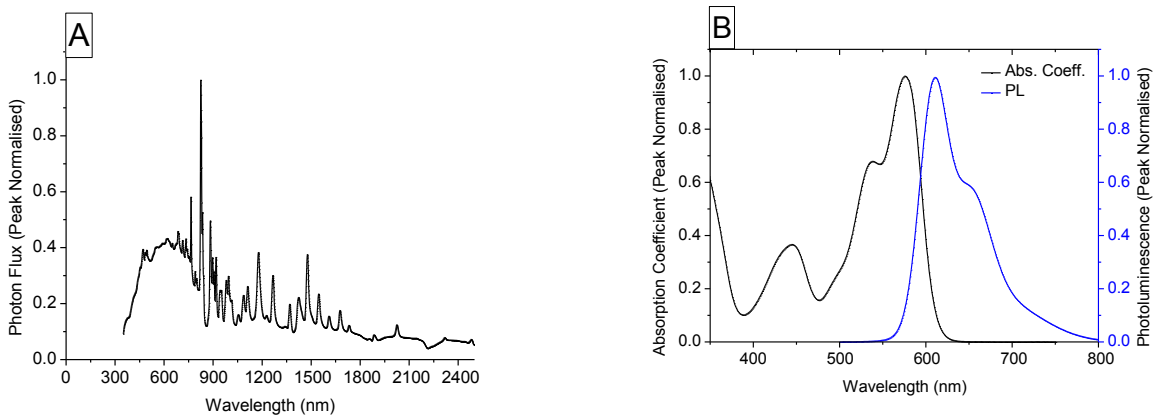


Figure 6-17A) shows the normalised photon flux spectrum from the NRL's solar simulator. B) gives the normalised absorption and emission spectrum from the Lumogen red 300 used in the initial flexible LSC prototype.

6.3.3 Second Generation Flexible LSC Prototype

A second generation prototype flexible LSC was made using a 90mm by 59mm by 0.5mm sheet of flexible PLEXIGLAS Film clear 99524 from Evonik Industries. This material was deemed appropriate for the prototype device due to its flexibility and transmission spectrum, high transparency between 300 to 700nm, and a refractive index of 1.49 [18] (close to that of standard PMMA, see Figure 6-20. Since the flexible LSC was intended only as a prototype device, Lumogen red 305 from BASF was chosen to be the luminescent species, since it has good photostability [19], a reasonable Stokes-shift, high LQY, is easy to process and is available in large quantities.

One issue to be addressed was how to make the thin-film matrix material, into which the dye was dispersed. When fabricating a non-flexible thin-film LSC with a Lumogen dye, typically the thin-film matrix material would be made by dissolving the dye into an appropriate solvent, PMMA crystals and PLMA [20]. However, PMMA is brittle and although PMMA based thin-films were initially tested on the flexible substrate, it was found (as expected) that

they cracked on flexing and, thicker films prevented the LSC from being flexible at all. A solution was achieved by cutting strips of the same PLEXIGLAS Film clear 99524 material used for the flexible substrate and dissolving them in chlorobenzene together with the Lumogen red 305 dye (at a dye concentration of 1wt%). The mixture was the then applied to the substrate using a wire bar coater (see chapter 4, section 4.13 for method), and, when dried the thin-films had an average thickness of 110 µm. An image of the finished prototype can be seen in Figure 6-18.

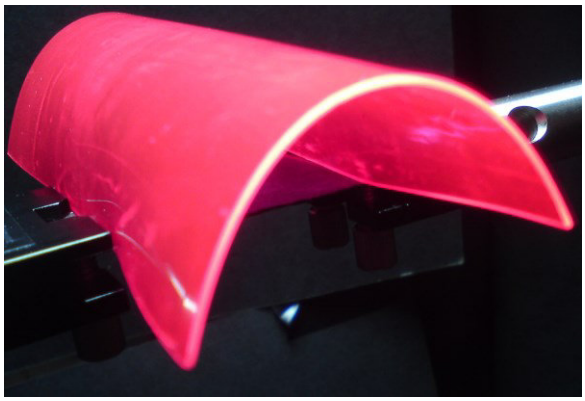


Figure 6-18 Photograph of a second generation prototype flexible LSC utilising Lumogen 305 red dye(BASF); dimensions 90 by 59 by 0.5mm, and a thin-film 0.110mm thick .

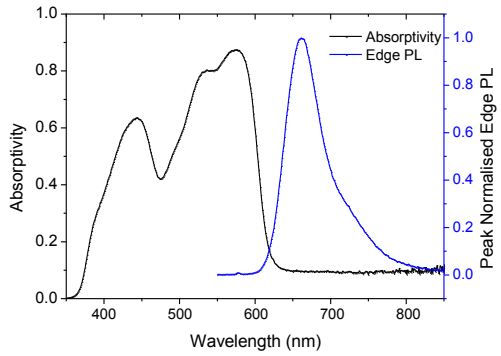


Figure 6-19 a graph of displaying the absorptivity and edge emission of the Lumogen red 305 prototype flexible LSC.

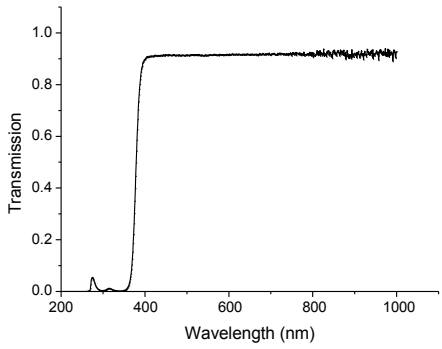


Figure 6-20 Transmission spectrum of the PLEXIGLAS Film clear 99524 flexible substrate material.

Figure 6-19 shows the absorptivity spectrum for Lumogen red 305 when deposited as a thin-film on a Plexiglas substrate (Evonik) and in a Plexiglas thin-film matrix. The absorption spectrum has been corrected for the absorption and reflectance associated with the Plexiglas material. From observations of the Plexiglas transmission spectrum shown in Figure 6-20 it can be seen that there is transmission of ~90% for wavelengths between 400nm and the NIR, where the missing 10% is largely due to normal incident reflection losses at the front and back surfaces. As mentioned above, since the vast majority of the Lumogen red 305 absorption and emission spectra falls within this wavelength range, there are few losses due to the substrate/matrix material itself, and coupled to the flexibility of the material, this makes it an ideal material for flexible LSC devices.

It should be noted that the Lumogen red 305 spectrum featured in Figure 6-19 is perhaps not optimum for maximising the optical efficiency of the prototype flexible LSC, and a higher wt% of dye would have provided a better result, though beyond a certain concentration reabsorption losses, and PL quenching due to dye agglomeration, would outweigh any further improvement (see section 2.6.4, chapter 2). The reason why a higher concentration of dye was not used was due to the thinness and flexibility of the substrate material during the sample fabrication process. Despite carefully pulling the substrate tight (to avoid any curvature of the substrate) before taping it down to the bed of the wire-bar coater, the inherent curvature of the substrate could not be completely eliminated prior to coating (see wire-bar coating methods, section 4.13, Chapter 4).

During coating the curvature of the substrate appeared to be exacerbated further, presumably due to the solvent used in the thin-film, as well as the blades motion. However, the net effect seems to have resulted in some streaks of Lumogen red 305 appearing at some locations on the sample's surface, particularly where the substrates curvature peaked, and higher dye concentrations appeared to make this issue worse. Attempts were made to produce thicker

thin-film samples, but at lower dye concentration to improve the film quality. This method had limited success as the substrates curvature allowed some of the excess material to run-off, and a higher viscosity matrix solution tested did not spread well. Furthermore, producing multiple low concentration thin-films with drying time in-between, created a very rough and scattering surface (likely due to the increased drag of the previous thin-film layer). After the completion of this work, the group has subsequently purchased a vacuum bed for the wire-bar coater, which should overcome the curvature observed in the flexible substrates and allow for superior flexible LSCs to be produced in future.

6.3.4 Considerations of the Number of Solar Cell/Mirrors used With a Flexible LSC

Whether solar cells are attached to one, two or more edges, is determined by factoring in desired cost versus performance. For example, since LSC/solar cell systems are low efficiency, and, as seen throughout this chapter, since thin and flexible, large area LSCs have even lower efficiencies having solar cells on all edges may be necessary in order to have meaningful power conversion efficiencies.

Adding mirrors to the LSC edges not covered by solar cells is usually assumed to be of value (see chapter 3, section 3.2.1) since their addition would boost the power conversion efficiency, as fewer photons will be lost from mirrored edges than from edges without solar cells or mirrors attached. Indeed the author considered running some computer simulations to determine how much improvement the addition of mirrors would have had. However, studying the literature of work related to mirrors and LSCs reveals that the addition of mirrors to edges which do not have solar cells, actually provides no benefit in terms of cost per unit power (due to increased reabsorption losses), when compared to using additional solar cells on the remaining edges [21,22] (see section 2.6.4, chapter 2 for more details). Further, from a practical point of view, although the weight of additional solar cells and LSC holders would make carrying the flexible LSC more difficult, additional solar cells do

provide redundancy to a portable LSC in the sense that if a solar cell is damaged, since there are additional solar cells available, the device will still work, albeit with a diminished output.

The practicality of using mirrors should also be considered, as using adhesive mirror materials (such as those sold by 3M) would likely peel off of a thin-flexible LSC when rolled up. Or perhaps mirrors could be used inside additional solar cell holders, but this obviously adds to weight and cost in a similar way to the use of additional solar cells, but without any of the added redundancy. Lastly, one might consider using highly reflective paint on the edges which are required to be reflective, but as well as losing the near unity reflectivity associated with TIR at the edges, such coatings could easily be damaged. Taking the evidence listed above, the author does not feel that the use of mirrored edges would be practical in a flexible LSC application, and instead believes that additional edges covered by solar cells would be a more logical option.

Due to the difficulty of measuring the photon flux from the edges of the second generation flexible LSC prototype, owing to the extreme thinness of the LSC as well as its natural curvature, measurements of the prototypes' optical efficiency and power conversion efficiency have not been reported. This was due to a low confidence in the accuracy of the standard short circuit current measurement (see chapter 4, section 4.9 for method) for such a challenging LSC geometry. Firstly, the incident light intensity from the solar simulator is highly dependent on the distance from the LSC and given the curvature of the LSC it was not possible to make an accurate determination. Therefore for future short circuit current measurements on very thin flexible LSCs, an adaptation of the method would be needed to grant greater confidence in the measured results. One possible method could be to specially design a flexible LSC holder which would close around the flexible LSC (on the top and bottom edges), removing the curvature. Of course, the reduced LSC surface area exposed to the incident light source (due to obstruction by the new LSC holder) would need to be taken

into account, and consideration would also have to be made to allow for the silicon solar cell (which measures the photon flux) to have access to at least part of each of the LSC's edges.

Another significant cause of concern in measuring the short circuit current from the edges of the flexible LSC prototype is the inaccurate masking of the unused regions of the silicon solar cell. This occurs both because of the natural curvature of the flexible LSC potentially lifting off the electrical tape used to mask off the solar cell (although this could be addressed with a special LSC holder as described above), and because of the LSC dimensions. The very low LSC thickness, ~0.61mm, makes accurate masking challenging. Therefore, any future measurements of the short circuit current (on a similar thin and flexible LSC) should require that an accurate, non-peelable mask is applied to the silicon solar cell. One useful method for making this mask could be to create the mask using photolithographic techniques.

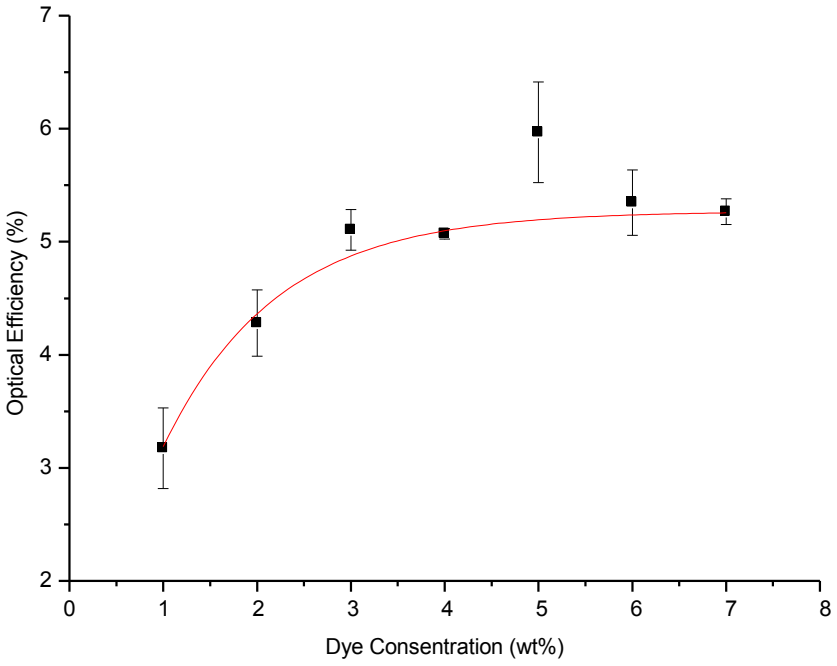


Figure 6-21 Plot of simulated optical efficiency (calculated for collection from all 4 edges) for the second generation flexible LSC prototype with a range of dye concentrations under AM1.5g at normal incidence.

Figure 6-21 is a plot of the variation of the optical efficiency of simulated Lumogen red 305 LSCs (with the dimensions of the second generation prototype, 90 by 59 by 0.5mm with a 0.11mm thin-film) with dye concentration. The figure also features a fitted exponential trendline, which serves to guide the eye. The full AM1.5g solar spectrum at normal incidence was used as the incident light source in the simulations. In the interest of time (at high concentrations the simulations are very slow), only 3000 incident photons were used in these simulations unlike the 10000 photons used in the other simulations in this thesis. However, as with the other simulations, at least 3 trials were performed for each simulation. The drawback to using fewer incident photons is greater variation in optical efficiency between trials. It is likely that that this is the reason why the 5wt% dye concentration appears as a significant outlier. Further evidence for this can be seen from the large error bars on the 5wt% point. The error bars were calculated from the standard deviation of the optical efficiency over the 3 trials, and in hindsight it would have been wise to perform further trials to give greater confidence in the result of fitting a trend line to the data. For a given size LSC the optical efficiency will at first increase owing to the better absorption but then, as the absorption begins to saturate at higher dye concentrations, the optical efficiency will start to plateau. Due to reabsorption further increasing the dye concentration is likely to then reduce the optical efficiency owing to greater reabsorption losses outweighing the small gain in absorption. Given the uncertainty in the results presented in Figure 6-21it is difficult to be sure exactly at which concentrations the plateau region and likely subsequent drop off (if indeed this concentration has actually been reached) in optical efficiency occur.

Figure 6-21 shows that a 5wt% dye concentration is the approximate dye concentration required to maximise the optical efficiency (in terms of simulated results). It is debatable whether or not a 4wt% concentration could have been chosen as the data is starting to plateau at this point. However, since 5wt% is the first measurement that is comfortably inside the

plateau region seen in the figure, it was deemed a better choice. Using this information it was possible to simulate optimal optical efficiencies based on the second generation flexible prototype, again using the full AM1.5g spectrum as the light source, but expanding the size of the prototype to more reasonable dimensions. The results are given in Table 6-7 and in all the simulations the substrate remained 0.5mm thick and the thin-film remained 0.11mm thick, as had been the case for the second generation flexible prototype. Table 6-7 shows that the decline in optical efficiency as the simulated prototypes dimensions are increased is quite rapid, with an approximately 41% decrease in optical efficiency between the 100 by 100m sample and 200 by 200mm sample. Since the simulations shown in Table 6-7 were modelled extrapolating from the second generation flexible prototype device (i.e. a LQY of 95%, and a loss coefficient of $0.3m^{-1}$ for the Plexiglass was used in all simulations), with the aforementioned optimisation of the dye concentration, neither the thin-film thickness nor the absorption coefficient (at the peak absorption wavelength) matched those of the ADS065BE 4wt% sample discussed in section 6.2.2.3, Table 6-5. As such it is difficult to directly compare the Lumogen red 305 and the ADS065BE 4wt% so further simulations with the same film thickness and peak absorption coefficient as the 4wt% ADS065BE were performed and the results given in Table 6-8.

It is possible to see from Table 6-7, that for all simulations the photon concentration from the 4 narrow edges is greater than unity. However, due to the re-absorption losses associated with Lumogen Red 305, the increase in photon concentration beyond an LSC size of 200mm by 200mm is limited, and indeed for the 1000mm by 1000mm LSC the photon concentration has begun to decrease. These results highlight the inappropriateness of using Lumogen Red 305 as the luminescent species in large area, thin LSCs, and provide strong motivation for finding luminescent materials with low or no spectral overlap between their absorption and emission spectra.

Length and Width (mm)	Geometric Concentration	Optical Efficiency (%)	Photon Concentration
90 by 59	29.2	5.07±0.13	1.48±0.04
100 by 100	41.0	4.35±0.04	1.78±0.02
200 by 200	82.0	2.57±0.01	2.11±0.01
500 by 500	205.0	1.09±0.05	2.23±0.10
1000 by 1000	410.0	0.51±0.07	2.09±0.29

Table 6-7 Table featuring optimised flexible LSC simulation results, using 5wt% Lumogen red 305 dye.

Table 6-8 shows clearly that despite the advantages of Lumogen red 305 (BASF): high LQY, relatively cheap, relatively high Stokes-shift and commercially available in large quantities; this dye is still not going to be appropriate for relatively large area, thin and flexible LSCs. A one meter squared LSC, which is probably the minimum practical size for a flexible LSCs, shows a reduction to ~13% of the optical efficiency that was simulated for the lowest dimension sample (which had length and width dimensions of 100 by 100mm), though this does represent a factor 100 difference in surface area.

Length and Width (mm)	Geometric Concentration	Optical Efficiency (%)	Photon Concentration
100 by 100	41.7	4.49±0.20	1.87±0.08
200 by 200	83.3	2.61±0.24	2.18±0.20
1000 by 1000	416.7	0.60±0.14	2.50±0.58

Table 6-8 A table containing computationally modelled optical efficiencies for LSC samples containing Lumogen red 305. All thin-film thicknesses are 100µm, substrates are 0.5mm thick and the absorption coefficient at the peak absorption wavelength is matched to that of the ADS065BE sample.

For simulated samples with length and width parameters of 100 by 100mm and 200 by 200mm, the simulated optical efficiencies are 4.49±0.20% and 2.61±0.24% respectively, meaning that there is an ~42% decrease in optical efficiency after doubling the LSCs length and width. The rate of the decrease in optical efficiency observed in Table 6-7 is particularly concerning given that the LQY of Lumogen red 305 is 95% (as modelled). Although a near unity LQY will not mitigate losses from escape cones it should largely reduce losses from non-radiative emission (which would be of benefit if there were significant reabsorption events, see chapter 2, section 2.6.4).

It is reasonable to compare the results in Table 6-5 (see section 6.2.2.3) and Table 6-8 as all simulation parameters were identical for the ADS065BE 4wt% simulated samples and the Lumogen red 305 simulated samples. Furthermore, the peak absorption coefficients for both samples were set to be identical to one-another, though their absorption peaks obviously still occurred at very different wavelengths. Observations of Table 6-5 reveal that the rate of optical efficiency decline for samples utilising the high Stokes-shift material ADS065BE was less severe at the small sizes, than is seen for the Lumogen red 305 samples in Table 6-8, even though the LQY values are significantly lower. For example, for the ADS065BE 4wt% sample a ~30% decrease in optical efficiency after a doubling of the length and width parameters is seen, which is far superior to the ~42% decrease described above (for identical sample dimensions) for Lumogen red 305. It should also be reiterated at this point that the lower optical efficiencies observed for the high Stokes-shift samples listed in Table 6-4 and Table 6-5, are due to the non-ideally located absorption spectrum of the ADS065BE material when compared to AM1.5g light source. Therefore, the photon concentrations of the Lumogen red 305 LSCs which had far superior light harvesting capability were also higher. The simulations gave photon concentrations of 1.87 and 2.18 for the 100mm and 200mm square devices respectively.

6.4 Conclusions

In this chapter a large surface area, thin and flexible LSC intended for portable power applications has been designed, fabricated and characterised. A holder was developed to allow solar cells to be easily clipped to the edges of the flexible LSC when needed, which also served to protect the silicon solar cells mounted within it from damage. The prototype holder was tested and characterised in conjunction with a first generation prototype LSC.

Raytrace simulations performed using experimental data collected from a small LSC sample utilising a tandem luminescent species PE-610 highlights the importance of having as thick a substrate as is reasonably possible to optimise the optical efficiency. Under illumination by the standard AM1.5g solar spectrum at normal incidence a 250 by 250mm LSC with a substrate thickness of 3mm gave an optical efficiency of 1.2±0.1% and reducing the substrate thickness to 0.5mm caused the optical efficiency to fall to just 0.5±0.1% (all other parameters were identical).

Experimental characterisation was performed on 3 materials with promising characteristics for this application. PE-610 was a tandem dye consisting of rhodamine B and R-phycoerythrin, which is extracted from algae, making it a potentially cheap and widely available material. This dye had a reasonable Stokes-shift but a relatively low measured LQY, of 53±0.5%, making it unsuitable for use in this project. A second material, ADS065BE was an iridium based electrophosphorescent complex, which had a large Stokes-shift with very little spectral overlap, and at a dye concentration of 4wt%, was measured to have a LQY of 70.7±7.1%, making this a useful material. However, iridium is an expensive material. A third material characterised was the common LSC material Lumogen red 305, which is relatively cheap and has a quoted LQY of 95%.

Comparisons between computationally modelled 100 by 100 by 0.5m and 200 by 200 by 0.5mm LSCs utilising Lumogen red 305 and ADS065BE 4wt% (all other parameters were identical, including peak absorptivity coefficient), showed declines in optical efficiencies of ~42% and ~30% respectively on doubling the lateral dimensions. This highlights the importance of very high Stokes-shifts to this application, and LSCs in general.

Finally, a prototype flexible LSC (second generation) was fabricated using a flexible substrate material called PLEXIGLAS Film clear 99524 (Evonik Industries), which was also used for the thin-film matrix. This material had ~90% transmission across the visible spectrum and after doping with Lumogen red 305, showed no signs of degradation after repeated flexing. Characterisation of the 90 by 59 by 0.5mm LSC (average thin-film thickness of 110μm), proved challenging due to the natural curvature of the flexible LSC prototype and its extreme thinness. It became apparent that the standard method of measuring the photon flux (as explained in chapter 4, section 4.9) would need to be adapted for future flexible LSC measurements (due to the challenging geometry of the flexible LSC prototype). The author believes that the adaptions to the short circuit current measurement outlined in this chapter would be able to provide optical and power conversion efficiencies with greater accuracy in future measurements on flexible LSCs.

Future work on this project should look into producing a flexible LSC prototype with a thicker substrate (thin enough to still be easily flexible). Other high Stokes-shift materials should also be investigated, which have a better absorption spectrum match to AM1.5g. Ideally these materials should also consist of common low cost materials, unlike the rare Earth material featured in this chapter.

Chapter 6 References

[1] Yoon, J.,Li, L., Semichaevsky, A., Ryu, J., Johnson, H., Nuzzo, R., and Rogers, J.,, "Flexible concentrator photovoltaics based on microscale silicon solar cells embedded in luminescent waveguides", Nature Communications. 3, 343, (2011).
[2] Trautz, K., Jenkins, P., Walters, R., Scheiman, D., Hoheisel, R., Tatavarti, R., Chan, R., Miyamoto, H., Adams, ., Elarde, V., and Grimsley, J., (2013). "Mobile Solar Power", IEEE journal of Photovoltaics, 3, 1.
[3] Farrell, D, J, PhD Thesis, "Characterising the Performance of Luminescent Solar Concentrators," University of London, 2008.
[4] Sholin, V., Olson, J., and Carter, A., (2007),"Semiconducting polymers and quantum dots in luminescent solar concentrators for solar energy harvesting" J. Appl. Phys. **101**, 123114.
[5] Gantt, E., (1981)."Phycobilisomes". Annual Review Plant Physiol. 32, p327-34.
[6] SpringerImages, data accessed (13/9/2013), http://www.springerimages.com/Images/Chemistry/1-10.1007_s00216-007-1182-6-1 .
[7] Prozyme. Accessed on (20/9/2013), http://www.prozyme.com/spectra/rpe.html .
[8] Kubin, R. and Fletcher, A., (1982). "Fluorescent Quantum Yields of Some Rhodamine dyes", Journal of Luminescence, 27, p455-462.
[9] Grabowski, J. and Gant, E., (1978). "Excitation-Energy Migration in Phycobilisomes – Comparison of Experimental Results and theoretical Predictions", Photochemistry and Photobiology, 28, 1, p47-54.
[10] Chen, Z., Samuelson, L., Akkaara, J., Kaplan, D., Gao, H., Kumar, J., Marx, K., and Tripathy, S., (1995). "Sol-Gel Encapsulated Light-Transducing Protein Phycoerythrin: A New Biomaterial", Chemistry of Materials, 7, p1779-1783.
[11] Suzuki, K., Kobayashi, A., Kaneko, S., Takehira, K., Yoshihara, T., Ishida, H., Shiina, Y., Oishi, S., and Tobita, S., (2009). "Reevaluation of absolute luminescence quantum yields of standard solutions using a spectrometer with an integrating sphere and a back-thinned CCD detector", Phys. Chem. Chem. Phys., 11, p. 9850-9860.
[12]Fisher, M., Ippen, C., Farrell, D., Walters, R., González, M., Trautz, K., Tischler, J., Morseman, J., and Chatten, A.,. (2012). "Flexible Luminescent Solar Concentrators Utilizing Bio-derived Tandem fluorophores", Proc. 38th IEEE Photovoltaic Specialists Conference, (Austin, USA), P3333-3338.
[13] Fisher, M., Farrell, D., González, M. Trautz, K., Walters, R., and Chatten, A., (2011). "Comparisons between Homogenous and Thin-film, Ultra-thin, Flexible Luminescent Solar Concentrators"7th Photovoltaic Science Application and Technology and Exhibition,(Edinburgh, Scotland).
[14] American Dye Source accessed (14/9/2013). http://www.adsdyes.com/products/ADS065BE.html .
[15] Lu, Y. and Penzkofer, A., (1986). "Absorption Behaviour of Methanolic Rhodamine 6G Solutions at High Concentrations", Chemical Physics, 107, p175-184.
[16] Chatten, A., Farrell, D., Bose, R., Dixon, A., Poelking, C., Gödel, K., Mazzer, M., andBarnham, K., (2011). "Luminescent and Geometric Concentrators for Building Integrated Photovoltaics", Proc. 37th IEEE Photovoltaic Specialists Conference, (Seattle, USA), p852-857.
[17] González, M, personal correspondence", NRL,, Washington D.C., USA, (2011).
[18] Evonik Industries, Accessed on (16/9/2013), http://www.plexiglas-shop.com/GB/en/details.htm?$product=7i1sm3nwogp~p&$category=5m9m5apyxic .

[19] Sloof, L., Budel, T., Burgers, A., Bakker, N., Buchtemann, A. Danz, R., Meyer, T., Meyer, A., (2007).“The Luminescent Concentrator: Stability Issues”, Proc. 22nd European Photovoltaic Solar Energy Conference, Milan, Italy.
[20] Buechtemann A, Private Correspondence, Fraunhofer IAP, Germany (2012).
[21] Bose, R., (2012). “Raytrace Simulations and Experimental Studies of Luminescent Solar Concentrators”, Doctoral Thesis, Imperial College London.
[22] Kennedy, M., McCormack, S., Doraon, J., and Norton, B., (2007). “Modelling the effect of device geometry on concentration ratios of quantum dot solar concentrators”, Proc. ISES World Solar Congress, (Beijing), pp. 1484–1487.

Chapter 7

LSC Utilisation to Enhance Water Splitting

7.1 Introduction

In this chapter a novel LSC/photoelectrochemical cell (PEC) cell hybrid has been designed, fabricated and characterised to determine its potential for effectively splitting water into O_2 and H_2. Molecular hydrogen is useful for a number of reasons, one of the most important of which is its use as an energy storage medium [1], which is potentially of great importance for the future of renewable energy sources.

The device setup in this work makes use of two 10cm by 10cm by 0.5cm LSCs which have wire-bar coated thin-films on their top surfaces. One LSC makes use of Fluorescent violet (Kremer) as the luminescent species; this dye is used to absorb photons from the UV region of the EM spectrum, and has an emission spectrum in the blue region of the spectrum. The PEC cell was optically coupled to the narrow edge of this violet LSC where the emission had a good spectral match to the absorption spectrum of the Fe_2O_3 working electrode of the PEC cell, and therefore had a high incident photon to current efficiency (IPCE). It was the intention that the violet LSC concentrated light to wavelengths at which IPCE is high onto the PEC cell to produce a more efficient PEC device, and thus more and potentially cheaper H_2 gas generation.

As described in section 2.10.2, chapter 2, Fe_2O_3 has a bandgap energy of ~2.1eV [2], and the position of its conduction and valence bands allow it to act as a photoanode. In order for water splitting to occur, there should be a difference in energy of at least 1.23eV between the two bands [3]. Equations 7.1 and 7.2 show the 2 half reactions that occur as well as the

relevant potentials vs. NHE (normal hydrogen electrode, highlighted in brackets) at the anode (Fe_2O_3) and cathode (platinum wire) respectively.

$$2H_2O + 4h^+ \rightarrow O_2 + 4H^+ \qquad (1.23eV\ vs.NHE) \qquad 7.1$$

$$4H^+ + 4e^- \rightarrow 2H_2 \qquad (0eV\ vs.NHE) \qquad 7.2$$

In the equations above h^+ is a positively charged hole, and e^- is a negatively charged electron. In reality however, the energy required is higher, and is usually quoted as being between 1.6-2.4eV [4]. The 1.23eV limit is quoted before factoring inefficiencies which exist at the interface between the semiconductor working electrode and the electrolyte solution, and the overpotentials [4]. As was discussed in chapter 2 section 2.10.3 the overpotential is the difference in potential between the thermodynamic potential for the half reaction and the potential actually measured at which a redox reaction occurs [5].

In essence, for water splitting to occur, the electrons in the conduction band need to have a potential which is more negative than the redox potential of reduction, H^+/H_2 (0V vs. NHE), and more positive than the redox potential of oxidisation, O_2/H_2O (1.23eV vs. NHE) [*5*,6]. This explains where the 1.23eV limiting value comes from, although as mentioned above losses and inefficiencies increase this value. Therefore, Fe_2O3 is an appropriate photoanode material since it has a conduction band which is not more negative than 0eV (vs. NHE) (so it cannot reduce protons), but its valence band is 2.1V (which is more positive than 1.23V vs. NHE), and as a result it can oxidise water. This being the case, the PEC cell is required to generate 4 electron-hole pairs in order to split water and produce a single O_2 molecule [4]. Therefore, in order to drive a "water splitting" reaction with a Fe_2O_3 based PEC cell, an additional source of potential is needed to rapidly separate the electrons from the electron-hole pairs to prevent recombination, and these electrons can then move to the platinum

counter electrode and proton (hydrogen) reduction can occur [6]. Working electrodes with a bandgap large enough to run hydrogen and oxygen evolution simultaneously are currently not known [4]. As a consequence, in this work the PEC cells potential is augmented by the addition of a second, red LSC (Lumogen red 305 (BASF)), which was used to concentrate light onto silicon cells, connected to one another in series along a single edge of the LSC. The silicon solar cells, with the optically coupled red LSC, were then connected in series to the PEC cell, to prevent electron-hole recombination, which would occur rapidly if no bias were applied.

In this chapter the fabrication and characterisation of the LSC/PEC device is reviewed and the results obtained are analysed in order to assess whether or not the use of LSCs offers any advantages to PECs.

7.2 Design Specifications for LSC/Electrode Device

This section outlines how the LSC/PEC device was fabricated and highlights the steps taken to maximise the device's efficiency.

7.2.1 LSCs and LSC Sample Holder

The two LSCs used in this chapter were made by depositing thin-film layers containing a luminescent dopant species onto the surface of 10cm by 10cm by 0.5cm borosilicate glass substrates using a wire-bar coater, and a general description of this method is outlined in chapter 4 sections 4.13.1 and 4.13.3. A violet LSC was made with a concentration of 2.5wt% of Fluorescent violet (Kremer), and a red LSC was made with a dye concentration of 3wt% Lumogen red 305. Further details for the samples can be found in chapter 4 section 4.15. Fluorescent violet has a quoted LQY of 79% [7] and Lumogen red 305 has a quoted LQY of >90% [8]. Characterisation of these LSCs is considered in section 7.3.

The LSC holder was very simple device as shown in Figure 7-1 (below). The LSC holder is made from stiff card with an open top surface to allow incident light in, and one open edge which allowed one narrow edge of each LSC to protrude from the holder, which in turn allows the PEC and solar cells to be coupled to the LSCs. The inside of the holder was lined with 2mm thick PTFE, which is a white diffuse scattering material with a reflectivity of ~95% over the wavelength range 300 to 650nm [9]. The PTFE was used for enhancing the efficiency of the LSCs by both scattering back in a large fraction of the light that would otherwise be lost from the 3 edges not coupled to the PEC cell or solar cells, and by providing a second pass (at wider angles) for a large fraction of the light that was not absorbed by the two LSCs on the first pass. Scattering photons lost through the escape cones back into the LSC provides another opportunity for some of these photons to be collected at the edges coupled to the PEC cell and solar cells as discussed in section 3.2.1, chapter 3. In addition, some incident light may also be directly scattered into the coupled PEC and solar cells as was seen in the record 7.1% efficient LSC described in [10] (see also chapter 3 section3.2.1).

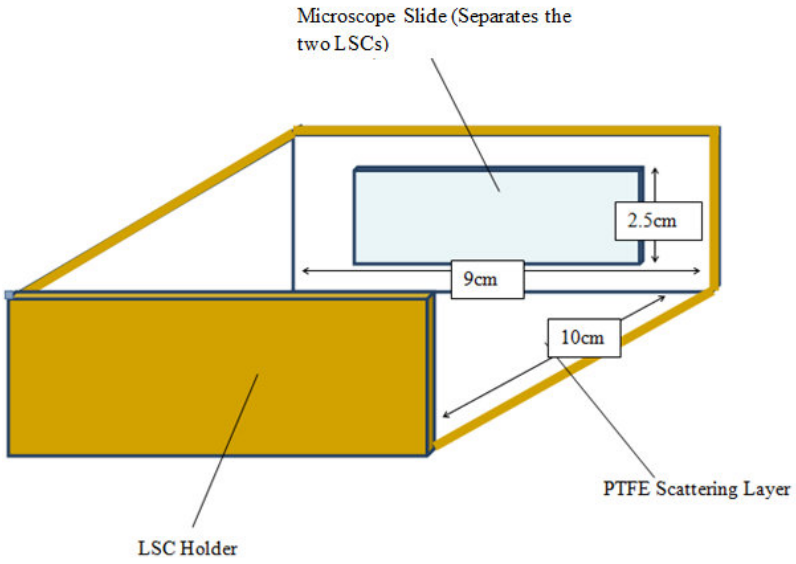


Figure 7-1 Diagram of the LSC sample holder used to hold the LSCs and provide sufficient spacing between them to allow the solar cells and PEC to be attached.

Inside the LSC sample holder, a standard glass microscope slide was affixed to each of the side walls (see Figure 7-1) in order to both support the upper violet LSC and to separate the two LSCs. The violet and red LSCs needed to be separated by sufficient distance to ensure enough space for the PEC cell and solar cells to be attached to the edges of the LSCs. As shown in Figure 7-1, the approximate dimensions of the holder were; 10cm in width, 9cm in length, and a LSC separation of 2.5cm.

7.2.2 The Photoelectrochemical Cell (PEC)

The PEC cell used in this work was designed and made by a collaborator, Federico Pesci, working in the Chemistry Department of Imperial College. This section of the report gives a brief description of the PEC cell. The PEC cell consists of a working electrode made by applying a Fe_2O_3 coating onto fluorine tin oxide (FTO) glass, towards which the negatively charged oxygen ions are attracted and then combine to form molecular O_2 gas. The PEC body, the container which holds the electrolyte material, is made from polyether ether ketone (PEEK), which was chosen due to its chemical stability (essential due to the alkaline pH of the electrolyte). The PEC also consists of a counter electrode made using a platinum wire, towards which positively charged hydrogen ions move and combine to form H_2 gas. The potential difference between the working and counter electrode, due to the red LSC/silicon solar cell system coupled in series, is then used to minimise recombination losses after carrier generation [6].

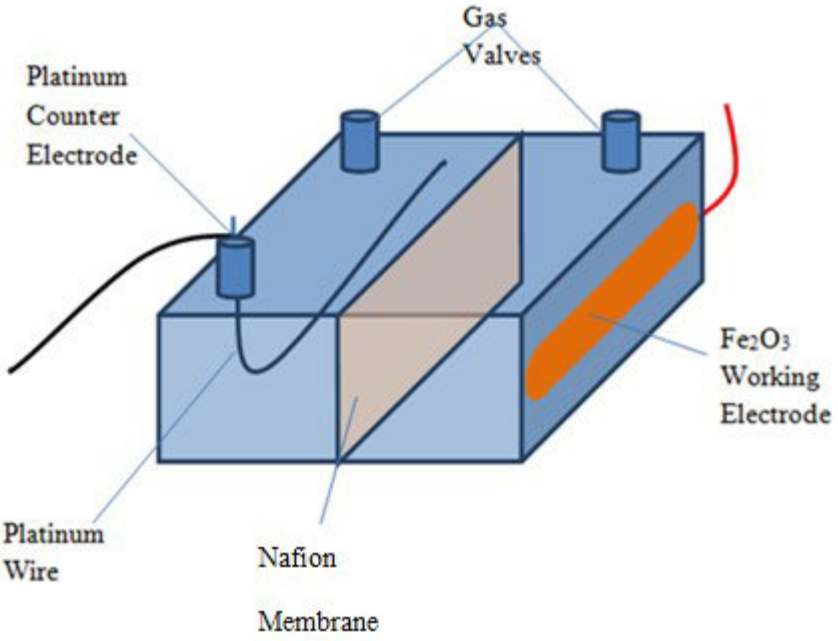


Figure 7-2 Schematic diagram of the PEC cell used in this work.

Figure 7-2 shows a diagram of the PEC cell. In addition to the working and counter electrodes the PEC cell contained an aqueous electrolyte solution (with 1 Molar NaOH added to bring the pH to the correct level). Within the PEC there is also a treated nafion membrane which is used to prevent positively charged ions (cations), H^+ ions in this case, from recombining with the negatively charged ions (anions), in this case O^{2-}. This is achievable because only cations can pass through the membrane. Lastly, the PEC has two sealable vents, one each side of the nafion membrane, which can be unsealed in the event O_2 or H_2 gas is to be collected/extracted from the PEC.

7.3 LSC Absorption and Emission

The following section describes the spectral characterisation of the violet and red LSCs.

7.3.1 Absorptivity

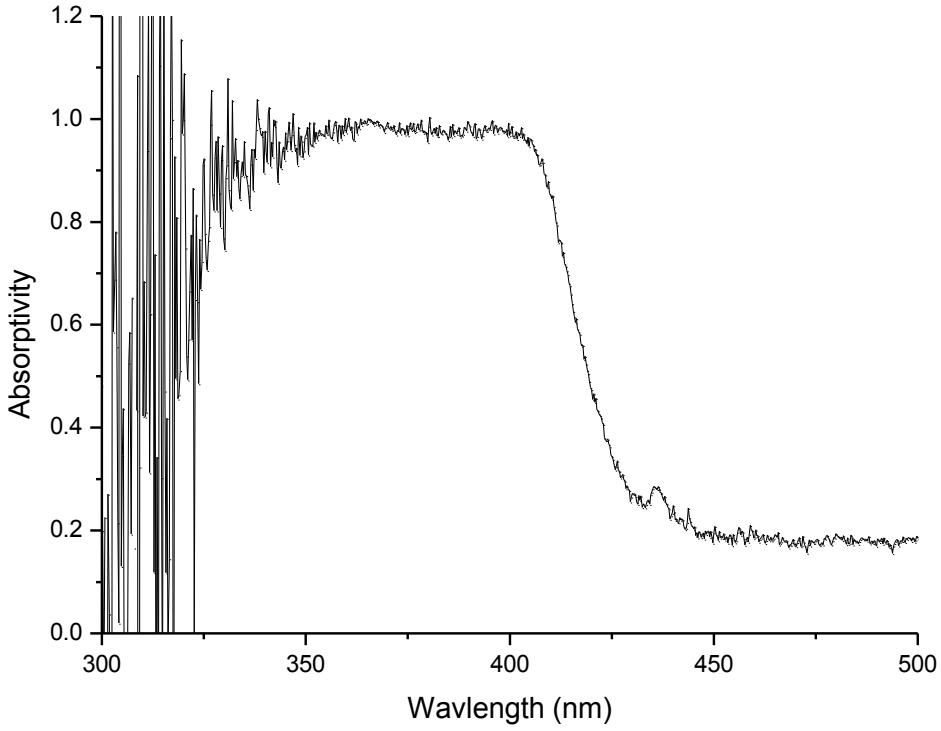


Figure 7-3 Absorptivity spectrum of the 2.5wt% Kremer violet LSC plate.

Figure 7-3 shows the absorptivity spectrum (not corrected for surface reflection and scattering losses) for the 10cm by 10cm by 0.5cm violet LSC which had a thin-film with an average thickness of 55μm. The solution used to make the thin-film consisted of a matrix material which was a mixture of PMMA crystals and PLMA, with a total mass of 4g (15% of which was PLMA), dissolved in 10ml of chlorobenzene. 2.5wt% of Fluorescent Violet (Kremer) dye material, in relation to the combined weight of PMMA/PLMA, was added to the solution. Figure 7-3 shows that the sample's high dye concentration resulted in a saturation of the absorptivity spectrum between ~350nm and ~410nm. The dye concentration was chosen to be sufficiently high so as to ensure the maximum possible absorption of light,

but also to be low enough to avoid noticeable dye agglomeration, with the overall intention of providing the highest possible intensity light emission for the PEC to absorb.

It was found that significant agglomeration of the dye was observable by eye at concentrations above 2.5wt%. Agglomeration of luminescent material will result in less light being emitted from the edges of the LSC, since dye agglomeration causes PL quenching. Computational modelling prior to fabricating the violet and red LSCs (see section 6.3.4, chapter 6 and chapter 4, section 4.14 for the computational modelling methodology) suggested that a dye concentration of ~5wt% would provide the highest optical efficiency for a Lumogen red 305 LSC with dimensions of 90 by 59 by 0.5mm with a 0.11mm thin-film. These high concentration simulations were not ideal since they were performed for a sample with different dimensions (since the simulations were being performed for a sample used in chapter 6). The mismatch in dimensions between the simulated sample and the LSC plates utilised in this chapter meant that the simulations could provide a good starting dye concentration for use in this work, rather than a definitive dye concentration to use. Furthermore, since these simulations were performed only for Lumogen red 305, which is a perylene based dye, and Fluorescent Violet is naphalimide based dye with a different molecular weight, the comparison is not ideal. However, the important point is that the simulations revealed that for these relatively small LSCs, maximising light harvesting is more important than minimising reabsorption losses, and saturation of the absorptivity over the wavelengths at which the dye absorbs is desirable. As was discussed above (see Figure 7-3) this was achieved over most of the wavelength range for which Kremer violet absorbs. At this point it is important to note that, at extreme dye concentrations the group's Raytrace computer model does not take into account agglomeration of the luminescent species, and the losses associated with this phenomenon, which explains why optimal dye concentrations in real samples are considerably lower than computational ones.

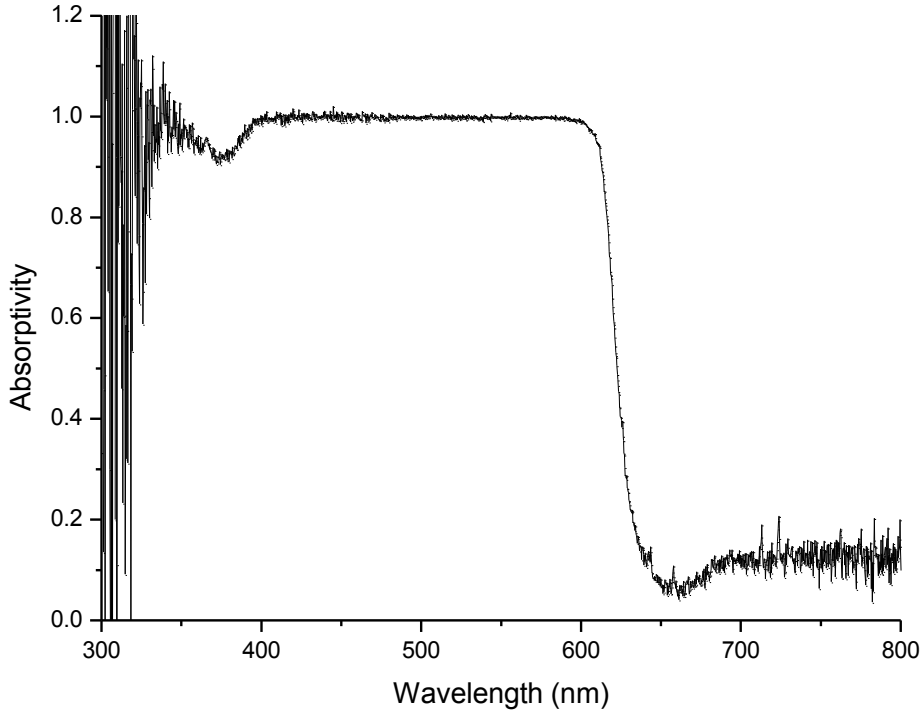


Figure 7-4 Absorptivity spectrum of the 3wt% Lumogen red 305 LSC plate.

Figure 7-4 shows the absorptivity spectrum (not corrected for surface reflection and scattering losses) for the 10cm by 10cm by 0.5cm red LSC which had a 107.5µm thick thin-film. This 3wt% Lumogen red LSC was fabricated in the same way as the 2.5wt% Fluorescent violet LSC. As was the case for the Fluorescent Violet dye, the Lumogen Red 305 dye has a high enough concentration to effectively saturate the absorptivity spectrum, so as to achieve very high photon absorption levels, and thus provide the silicon solar cells with the highest possible photon flux density. It can be seen from Figure 7-4 that absorptivity saturation occurred between ~400nm to 610nm. Visual observations again determined that there was no significant agglomeration of the luminescent species at this weight percentage. It was found that a higher weight fraction of Lumogen red 305 dye could be used than for Fluorescent violet, 3wt% and 2.5wt% respectively.

Ultimately, as will be shown in the next section, the dye concentrations being used were too high. Significant scattering of the incident light source out of the narrow LSC edges was occurring, likely as a result of agglomeration of the dye (which will cause PL quenching), due to the high concentrations, that was not visible by eye. This was particularly severe in the case of the violet LSC and in future edge PL measurements should be made to check for scatter due to dye agglomeration or the plates should be examined under a microscope. Production of multiple plates for this type of analysis was not possible in this case owing to the limited number of expensive polished substrates available. Such measurements would likely have led to the conclusion that lower dye concentrations would have been preferable. However, LSCs made with lower dye concentrations would have given lower incident light absorption, but would likely still allow for a more efficient device as there would probably have been more photoluminescence.

7.3.2 Emission Spectra

Edge emission spectra were taken using a variation on the edge emission measurement experiment as described in section 4.5.2, chapter 4. Figure 7-5 shows the altered experimental setup, and the resulting emission spectra can be seen in Figure 7-6 and Figure 7-7. Figure 7-6 shows the edge emission spectra from the 3wt% Lumogen Red 305 LSC. This figure contains edge emission spectra taken both for when the red LSC was independently mounted on the sample mount, and also for when the red LSC was mounted inside the sample holder, with the height of the sample mount adjusted to compensate for the variation in height due to the sample holder.

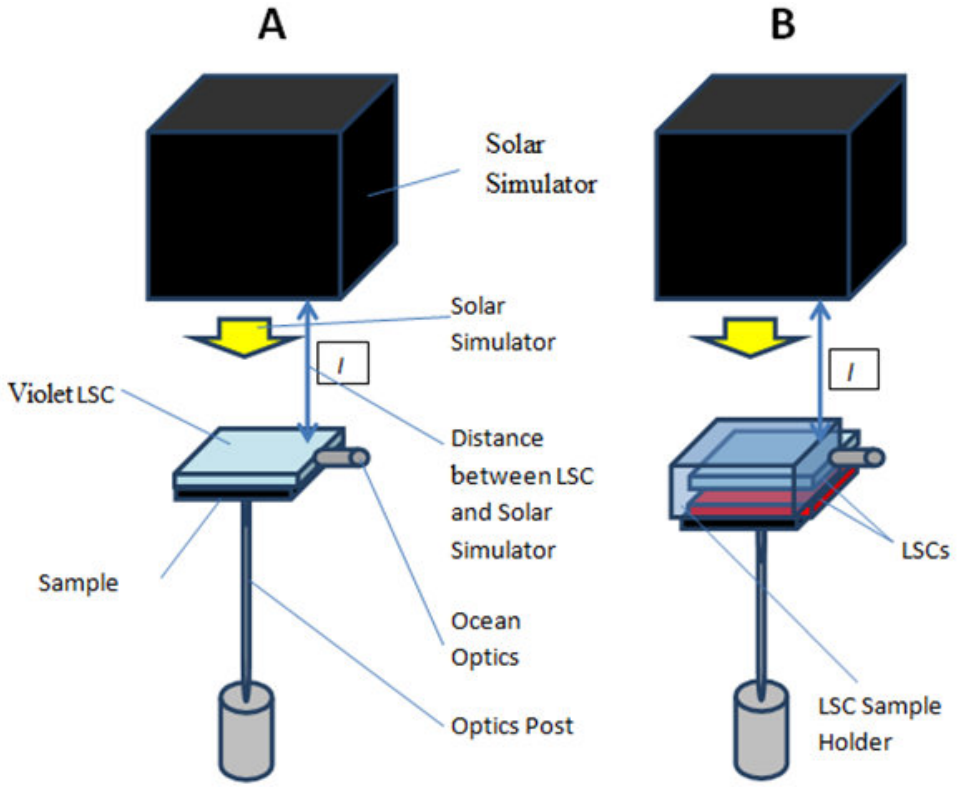


Figure 7-5 A) Shows how edge emission was collected from the LSCs when placed on sample mount, and B) when the LSCs were mounted in the holder. The distance *l* is the same in both A) and B).

As can be seen from Figure 7-6 (for the red LSC), there is only a marginal change between the emission spectra produced in the LSC holder and the spectra produced outside the LSC holder, though it should be noted that both have been peak normalised. There is a slight observable red-shifting of the emission spectrum when the red LSC was inside the LSC holder, and a small increase in the noise peaks at 855nm and 890nm, with respect to when the red LSC was outside the holder. The very slight increase in red-shifting seen for the results taken in the holder is a result of increases in reabsorption losses (see section 2.6.4, chapter 2) due to the increased pathlength when using the PTFE white diffuse scattering layer that lines the inside of the LSC sample holder.

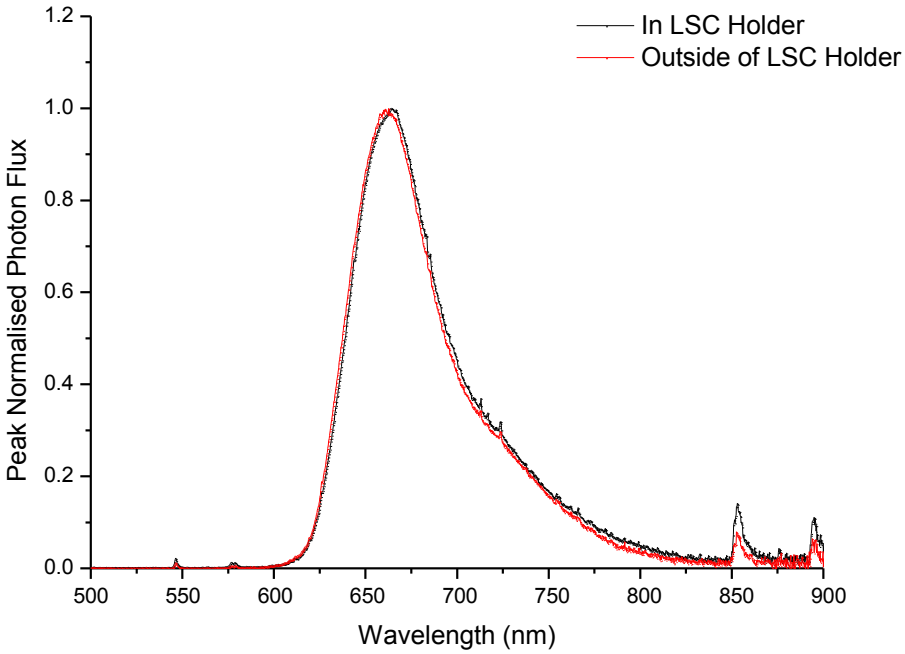


Figure 7-6 Lumogen red 305 LSC plate edge emission in terms of peak normalised photon flux.

Figure 7-7 (below) shows the edge emission measured for the 2.5wt% Fluorescent Violet LSC plate both when inside the LSC holder and outside of the LSC holder (see Figure 7-5 above). What is clear for both measurements is that the emission from the edge of the violet LSC includes scattered photons from the incident light source, in addition to the PL emission from the Fluorescent violet dye. This may simply be due to the fluorescent dye being a good scattering material, or it may be a result of dye agglomeration, unseen to the naked eye, or irregularities in the surface of the thin-film being causes of additional scatter. In general, the addition of scattered incident light to the edge is of benefit to a LSC's efficiency. This is of course provided that the phenomenon which is causing the scattering is not reducing PL emission from the luminescent species, for example, scatter due to dye agglomeration which will reduce the overall edge emission. Alternatively, some or all of the scattered photons may fall outside of the absorption range of the attached solar cell(s), or in the case of the violet

LSC the working electrode of the PEC. An observation of the IPCE data for the Fe_2O_3 electrode, see Figure 7-8, which was later attached to one edge of the violet LSC, reveals that some of scattered photons will be of use to the electrode. However, fewer photons will be collected as their wavelengths get longer, due to the loss in sensitivity of the electrode.

Figure 7-7 also shows a slight red-shifting of the emission from the violet LSC when in the LSC holder, in the same way the emission from the red LSC did. There is also a clearly visible additional peak in the spectrum when the violet LSC is in the LSC holder. This additional peak is a result of PL emission from the red LSC, which is positioned in the LSC holder just beneath the violet LSC, and as a result some of the red PL emission is scattered to the edge(s) of the violet LSC. The two LSCs were positioned in the LSC holder at the same time so as to give a true representation of the emitted light which the Fe_2O_3 electrode and Si cells would collect when attached to the LSCs.

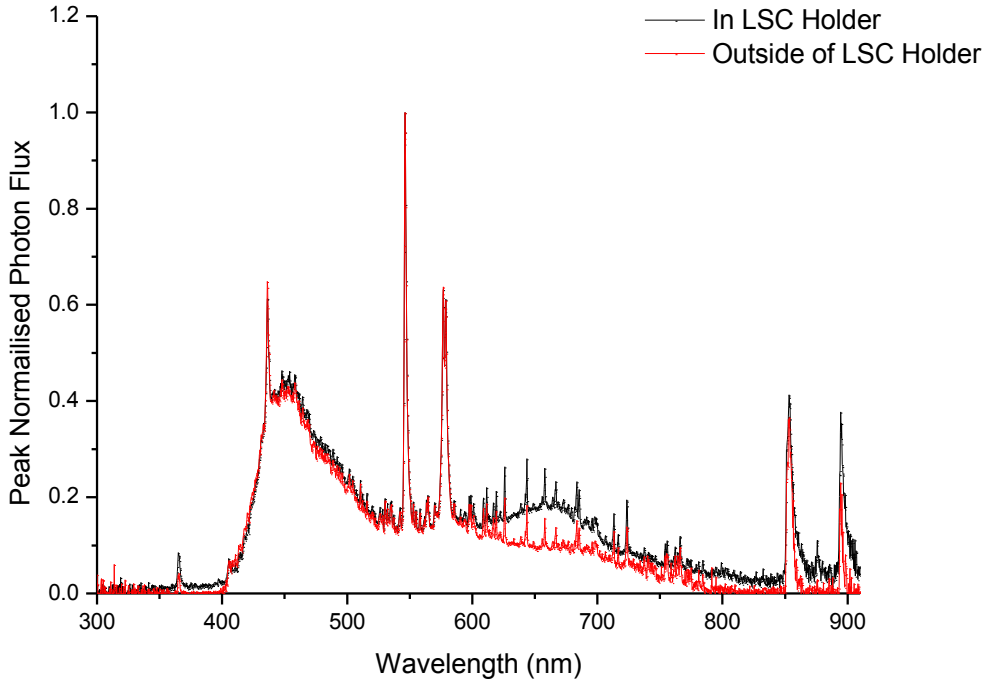


Figure 7-7 Fluorescent Violet LSC plate edge emission in terms of normalised photon flux.

7.4 IPCE

The IPCE (see section 2.10.4, chapter 2 for definition and formula) or incident photon to current efficiency for the Fe_2O_3 PEC cell working electrode is shown in Figure 7-8. This measurement was performed by a collaborator, Federico Pesci, (Imperial College, Department of Chemistry), and shows that the working electrode in the PEC has a maximum IPCE value of ~9.8%, for light at ~350nm. It is also obvious from Figure 7-8 that the IPCE rapidly decreases at longer wavelengths, and therefore, for the PEC to maximise photon conversion it is essential that the emission spectrum of the violet LSC, from which the PEC receives light, is as close to 350nm as possible. The IPCE measurement was performed with an applied bias of +1.6V vs. the Real Hydrogen electrode (RHE). It is difficult to do a direct comparison between the working electrode used in this chapter (a Fe_2O_3 working electrode without the application of the CO(II) catalyst) and the record reported electrode (in terms of IPCE) shown in the work of Kay *et al.* [11], since their measurement of IPCE was performed under the AM1.5G solar spectrum (which was not the case for the electrode in this chapter). The Fe_2O_3 working electrode in this chapter had an IPCE = ~7.9% at 370nm and at 1.6V vs. RHE, while the working electrode in the work of Kay *et al.* (which consisted of an Fe_2O_3 thin-film on an interface layer of SiO_2 and a substrate of SnO_2 glass) had an IPCE=42% at 370nm at an applied voltage of 1.23V vs. RHE. Despite the different light sources used to perform each of these respective measurements, the relatively low IPCE recorded for the Fe_2O_3 electrode in this chapter suggests that significant optimisation of the working electrode will be required in future versions of the LSC PEC device in order to be closer to the efficiency of the Kay *et al.* device.

There is a trade-off between having a dye absorbing and emitting at longer wavelengths, in which case more of the incident light can be harvested but for which the emission will correspond to lower IPCE and thus lower conversion efficiency at the electrode, and having a

dye absorbing and emitting at shorter wavelengths, in which case less of the incident light can be harvested but for which the emission will correspond to a higher IPCE and thus a higher conversion efficiency at the electrode. Looking at the available commercial fluorescent dyes it was decided that the Kremer violet dye was the best compromise in absorbing a significant fraction of the incident light but also emitting at wavelengths for which the IPCE was not too low (which would be the case for green, yellow, orange and red emitting dyes). The Fluorescent violet dye (Kremer) used to produce the violet LSC (see edge emission spectrum in Figure 7-7) has an edge emission peak wavelength located at approximately 450nm, though the spectrum shows that there is significant light before 450nm, and even more after the 450nm peak due to the tail of the measured spectrum. As discussed in section 7.3.2, a considerable amount of the light observed in the violet LSC emission spectrum is due to scattered light from the solar simulator incident light source. However, if the 450nm peak observed in Figure 7-7 is taken as the peak wavelength, then this will correspond to a peak IPCE value of ~4% although the IPCE across the entire violet LSC edge emission spectrum should be considered.

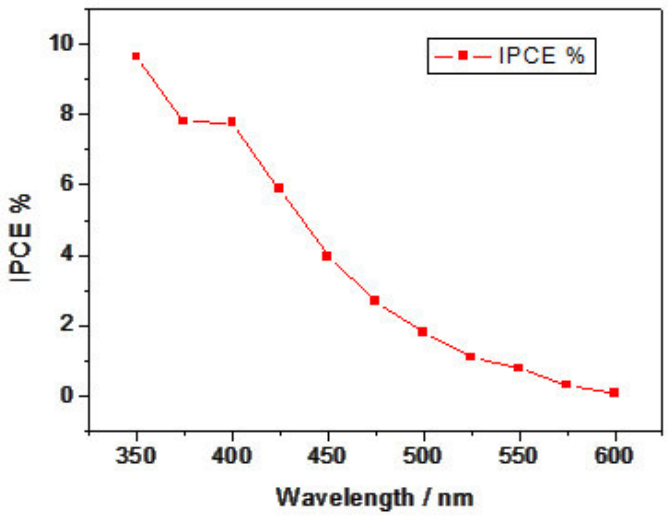


Figure 7-8 IPCE of the Fe_2O_3 working electrode (without catalyst) of the PEC, figure supplied by Federico Pesci [6].

It should be noted that Figure 7-8 only contains the IPCE for the Fe_2O_3 working electrode without the Co(II) catalyst. It was intended that measurements on the Fe_2O_3 working electrode with the Co(II) catalyst would also be included, but unfortunately, since the measurements on the Co(II) treated electrode and the standard Fe_2O_3 electrode did not take place on the same day, the experimental setup required for this additional measurement was not working at that time and ultimately there was no time left to repeat the experiment. However, it can be expected that the after adding the Co(II) catalyst material, there would have been some level of increase in the IPCE, since Co(II) has been shown to be an effective oxygen evolving catalyst [12].

7.5 LSC Short Circuit Current Measurements, Photon Concentration and Optical Efficiency

Short circuit current measurements were performed on both the violet LSC and the red LSC to allow for the photon concentration and the optical efficiency of each plate to be determined (see chapter 4, section 4.9 for full method). The short circuit current measurements were performed whilst both the red and violet LSCs were in their final working positions in the LSC holder, as shown in Figure 7-10, though a 2.65mm by 2.65mm solar cell was used in place of the Ocean Optics spectrometer. Due the thickness of the LSCs' substrates and thin-films, the photocurrent measurements had to be performed at both an upper and lower location (see Figure 7-9) at each position, and the two measurements were then added.

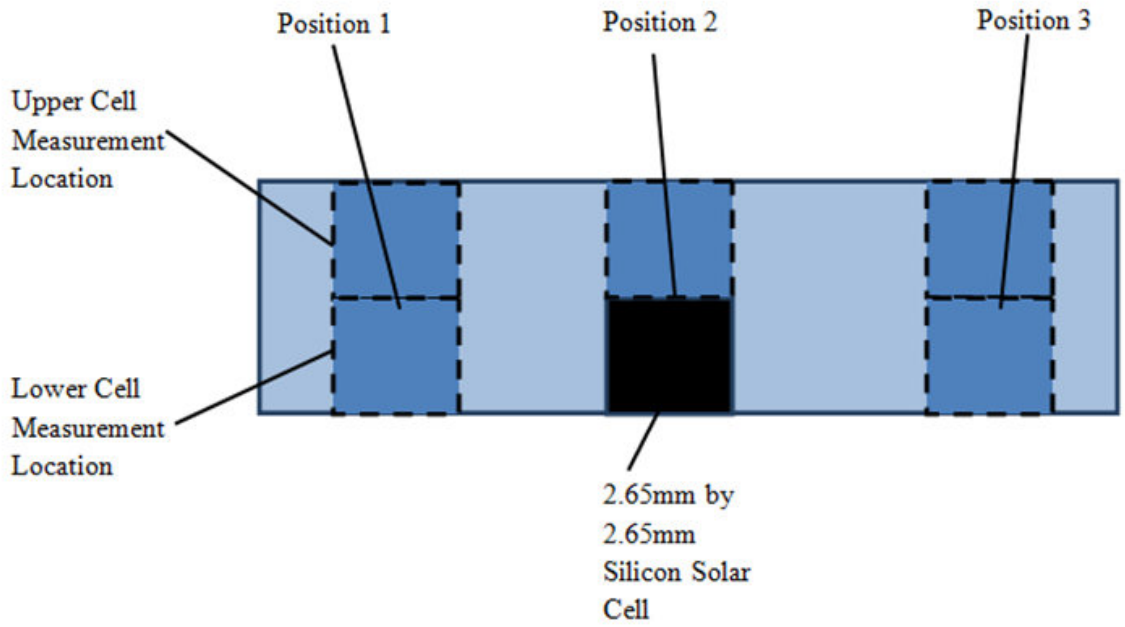


Figure 7-9 Side-on view of the LSC showing the locations of three measurement positions as well as the upper and lower solar cell locations.

After all the measurements had been performed, the average short circuit current data was then used to calculate the optical efficiency and photon concentration from one edge of each LSC as detailed in section 4.9 of chapter 4. Table 7-1 and Table 7-2 show the results for the violet and red LSCs respectively, it should be noted that the photocurrent from each edge of each LSC was measured, one at a time, by rotating the LSC samples around in the holder. It was important to determine if there was any variation in photocurrent for the different LSC edges, as this provided information related to the regional quality of the thin-film layer. Additionally, this knowledge made it possible to couple the highest photocurrent edge of the violet and red LSCs to the PEC cell and solar cells respectively.

For both samples the same incident photon count was used, and this was calculated from the short circuit currents recorded over the top surface of the violet LSC as detailed in section 4.9 of chapter 4. The light source used was the Steuernagel Lichttechnik solar simulator (with the

UV filter removed to give a spectrum closer to that of the AM1.5g solar spectrum, see chapter ,4 section 4.2). It was appropriate to use the same incident photon count for the red LSC in the calculations as was used for the violet LSC since the top surface of the violet LSC corresponds to the top surface of the whole system and the efficiency of the red LSC in this configuration, rather than when it is directly exposed to the incident light, is the relevant figure of merit.

Measurement	Side 1	Side 2	Side 3	Side 4	Average
Short Circuit Current (mA)	1.721±0.017	1.688±0.017	1.636±0.016	1.635±0.016	1.670±0.209
Optical Efficiency (%)	2.90±0.03%	2.80±0.03%	2.70±0.03%	2.70±0.03%	2.80±0.08%
Photon Concentration	0.553±0.006	0.542±0.005	0.526±0.005	0.525±0.005	0.536±0.012
Power Conversion Efficiency (%)	n/a	n/a	n/a	n/a	2.92±0.29

Table 7-1 The short circuit currents, optical efficiency, photon concentration and power conversion efficiency data for the violet LSC, from each edge.

In addition to the short circuit current, optical efficiency and the photon concentration, Table 7-1 also contains the calculated average power conversion efficiency from a single narrow edge of the violet LSC, whilst mounted in the LSC holder. As stated above, the incident light source was the Steuernagel Lichttechnik solar simulator (with the UV filter removed to give a spectrum closer to that of the AM1.5g solar spectrum, see chapter ,4 section 4.2). The power conversion efficiency was calculated using the method described in section 4.10, chapter 4, and was found to be 2.92±0.29% (when using the silicon solar cells described in section 7.6), which nearly identical to the average optical efficiency from one narrow edge, which was 2.80±0.08%.

The record power conversion efficiency reported for an LSC is 7.1%, which was achieved in the work of Sloof *et al.* [10] (see section 3.2.1, chapter 3 or [10] for more detail). It is difficult to directly compare the power conversion efficiency of the violet LSC to that of the LSC in Sloof's work for a number of reasons. Firstly, the surface area of the violet LSC is 4 times larger than that in [10]. Secondly, the record result was achieved using GaAs solar cells on all four edges of the LSC, but measurements were also taken when a single GaAs solar cell was coupled to one narrow edge of the LSC and the other 3 edges were covered with mirrors. This resulted in a power conversion efficiency of 4.6%. Lastly, and most importantly, the Sloof LSC was measured under the AM1.5G solar spectrum, which has a considerably longer spectral range than that of the Steuernagel Lichttechnik solar simulator used to characterise the violet LSC in this chapter, which means the power conversion efficiency of the violet LSC is artificially high compared to the result in [10]. However, all things considered, it would appear that the power conversion efficiency of the violet LSC is significantly lower than that of the record LSC. This is mostly due to the spectral range of the absorption of the Kremer violet dye which only absorbs efficiently out to ~430nm whereas the LSC in [10] absorbed efficiently out to ~630nm and thus had far superior light harvesting capability. Similarly, Table 7-2 includes the average power conversion efficiency for the Red LSC, which was measured to be 4.54±0.45%, which although more efficient than Violet LSC, still cannot be easily compared to the record efficiency shown in [10] for the reasons outlined above.

Measurement	Side 1	Side 2	Side 3	Side 4	Average
Short Circuit Current (mA)	2.298±0.023	2.367±0.024	3.267±0.033	3.226±0.032	2.790±0.458
Optical Efficiency (%)	3.7±0.04%	3.8±0.04%	5.2±0.05%	5.2±0.05%	4.5±0.73%
Photon Concentration	0.715±0.007	0.737±0.007	1.017±0.010	1.004±0.010	0.868±0.143
Power Conversion Efficiency (%)	n/a	n/a	n/a	n/a	4.54±0.45

Table 7-2 Table shows the photon flux, optical efficiency and photon concentration data for the red LSC, from each edge.

As can be seen from Table 7-1 and Table 7-2, the average photon concentration from each of the 4 edges is 0.536±0.012 and 0.868±0.143 for the violet and red LSCs respectively. On first inspection this would seem to indicate that it would be more efficient to direct the PEC cell or the solar cells directly at the solar simulator light source. However, the PEC cannot utilise the whole of the broad solar simulator spectrum (beyond 550nm the IPCE is very low) whereas it can convert all of the narrow band edge emission from the violet dye between 400-500nm (most of the scattered incident light seen beyond 500nm in Figure 7-7will not be converted). Therefore, in order to be more conclusive as to whether removing the violet LSC and then pointing the PEC cell's working electrode directly at the solar simulators light source would be more or less efficient, a simple calculation was performed. By normalising the area of the solar simulators light spectrum to 1 and then multiplying this by the IPCE spectrum (see Figure 7-8), then integrating the result, it was possible to determine the fraction of the solar simulator photons the PEC cell would have converted to current without the violet LSC being used. Next the violet LSC was evaluated by having its edge emission spectrum area normalised to 1 and then multiplying this with IPCE spectrum. Integration of this result

provided the photon fraction converted to current by the PEC cell. However, the inefficiencies of the LSC then needed to be factored in to the calculation. This was achieved by multiplying the fraction of light converted by the PEC cell from the violet LSC's edge emission, by the photon concentration measured for the violet LSC in Table 7-1. The results of this calculation are given in Table 7-3, and it can be seen that although the PEC cell would have been more efficient under direct illumination, rather than using an LSC, after factoring in the IPCE of the PEC cell it can be seen that the photon concentration is improved, being 0.635 compared to the initial value of 0.536±0.012.

Fraction of Solar Simulator Spectrum Converted by PEC Cell	Fraction of Violet Emission Converted by PEC Cell	Average Photon Concentration, 1 Edge of Violet LSC	Average Photon Concentration from 1 Edge of Violet LSC Coupled to PEC Cell
0.013	0.008	0.536±0.012	0.635

Table 7-3 Table showing the average photon concentration of from one edge of the violet LSC factoring in IPCE of the PEC cell.

Fraction of Solar Simulator Spectrum Converted by Solar Cells	Fraction of Red Emission Converted by EQE Cell	Average Photon Concentration, 1 Edge of Red LSC	Average Photon Concentration from 1 Edge of Red LSC Coupled to Solar Cells
0.771	0.773	0.868±0.143	1.003

Table 7-4 Table showing the average photon concentration of from one edge of the red LSC factoring in EQE of the silicon solar cells.

For the red LSC it must be remembered that while most of the incident spectrum can be harvested by the solar cells, the EQE is low both at short wavelengths and long wavelengths whereas it is high over the whole of the narrow band edge emission from the red dye so the emitted light is converted more efficiently. Therefore, a similar calculation was performed for

the red LSC, as was described above for the violet LSC, only this time the area normalised spectra from the solar simulator and the red LSC's edge emission were multiplied by the EQE spectrum of the silicon solar cells (instead of the IPCE), to determine the light fractions converted by the solar cells. Next, the fraction of red emission photons needed to be multiplied by the red LSC's photon concentration, included in Table 7-2. It was then possible to see that by using the red LSC with the solar cells, the photon concentration was 1.003 (results in Table 7-4). So after factoring in the EQE spectrum of the silicon solar cells, it can be seen that there is little difference between using the red LSC coupled to the solar cells, or by not using the LSC and instead aiming the solar cells directly at the solar simulator. However, for the red LSC it is important to note that there is considerable variation in the photon concentrations measured from each edge, and, as can be seen in Table 7-2, two edges of the red LSC actually emit more photons per unit area than the simulator provides. It must also be remembered that the square LSC devices tested here are rather small owing to the edge dimensions needing to match the window dimensions of the PEC cell. If larger LSC plates were used then higher photon concentrations could be achieved.

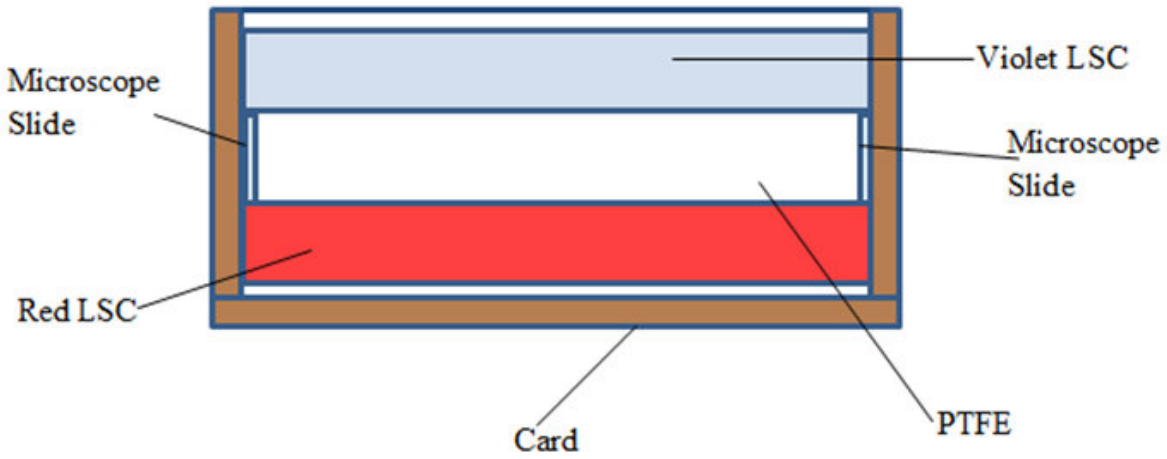


Figure 7-10 Schematic diagram of the side-on view of the LSC sample holder with the violet and red LSCs protruding slightly from the open edge.

There may be a number of explanations for the variations between the photon concentrations measured from the different edges of each LSC. One explanation is that there may have been large scale variations in the optical density of the LSCs at different regions across the surface. On a limited scale, this is observable in thickness measurements taken at different positions on each LSC surface which are given in Table 7-5 (measurements performed using digital callipers). Another cause of variation may be due to surface texturing caused by the wire-bar coater. This is very similar to the different thin-film thicknesses mentioned above, but is far more localised and essentially makes regions on the thin-film surface rougher, which will result in more light being lost due to surface scatter. This may well have a directional effect as ripples in one direction (the coating direction) can be seen across the whole of the thin-film. The variations in photon concentration seen between the different edges are likely due to all of the factors described above.

LSC	Side 1 (µm)	Side 2 (µm)	Side 3 (µm)	Side 4 (µm)	Average (µm)
Red	140±7	80±4	80±4	130±7	107.5±27.7
Violet	40±2	40±2	70±4	70±4	55±15

Table 7-5 Thin-film thickness measurements taken at the centre point of each LSC edge, for the violet and red LSCs.

As well as by increasing the size of the device (and also the window and working electrode dimensions of the PEC cell) it may also be possible to achieve higher photon concentrations by increasing the optical density of the two LSCs. This could be achieved by increasing the thickness of the thin-film layer (see Table 7-5 for the current thin-film thicknesses) rather than by further increasing the dye concentration, although this would also increase reabsorption losses. Due to the high dye concentrations already used, 2.5wt% in the violet LSC and 3.0wt% in the red LSC, higher dye concentrations were deemed to be

counterproductive as a result of the visible dye agglomeration witnessed in equivalent LSC plates with higher dye concentrations (at preliminary stages of this work). Other methods of enhancing photon concentration could include using a different short wavelength absorbing dye, or producing a smoother thin-film to reduce surface scatter, or by making the LSC (substrate + thin-film) thinner to increase photon concentration (again this would require modifying the PEC cell dimensions to fit). Making the LSC thinner would present its own problems though, such as increasing the pathlength of a photon through the thin-film layer, which increases re-absorption losses, which was clearly observable in chapter 6, section 6.2.1 for the PE-610 LSC.

To summarise, the photon concentration ratio of the violet LSC in particular must be improved in future iterations of this device. This will allow for higher PEC cell efficiencies and thus the production of more hydrogen gas, potentially leading to a reduction in the cost of hydrogen production in the future (depending on the cost of improving the violet LSC efficiency).

7.6 Dark IV, EQE, Chronoamperometry and Light IV for Solar Cells and PEC

In this work three single junction silicon solar cells were used to collect emitted photons from one of the narrow edges of the red LSC. The three solar cells each had dimensions of ~30mm by ~6mm. The solar cells were connected in series and mounted on a conductive board, which was etched so as to electrically isolate the individual back contacts of each cell from one another, in order to maintain the series circuit as shown in Figure 7-11. The three board mounted solar cells were attached to one of the narrow edges of the red LSC, which protrudes slightly from the LSC holder, with acrylic matching fluid (Cargille), refractive index 1.4917. The matching fluid was applied to the front surface of the solar cells to remove the air gap between the solar cells and the LSC, to prevent TIR at the LSC/cell interface. It should be

noted that when current sources, in this case solar cells, are added together in series, although the voltages add, the combined current of the three solar cells is equal to that of the solar cell with the lowest current, and so the three solar cells are in fact current limited by the lowest current device.

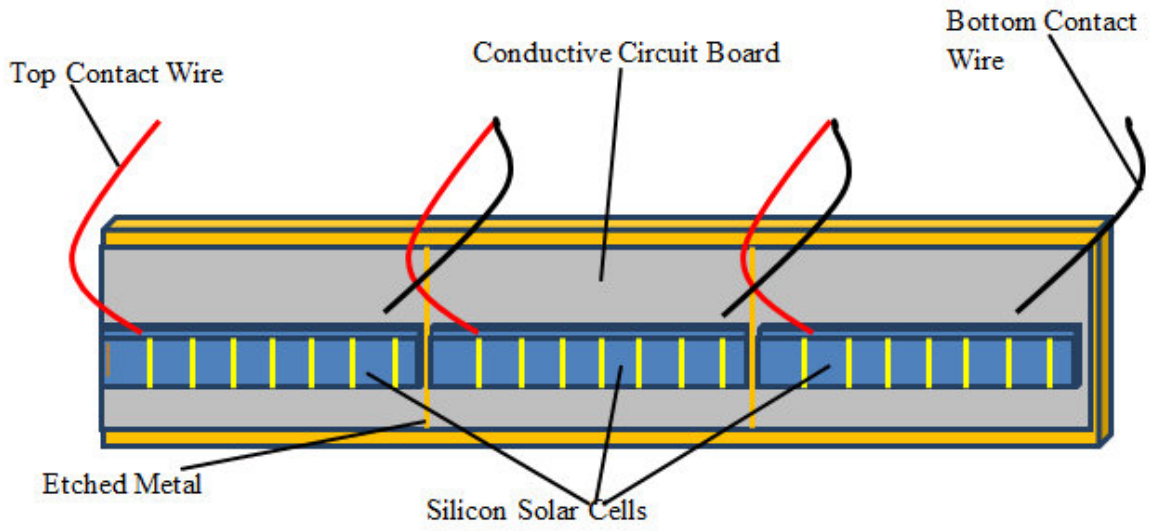


Figure 7-11 silicon solar cells connected in series mounted on a circuit board.

7.6.1 Dark IV

Figure 7-12, gives the dark IV measurements for the 3 silicon solar cells as well as the average of the 3 cells, prior to being connected in series. Although the dark current characteristics of cells p35.18.4 and p35.15.16 are similar to one another, there is a noticeable difference between these two cells and cell p35.15.13. The silicon cells were provided by Jan Goldschmidt's group at the Fraunhofer Institute for Solar Energy Systems, Germany, and the cell identifiers are those assigned by them. The shape of the dark IV curve, which has a very low current at V<0 and a larger current when V>0 is due to the asymmetric junction which is present in solar cells, which is required for the separation of charge [13]. A lower dark current is desirable as this is the recombination current, and so solar cells with lower dark currents will have a higher efficiency under light exposure.

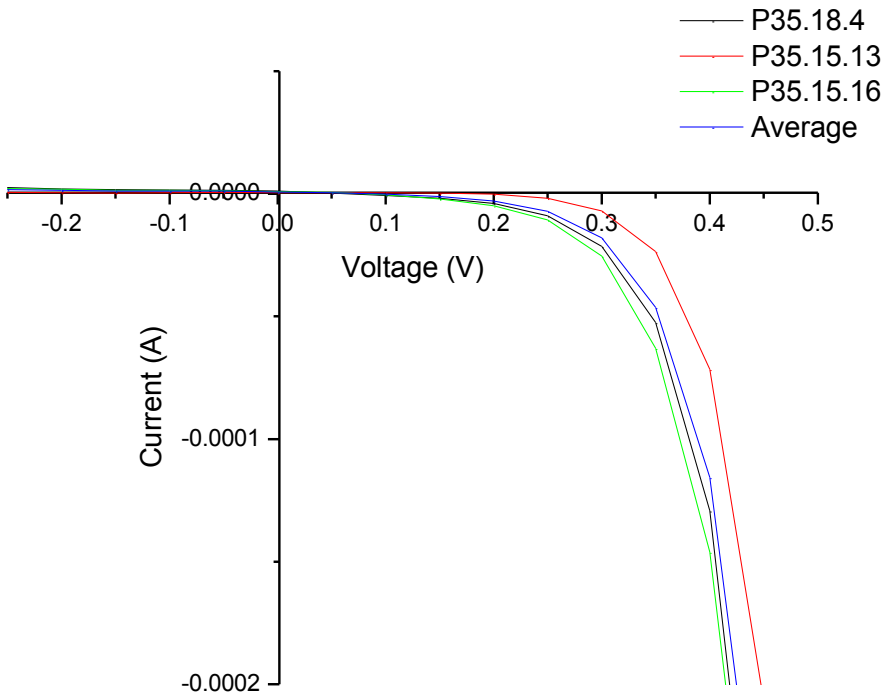


Figure 7-12 Dark IV curves for the 3 silicon solar cells measured individually and the average for the 3.

7.6.2 EQE

Figure 7-13 gives the EQE (see section 4.8 chapter 4) data for the three silicon solar cells used in this work. As can be seen in this figure, the three cells have a broad spectrum, giving high conversion efficiency ranging from a peak efficiency at ~710nm, of 90.2% for the most efficient cell, p35.15.13, to 88.8% for the least efficient cell, p35.18.4. At a wavelength of 662nm, the peak emission wavelength of the red LSC, the EQE is ~90% for the most efficient cell and ~88% for the least efficient cell.

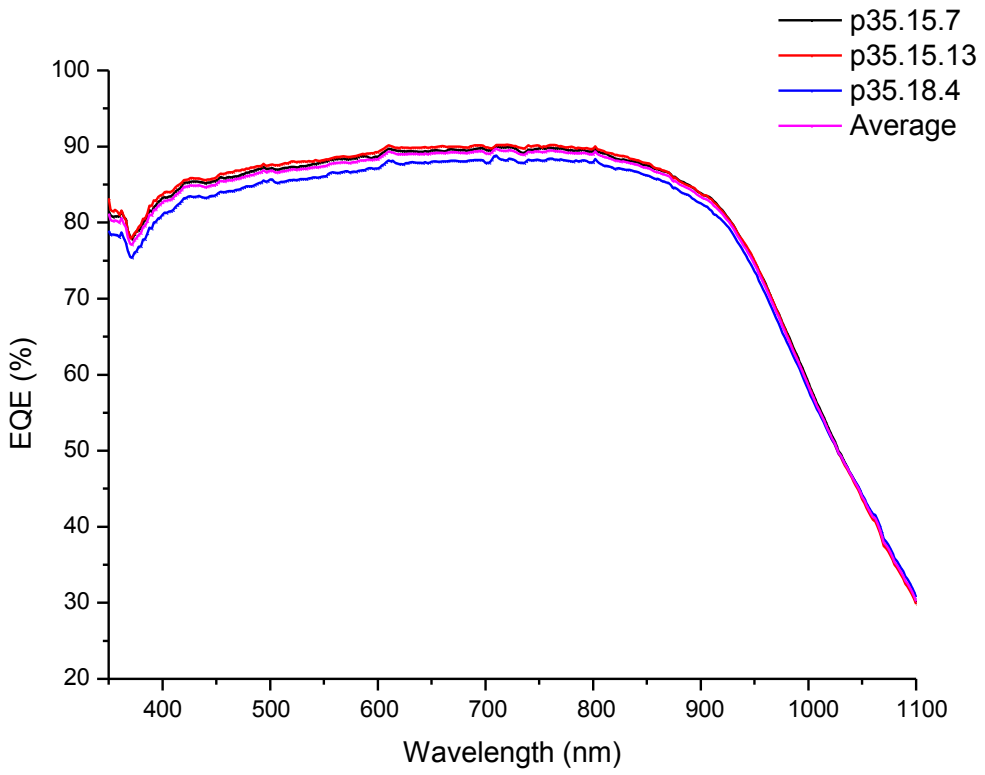


Figure 7-13 EQE spectra for each of the 3 silicon solar cells as well as an average of the 3.

High external quantum efficiencies are obviously important in order for a solar cell to achieve high power conversion efficiency, though it should be noted that for an ideal solar cell, in order to avoid undesirable thermalisation losses, the emission peak should be as close to the bandgap of the solar cell as possible. However, as can be seen from Figure 7-13, the EQE close to the bandgap of these cells is low and it only increases with a relatively shallow gradient. Therefore, even if a luminescent species with an emission spectrum located closer to the bandgap was used, the emission spectrum could only be moved ~100nm or so closer to the silicon band edge before experiencing heavy losses due to the lower EQE of the solar cell at wavelengths beyond 900nm. Alternatively, different solar cells could be selected, such as GaAs solar cells which have a bandgap at ~867nm, and usually high EQEs with a steep gradient at the threshold. However, these cells would prove significantly more expensive than silicon cells.

In summary the high EQE values of the silicon solar cells will allow them to efficiently capture the emission from the red LSC (and thus provide the potential required for the LSC/PEC device). However, there will be some thermalisation losses due to the relative positions of the emission spectrum and the bandgap.

7.6.3 Light and Dark IV for the Photoelectrochemical Cell

Figure 7-15 shows both the light and dark IV behaviour for the PEC cell alone, for instances where the Fe_2O_3 working electrode either had Co(II) catalyst applied (cobalt oxide) or not. The shape of the Fe_2O_3 light IV (blue solid line) curve is of vital important since different regions on the curve correspond to different energy regimes. For example, Figure 7-15 indicates three important regions of the light IV curve (since it is easiest to identify these regions from the IV data). Region 1 has insufficient potential difference to split water (as electron-hole recombination rates would still be too high), region 2 is a plateau region where the PEC potential difference is sufficient for water splitting to occur (electrons can be separated from holes before recombination of the two can occur), and region 3 where electrolysis is occurring.

Electrolysis is undesirable, since the LSC/PEC/solar-cell device being used in this work, is in effect a single device, whereas water electrolysis may typically be performed by using a solar cell to generate a potential between platinum electrodes (which are a separate entity from the solar cells), and which according to calculations by Brent-MacQueen [14], will be 30% less efficient than using the PEC device. If the LSC/PEC/solar-cell device had been operated in this electrolysis regime, the PEC cell would have been rendered useless and the water splitting reaction would have been run directly by the solar cells, with a lower efficiency as stated above.

Light IV measurements were performed by connecting the working and counter electrodes of the PEC to a ministat device. The ministat device was set to collect current/voltage data, and the voltage range of the IV curve was 0.6V to 1.0V vs. RHE at a scan rate of 20mV/sec, see Figure 7-14. The incident light source used was the Steuernagel Lichttechnik solar simulator with its UV filter removed (see chapter 4, section 4.2), and the PEC cell was mounted underneath the solar simulator.

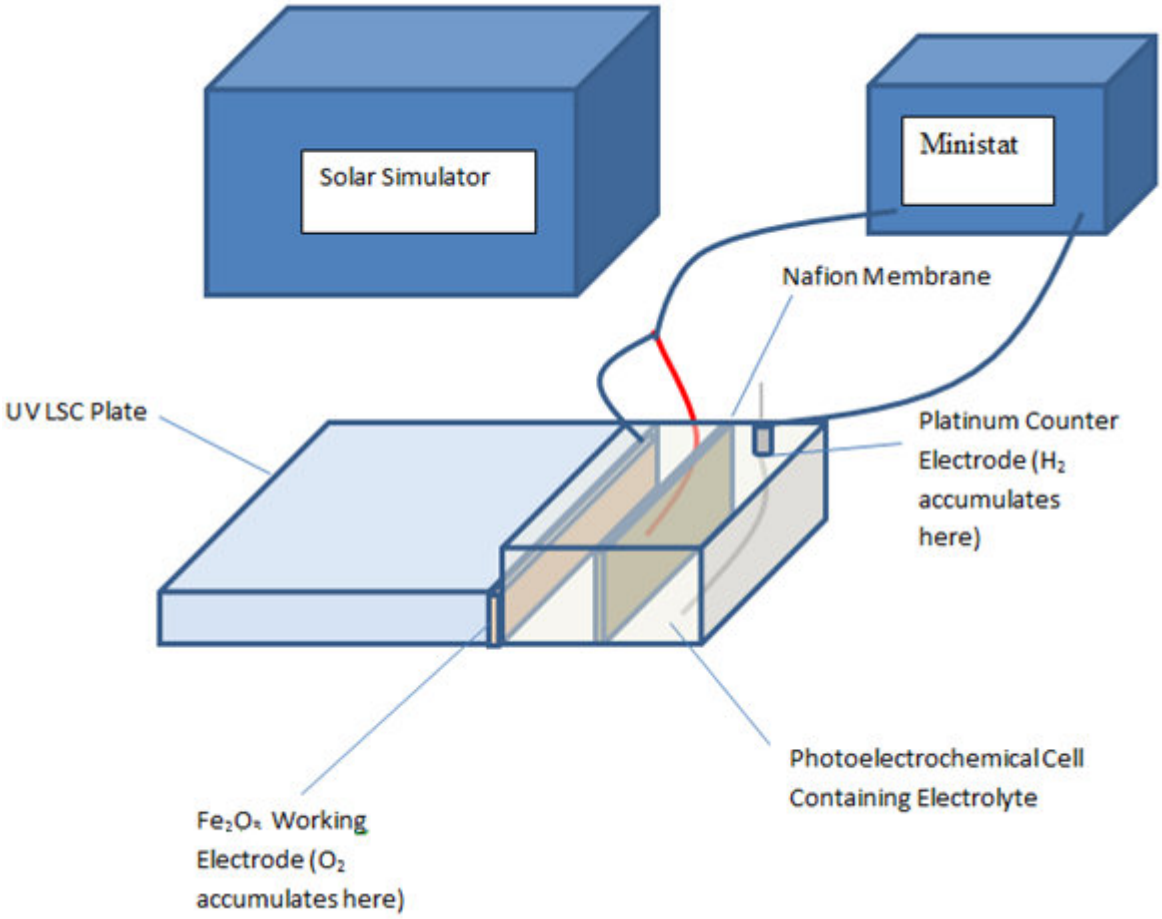


Figure 7-14 Diagram of the PEC cell light IV setup. The LSC sample holder is not shown to make the diagram clearer.

Applying a Co(II) catalyst to an Fe_2O_3 working electrode, served to shift the photocurrent onset point to a lower voltage (see Figure 7-15). This in turn raised the photocurrent in the plateau region, and ultimately results in a lower required potential for water splitting.

Additionally, the catalyst material had an effect on the shape of the light IV curve, when compared to the standard Fe_2O_3 IV curve. The difference is particularly noticeable between ~0.9V and ~1.3V, and results in the current density being higher than expected in this region. The distortion of the IV curve makes it difficult to identify where the plateau region begins. One possible explanation for this unexpected shape change may be degradation of the nafion membrane used to separate the working electrode from the counter electrode, since the non-catalyst and catalyst measurements were not performed on the same day, which in turn may have led to contaminates forming on the Fe_2O_3 working electrode [6].

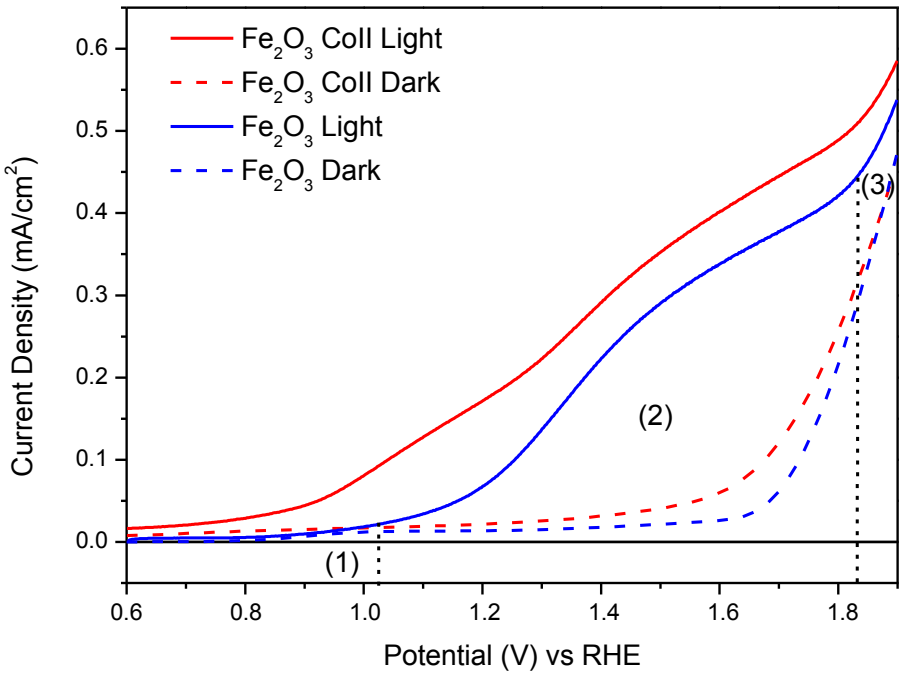


Figure 7-15 Light and dark IV curves for the Fe_2O_3 electrode, both with and without the application of the Co(II) catalyst, in the PEC, where vs. RHE means with respect to the reversible hydrogen electrode.

7.6.4 Combined Light/Dark IV curves for the Silicon Solar Cells and the PEC Cell

Figure 7-16, gives the light and dark IV curves for both the series connected silicon solar cells, and for the PEC cell utilising the Fe_2O_3 working electrode without the application of Co(II) catalyst. This figure combines all the IV data measured, which allows the intercept between the solar cells' light IV curve and the PEC cell's light IV curve to be more easily identified. The intercept, as can be seen in Figure 7-16 occurs at an operating potential, U_{op}, equal to ~1.58V, while the operating current, J_{op}, is ~1.68mA. It was necessary for the LSC/PEC/solar cell to function at, or near to these current and voltage values, so as to have the potential from the red LSC/silicon solar cells augment that of the PEC, and allow the water splitting reaction to occur, by removing excess electrons and making recombination of electrons and holes less probable. If the potential provided by the red LSC and the coupled silicon solar cells had been sufficient to raise the potential into the electrolysis regime (see region 3, Figure 7-15), then the potential would have been too high and the red LSC and silicon solar cells would have been responsible for an electrolysis reaction (see section 7.6.3). As Figure 7-16 shows, the potential generated across the solar cells was sufficient to allow for an intercept in the PEC's plateau region, allowing photoelectrochemical water splitting to occur and not electrolysis.

In Figure 7-16, the term U_{on} is the onset potential at which the photocurrent starts to rise and the plateau region begins. U_{oc} is the open circuit potential, beyond at this point the plateau region ends, and the potential is sufficient to drive electrolysis.

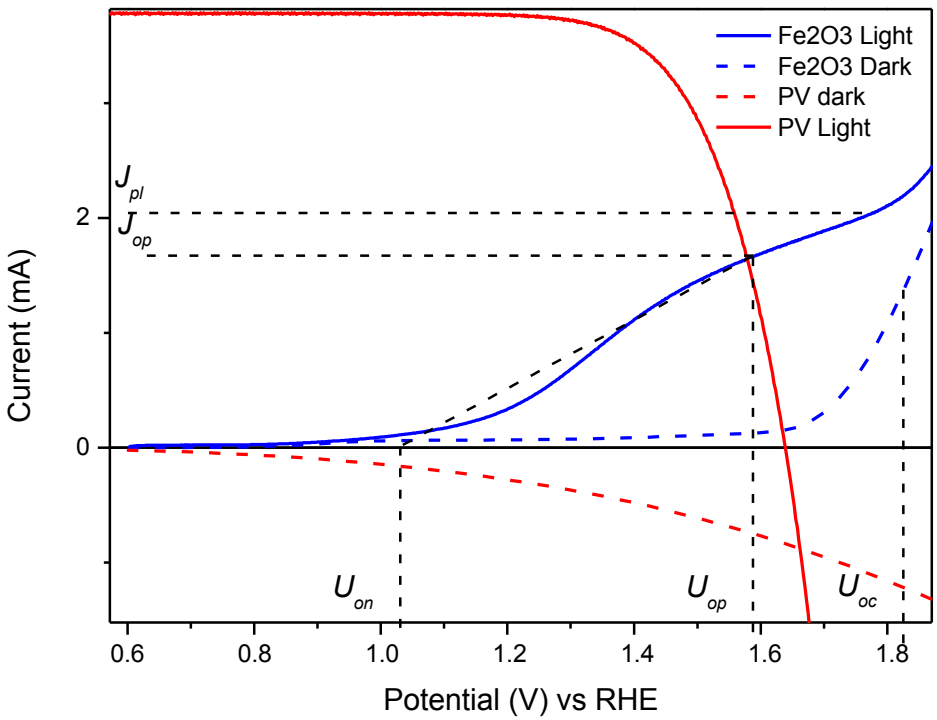


Figure 7-16 Combined light and dark IV measurements on the Fe_2O_3 working electrode (without catalyst) and the silicon solar cells in the completed PEC/LSC/solar cell device. Where RHE stands for reference hydrogen electrode.

7.6.5 Chronoampereomtry

Chronoamperometry measurements were performed by connecting the working and counter electrodes of the PEC in series with the silicon solar cells, which were optically matched to the red LSC. The LSC/PEC/solarcell system was then connected to a ministat device, and placed under a Steuernagel Lichttechnik solar simulator with its UV filter removed as shown in Figure 7-17. Figure 7-18 shows the difference between the current density measurements for when the Fe_2O_3 working electrode was without Co(II) catalyst and when the Fe_2O_3 electrode had a Co(II) catalyst. Applying the catalyst to the working electrode had a large effect on the current density, and is responsible for a ~0.074mA/cm^2 increase in the current density of the electrode, relative to the standard electrode.

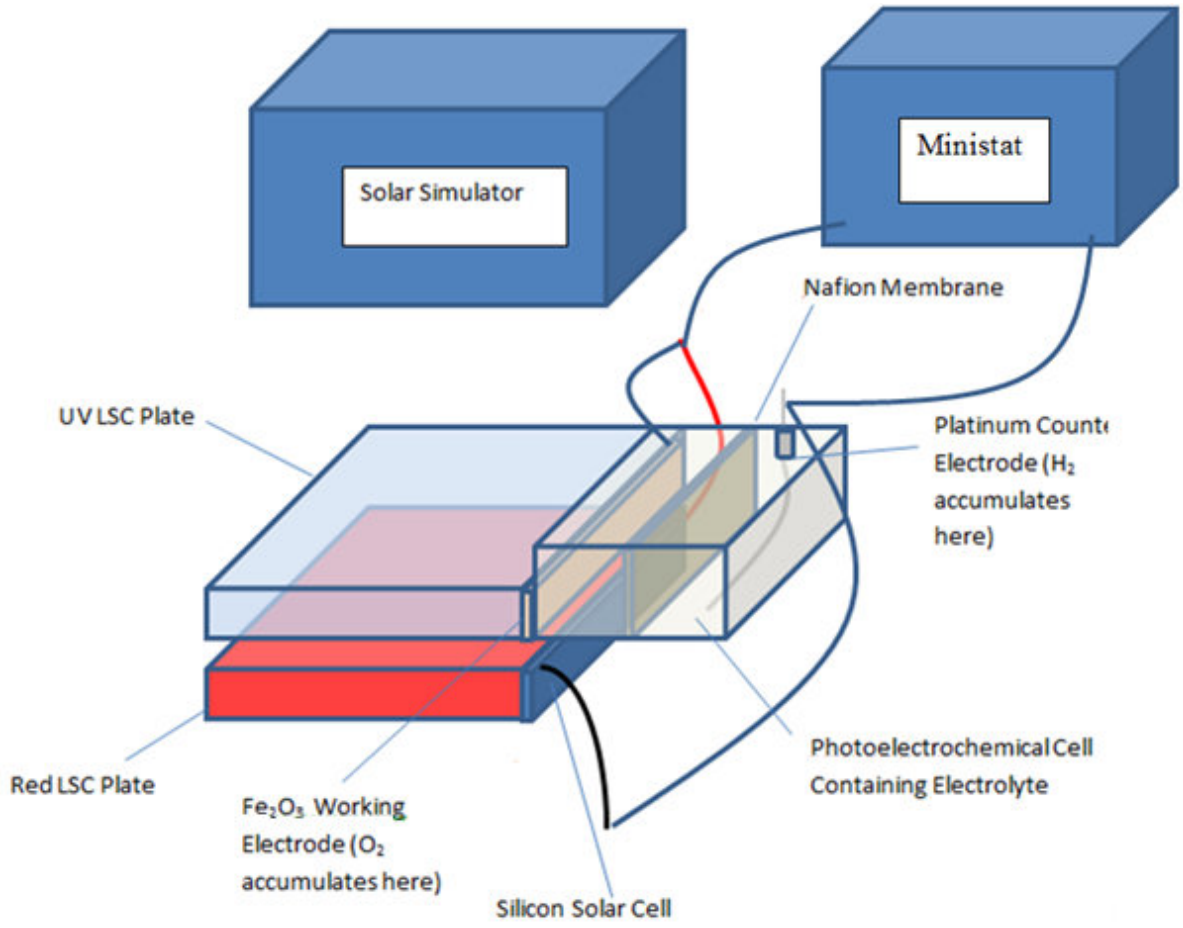


Figure 7-17 Diagram of the chronoamperometry/PEC light IV setup., The LSC sample holder is not shown to make the diagram clearer.

Chronoamperometry measurements are used to determine the photocurrent generated by the PEC/LSC system, and thus provide a comparison between the Fe_2O_3 working electrode with and without Co(II) catalyst. For each of the traces in Figure 7-18, the measurements were performed by firstly blocking the incident light source, using a thick black board, thereby preventing the light from impinging on the violet LSC and the optically coupled PEC cell. When the board was removed and the incident light was able to irradiate the violet LSC and the PEC cell again, this resulted in an effectively instantaneous peak in the measured current density induced in the PEC cell. The incident measurements were carried out for both the

PEC cell utilising the Fe_2O_3 electrode with the catalyst applied, and the Fe_2O_3 electrode without the catalyst, and in both cases the incident light was restored after ~100s, which allowed for easier comparison between the two. In addition, the long dark time duration was used to prove that only dark current was being measured (and not residual current from previous exposure to the light). After the current density peak, which occurred when the incident light was restored to the device, there was a rapid exponential decay in current density with time for both versions of the PEC (with and without photocatalyst). An average of the current density was taken for the plateau region of each graph, and each was dark current corrected. The result was an average photocurrent density of 0.30mA/cm^2 and 0.374mA/cm^2 for the standard and catalyst versions of the Fe_2O_3 electrodes respectively.

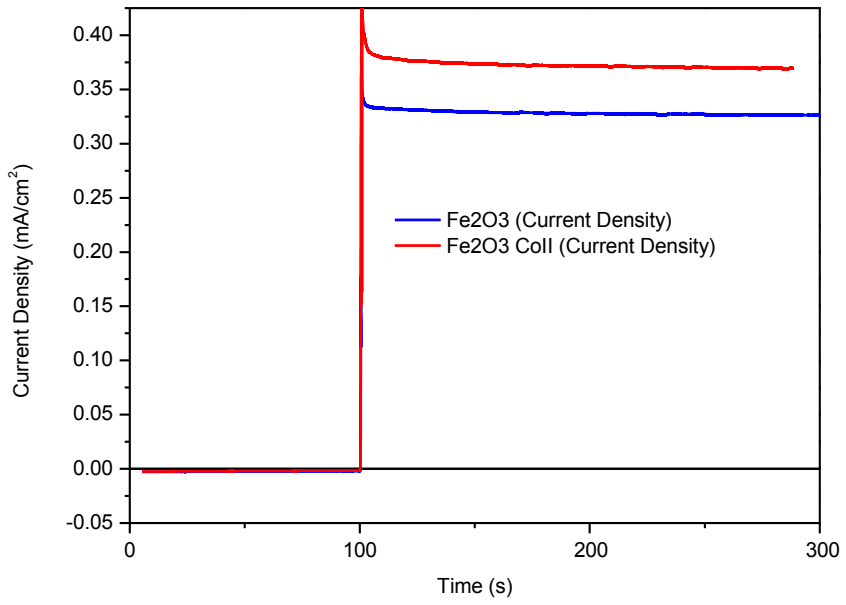


Figure 7-18 Chronoamperometry results (current against time) for both the Co(II) catalyst version of the Fe_2O_3 working electrode, and the non-catalyst version.

7.7 Red LSC Incremental light exposure

Initial measurements of current and voltage from the silicon solar cells light IV curve, when the 3 silicon solar cells were in connected series and were in contact with the edge of the red LSC, revealed that the intercept between the solar cell light IV curve and the electrode light IV curve occurred at the wrong location. The current generated by the red LSC and silicon solar cells was too high, and as a result, the intercept point (as shown by the working electrode light IV curve) occurred at too high a current and voltage, and so an electrolysis reaction was occurring. As a result, instead of the solar cells simply providing sufficient potential to prevent recombination of electrons and holes by removing excess electrons, the cells instead forced electrolysis to take place.

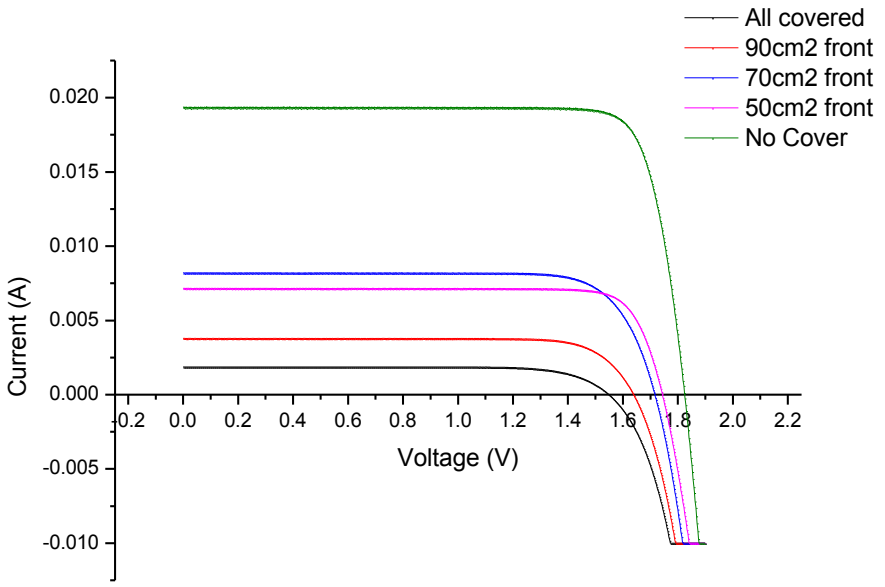


Figure 7-19 Light IV data with the red LSC coupled to the silicon solar cells, with different fractions of the red LSC's surface obstructed to control the quantity of incident light.

Figure 7-19 shows how the overabundance of photocurrent produced in the solar cells was addressed. The silicon solar cells used in this chapter had a power conversion efficiency

which was too high for their intended purpose, or alternately, it can be considered that the PL emission from the edge of the red LSC was too intense (although as stated in section 7.5, the photon concentration was just below 1). A reduction in the light intensity coupled from the edge of the red LSC was the most logical solution, since this would bring the light IV curve to an appropriate intercept point with PEC cell light IV curve as seen in Figure 7-16.

In Figure 7-19 the green curve, which has by far the highest current corresponds to the emission from the red LSC under full exposure by the incident solar simulator light source. The other IV curves in this figure are the result of partial or total coverage of the red LSC using black card positioned on the top surface of the red LSC. The black card served to obstruct a specific area of the LSC from receiving light from the incident light source. The areas covered by the card in these measurements were; $0cm^2$ (no coverage), $50cm^2$ coverage, $70cm^2$ coverage and $90cm^2$ coverage (the LSCs top surface had an area of $100m^2$). In each case the coverage started from the edge of the red LSC which was coupled to the solar cells, as demonstrated in Figure 7-20. It was found that coverage of $90cm^2$ was required in order to bring the solar cells' light IV curve to a position appropriate to intercept the PEC cell's light IV curve that optimises the photoelectrochemical process and prevents electrolysis.

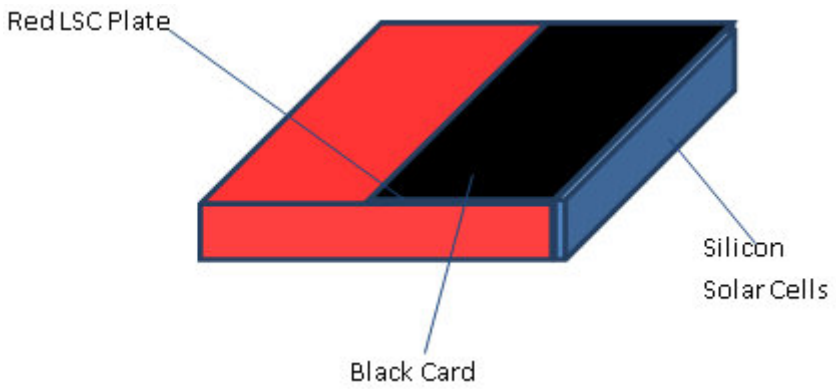


Figure 7-20 Diagram of red LSC/silicon solar cell incident light intensity obstruction.

7.8 Conclusions

In this chapter LSCs were used as a means to assist with, and to potentially reduce the cost of, producing hydrogen gas by aiding the splitting of molecules within an appropriate electrolyte material into O_2 and H_2. IPCE measurements performed on the Fe_2O_3 working electrode of the PEC, and the edge emission spectrum from a 10cm by 10cm by 0.5cm LSC doped with Fluorescent violet (Kremer), were found to be an appropriate match for one another. This was due to the IPCE of the Fe_2O_3 electrode being relatively high at, and near to, the ~450nm edge emission peak of this LSC. The fluorescent violet LSC was used to concentrate edge emitted photons onto the surface of the Fe_2O_3 electrode, serving to increase the efficiency of the PEC device.

The operating potential across the PEC cell occurs at a point at the centre of the plateau region on the PEC light IV curve, where the potential was high enough to split water, but lower than that needed for electrolysis. This point was measured to be ~1.58V, while the operating current was measured as ~1.68mA. Individually, the potential generated by the PEC/violet LSC would be sufficient to split water molecules (though it must be remembered that 4 electron-hole pairs are required to produce a single O_2 molecule [*4*]), but insufficient to prevent significant electron-hole recombination. Therefore, an additional red LSC, doped with Lumogen red 305 dye (BASF), was positioned underneath the violet LSC and optically coupled to 3 series connected silicon solar cells, attached to one of the red LSC narrow edges. The added potential generated by the red LSC/silicon solar cells was used to reduce electron-hole recombination by removing excess electrons allowing H_2 and O_2 gases to accumulate at the counter electrode and the working electrode respectively. A nafion membrane between the two electrodes served to prevent the recombination of the O2- and the H+ ions.

The IPCE of the Fe_2O_3 working electrode was measured to be ~7.9% at 370nm and at 1.6V vs. RHE, while the working electrode in the record breaking work of Kay *et al.* [11] (which

consisted of an Fe_2O_3 thin-film on an interface layer of SiO_2 and a substrate of SnO_2 glass) had an IPCE=42% at 370nm at an applied voltage of 1.23V vs. RHE. The working electrode in the work of Kay *et al.* was measured under an AM1.5G spectrum whereas the Fe_2O_3 working electrode in this chapter was measured under a solar simulator; therefore a direct comparison between the electrodes in each piece of work is difficult. However, the IPCE measured in this chapter is significantly lower than that of Kay *et al.* which suggests there is significant room for improvement of the Fe_2O_3 characterised in this chapter.

The potential generated in the red LSC/silicon solar cell system was initially too great, and as a result was responsible for driving an electrolysis reaction. Therefore, the incident light source was partially blocked from entering the red LSC by covering parts of it. Ultimately, by decreasing the red LSCs exposure to incident light from the solar simulator (by ~90%) this allowed the light IV curve of the silicon solar cells to intercept the light IV of the PEC cell at the operating current/voltage point, and thus allowed the water splitting device to work as intended, via a photoelectrochemical reaction.

Although, the device worked as intended from a potential difference generation point of view, in actuality it was far less efficient than it ultimately could have been. The average power conversion efficiency from one edge of the violet LSC, when using the Steuernagel Lichttechnik solar simulator (UV filter removed), was calculated to be 2.92±0.29%, while 4.54±0.45% for measured from one edge of the Red LSC. The largest problem was the low photon concentration of the violet LSC, which was measured at just 0.536±0.012 (for an uncoupled LSC, under a Steuernagel Lichttechnik solar simulator), but this value did not factor in the IPCE of the PEC cell. Simple calculations which did take the IPCE of PEC cell into account showed that the photon concentration had risen to 0.635, thought this result still shows that the PEC cell would have been more efficient had it been aimed at the solar simulator light source, with no LSC present. Furthermore, although the photon concentration

from the red LSC was measured on average at just 0.868±0.143 (this measurement was for the LSC without solar cells coupled). After factoring in the EQE of the silicon solar cells, the photon concentration for the red LSC rose to 1.003. Despite the relatively low efficiency of the red LSC, the coupled silicon solar cells still generated too much potential which required the red LSC to be mostly covered to reduce the output. A future, more efficient version of this device should attempt to enhance the photon concentration of the violet LSC in particular, which might be achieved by lowering the dye concentration, but simultaneously making the absorbing thin-film thicker, this may reduce any losses associated with high concentration emission quenching (but at the same time maintains or even increases the optical density). Furthermore, a better fabrication method may be used to reduce losses associated with surface roughness and defects, and a different dye might be chosen with a higher LQY (although the manufacturer claims an LQY of 82.7% [*7*], which is quite high but may have been compromised by PL quenching), less spectral overlap and a narrower emission spectrum so as to localise the emission to where the PEC cell's IPCE is higher. This study was limited by the size of the working electrode in the PEC and the size of LSC that could be easily fabricated and characterised under the solar simulator. Square substrates for the LSC were purchased but, in hindsight, 20x10cm rectangular substrates (which are still just within the limits of what can be handled in the laboratory) would have given higher concentration. In future work narrower electrodes could be used with thinner LSCs that have a greater geometric concentration. Longer electrodes allowing larger LSCs would also give higher concentration.

As far as the red LSC/solar cell system is concerned, a couple of the narrow edges had measured photon concentrations in excess of 1, with a high of 1.017±0.010 being measured, suggesting a more uniform thin-film layer would be able to increase the average photon concentration to greater than 1. Again, due to the high dye concentrations utilised in this

sample, emission quenching likely occurred, and this may be addressed in the same way as discussed above for the violet LSC. Finally, since it is wasteful in terms of resources and money to have to partially cover the red LSC to reduce solar cell potential, this might be addressed either by using lower efficiency (and cheaper solar cells), since the ones available for this project were relatively high efficiency, or by using a smaller area or thinner red LSC with a smaller area of solar cells.

Overall, despite its limitations, the proof of concept device was successful. Indeed this design has a number of significant advantages for photoelectrochemical water splitting. Previous systems [2] have always relied on transmitting the red portion of the solar spectrum directly through the photoelectrode to the solar cells (dye sensitised cells in [2]) beneath. This leads to large losses as well as a high cost owing to the need to prepare materials on transparent conductive substrates. In the approach taken in this work the LSCs remove the need to pass the red portion of the solar spectrum through the photoelectrode. Other significant advantages include reduced electrical resistances due to small area electrodes, decreased proton conducting membrane (another expensive component) areas, and the ability to prepare electrodes on non-transparent materials. Taking all these advantages into account, together with the fact that the problems encountered in this first prototype of matching of the LSC/PV output to the requirements of the LSC/PEC cell and the low concentration can be addressed in future work, this seems a promising approach worthy of further study.

Chapter 7 References

[1] Energy Technology Analysis: Prospects for Hydrogen and Fuel Cells, (2005), International Energy Agency, p70.
[2] Grätzel, M., (2001), "Photoelectrochemical Cells", Nature, 414, 338-344.
[3] Fujishima, A., and Honda, K., (1972). "Electrochemical Photolysis of Water at a Semiconductor Electrode", Nature, 238, 37-38.
[4] Walter, M., Warren, E., McKone, J., Boettcher, S., Mi, Q., Santori, E., and Lwis, N., (2010). "Solar Water Splitting Cells", Chemical Reviews, 110, p6446-6473.
[5] Bard, A. J, and Faulkner, L, R., (2001). "Electrochemicl Methods: Fundamentals and Applications: 2nd Edition", John Wiley Sons, New York.
[6] Pesci, F., (2013). Personal consultation, Imperial College London, UK.
[7] Kremer Pigmente, Pigments, Dyes and Fillers: Flourescent Violet, http://www.kremerpigments.com/shopus/index.php?cat=010703&lang=eng&product=94730 [accessed 27/6/2013].
[8] BASF, Lumogen Colorants, http://www.dispersions-pigments.basf.us/p02/USWeb-Internet/pigments/en_GB/content/microsites/pigmentsdispersions/products/Lumogen [accessed 27/6/2013].
[9] Janecek, M., (2012). "Reflectivity Spectra For Commonly Used Reflectors"Ieee Transactions On Nuclear Science, Vol. 59, No. 3,, p490-497
[10] Slooff, L., Bende, E., Burgers, A., Budel, T., Pravettoni, M., Kenny, R., Dunlop, E., and Buchtemann, A., (2008). "A luminescent solar concentrator with 7.1% power conversion efficiency", Phys. Status Solidi (RRL), 2, p257-259,
[11] Kay, A,. Cesar, I. and Gratzel, M., (2006). "New Benchmark for water Photooxidation by Nanostructured α-Fe_2O_3 Films", Journal of American Chemical Society.128, 15721-15721.
[12] Steinmiller, E., and Choi, K-S., (2009). "Photochemical deposition of cobalt-based oxygen evolving catalyst on a semiconductor photoanode for solar oxygen production", PNAS, 106, 49, p20633-20636.
[13] Nelson, J., (2003). "The Physics of Solar Cells" London: Imperial College Press.
[14] Brent MacQueen, D., (2003). "Photoelectrochemical Water Splitting", GCEP Hydrogen Workshop", Stanford University, USA, April.

Chapter 8

Conclusion

In this thesis research has been performed on the luminescent solar concentrator (LSC), a potentially low cost device used to absorb incident solar irradiation, before guiding emitted photons to its narrow edges, where solar cells are attached, for low level light concentration. Originally proposed as a method for reducing the cost of solar power generation by reducing the size of the required solar cells, the LSC has more recently found use in more novel applications, some of which feature in this thesis and are described below.

Chapter 1 of this thesis served to identify the world's growing desire, and indeed need, for additional sources of renewable energy, as a way of providing a cleaner safer environment, energy security and relief from rising energy prices. This chapter went on to identify the various technologies used in an attempt to efficiently harvest the sun's vast energy output, on both a household and industrial level. Next the LSC was described, including its benefits as a low cost solar energy harvesting device, which does not require solar tracking systems, and is capable of absorbing diffuse light opening up novel applications such as building integrated photovoltaics (PVs).

Chapter 2 described the theory behind how the LSC operates, which included information related to the incident solar spectrum and the optical behaviour of the LSC (including reflection, refraction, absorption, transmission etc.). It also described how different types of luminescent species absorb and emit radiation, before going on to identify processes that limit the optical efficiency, such as escape cone losses, common to LSCs. Lastly, this chapter

provided a brief overview of the physics involved in the operation of PV cells and photoelectrochemical cells (PECs); the two devices used in conjunction with LSCs in this work.

Chapter 3 describes the various techniques and materials which have been investigated over the years since the LSC's inception to compensate for the efficiency limitations identified in chapter 2. Such methods include the use of specular and diffuse mirrors, non-traditional mirrors such as cholesteric mirrors, plasmonics, alignment of luminescent species for directional emission, multiple stack LSCs and multiple dye LSCs. This chapter also includes information on a number of luminescent species which have been used in LSC research, for example, nanocrystals, organic dyes, metal complexes and bio-derived dyes.

Chapter 4 identifies the experimental methods used throughout this study for characterising LSCs, solar cells and PEC cells. This section also includes the methodology for fabricating LSCs including the use of spin coaters and wire-bar coaters. A description of the raytrace program used for simulation studies is also given in this chapter, as well as a list detailing all the samples featured in this work.

Chapter 5 is the first of the results chapters. This chapter discussed the characterisation of a CdSe/CdS core/shell nanorod sample, in which the nanorods were vertically self-aligned. The aims of this chapter were to assess the worth of the CdSe/CdS nanorods as an appropriate luminescent species for use in an LSC, to determine whether or not the sample did indeed contain aligned nanorods, as well as to determine the extent of the nanorod alignment and whether this method of nanorod alignment would be practical for larger LSCs. Vertical nanorod alignment was identified at the centre of the nanorod sample via the use of angular dependent spectroscopy techniques, though the alignment was found to have been lost away from sample's centre.

Raytrace simulations revealed that under a diffuse light source ideal LSC samples with vertically aligned nanorods had higher optical efficiencies than simulated samples with horizontal alignment or random orientation; a useful result for LSCs given their ability to absorb diffuse light. Due to the rapidly lost nanorod alignment away from the centre of the nanorod sample (likely due to different rates of solvent evaporation), this method of self-alignment was deemed to likely be impractical for use in practical sized LSCs. However, it is conceivable that larger LSC samples would have a correspondingly larger central region of vertically aligned nanorods.

Taking the conclusions from chapter 5 into account, future work on this project should include studying larger LSCs made with the same nanorod alignment technique, to determine if a larger central area of aligned nanorods forms (proportional to the increase in the sample's dimensions). If this is indeed the case, the edges of the sample, which contain randomly aligned nanorods, could be cut away allowing the study of a LSC which has good vertical nanorod alignment across its entire surface. Alternately, if a larger sample using this self-alignment technique did not show significant evidence of a larger region of vertical nanorod self-alignment, then efforts could be made to try and add some level of control to the rate of solvent evaporation across the surface during the fabrication process. One such method of doing this might be to control the rate of evaporation at different locations on the sample by heating specific points on the substrate. In practice such a technique would prove difficult due to heat conductance, but if successful it could prove to be a less wasteful solution than the aforementioned removal of the LSC edges (where randomly oriented nanorods exist). Ultimately, it may prove to be more appropriate to use another alignment technique such as the approach using liquid crystals described in the work of Verbunt *et al.* [1]. Such a technique, coupled to the advantages of using CdSe/CdS core/shell nanorods, could lead to a more efficient and versatile LSC.

Additional raytrace simulations could be of use in any future work on this topic. The advantages of vertically aligned nanorod LSCs under diffuse illumination have been identified in this work. However, work could be taken to further this study, by perhaps using real solar irradiance data at different locations, for example at different latitudes with different percentages of diffuse irradiance. Simulations could also factor in the changes in the sun's position, intensity and irradiance spectra at different times of the day and year, as well as testing different orientations of the nanorod sample, with the aim being to ascertain under which circumstances a vertically aligned nanorod LSC is best suited.

Chapter 6 of this thesis included work on a novel LSC concept, the large surface area, thin and flexible LSC, for low cost portable power generation. In this chapter a description is given of how a prototype flexible LSC and an accompanying solar cell holder (designed to clip solar cells to the edges of the flexible LSC) was designed, constructed and characterised. In addition, three luminescent species were considered for use in the flexible LSC, including a bio-derived species offering potentially low costs, a high Stokes-shift material with very little spectral overlap and lastly, a commonly used dye Lumogen red 305, which has a very high luminescence quantum yield. Raytrace simulations showed the value in making the substrate of the flexible LSCs as thick as is practically possible in order to optimise the optical efficiency. Raytrace simulations also revealed that for near identical simulations (with matched peak absorption coefficients), a doubling of sample size resulted in a lower rate of decrease in optical efficiency for the high Stokes-shift material, since photon pathlengths, and thus reabsorption losses, are particularly large in large, thin LSCs. Although the high Stokes-shift material proved its worth in reducing reabsorption losses, the material had a poor absorption spectrum match for harvesting the standard AM1.5g solar spectrum (and thus may be useful for a power generating window), and moreover, was made from an expensive rare earth element. Both issues would need to be addressed in future work.

Future studies on this application should include the fabrication of a larger prototype flexible LSC, with a particular focus on determining the thickest practical substrate possible e.g. thick but still light and flexible. Furthermore, work should be done to improve the quality of the thin-film layer on the flexible LSC, which should be possible since the group has subsequently acquired a vacuum bed for its wire-bar coater. Since the vacuum bed should eliminate the natural curvature of the flexible substrate material (during fabrication), this should result in better quality, more even thin-films which may also allow for thicker films to be fabricated.

Another important area of future research, as highlighted by the results in chapter 6, should be to investigate additional high Stokes-shift luminescent materials which would be useful for flexible LSCs (and LSCs in general). Although the ADS065BE material featured in chapter 6 showed promise, it was let down particularly by its high cost (as it contained a rare earth element), and poor absorption spectrum match to the AM1.5g solar spectrum. While materials with better absorption spectra are common enough, finding low cost materials with a high Stokes-shift and a good LQY presents more of a challenge. Realistically, many apparently promising luminescent materials will need to characterised in an attempt to find a material which surpasses the ADS065BE on all fronts.

Chapter 7 contained work on another novel LSC application, which focused on the use of the LSC's light concentration properties for focusing specific wavelength ranges onto the surface of a PEC (which had an Fe_2O_3 working electrode) device, and onto series connected silicon solar cells, in order to enhance the efficiency of water splitting to form H_2 gas. H_2 is a useful molecule for storing energy, and the ability to produce it cheaply is a prerequisite for a hydrogen economy.

An LSC/PEC prototype system was operated in an LSC stack configuration, in which a top violet LSC was coupled to the PEC cell, while a bottom red LSC was coupled to the silicon solar cells. The remaining edges of the LSCs were surrounded by a diffuse scattering material (to increase efficiency). The solar cells provided additional potential, which was required to reduce the recombination rate of electrons and holes. Experimental results showed that the LSC/PEC device operated at the correct voltage to photoelectrochemically split water molecules, and avoid electrolysis. However, it must be noted that as a prototype, further optimisation of the device will be needed for it reach its peak efficiency. The violet LSC in particular suffered from a low photon concentration ratio, even after taking into consideration the IPCE of the PEC cell.

Future work related to using LSCs to enhance water splitting should focus on enhancing the photon concentration of the LSCs (particularly the violet LSC). Although when the IPCE response for the PEC cell was factored in it revealed a higher effective photon concentration from the violet LSC, compared to just considering light in/light out and the dimensions of the LSC, the measurements indicated that the PEC cell would still have been more efficient if it was aimed directly at the solar simulator. Therefore, any future work would need to address the quality of the violet LSC, and the most obvious way to do this would be to fabricate a more even thin-film layer, which would cut down the obvious surface scattering. Furthermore, reducing the dye concentration, but at the same time making the thin-film layer thicker, may result in a reduction in (suspected) PL quenching losses, but would still allow the LSC to absorb plenty of incident light (similar methods would be of use for the red LSC as well). Lastly, the choice of violet dye might be worth changing to a dye with a narrower emission spectrum, so that more of the emitted photons are located closer to the higher IPCE wavelengths (although a good Stokes-shift must be maintained).

Another experiment which should be considered for future work would be to measure the amount of molecular hydrogen or oxygen extracted from the PEC cell. Although this measurement is not needed to prove the LSC/PEC/solar cell device is working, it would certainly help to determine the rate at which the device is functioning.

8.1 Outlook

At present, as was discussed in chapter 2 section 2.8, the LSC cannot compete with solar cells directly on cost per Watt terms, as was the original intention of the LSC. Due largely to the steep reduction in price of solar cells (particularly silicon solar cells) since the 1970s when the LSC was first proposed. However, this does not mean that the LSC is not of value; in fact LSCs are finding use in a variety of novel applications for which traditional solar cells are ill equipped. Building integration is an area where LSCs could find particular use, such as in power generating windows, which still allow significant visual light to pass, or in decorative facades. Chapters 6 and 7 of this thesis in particular focus on two novel LSC applications.

The LSC currently suffers from a number of sources of efficiency loss which have so far prevented it from achieving widespread use. These losses include escape cone losses, non unity LQY and narrow, or inappropriately positioned, absorption spectra. The most difficult of these losses to address has been escape cone losses, which are exacerbated by reabsorption, and it is for this reason that many LSC publications have been focused on limiting these losses. Techniques have included the investigation of high Stokes-shift materials, directional emission (alignment techniques) and a variety of wavelength selective mirrors. Crucially, some success has been demonstrated in recent years with each of these approaches, which will hopefully lead to a more promising future for LSCs.

However, it must be remembered that in order for LSCs to attain widespread use, they will have to not only increase in efficiency, but at the same time, limit costs. The author feels that

there is enough evidence it the literature, and indeed in this thesis to suggest that LSCs still have plenty of promise, especially in a world where people are becoming more conscious of the environment.

Chapter 8 References

[1] Verbunt, P., Bastiansen, C., Broer, D., and Debije. M., (2009). "The Effect of Dyes Aligned by Liquid Crystals on Luminescent Solar Concentrator Performance", Proc. 24th European Photovoltaic Solar Energy Conference, p381-384, Hamburg, Germany.

Appendix A

Authors Papers

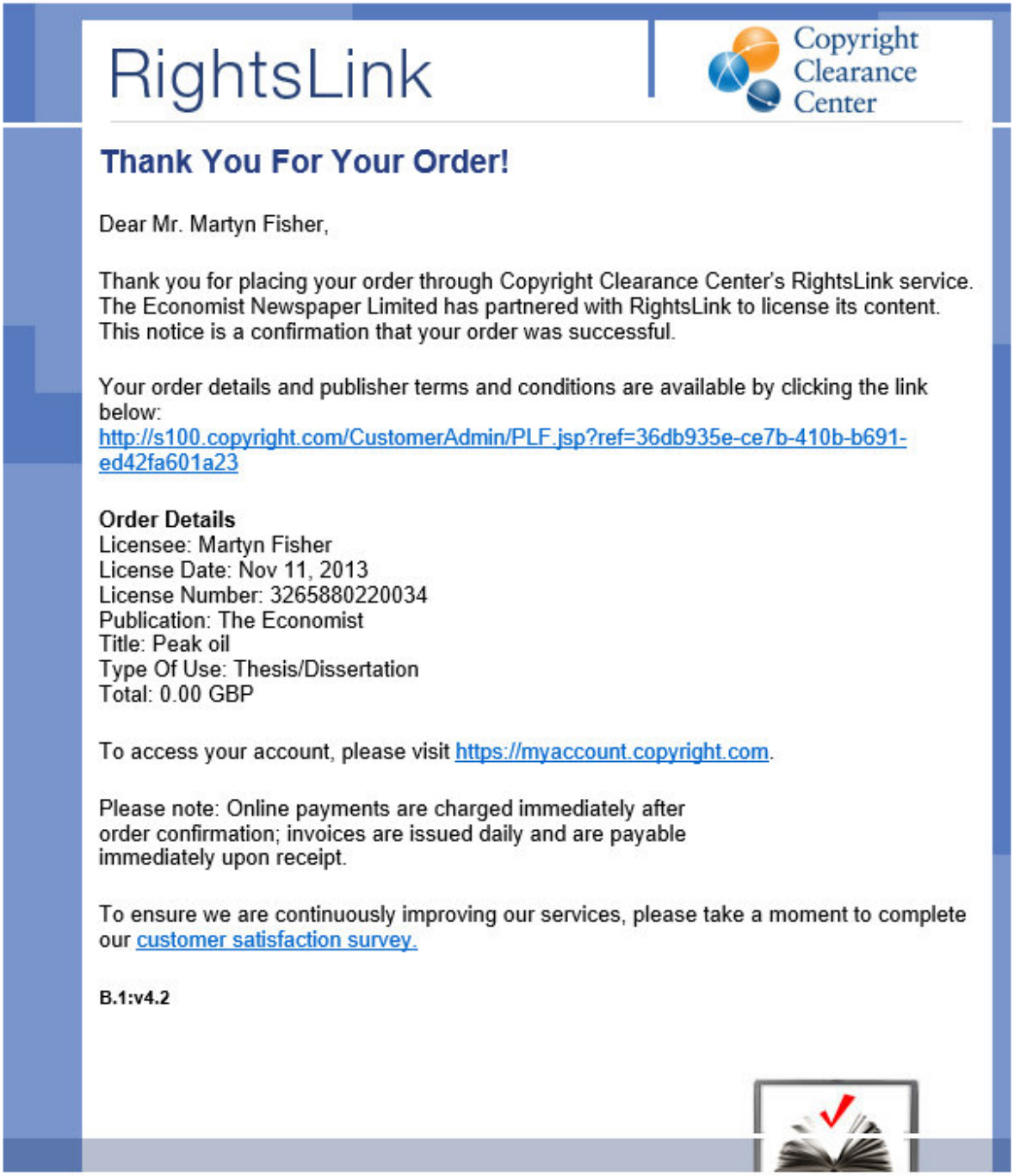
1. M Gonzalez, R Bose, M Fisher, D J Farrell, A J Chatten, J P Morseman, M W Moss, C Mclain, A Büchtemann, P P Jenkins, R J Walters, "Bio-Derived Luminescent Solar Concentrators Using Phycobilisomes", Proc. 25th European photovoltaic Solar Energy Conference / 5th World Conference on Photovoltaic Energy Conversion, (Valencia, Spain, 2010), p441-444.
2. M Fisher, D J Farrell, M González, K Trautz, R Walters and A J Chatten, "Comparisons between Homogenous and Thin-film, Ultra-thin, Flexible Luminescent Solar Concentrators"7th Photovoltaic Science Application and Technology and Exhibition,(Edinburgh, Scotland, 2011).
3. M Fisher, M Zanella, D J Farrell, L Manna, P Stavrinou, A J Chatten, "Luminescent Solar Concentrators Utilizing Aligned CdSe/CdS Nanorods", Proc. 37th IEEE Photovoltaic Specialists Conference, (Seattle, USA, 2011), P858-863.
4. M Fisher, C Ippen, D J Farrell, R J Walters, M González, K Trautz, J Tischler, J P Morseman, A Büchtemann and A J Chatten. "Flexible Luminescent Solar Concentrators Utilizing Bio-derived Tandem fluorophores", Proc. 38th IEEE Photovoltaic Specialists Conference, (Austin, USA, 2012), P3333-3338.
5. O Y Edenbosch, M Fisher, L Patrignani, W G J H M van Sark and A J Chatten, "Luminescent Solar Concentrators with a fibre Geometry", Optics Express. Accepted, March 2013.
6. F M Pesci, M Fisher, J Videira, D R Klug, A J Chatten and A J Cowan, "A Novel Luminescent Concentrator Based Solar Fuels Reactor" Under Preparation.
7. M Fisher, D J Farrell, P Stavrinou and A J Chatten, "Luminescent Solar Concentrator Utilising Aligned Arrays of Nanorods", Under Preparation.

List of Permissions Granted for Copyright Material

Page Number	Type of work: text, figure, map, etc.	Source work	Copyright holder & year	Permission to re-use
Page 24	**Figure**	The Economist, "Peak Oil", March 5th 2013. Accessed on (11/11/2013), http://www.economist.com/blogs/graphicdetail/2013/03/focus-0	**The Economist 2013**	✓
Page 31	**Chart**	NREL, "Best Research-Cell Efficiencies", www.nrel.gov/ncpv/ . Accessed on (31/8/2013).	**National Renewable Energy**	✓

			Laboratory (NREL)	
Page 33	**Figure**	Edelenbosch, O., Fisher, M., Patrignani, L., van Sark, W., and Chatten, A., (2013). "Luminescent solar concentrators with fiber geometry", Optics Express, 21, S3, pA503-A514.	**Optical Society (OSA)**	✓
Page 68	**Figure**	The Economist (cited from Bloomberg New Energy Finance), "Sunny Uplands", http://www.economist.com/news/21566414-alternative-energy-will-no-longer-be-alternative-sunny-uplands , accessed (28/8/2013).	**The Economist 2012**	✓
Page 110	**Figure**	Bailey, S., Lokey, G., Hanes, M., Shearer, J., McLafferty, J., Beaumont, G., Baseler, T., Layhue, J., Broussard, D., Zhang, Y,. Wittmershaus, B., (2007) "Optimized excitation energy transfer in a three-dye luminescent solar concentrator", Solar Energy Materials and Solar Cells, 91, p67-75.	**Elsevier Limited**	✓
Page 114	**Figure**	Mulder C., Theogarajan, L., Currie, M., Mapel, J., Baldo, M., Vaughn, M., Willard, P., Bruce, B., Moss, M., McLain, C., and Morseman, J., (2009). "Luminescent Solar Concentrators Employing Phycobilisomes", Advanced Materials, 21, 1.	**John Wiley and Sons**	✓
Page 230	**Figure**	Fisher, M., Ippen, C., Farrell, D., Walters, R., González, M., Trautz, K., Tischler, J., Morseman, J., and Chatten, A.,. (2012). "Flexible Luminescent Solar Concentrators Utilizing Bio-derived Tandem fluorophores", Proc. 38th IEEE Photovoltaic Specialists Conference, (Austin, USA), P3333-3338.	**IEEE**	✓
Page 249	**Figure**	Fisher, M., Ippen, C., Farrell, D., Walters, R., González, M., Trautz, K., Tischler, J., Morseman, J., and Chatten, A.,. (2012). "Flexible Luminescent Solar Concentrators Utilizing Bio-derived Tandem fluorophores", Proc. 38th IEEE Photovoltaic Specialists Conference, (Austin, USA), P3333-3338.	**IEEE**	✓

Proof of Permission for Copyright Material



RightsLink

Copyright Clearance Center

Thank You For Your Order!

Dear Mr. Martyn Fisher,

Thank you for placing your order through Copyright Clearance Center's RightsLink service. The Economist Newspaper Limited has partnered with RightsLink to license its content. This notice is a confirmation that your order was successful.

Your order details and publisher terms and conditions are available by clicking the link below:
http://s100.copyright.com/CustomerAdmin/PLF.jsp?ref=36db935e-ce7b-410b-b691-ed42fa601a23

Order Details
Licensee: Martyn Fisher
License Date: Nov 11, 2013
License Number: 3265880220034
Publication: The Economist
Title: Peak oil
Type Of Use: Thesis/Dissertation
Total: 0.00 GBP

To access your account, please visit https://myaccount.copyright.com.

Please note: Online payments are charged immediately after order confirmation; invoices are issued daily and are payable immediately upon receipt.

To ensure we are continuously improving our services, please take a moment to complete our customer satisfaction survey.

B.1:v4.2

Dynamic Maps, GIS Data, and Analysis Tools NREL.gov website inqu

Fisher, Martyn Hello Pamela, Yes that was exactly what I was after. I will be sure to reference NREL. Many thanks,...

Gray-Hann, Pamela [Pamela.Gray.Hann@nrel.gov]

To: Fisher, Martyn

Inbox 01 Nov

- You replied on 02/11/2013 10:27.

Martyn, sorry for the delay in responding. I've been out of the office for about a month and consequently a bit behind in
Did you still need permission to use the chart in your thesis?
Is the chart you want to use? http://www.nrel.gov/ncpv/images/efficiency_chart.jpg

If so, permission is granted as long as you reference NREL.
Thanks

Permission to use a diagram

Actions

prvs=021b47522=copyright@osa.org on behalf of pubscopyright [copy...

To: Fisher, Martyn

Inbox 12 November 2013 14:54

Dear Martyn,

Thank you for contacting The Optical Society.

Because you are the author of the source paper from which you wish to reproduce material, OSA considers your requested use of its copyrighted materials to be permissible within the author rights granted in the Copyright Transfer Agreement submitted by the requester on acceptance for publication of his/her manuscript. It is requested that a complete citation of the original material be included in any publication. This permission assumes that the material was not reproduced from another source when published in the original publication.

Please let me know if you have any questions.

Best,

Hannah

Hannah Bembia
November 12, 2013
Authorized Agent, The Optical Society

OSA Light in Focus

© The Economist Newspaper Limited, London 2012

Order Completed

Thank you very much for your order.

This is a License Agreement between Martyn Fisher ("You") and The Economist Newspaper Limited ("The Economist Newspaper Limited"). The license consists of your order details, the terms and conditions provided by The Economist Newspaper Limited, and the payment terms and conditions.

Get the printable license.

License Number	3270120267705
License date	Nov 15, 2013
Licensed content publisher	The Economist Newspaper Limited
Licensed content publication	The World In
Licensed content title	Sunny uplands
Licensed content author	
Licensed content date	Nov 21, 2012
Volume number	
Issue number	
Pages	1
Type of Use	Thesis/Dissertation
Requestor type	Student
Portion	Charts/Graphs
Circulation	1
Format	Print and electronic
Geographic Rights	Other and/or Multiple Countries
	UK
Order Reference Number	
Institution name	n/a
Course name	Optimization and Novel Applications of Luminescent Solar Concentrators
Name of instructor	
Billing Type	Invoice
Billing address	1 Patching Close
	Worthing, Bn12 6AU
	United Kingdom
Economist VAT number	GB 340 4368 76
Permissions price	0.00 USD / 0.00 GBP
VAT/Local Sales Tax	0.00 USD / 0.00 GBP
Total	0.00 USD / 0.00 GBP

ORDER MORE... CLOSE WINDOW

Copyright © 2013 Copyright Clearance Center, Inc. All Rights Reserved. Privacy statement.
Comments? We would like to hear from you. E-mail us at customercare@copyright.com

RightsLink

Copyright Clearance Center

Thank You For Your Order!

Dear Mr. Martyn Fisher,

Thank you for placing your order through Copyright Clearance Center's RightsLink service. Elsevier has partnered with RightsLink to license its content. This notice is a confirmation that your order was successful.

Your order details and publisher terms and conditions are available by clicking the link below:
http://s100.copyright.com/CustomerAdmin/PLF.jsp?ref=6583ca43-057e-4d52-acc1-6c959e1cb08c

Order Details
Licensee: Martyn Fisher
License Date: Oct 10, 2013
License Number: 3245340616349
Publication: Solar Energy Materials and Solar Cells
Title: Optimized excitation energy transfer in a three-dye luminescent solar concentrator
Type Of Use: reuse in a thesis/dissertation
Total: 0.00 GBP

To access your account, please visit https://myaccount.copyright.com.

Please note: Online payments are charged immediately after order confirmation; invoices are issued daily and are payable immediately upon receipt.

To ensure we are continuously improving our services, please take a moment to complete our customer satisfaction survey.

B.1:v4.2



RightsLink

Copyright Clearance Center

Thank You For Your Order!

Dear Mr. Martyn Fisher,

Thank you for placing your order through Copyright Clearance Center's RightsLink service. John Wiley and Sons has partnered with RightsLink to license its content. This notice is a confirmation that your order was successful.

Your order details and publisher terms and conditions are available by clicking the link below:
http://s100.copyright.com/CustomerAdmin/PLF.jsp?ref=21af4b45-063e-40a2-9869-007f26001da4

Order Details
Licensee: Martyn Fisher
License Date: Oct 14, 2013
License Number: 3247590135094
Publication: Advanced Materials
Title: Luminescent Solar Concentrators Employing Phycobilisomes
Type Of Use: Dissertation/Thesis
Total: 0.00 USD

To access your account, please visit https://myaccount.copyright.com.

Please note: Online payments are charged immediately after order confirmation; invoices are issued daily and are payable immediately upon receipt.

To ensure we are continuously improving our services, please take a moment to complete our customer satisfaction survey.

B.1:v4.2



Copyright Clearance Center RightsLink®

Home | Account Info | Help

IEEE Requesting permission to reuse content from an IEEE publication

Title:	Flexible luminescent solar concentrators utilizing bio-derived tandem fluorophores
Conference Proceedings:	Photovoltaic Specialists Conference (PVSC), 2012 38th IEEE
Author:	Fisher, M.; Ippen, C.; Farrell, D.; Walters, R.; Gonzalez, M.; Trautz, K.; Tischler, J.; Morseman, J.; Buchtemann, A.; Chatten, A.
Publisher:	IEEE
Date:	3-8 June 2012

Copyright © 2012, IEEE

Logged in as:
Martyn Fisher
Account #:
3000705971
LOGOUT

Thesis / Dissertation Reuse

The IEEE does not require individuals working on a thesis to obtain a formal reuse license, however, you may print out this statement to be used as a permission grant:

Requirements to be followed when using any portion (e.g., figure, graph, table, or textual material) of an IEEE copyrighted paper in a thesis:

1) In the case of textual material (e.g., using short quotes or referring to the work within these papers) users must give full credit to the original source (author, paper, publication) followed by the IEEE copyright line © 2011 IEEE.
2) In the case of illustrations or tabular material, we require that the copyright line © [Year of original publication] IEEE appear prominently with each reprinted figure and/or table.
3) If a substantial portion of the original paper is to be used, and if you are not the senior author, also obtain the senior author's approval.

Requirements to be followed when using an entire IEEE copyrighted paper in a thesis:

1) The following IEEE copyright/ credit notice should be placed prominently in the references: © [year of original publication] IEEE. Reprinted, with permission, from [author names, paper title, IEEE publication title, and month/year of publication]
2) Only the accepted version of an IEEE copyrighted paper can be used when posting the paper or your thesis on-line.
3) In placing the thesis on the author's university website, please display the following message in a prominent place on the website: In reference to IEEE copyrighted material which is used with permission in this thesis, the IEEE does not endorse any of [university/educational entity's name goes here]'s products or services. Internal or personal use of this material is permitted. If interested in reprinting/republishing IEEE copyrighted material for advertising or promotional purposes or for creating new collective works for resale or redistribution, please go to http://www.ieee.org/publications_standards/publications/rights/rights_link.html to learn how to obtain